

DIFFUSE PHOTON PROBES OF STRUCTURAL AND DYNAMICAL
PROPERTIES OF TURBID MEDIA:
THEORY AND BIOMEDICAL APPLICATIONS

David A. Boas
A DISSERTATION
in
PHYSICS

Presented to the Faculties of the University of Pennsylvania in Partial Fulfillment of
the Requirements for the Degree of Doctor of Philosophy

1996

Arjun G. Yodh

Supervisor of Dissertation

Robert Hollebeek

Graduate Group Chairperson

COPYRIGHT

David Alan Boas

1996

ABSTRACT

DIFFUSE PHOTON PROBES OF STRUCTURAL AND DYNAMICAL
PROPERTIES OF TURBID MEDIA:
THEORY AND BIOMEDICAL APPLICATIONS

David A. Boas

Arjun G. Yodh

Diffusing photons can be used to detect, localize, and characterize optical and dynamical spatial inhomogeneities embedded in turbid media. Measurements of the intensity of diffuse photons reveal information about the optical properties of a system. Speckle fluctuations carry information about the dynamical and optical properties. This dissertation shows that simple diffusion theories accurately model the intensity and speckle correlation signals that diffuse through turbid media with spatially varying properties and discusses possible biomedical applications.

We first look at the intensity of diffuse photons provided by a light source that is intensity modulated. This generates diffuse photon density waves (DPDW's) which exhibit classical wave behavior. We demonstrate experimentally and theoretically the refraction, diffraction, and scattering of DPDW's. Using accurate signal and noise models, we then present a detailed analysis which shows that DPDW's can be used to detect and locate objects larger than 3 mm and to characterize objects larger than 1 cm which are embedded inside turbid media with biologically relevant parameters. This diffuse photon probe should may find applications in medicine as a bed-side brain hematoma monitor, or for screening breast cancer, or other functional imaging applications.

We then consider the coherence properties of the diffuse photons as revealed by speckle intensity fluctuations and show that the temporal autocorrelation function of these fluctuations is accurately modeled by a correlation diffusion equation. Because the correlation diffusion equation is analogous to the photon diffusion equation, all concepts and ideas developed for DPDW's can be directly applied to the diffusion of correlation. We show experimentally and with Monte Carlo simulations that the dif-

fusion of correlation can be viewed as a correlation wave that propagates spherically outwards from the source and scatters from macroscopic spatial variations in dynamical and/or optical properties. We also demonstrate the utility of inverse scattering algorithms for reconstructing images of the spatially varying dynamical properties of turbid media. The biomedical applicability of this diffuse probe is illustrated with examples of monitoring blood flow and probing the depth of burned tissue.

ACKNOWLEDGEMENTS

My time spent working on this dissertation has been filled with good times during which I learned and grew intellectually and personally. It is with great pleasure that I acknowledge the many people that made this experience possible and enjoyable.

Without my advisors Arjun Yodh and Britton Chance, I would have missed the exciting developments in biomedical diffuse optics that have taken place during the last four years and the unique combination of applying their physical and physiological insights. Arjun has exposed me to the power of brainstorming, that is the process of viewing a particular problem from every imaginable angle, drawing connections to related problems, and then weeding the abundance of ideas down to a few that warrant further pursuit. I hope that I have acquired this ability from Arjun as well as the critical thinking and excitement with which he approaches scientific projects. My interactions with Brit complemented well my interactions with Arjun. Second opinions (as well as the first) are a valuable commodity and Brit's are not to be taken lightly, which is why I treasure the opportunities to discuss new and continuing projects with him. Brit's uncanny ability to sort through numerous ideas, seemingly similar and orthogonal, and pursue a long term goal has kept me pointed in the right direction at times when forces were pulling me every which way. A treasure chest of new research projects is a curse without the ability to stay focussed on a well-defined track. I am also grateful to Brit for the many opportunities that he directed my way despite my sometimes hesitant approach. His faith in my abilities has gone a long way towards my intellectual growth. Let me not forget to acknowledge the many wonderful sailing and windsurfing trips with Olympic gold medalist Britton Chance. I am deeply indebted to Arjun and Brit for their guidance. I hope to utilize the skills and knowledge that they have passed to me and pursue a healthy scientific career.

I thank the faculty of the Department of Physics and Astronomy and the Department of Biochemistry and Biophysics for exposing me to their respective disciplines in and out of the class room. I single out Michael Cohen for his sharing with me the joys of becoming intimate with Bessel functions, and the rest of my dissertation

committee, Tom Lubensky, Charlie Johnson, and Larry Gladney, for their time and interest in my dissertation research.

The support from Britton Chance's right hand, voice, feet, and artistic consultant, respectively Dot McGovern, Pat Daley, Henry Williams, and Mary Leonard, have made this dissertation possible through their efforts to keep our work funded and the lab atmosphere friendly. I appreciate their efforts as well as the efforts of Bill Penney, Alan Bonner, and Mike Carmen in the Biophysics Shop for their four years of teaching me the ins and outs of a machine shop.

Maureen O'Leary has been a friend and colleague during my five years in graduate school, starting with qualifying exam preparation, through the ups and downs of research, and the excitement and turmoil of writing a dissertation. I am happy to have had the opportunity to work through so many challenges with Maureen. I am also grateful to have had various interactions with post-docs and graduate students Hanli Liu, Peter Kaplan, Tony Dinsmore, Joe Culver, Bill Angerer, Kristin Jester, Jining Qi, and Ming Kao, Chunhua Xie, and Yunsong Yang in and out of the lab, including the many hiking expeditions with Ravi Sachidanandam.

Visiting scholar Larry Campbell made strong contributions to my understanding of photon correlation spectroscopy through our many detailed discussions on the subject. His tendency to question every confusing aspect of a problem is admirable and on many occasions led me to new levels of understanding. I hope that I have acquired some of his tenacity. Laura Zemany and Igor Meglinsky were especially helpful with the correlation measurements of flow in turbid media. I am indebted to Norm Nishioka, Kevin Schomaker, and Tom Deutsch of the Wellman Institute for the opportunity to apply correlation techniques to a clinical problem.

I am indebted to Mary Leonard for her help with many of the figures that appear in this dissertation, and to Arjun Yodh and Naomi Nagy for their comments on drafts of this dissertation.

I wish to thank my mother Karen for stimulating and encouraging my joy for problem solving which has lead me to where I am today. I thank my father Raymond

for teaching me my first computer program in 1980, which enabled me to solve ever more complicated problems.

Naomi Nagy has provided a constant supply of support and encouragement and most importantly has helped me realize that seemingly impossible goals are easily achieved through confidence and a positive outlook. I owe my future to her.

Contents

1	Introduction	1
2	The Migration of Diffuse Photon Density Waves through Highly Scattering Media	5
2.1	Diffusion Approximation to the Transport Equation	6
2.2	Diffuse Photon Density Waves	10
2.3	Interaction with Free-Space Boundaries	13
2.4	Refraction and Diffraction of Diffuse Photon Density Waves	17
2.4.1	Refraction at planar interfaces	18
2.4.2	Refraction and diffraction by spherical inhomogeneities	20
2.5	Scattering of Diffuse Photon Density Waves	24
2.5.1	An Analytic Solution	25
2.5.2	Experimental Verification of the Analytic Solution	29
2.5.3	Scattering from Multiple Objects	33
2.5.4	Semi-Infinite Media	36
2.5.5	General Heterogeneous Media	36
2.6	Time-Domain Measurements	39
2.7	Photon Migration within the P_3 Approximation	40
2.7.1	P_3 Theory	41
2.7.2	Comparison of P_3 and Diffusion Theories	43
2.8	Summary	46

3 Practical Limits to the Detection, Localization, and Characterization of Optical Inhomogeneities with Diffuse Photon Density Waves	49
3.1 The Models	50
3.1.1 Analytic Solution for the Signal	52
3.1.2 Noise Models	54
3.2 Description of Simulations	57
3.3 Detection and Localization	59
3.3.1 Detection of Absorbing Objects	60
3.3.2 Detection of Scattering Objects	64
3.4 Characterization	64
3.4.1 Characterization of Absorbing Objects	67
3.4.2 Characterization of Scattering Objects	71
3.5 Optimizing the Experimental Design	74
3.5.1 Optimizing Measurement Geometry	75
3.5.2 Optimal Modulation Frequency	78
3.5.3 Utilizing Spectral Information	80
3.5.4 Measurements at Multiple Optical Wavelengths	84
3.6 Summary	86
4 Correlation Diffusion	91
4.1 Introduction	91
4.2 Theory	92
4.2.1 Single Scattering	93
4.2.2 Multiple Scattering - Diffusing Wave Spectroscopy	97
4.2.3 Correlation Transport and Correlation Diffusion	102
4.2.4 Ergodicity	106
4.3 Experimental Results	113
4.3.1 Validity of Diffusion Equation for Media with Spatially Varying Brownian Motion	113
4.3.2 Imaging Media with Spatially Varying Brownian Motion	120

4.3.3	Validity of Diffusion Equation for Media with Spatially Varying Flow Properties	125
4.4	Monte Carlo Simulations	129
4.4.1	Homogeneous Media with Brownian Motion	130
4.4.2	Media with Spatially Varying Brownian Motion	133
4.4.3	Media with Random Flow	137
4.5	Summary	140
5	Biomedical Applications for Correlation Diffusion	143
5.1	Blood Flow Monitoring	143
5.2	Burn Diagnosis	152
5.2.1	Experiments on Phantoms	153
5.2.2	Clinical Work	163
6	Experimental Methods	171
6.1	Measuring Diffuse Photon Density Waves	171
6.1.1	Experimental	172
6.1.2	Monte Carlo	177
6.2	Photon Correlation Spectroscopy Techniques	179
6.2.1	Experimental	180
6.2.2	Monte Carlo	185
6.3	Making Resin Phantoms	187
6.3.1	Recipe for Resin Phantoms	189
6.3.2	Molds	190
6.3.3	Machining	191
6.3.4	Warnings	192
7	Summary	195
A	P_N Approximation Method	199
A.1	Photon Transport Equation	199

A.1.1	P_1 and Diffusion Approximation	203
A.1.2	P_3 Approximation	204
A.2	Correlation Transport Equation	208
B	Henyey-Greenstein Phase Function	215
C	Monte Carlo Code	217
C.1	monte.c	218
C.2	ran.c	225
C.3	ran2.c	226
C.4	ran3.c	226

List of Tables

2.1	Fits of the Analytic Scattering Theory to Experimental Measurements	31
2.2	Results of Fitting for the Optical Properties	34
5.1	Tissue Burn Depths	164
6.1	Configuration of Parallel Port	176

List of Figures

2.1	Photon Transport	7
2.2	Experimental Observation of Diffuse Photon Density Waves	14
2.3	Extrapolated Zero Boundary Condition	15
2.4	Method of Images for Semi-Infinite Media	16
2.5	Refraction of Diffuse Photon Density Waves by a Planar Interface .	19
2.6	Diffraction of Diffuse Photon Density Waves by Spherical Absorbers .	21
2.7	Diffraction Model and Ray Optics Model	22
2.8	Experimental Observation of Refraction and Diffraction by Spherical Scatterers	23
2.9	Diagram of Diffuse Photon Density Waves Scattering from Spherical Objects	27
2.10	Diffuse Photon Density Wave Sensitivity Curves	28
2.11	Validation of the Analytic Scattering Theory	30
2.12	Fitting the Analytic Scattering Theory to Experimental Measurements	32
2.13	Fitting for the Optical Properties	33
2.14	Summary of Fits for Optical Properties	35
2.15	Pulse-Train and Power Spectrum	40
2.16	Comparison of Diffusion Theory and P_3 Theory for Optical Characterization Versus Absorption Coefficient	45
2.17	Comparison of Diffusion Theory and P_3 Theory for Optical Characterization Versus Modulation Frequency	47

3.1	Experimental System for Investigating the Limits to Detection, Localization, and Characterization	51
3.2	Sources of Noise in the Amplitude and Phase of Diffuse Photon Density Waves	56
3.3	Detection of Absorbing Objects	61
3.4	Smallest Detectable Absorbing Objects	63
3.5	Detection of Scattering Objects	65
3.6	Smallest Detectable Scattering Objects	66
3.7	Simultaneous Characterization of the Object Diameter and Absorption Coefficient	69
3.8	Contributions of the Different Multimoments of the Scattered Diffuse Photon Density Wave	71
3.9	Simultaneous Characterization of Object Diameter and Scattering Coefficient	73
3.10	Optimizing the Source-Detector Geometry for Object Characterization	76
3.11	Moments Analysis of Optimizing Source-Detector Geometry	77
3.12	Optimal Modulation Frequency for Characterizing Absorbing Objects	81
3.13	Optimal Modulation Frequency for Characterizing Scattering Objects	82
3.14	Utilizing Multiple Modulation Frequencies for Characterizing Absorbing and Scattering Objects	83
3.15	Chi-Squared Valleys	85
3.16	Universal Curve for Optical Characterization	89
4.1	Speckles	93
4.2	Single Scattering Setup	95
4.3	Multiple Scattering Setup	99
4.4	Pulsed Diffusing-Wave Spectroscopy	100
4.5	Ensemble Averaged Correlation Function from a Non-ergodic System	111
4.6	Experimental Setup for Heterogeneous Brownian Motion	115
4.7	Correlation Scattering from a Spherical Inhomogeneity - Raw Data .	116

4.8	Correlation Scattering from a Spherical Inhomogeneity	118
4.9	Correlation Scattering for Different Optical Properties	119
4.10	Correlation Scattering for Different Brownian Diffusion Coefficients .	121
4.11	Tomographic Image of Brownian Motion	123
4.12	Experimental Setup of Flow through a Cylindrical Vein	126
4.13	Correlation Measurements of Flow in a Cylindrical Vein	127
4.14	Monte Carlo Simulations of Correlation Diffusion: Homogeneous Media	131
4.15	Breakdown of the Correlation Diffusion equation: Homogeneous Media	132
4.16	Monte Carlo Spherical Object Setup	134
4.17	Monte Carlo Results for Spatially Varying Brownian Motion	135
4.18	Total Momentum Transfer Distribution	136
4.19	Monte Carlo Results for Spatially Varying Brownian Motion and Ab-sorption	138
4.20	Monte Carlo Results for Spatially Varying Brownian Motion and Scat-tering	139
4.21	Random Flow	141
5.1	Absorption Spectra of Oxy- and Deoxy- Hemoglobin and Water . . .	145
5.2	Setup for Cuff Ischemia Experiments	149
5.3	Correlation Function Measured with Different Cuff Pressures	150
5.4	Measured Flow Correlated with Blood Deoxygenation and Volume .	151
5.5	Schematic of Burn Phantom	153
5.6	Schematic of Experimental Setup for Burn Study	154
5.7	Burn Phantom: $g_1(\tau)$ for Different Source-Detector Separations . .	155
5.8	Burn Phantom: $g_1(\tau)$ for Different Burn Thicknesses	157
5.9	Burn Phantom: Summary of Decay Rates	158
5.10	Solution of Diffusion Equation for Layered Media	159
5.11	Comparison of Correlation Diffusion Theory and Burn Phantom Data	162
5.12	Setup for Pig Experiments	165
5.13	Preburn Measurements	166

5.14	Correlation Functions for 48 Hour Old Burns	167
5.15	Comparison of Different Burns	168
6.1	Experimental System for Measuring Diffuse Photon Density Waves . .	173
6.2	Stepper Motor Driven Translation Stage	174
6.3	Circuit Diagram for Stepper Motor Controller	175
6.4	Monte Carlo Flow Chart	178
6.5	Experimental Setup for Photon Correlation Spectroscopy	181
6.6	Set-up for Ensemble Averaging	184

Chapter 1

Introduction

The potential to acquire information about tissue optical and dynamical properties non-invasively offers exciting possibilities for medical imaging. For this reason, the diffusion of near infrared photons (NIR) in turbid media has been the focus of substantial recent research [1, 2, 3, 4]. Applications range from pulse oximetry [5, 6, 7, 8, 9, 10] to tissue characterization [11, 12] to imaging of breast and brain tumors [13, 14, 15] and to probing blood flow [16, 17, 18, 19]. Presently, pulse-time [4, 12, 20], amplitude modulated [3, 21, 22, 23], and continuous wave sources of light [7, 24, 25] are used to probe turbid media for optical anomalies such as tumors and hematomas.

These procedures are complicated by the fact that light does not travel ballistically through turbid media. Rather, photons experience many scattering events prior to their absorption or transmission through boundaries. For many biological tissues, the absorption length for NIR light is much longer than the scattering length. Furthermore, the scattering length is much smaller than the dimensions of the sample. In this case the migration of photons is accurately described as a diffusional process. These conditions are met in breast tissue for which the reduced scattering coefficient, μ'_s (which is the reciprocal of the photon random walk step), is approximately 10 cm^{-1} and the absorption coefficient, μ_a (which is the reciprocal of the photon absorption length), is approximately 0.03 cm^{-1} [26, 27].

An intensity modulated source of light produces a wave of light energy density which propagates spherically outwards from the source through the turbid medium.

This intensity wave is called a diffuse photon density wave (DPDW) [3, 21, 22, 23]. Although microscopically the photons are diffusing and have thus lost memory of their initial direction, macroscopically the photons combine incoherently to produce a scalar wave of light energy density with a well defined phase front. The wavelength of the DPDW depends on the optical properties and source modulation frequency and is around 10 cm for typical biological samples and modulation frequencies (~ 200 MHz). The optics of DPDW's have been well defined in the recent literature [3, 21, 22, 28, 29, 30, 31, 32, 33]. In particular, studies of the distortion of DPDW's by optical inhomogeneities demonstrate that heterogeneities may be found and characterized by measuring distortions in the DPDW wavefront [28, 29, 30, 31, 34, 35].

In a different vein, when a photon scatters from a moving particle, its frequency is Doppler-shifted by an amount that is proportional to the speed of the scattering particle and dependent on the scattering angle relative to the velocity of the scatterer. Under certain conditions it is possible to measure these small frequency shifts caused by Doppler scattering events. Thus it is possible to non-invasively measure particle motions and density fluctuations in a wide range of systems. Applications include measuring the Brownian motion of suspended macromolecules [36, 37, 38, 39], velocimetry of flow fields [40, 41, 42, 43], and *in-vivo* blood flow monitoring [44, 45, 46].

Methods for using light to measure flow and density fluctuations have appeared with numerous names including Photon Correlation Spectroscopy [47], Dynamic Light Scattering [38, 39], Quasi-Elastic Light Scattering, and Diffusing Wave Spectroscopy [48, 49, 50, 51]. These methods basically fall into two categories: Doppler methods and speckle methods. The Doppler methods measure the Doppler broadening of the laser light linewidth directly using tunable optical filters. Speckle methods monitor the intensity fluctuations that arise from the beating of electric fields with slightly different frequencies. This is analogous to the acoustic beat notes that a musician uses to tune a musical instrument. The two different methods essentially give access to the same information, as is discussed by Briers [52].

Intensity and Doppler/speckle probes of random media are connected since they

both rely on the behavior of the migrating photons. The two different probes require different equipment since the first measures the average intensity and the other indirectly measures the light coherence properties, but I show that the measured signals can be accurately predicted and quantified using analogous diffusion models.

Spectroscopic intensity probes have been used since the 1930's to measure blood oxygenation non-invasively and to detect hematomas and various breast cancers. Non-invasive monitoring of average blood oxygenation is successful and widely accepted. Detection of hematomas and cancers has also been successful but is not widely accepted because of the inability to accurately characterize the anomalies. To improve anomaly characterization it is necessary to have models which accurately predict the migration of photons through turbid media with spatially varying optical properties. The photon diffusion model has been shown to work well [4, 28, 29, 53] as I will show in this dissertation.

Photon correlation spectroscopy (specifically speckle probes but including Doppler probes because of their similarity) is successfully used in industry and biology for measuring and monitoring particle size, aggregation, gelation, and flow in optically dilute and concentrated samples. Medical applications include monitoring blood flow and diagnosing the viability of burned tissue. Quantification of correlation signals from turbid samples has been limited to systems with spatially uniform optical and dynamical properties. The models I present here, which permit the quantitative analysis of signals from samples with spatially varying properties, increase the range of applicability for photon correlation spectroscopy.

The work I present here is a unification of intensity and speckle probes of turbid media. By treating them with similar theoretical models, ideas and concepts developed for one probe to be easily applied to the other probe. Chapter 2 reviews the photon diffusion model, discusses macroscopic scalar wave solutions that arise in this model (otherwise known as diffuse photon density waves) including the scattering of diffuse photon density waves from macroscopic heterogeneities, and experimentally demonstrates the validity and accuracy of this model. Chapter 3 presents a signal-to-noise

analysis which reveals the power and practical limits to the detection, localization, and characterization of optical inhomogeneities using diffuse photon density waves. Chapter 4 presents a diffusion equation for correlation and experimentally demonstrates its validity and accuracy for turbid media with spatially varying Brownian motion, flow, and optical properties. Chapter 5 discusses two biomedical applications for correlation diffusion, monitoring blood flow, and probing tissue burn depths. Chapter 6 describes the experimental methodology used throughout.

Chapter 2

The Migration of Diffuse Photon Density Waves through Highly Scattering Media

When light enters a highly scattering (or turbid) medium such as a cloud, milk, or tissue, the photons do not simply reflect back from or transmit through the medium as they would for a pane of glass. Instead, the individual photons scatter many times and thus trace out random paths before escaping from or being absorbed by the medium.

In this chapter I consider the collective properties of these scattered photons. When the intensity of a point source in a turbid medium with uniform optical properties is sinusoidally modulated, a macroscopic wave of photon density develops, and propagates spherically outwards from the source. Although microscopically the individual photons follow random walk-like trajectories, macroscopically a coherent photon density wave is created.

After experimentally verifying the existence of these waves, I examine their refraction at planar interfaces between media with different optical properties and their refraction and diffraction by objects with different optical properties than the surrounding media. I show that the perturbation of the diffuse photon density wavefronts is captured by standard refraction, diffraction, and scattering models.

The theoretical basis of this work derives from the photon diffusion equation. The radiative transport equation is a more accurate model for the migration of photons in general, but is typically difficult to handle. I start this chapter by reviewing the

assumptions that reduce the general transport equation to a diffusion equation. The classical wave behavior of DPDW's is then considered. At the end of the chapter, the breakdown of the diffusion approximation is considered as well as higher order approximations to the transport equation.

2.1 Diffusion Approximation to the Transport Equation

The linear transport equation for photons propagating in media that scatters and absorbs photons is [54, 55, 56]

$$\frac{1}{v} \frac{\partial L(\mathbf{r}, \hat{\Omega}, t)}{\partial t} + \nabla \cdot L(\mathbf{r}, \hat{\Omega}, t) \hat{\Omega} + \mu_t L(\mathbf{r}, \hat{\Omega}, t) = \mu_s \int L(\mathbf{r}, \hat{\Omega}', t) f(\hat{\Omega}, \hat{\Omega}') d\hat{\Omega}' + S(\mathbf{r}, \hat{\Omega}, t) . \quad (2.1)$$

$L(\mathbf{r}, \hat{\Omega}, t)$ is the radiance at position \mathbf{r} , traveling in direction $\hat{\Omega}$, at time t , with units of $\text{W m}^{-2} \text{ sr}^{-1}$ ($\text{sr} = \text{steradian} = \text{unit solid angle}$). The normalized phase function $f(\hat{\Omega}, \hat{\Omega}')$ represents the probability of scattering into a direction $\hat{\Omega}'$ from direction $\hat{\Omega}$. v is the speed of light in the medium and $\mu_t = \mu_s + \mu_a$ is the transport coefficient where μ_s is the scattering coefficient and μ_a is the absorption coefficient. $S(\mathbf{r}, \hat{\Omega}, t)$ is the spatial and angular distribution of the source with units of $\text{W m}^{-3} \text{ sr}^{-1}$. The photon fluence is given by

$$\Phi(\mathbf{r}, t) = \int d\hat{\Omega} L(\mathbf{r}, \hat{\Omega}, t) . \quad (2.2)$$

The photon flux, or current density, is given by

$$\mathbf{J}(\mathbf{r}, t) = \int d\hat{\Omega} L(\mathbf{r}, \hat{\Omega}, t) \hat{\Omega} . \quad (2.3)$$

Both the fluence and the flux have units of W m^{-2} . The linear transport equation neglects coherence and polarization effects. Recently, however, Ackerson *et al.* have successfully included coherence effects within a transport model [57, 58]. Photon polarization within the transport equation has also been considered by Fernandez and Molinari [59].

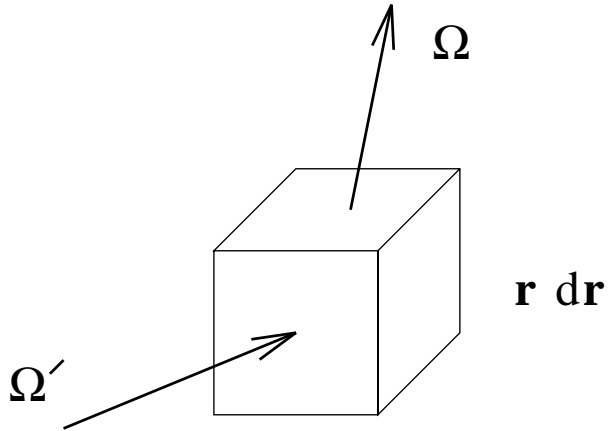


Figure 2.1: A schematic of the conservation of photons in a small element in phase space. The phase element is at position \mathbf{r} , time t , and direction $\hat{\Omega}$. Photons scattered from all directions $\hat{\Omega}'$ into direction $\hat{\Omega}$ at position \mathbf{r} must be considered. Also, the scattering from direction $\hat{\Omega}$ and absorption within the phase element must be considered as well as the flux of photons through the phase element.

The transport equation can be thought of as a conservation equation for the radiance. If we consider a small element in phase space, that is a small volume around position \mathbf{r} and a small solid angle around $\hat{\Omega}$ at time t (see fig. 2.1), the left-hand side of eq. (2.1) accounts for photons leaving the small element, and the right-hand side accounts for photons entering the small element. The first term on the left-hand side is the time-derivative of the radiance which equals the number of photons entering the element minus the number leaving. The second term accounts for the flux of photons along the direction $\hat{\Omega}$. The third term accounts for the scattering and absorption of photons within the phase element. Photons scattered from an element in phase space are balanced by the scattering into another element in phase space. The balance is handled by the integral on the right-hand side of eq. (2.1) which accounts for photons at position \mathbf{r} being scattered from all directions $\hat{\Omega}'$ into direction $\hat{\Omega}$. The second term on the right-hand side is the source of photons.

Analytic solutions of the transport equation are difficult to obtain and numerical calculations require large amounts of computational power. Solutions typically exist only for simple geometries such as planar geometries with plane wave illumination

[60], some spherical geometries [61], and a few other special cases [62].

These difficulties are reduced by considering approximate solutions to the transport equation. A standard approximation method for the transport equation is known as the P_N approximation [54, 55, 56]. The method of the P_N approximation is simply to expand the radiance, phase function, and source in spherical harmonics $Y_{l,m}$, truncating the series for the radiance at $l = N$. The radiance and source are expanded as

$$L(\mathbf{r}, \hat{\Omega}, t) = \sum_{l=0}^N \sum_{m=-l}^l \phi_{l,m}(\mathbf{r}, t) Y_{l,m}(\hat{\Omega}) , \quad (2.4)$$

and

$$S(\mathbf{r}, \hat{\Omega}, t) = \sum_{l=0}^N \sum_{m=-l}^l q_{l,m}(\mathbf{r}, t) Y_{l,m}(\hat{\Omega}) . \quad (2.5)$$

By substituting eq. (2.4) into eq. (2.2) we see that $\phi_{0,0}$ is proportional to the photon fluence. By substituting eq. (2.4) into eq. (2.3) we see that $\phi_{1,m}$ are the components of the photon flux. The $q_{l,m}(\mathbf{r}, t)$ are the amplitudes of the different angular moments of the source at position \mathbf{r} and time t .

For the phase function, we make the reasonable assumption that the scattering amplitude is only dependent on the change in direction of the photon, and thus

$$\begin{aligned} f(\hat{\Omega} \cdot \hat{\Omega}') &= \sum_{l=0}^{\infty} \frac{2l+1}{4\pi} g_l P_l(\hat{\Omega} \cdot \hat{\Omega}') \\ &= \sum_{l=0}^{\infty} \sum_{m=-l}^l g_l Y_{l,m}^*(\hat{\Omega}') Y_{l,m}(\hat{\Omega}) , \end{aligned} \quad (2.6)$$

where P_l is a Legendre Polynomial of order l and the second line is obtained using the standard angular addition rule [63]. The phase function is normalized so that $g_0 = 1$. Note that g_1 is the average cosine of the scattering angle.

The P_1 approximation is quite good when the albedo $c = \mu_s / (\mu_s + \mu_a)$ is close to unity, the phase function is not too anisotropic (e.g. $g_1 < .99$, but this depends on the optical properties), and the source-detector separation is large compared to $1/(\mu_s(1 - g_1))$. Within the P_1 approximation the radiance can be written as

$$L(\mathbf{r}, \hat{\Omega}, t) = \frac{1}{4\pi} \Phi(\mathbf{r}, t) + \frac{3}{4\pi} \mathbf{J}(\mathbf{r}, t) \cdot \hat{\Omega} . \quad (2.7)$$

Similarly the photon source can be written as

$$S(\mathbf{r}, \hat{\Omega}, t) = \frac{1}{4\pi} S_0(\mathbf{r}, t) + \frac{3}{4\pi} \mathbf{S}_1(\mathbf{r}, t) \cdot \hat{\Omega} , \quad (2.8)$$

where $S_0(\mathbf{r}, t)$ and $\mathbf{S}_1(\mathbf{r}, t)$ are respectively the monopole (isotropic) and dipole moments of the source.

Inserting eq. (2.7) and eq. (2.8) into eq. (2.1) and integrating over $\hat{\Omega}$ yields

$$\frac{1}{v} \frac{\partial}{\partial t} \Phi(\mathbf{r}, t) + \mu_a \Phi(\mathbf{r}, t) + \nabla \cdot \mathbf{J}(\mathbf{r}, t) = S_0(\mathbf{r}, t) . \quad (2.9)$$

Inserting eq. (2.7) and eq. (2.8) into eq. (2.1), multiplying by $\hat{\Omega}$, and integrating over $\hat{\Omega}$ yields

$$\frac{1}{v} \frac{\partial}{\partial t} \mathbf{J}(\mathbf{r}, t) + (\mu'_s + \mu_a) \mathbf{J}(\mathbf{r}, t) + \frac{1}{3} \nabla \Phi(\mathbf{r}, t) = \mathbf{S}_1(\mathbf{r}, t) , \quad (2.10)$$

where $\mu'_s = \mu_s(1 - g_1)$ is the reduced scattering coefficient.

We obtain the P_1 equation by decoupling eq. (2.9) and eq. (2.10) for $\Phi(\mathbf{r}, t)$,

$$\begin{aligned} & -D \nabla^2 \Phi(\mathbf{r}, t) + v \mu_a \Phi(\mathbf{r}, t) + \underline{\frac{\partial \Phi(\mathbf{r}, t)}{\partial t} + \frac{3D}{v} \left[\mu_a \frac{\partial \Phi(\mathbf{r}, t)}{\partial t} + \frac{1}{v} \frac{\partial^2 \Phi(\mathbf{r}, t)}{\partial t^2} \right]} \\ & = v S_0(\mathbf{r}, t) + \underline{\frac{3D}{v} \frac{\partial S_0}{\partial t}} - 3D \nabla \cdot \mathbf{S}_1(\mathbf{r}, t) . \end{aligned} \quad (2.11)$$

$D = v/(3\mu'_s)$ is the photon diffusion coefficient. The absorption coefficient is dropped from the photon diffusion coefficient to keep the set of approximations consistent. That is, the P_1 approximation is valid when the albedo is close to unity and the scattering is not highly anisotropic and thus $\mu_a \ll \mu'_s$. This has been discussed in greater detail by Furutsu and Yamada [64]. The scattering coefficient and scattering anisotropy do not explicitly appear in the P_1 equation (and subsequently the diffusion equation) but instead appear together as the reduced scattering coefficient. This interplay between the scattering coefficient and anisotropy to produce an “effective” scattering coefficient is known as the similarity relation [65, 66, 67].

The standard photon diffusion equation is obtained when the underlined terms in eq. (2.11) are dropped. Dropping the dipole moment of the source is justified by assuming an isotropic source. This assumption is usually supported by treating

collimated sources as isotropic sources displaced one transport mean free path into the scattering medium from the collimated source. The assumption for dropping the other terms is best seen in the frequency-domain where the time dependence of the source is taken as $\exp(-i\omega t)$. When the intensity of the source is sinusoidally modulated then the photon fluence becomes $\Phi(\mathbf{r}) \exp(-i\omega t)$. The time derivatives can then be replaced by $-i\omega$ and the rest of the underlined terms can be ignored when $3D\omega/v^2 \ll 1$. This assumption is equivalent to $v\mu'_s/\omega \gg 1$, that is the scattering frequency must be much larger than the modulation frequency.

Given these assumptions we arrive at the photon diffusion equation for $\Phi(\mathbf{r}, t)$,

$$-D\nabla^2\Phi(\mathbf{r}, t) + v\mu_a\Phi(\mathbf{r}, t) + \frac{\partial\Phi(\mathbf{r}, t)}{\partial t} = vS_0(\mathbf{r}, t) . \quad (2.12)$$

Note that in the frequency-domain the photon diffusion equation can be rewritten as the Helmholtz equation

$$(\nabla^2 + k_{AC}^2)\Phi_{AC}(\mathbf{r}) = \frac{-v}{D}S_0(\mathbf{r}) , \quad (2.13)$$

where the wavenumber is complex, i.e.

$$k_{AC}^2 = \frac{-v\mu_a + i\omega}{D} . \quad (2.14)$$

2.2 Diffuse Photon Density Waves

When the source of photons in a turbid medium is intensity modulated, e.g. $S(\mathbf{r}, t) = S_{DC}(\mathbf{r}) + S_{AC}(\mathbf{r}) \exp(-i\omega t)$, then the photon fluence will oscillate at the same frequency. This small but measurable traveling wave disturbance of the light energy density is referred to as a diffuse photon density wave [3, 21, 22, 23, 68].

Diffuse photon density waves are scalar, damped, traveling waves. These traveling waves arise formally in any diffusive system that is driven by an oscillating source such as in heat conduction [69] and chemical waves [70]. Fishkin and Gratton for example [21], have calculated the light energy density, $U(\mathbf{r}, t)$, within an optically dense homogenous media in the presence of a modulated point light source at the

origin. They then used the result and the principle of superposition to derive the light energy density in the presence of an absorbing semi-infinite plane. The oscillatory part of the solution for an infinite, homogenous dense random media with an intensity modulated point source is [21, 68]

$$\Phi_{AC}(\mathbf{r}, t) = \frac{v S_{AC}}{4\pi D r} \exp(ikr) \exp(-i\omega t). \quad (2.15)$$

S_{AC} is the source modulation amplitude, $D = v/(3\mu'_s)$ is the photon diffusion coefficient in the turbid medium where v is the speed of light in the medium and μ'_s is the reduced scattering coefficient, ω is the angular modulation frequency, and the wavenumber k is given by

$$\begin{aligned} k &= \sqrt{\frac{-v\mu_a + i\omega}{D}} \\ &= (-1)^{1/2} \left(\frac{v^2\mu_a^2 + \omega^2}{D^2} \right)^{1/4} \exp\left(-\frac{i}{2} \tan^{-1} \frac{\omega}{v\mu_a}\right) \\ &= \left(\frac{v^2\mu_a^2 + \omega^2}{D^2} \right)^{1/4} \left[i \cos\left(\frac{1}{2} \tan^{-1} \frac{\omega}{v\mu_a}\right) + \sin\left(\frac{1}{2} \tan^{-1} \frac{\omega}{v\mu_a}\right) \right]. \end{aligned} \quad (2.16)$$

This is not the only solution for k , however it is the solution which satisfies the physical condition that the amplitude is exponentially attenuated rather than growing (i.e. the imaginary part of k is greater than zero). This particular solution is obtained by extracting the -1 from the rest of the equation on the second line. An analogous equation for k can be found using the following approach (still requiring the imaginary part of k to be greater than zero):

$$\begin{aligned} k &= x + iy, \\ k^2 &= (x^2 - y^2) + i2xy, \\ x^2 - y^2 &= \frac{-v\mu_a}{D}, \\ 2xy &= \frac{\omega}{D}, \\ k &= \sqrt{\frac{v\mu_a}{2D}} \left[\left(\sqrt{1 + \left(\frac{\omega}{v\mu_a} \right)^2} + 1 \right)^{1/2} + i \left(\sqrt{1 + \left(\frac{\omega}{v\mu_a} \right)^2} - 1 \right)^{1/2} \right] \end{aligned} \quad (2.17)$$

Note that the solution for an intensity modulated point source, eq. (2.15), is a spherical wave with a complex wavenumber. The complex wavenumber indicates that the wave is exponentially attenuated and has a well defined wavelength, amplitude, and phase at all points. Qualitatively this wavelength corresponds to the root-mean-square displacement experienced by a typical photon during a single modulation period. It can be altered by modifying D , μ_a , or ω . This wave does not, on average, transport any energy. The net diffusive energy transport arises in the DC (i.e. non-oscillating) part of the process.

To experimentally verify the existence of diffuse photon density waves, we used the experimental system described in section 6.1 to generate and measure a modulated photon fluence. The measurements were made in a tank containing a highly scattering emulsion known as Intralipid [71, 72, 73, 74]. Measurements of the phase and amplitude of the diffuse photon density wave (DPDW) were measured with respect to the source at each point on a 0.5 cm square grid. The dimensions of the grid were small compared with the dimensions of the tank so that the medium is a good approximation of an infinite medium.

The results for an Intralipid concentration of 0.5% are exhibited in fig. 2.2. Constant phase countours are shown at 20 degree intervals about the source. Notice that the contours are circular, and that their radii can be extrapolated back to the source. The phase shift and the quantity $\ln|r\Phi_{AC}(\mathbf{r})|$ are plotted as a function of radial distance from the source in the inset of fig. 2.2. The relationships are linear as expected and give us the real and imaginary parts of the diffuse photon density wavenumber. From these measurements we deduce the wavelength of the diffuse photon density wave (11.2 cm). The equations for the real and imaginary parts of the wavenumber can be solved for the reduced scattering coefficient and absorption coefficient of the medium, i.e.

$$\mu_a = \frac{\omega}{v} \left[\tan \left(2 \tan^{-1} \frac{k_r}{k_i} \right) \right]^{-1}, \quad (2.18)$$

$$\mu'_s = \frac{k_r^2 + k_i^2}{3 \left(\mu_a^2 + \frac{\omega^2}{v^2} \right)^{1/2}} . \quad (2.19)$$

Here k_r and k_i are respectively the real and imaginary parts of the wavenumber. Using eq. (2.18) and eq. (2.19) we find that $\mu'_s=5.0\text{ cm}^{-1}$ and $\mu_a=0.019\text{ cm}^{-1}$ for 0.5% Intralipid at 22°C. The photon absorption can be attributed almost entirely to water [75].

2.3 Interaction with Free-Space Boundaries

Diffuse photon density waves propagating in infinite homogeneous media are spherical waves. If the turbid medium is not infinite or homogeneous, then the wave fronts are distorted. Here I consider homogeneous media that have a boundary between the turbid media and media which do not scatter light. Microscopically, the perturbation of the diffuse photon density wave arises from photons escaping into the non-scattering medium. When a photon crosses the boundary from the turbid medium into the non-scattering medium, there is no mechanism for changing the direction of the photon to return it to the turbid medium except for Fresnel reflections at the boundary. This photon escape reduces the number of photons in the wave front, thus reducing the amplitude and altering the phase. Generally the long path length photons are more likely to escape, reducing the mean path length and the DPDW wavelength. Thus the phase tends to increase because of the presence of a free-space boundary.

Within the diffusion approximation, the exact boundary condition for an index matched free-space boundary is that the component of the flux normal to the interface, pointing from the non-scattering medium into the turbid medium, must be zero. Specifically, [76, 77]

$$J_{in}(\mathbf{r}) = \frac{1}{4}\Phi(\mathbf{r}) + \frac{D}{2v}\hat{n} \cdot \nabla\Phi(\mathbf{r}) = 0 , \quad (2.20)$$

where \hat{n} is the normal to the boundary pointing away from the turbid medium and \mathbf{r} is on the boundary. This boundary condition is known as the zero partial flux boundary

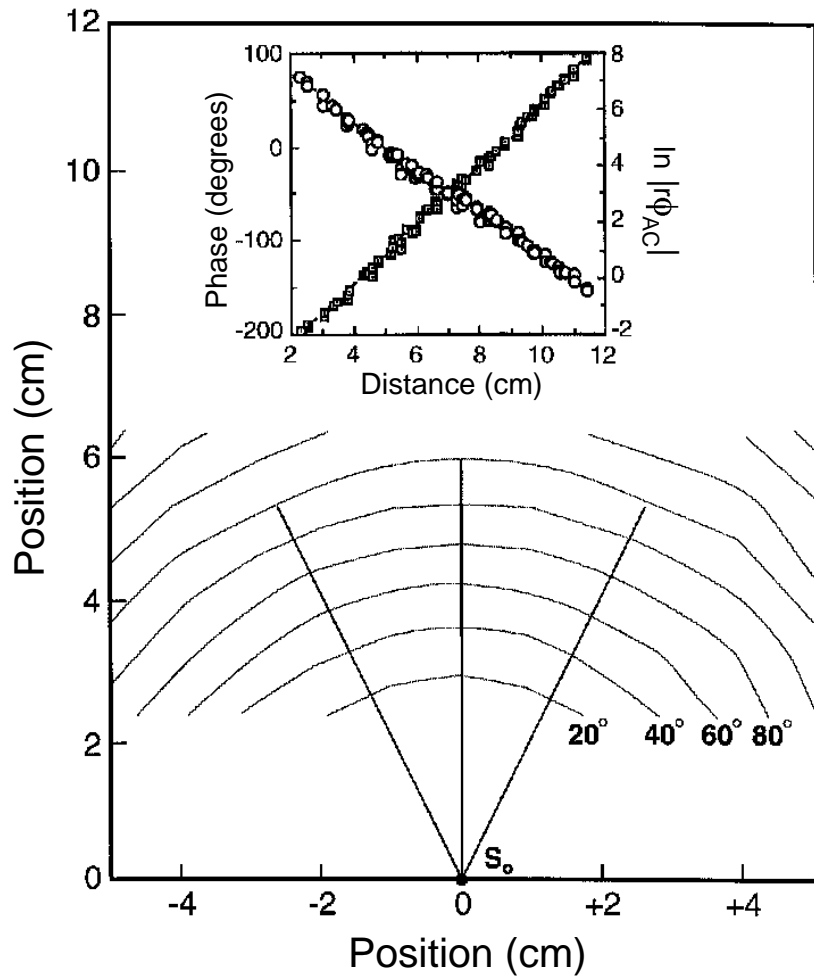


Figure 2.2: Constant phase contours shown as a function of position for a homogeneous, 0.5% solution of Intralipid. The contours are shown in 20 degree intervals. Inset: The measured phase shift (circles), and $\ln|r\Phi_{AC}(\mathbf{r})|$ (squares) are plotted as a function of radial distance from the source S_0 .

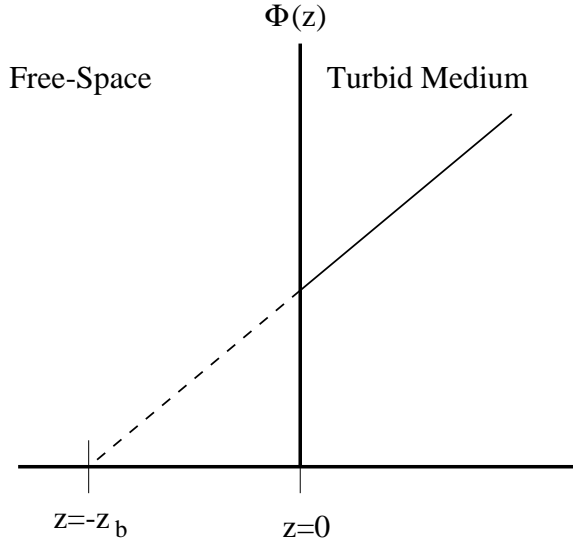


Figure 2.3: Schematic of the extrapolated zero boundary condition.

condition. At the boundary, we measure the outward component of the flux

$$\begin{aligned} J_{out}(\mathbf{r}) &= \frac{1}{4}\Phi(\mathbf{r}) - \frac{D}{2v}\hat{n} \cdot \nabla\Phi(\mathbf{r}) \\ &= \frac{1}{2}\Phi(\mathbf{r}) = -\frac{D}{v}\hat{n} \cdot \nabla\Phi(\mathbf{r}). \end{aligned} \quad (2.21)$$

The second line is derived from the condition that $J_{in} = 0$ on the boundary and shows that what we measure on the boundary is proportional to the fluence and the component of the flux normal to the boundary.

Generally it is difficult to obtain analytic solutions of the diffusion equation using the zero partial flux boundary condition. Instead the approximate extrapolated zero boundary condition is used. This requires the fluence to be zero at a distance of $2/(3\mu'_s)$ from the actual boundary. For example, for a semi-infinite medium with the boundary at $z = 0$ and the turbid medium at $z > 0$ the extrapolated zero boundary condition requires $\Phi(z_b) = 0$, where $z_b = -2/(3\mu'_s)$. This extrapolation distance comes from a linear extrapolation of the fluence at the boundary to the zero crossing point (see fig. 2.3). It is argued that $z_b = -0.7104/\mu'_s$ gives better agreement with the photon transport equation [78, 79]. Here I use $z_b = -2/(3\mu'_s)$ to remain consistent with the recent literature (e.g [76]).

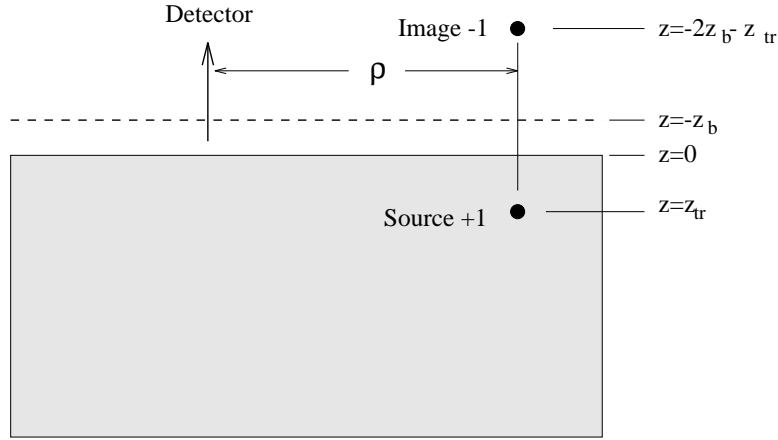


Figure 2.4: Schematic of source and image source positions for a semi-infinite medium.

For a semi-infinite medium, the solution of the diffusion equation (with the extrapolated zero boundary condition) is easily obtained by using image sources. That is an image of the real source is formed by reflection of the real source about the plane of the extrapolated zero boundary (see fig. 2.4). Note that collimated sources are usually approximated as isotropic point sources which are displaced a distance $z_{tr} = l^* = 1/\mu'_s$ from the collimated source. Given the source and image source configuration shown in fig. 2.4, the solution of the diffusion equation for a semi-infinite medium with a collimated source on the real boundary is

$$\Phi(\rho_d, z_d) = \frac{vS \exp(ik\sqrt{\rho_d^2 + (z_d - z_{tr})^2})}{4\pi D \sqrt{\rho_d^2 + (z_d - z_{tr})^2}} - \frac{vS \exp(ik\sqrt{\rho_d^2 + (z_d + z_{tr} + 2z_b)^2})}{4\pi D \sqrt{\rho_d^2 + (z_d + z_{tr} + 2z_b)^2}}. \quad (2.22)$$

The source is at $\rho = 0$ and $z = 0$ while the detector is at $\rho = \rho_d$ and $z = z_d$. A useful form of eq. (2.22) is when the detector is on the real boundary ($z_d = 0$) and $\rho \gg z_{tr}$. Under these conditions eq. (2.22) reduces to

$$\Phi(\rho_d, 0) = \frac{vS \exp(ik\rho)}{4\pi D \rho^2} \left[-4ik(z_b^2 + z_b z_{tr}) \right]. \quad (2.23)$$

If there is a mismatch in the indices of refraction between the turbid medium and free-space then the exact boundary condition is not the zero partial flux boundary condition because photons are being reflected at the interface back into the turbid

medium. In this case the exact boundary condition is [76, 77]

$$J_{in}(\mathbf{r}) = \frac{1}{4}\Phi(\mathbf{r}) + \frac{D}{2v}\hat{n} \cdot \nabla\Phi(\mathbf{r}) = R_\phi \frac{1}{4}\Phi(\mathbf{r}) - R_j \frac{D}{2v}\hat{n} \cdot \nabla\Phi(\mathbf{r}), \quad (2.24)$$

where R_ϕ and R_j are respectively the reflection coefficient for the isotropic fluence and the reflection coefficient for the anisotropic flux. They are given by [76]

$$R_\phi = \int_0^{\pi/2} 2 \sin \theta \cos \theta R_{\text{Fresnel}}(\theta) d\theta, \quad (2.25)$$

$$R_j = \int_0^{\pi/2} 3 \sin \theta \cos^2 \theta R_{\text{Fresnel}}(\theta) d\theta, \quad (2.26)$$

where $R_{\text{Fresnel}}(\theta)$ is the Fresnel reflection coefficient for unpolarized light [76]

$$\begin{aligned} R_{\text{Fresnel}}(\theta) &= \frac{1}{2} \left(\frac{n_{in} \cos \theta' - n_{out} \cos \theta}{n_{in} \cos \theta' + n_{out} \cos \theta} \right)^2 \\ &+ \frac{1}{2} \left(\frac{n_{in} \cos \theta - n_{out} \cos \theta'}{n_{in} \cos \theta + n_{out} \cos \theta'} \right)^2 \quad \text{when } 0 \leq \theta \leq \theta_c, \\ &= 1 \quad \text{when } \theta_c \leq \theta \leq \pi/2. \end{aligned} \quad (2.27)$$

The angle of incidence, θ , is given with respect to the boundary normal, the refracted angle, θ' , is given by $n_{in} \sin \theta = n_{out} \sin \theta'$, and n_{in} and n_{out} are respectively the index of refraction inside and outside the turbid medium. This condition is called the partial flux boundary condition. The partial flux boundary condition can be reduced to an extrapolated zero boundary condition where

$$z_b = \frac{1 + R_{eff}}{1 - R_{eff}} \frac{2}{3} l^*, \quad (2.28)$$

where

$$R_{eff} = \frac{R_\phi + R_j}{2 - R_\phi + R_j}. \quad (2.29)$$

This boundary condition is described in detail by Haskell *et al.* [76] and Aronson [77].

2.4 Refraction and Diffraction of Diffuse Photon Density Waves

In this section I present experiments which illustrate the refraction and diffraction of diffuse photon density waves. I demonstrate that the refraction of these waves at

planar interfaces is well described by Snell's Law [22]. In addition, I demonstrate that simple diffractive and refractive models can be used to understand the scattering of these waves by absorptive and dispersive objects embedded in an otherwise uniform system [28].

2.4.1 Refraction at planar interfaces

Fig. 2.5 demonstrates the refraction of these waves in three ways. A planar boundary has been introduced, separating the lower medium, with Intralipid concentration $c_l=1.0\%$ and light diffusion coefficient D_l , from the upper medium, with Intralipid concentration $c_u= 0.25\%$ and light diffusion coefficient D_u . In fig. 2.5 contours of constant phase are drawn every 20° for the propagation of the DPDW from the lower medium to the upper medium. The contours below the boundary are the homogenous media contours (without reflection); they are obtained before the partition is introduced into the sample. The contours above the boundary are derived from the diffuse photon density waves transmitted into the less concentrated medium. As a result of the detector geometry, the closest approach to the partition is about 1 cm.

We expect a number of general results. First, the wavelength in the less dense medium ($\lambda_u = 14.8$ cm) should be greater than the wavelength of the diffuse photon density wave in the incident medium ($\lambda_l = 8.17$ cm). This was observed. The ratio of the two wavelengths should equal the ratio of the diffusional indices of refraction of the two media. Specifically we see, as expected, that $\lambda_u = \lambda_l \sqrt{D_l/D_u} = \lambda_l \sqrt{c_l/c_u}$ (this relation holds when absorption is negligible). Furthermore, we would expect that the apparent source position (S_i), as viewed from within the upper medium, should be shifted from the real source position ($S_o = 4.0 \pm 0.2$ cm) by a factor $\lambda_l/\lambda_u = 0.55$ as predicted by Snell's law for paraxial waves. This is what we find within the accuracy of this measurement. Using the radii from the full contour plots we see that the apparent source position is shifted from 4.0 ± 0.2 cm to 2.0 ± 0.25 cm from the planar interface.

Finally, fig. 2.5 explicitly demonstrates Snell's law for diffuse photon density

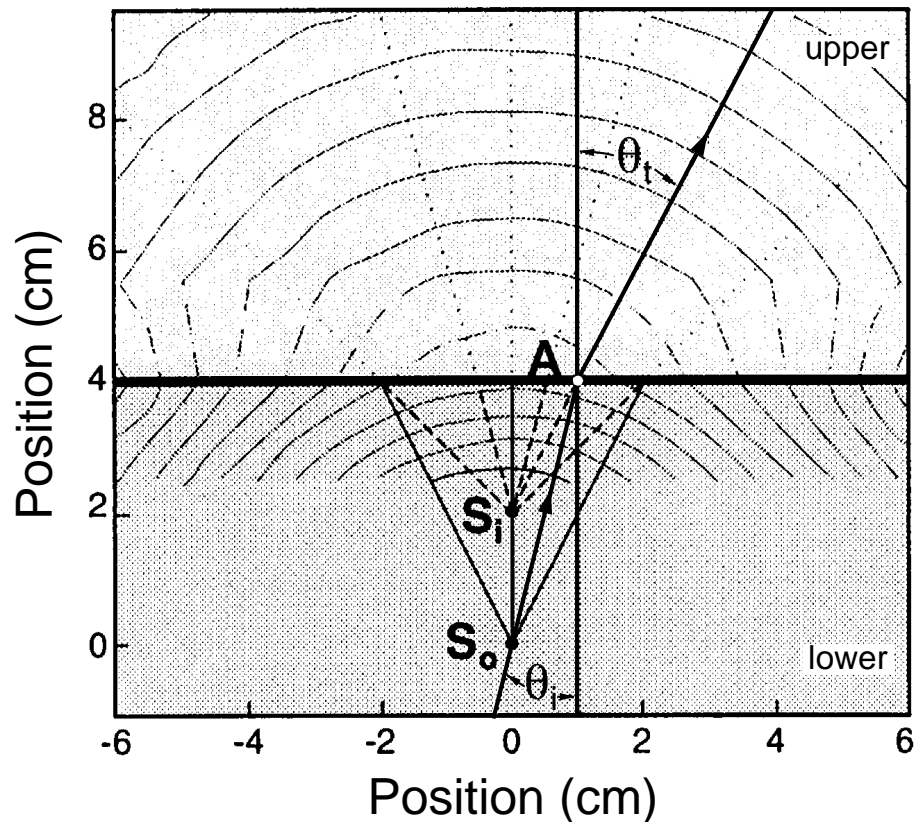


Figure 2.5: Constant phase contours (in 20 degree intervals) as a function of position showing the propagation of a diffuse photon density wave across a planar boundary that separates 1% concentrated Intralipid from 0.25% Intralipid. S_o , source position; S_i , apparent source position ; A, point on boundary; θ_i , angle of incident ray; θ_t , angle of refracted ray. The solid lines are obtained directly from data. The dot-dashed lines are obtained by interpolation over large distances, and are drawn to show the irregularities at large angles.

waves. This can be seen by following the ray from S_o to the point A at the boundary, and then into the upper medium. The ray in the lower medium makes an angle $\theta_i = 14^\circ$ with respect to the surface normal. The upper ray is constructed in the standard way between the apparent source position S_i , through the point A on the boundary, and into the medium above the boundary [80]. It is perpendicular to the circular wavefronts in the less dense medium and makes an angle $\theta_t = 26.6^\circ$ with respect to the boundary normal. Within the accuracy of the experiment, we see that $\sin \theta_i / \sin \theta_t = 0.54 \approx \lambda_l / \lambda_u$, so that Snell's law accurately describes the propagation of diffuse photon density waves across the boundary. The wavefronts become quite distorted when the source ray angle exceeds ~ 30 degrees. These irregularities are a consequence of total internal reflection, diffraction, and spurious boundary effects.

2.4.2 Refraction and diffraction by spherical inhomogeneities

Here I present measurements of diffuse photon density wavefront distortions that arise when these waves are perturbed by purely absorptive or dispersive homogeneous spheres. In general one would expect both refractive and diffractive processes to affect the wavefronts. Unfortunately, our intuition from conventional optics is of limited applicability, since we must work in the near field. Measurements of wavefront distortions from purely absorbing spheres are reasonably well described by a simple diffraction model whereby the diffuse photon density wave is scattered by an absorbing disk of the same diameter. The pure dispersive case is qualitatively different. Here a ray optic model works well for scatterers characterized by a larger light diffusion coefficient relative to that of the surrounding turbid medium, but a diffractive model is required under the opposite conditions.

The diffraction of DPDW's by absorptive spheres is illustrated in fig. 2.6. The contours of constant phase and amplitude are plotted for a DPDW traveling in different concentrations of Intralipid and diffracting around a 4.0 cm diameter absorptive sphere. The sphere was saturated with ink so that the fraction of incident light transmitted through the sphere was below the detection limit of $\sim 10^{-6}$. Nevertheless, the

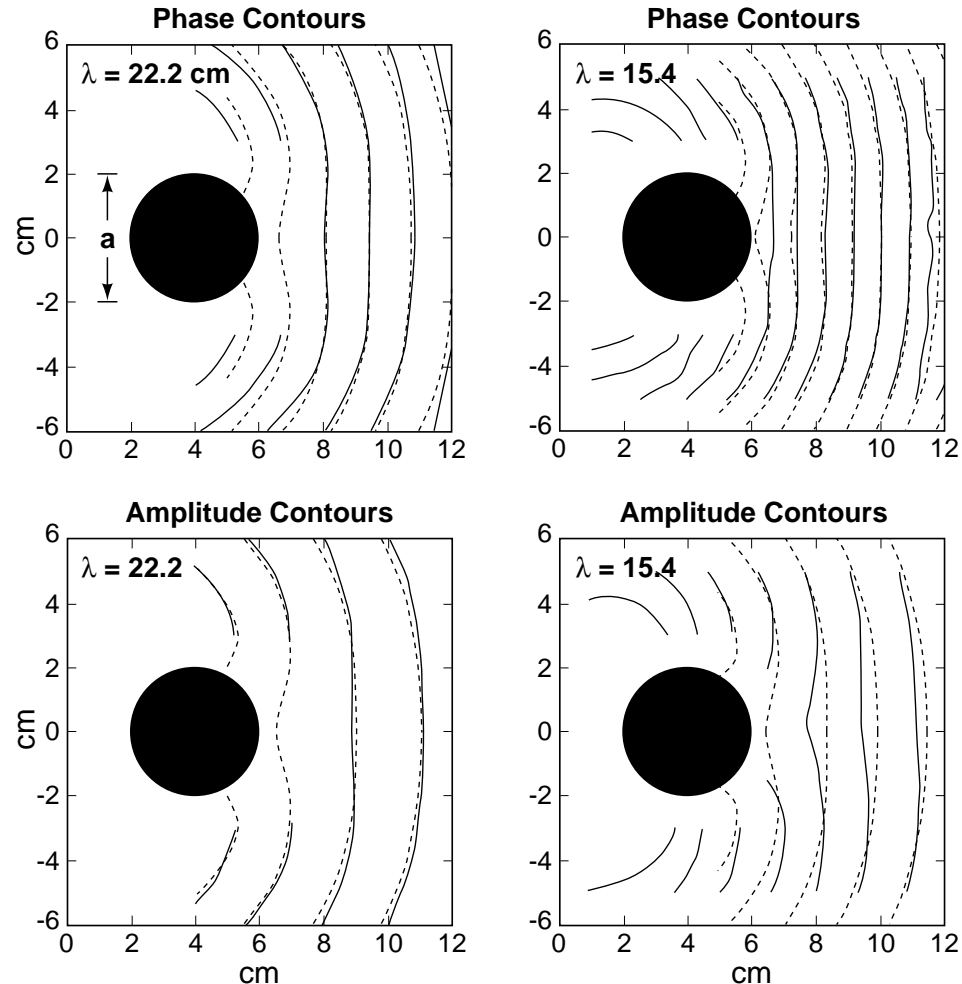


Figure 2.6: The diffraction of a diffuse photon density wave by a spherical absorber with a diameter of 4.0 cm. The light source is at the origin and generates a wave with a wavelength of 22.2 cm in the plots on the left, and a wavelength of 15.4 cm in the plots on the right. Our experimental (theoretical) results are the solid (dashed) curves. The phase contours are plotted every 20 degrees and the amplitude contours are plotted in decreasing intervals of e^{-1} .

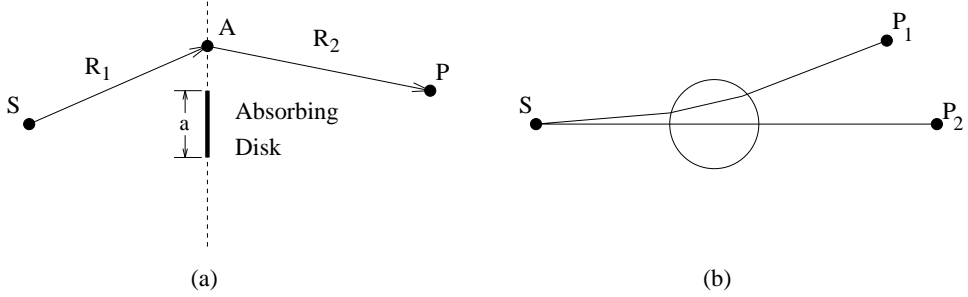


Figure 2.7: (a) In the diffraction model the sphere is replaced by an absorbing disk of the same diameter ($a=4.0$ cm) which lies in a plane through the center of the sphere. R_1 is the distance from the source, S , to a point A in the diffraction plane (dashed line) and R_2 is the distance from A to the image point, P . Here we take the z-axis to be normal to the diffraction plane, and we let the diffraction plane coincide with the xy-plane (i.e. $z=0$). The wavefront at P is calculated by integrating the standard Kirchoff equation over the diffraction plane. (b) In the ray model the wavefront is calculated by determining the phase and amplitude of rays which are refracted through a spherical lens.

wavefronts on the other side of the sphere are detected. These wavefronts are formed by the diffraction of the wave around the sphere.

Here, I have modeled this effect in a simple way. In the model, I replaced the sphere by a totally absorbing disk of the same diameter. The disk was chosen to lie in a plane containing the center of the sphere, with surface normal pointing in the z direction. The diffraction from this disk can be calculated using the standard Kirchoff construction [81]

$$\Phi(x_p, y_p = 0, z_p) = \frac{kz_p}{2\pi i} \int_S dx dy \Phi(R_1) \frac{\exp(ikR_2)}{R_2^2} \left[\frac{i}{kR_2} + 1 \right]. \quad (2.30)$$

The construction is depicted in fig. 2.7a. Here $\Phi(R_1)$ is the complex amplitude of the photon fluence in the plane of the disk, R_1 is the length of the vector from the source at position $R_s = (x_s = 0, y_s = 0, z_s)$ to a point $A = (x, y, z = 0)$ on the diffraction plane, R_2 is the length of the vector going from A to the detection point $R_p = (x_p, y_p = 0, z_p)$. The Green's function is derived from the point source solution for diffuse photon density waves in an infinite homogeneous medium so that k is complex. Specifically, the Green's function for this problem is derived from

a superposition of Green's function solutions of the Helmholtz equation. I chose a superposition to satisfy Dirichlet boundary conditions on the diffraction plane at $z=0$. Therefore, eq. (2.30) is derived from the integral of $\Phi(R_1)\frac{\partial G_D(R_2, R'_2)}{\partial z}dxdy$ over the diffraction plane, with $G_D(R_2, R'_2) = [\exp(ikR_2)/R_2 - \exp(ikR'_2)/R'_2]/4\pi$, where $\mathbf{R}_2 = \mathbf{R}_p - \mathbf{A}$, $\mathbf{R}'_2 = \mathbf{R}'_p - \mathbf{A}$, and \mathbf{R}'_p is just the image of \mathbf{R}_p reflected about the diffraction plane.

The experimental (theoretical) results are the solid (dotted) curves in fig. 2.6. The simple model approximates the measured wavefront distortion reasonably well. Note that there are no free parameters in the fit. The model appears to fit the experimental results better for bigger ratios of diffuse photon density wavelength to object diameter. Of course, the function $\Phi(R_1)$ in the plane of the disk is only approximately correct as a result of shadowing and diffraction by the front portion of the sphere. A similar effect will modify the scattered wave. This effect is expected to be larger as the wavelength decreases as observed in fig. 2.6. Nevertheless the model captures the qualitative physics of the scattering.

The constant phase contours (solid line) arising from the scattering of a non-absorptive sphere are shown in fig. 2.8. The Intralipid surrounding the sphere had the same concentration in both experiments, but the concentration of Intralipid inside the sphere was either lesser (fig. 2.8a) or greater (fig. 2.8b) than the surrounding medium. The observed patterns are different. These effects can be approximated using a ray optics model in the first case and a diffraction model in the second case.

In the ray optic model the scatterer is treated like a spherical lens with a different diffusional index of refraction than the surrounding medium. The basic idea of the model is depicted in fig. 2.7b. The complex wave amplitude is calculated from the amplitude and phase for points along the rays emerging from the source. Some of the rays were refracted through the sphere, others were not. This model ignores multiple scattering in the sphere since the waves are heavily damped.

Again, we do not expect the model to give perfect quantitative agreement with the measurements since diffraction effects are omitted. However, when the rays trans-

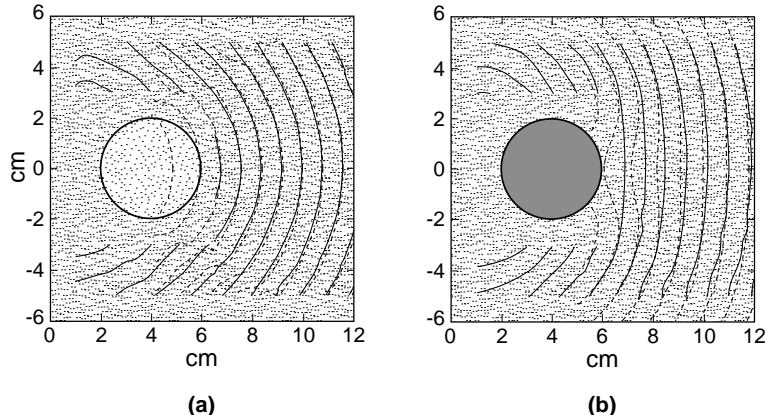


Figure 2.8: The scattering of a diffuse photon density waves by purely dispersive spheres. (a) The Intralipid concentration within the spherical shell is 0.125%, less than the surrounding medium. (b) The Intralipid concentration is 2.8%, greater than the surrounding medium. For both, the surrounding Intralipid is the same, the source is located at the origin, the sphere has a diameter of 4.0 cm, and is centered at $x=4.0$ cm, $y=0.0$ cm. The phase contours are drawn every 20 degrees for the experimental (solid lines) and theoretical (dashed lines) results. The theoretical results were calculated in (a) by the ray model and in (b) by the diffraction model.

mitted through the sphere are attenuated less than the rays outside of the sphere, we would expect diffraction effects to be negligible. This is the case when the sphere has a smaller concentration of Intralipid than the surrounding medium, and the expected behavior was observed (see fig. 2.8a). For near axis rays the model also predicts an apparent source position at $z_s = 3.5$ cm. This is easily verified by standard ray construction techniques.

The ray method does not work well for dense spheres. The dense sphere acts more like an absorber, since the diffuse photon density wave is significantly attenuated upon traveling through the sphere. For this reason one might expect the purely diffractive model discussed earlier to work better. Indeed this is what was observed (see fig. 2.8b).

2.5 Scattering of Diffuse Photon Density Waves

The previous section showed that diffuse photon density waves are distorted by the presence of optical inhomogeneities. The degree of distortion is determined by the characteristics of the inhomogeneity such as its position, shape, size, and scattering and absorption properties. We saw that in some cases the perturbation can be modeled using a simple diffraction or ray optic model. A better theory for the observed perturbation is desirable for many reasons. In particular, the simple models discussed in the previous section only work for specific differences in the optical properties and specific source-detector positions relative to the inhomogeneity. That is, the object must be placed between the source and detector, and it must be highly absorbing relative to the background or have a smaller scattering coefficient with no absorption contrast. Since the Helmholtz equation is known to describe the transport of DPDW's in a piecewise homogeneous media [22, 82], we expect that an exact solution exists for the scattering of DPDW's by spherical objects [29, 30, 31]. The solutions will be similar to, and simpler than, the theory of Mie scattering [83] often used in optics.

In this section I derive the analytic solution of the Helmholtz equation for a piecewise homogeneous system consisting of a spherical object composed of one highly scattering medium embedded in a second highly scattering medium of infinite spatial extent. This solution is easily extended to semi-infinite media using the extrapolated zero boundary condition [4, 54, 56, 76]. The analytic solution is compared with experimental data in order to assess the theory's predictive power, and a simple inverse localization algorithm is demonstrated to determine the size and location of a spherical object. Finally, the theory is extended to include more complex problems in imaging.

2.5.1 An Analytic Solution

The derivation of the analytic solution for the scattering of DPDW's from spherical inhomogeneities begins with the Helmholtz equation (eq. (2.13)). In the presence of a spherical heterogeneity, the photon fluence is found by constructing a general solution

to eq. (2.13) outside and inside the sphere and applying the appropriate boundary conditions. It is natural to analyze the problem in spherical coordinates whose origin coincides with the center of the spherical object (see fig. 2.9). The general solution outside the sphere is a superposition of incident and scattered waves [63], i.e.

$$\Phi_{out} = \Phi_{inc} + \Phi_{scatt} \quad (2.31)$$

where

$$\begin{aligned} \Phi_{inc} &= \frac{vS_{AC}}{4\pi D|\mathbf{r} - \mathbf{r}_s|} \exp(ik^{out}|\mathbf{r} - \mathbf{r}_s|) \\ &= i \frac{vS_{AC}k^{out}}{D} \sum_{l=0}^{\infty} j_l(k^{out}r_<) h_l^{(1)}(k^{out}r_>) \sum_{m=-l}^l Y_{l,m}^*(\theta_s, \phi_s) Y_{l,m}(\theta, \phi) \end{aligned} \quad (2.32)$$

is the spherical wave created by the source and incident on the sphere.

$$\Phi_{scatt} = \sum_{l,m} \left[A_{l,m} j_l(k^{out}r) + B_{l,m} n_l(k^{out}r) \right] Y_{l,m}(\theta, \phi) \quad (2.33)$$

is the wave scattered from the object.

Inside the sphere, the general solution is

$$\Phi_{in} = \sum_{l,m} \left[C_{l,m} j_l(k^{in}r) + D_{l,m} n_l(k^{in}r) \right] Y_{l,m}(\theta, \phi) . \quad (2.34)$$

Here, $j_l(x)$ and $n_l(x)$ are Spherical Bessel and Neumann functions respectively, $h_l^{(1)}(x)$ are the Hankel functions of the first kind, $Y_{l,m}(\theta, \phi)$ are the spherical harmonics, k^{out} and k^{in} are the complex wavenumbers outside and inside the sphere respectively, \mathbf{r} (\mathbf{r}_s) is the position of the detector (source) measured from the center of the sphere, and $r_<$ ($r_>$) is the smaller (larger) of $|\mathbf{r}|$ and $|\mathbf{r}_s|$. The unknown parameters ($A_{l,m}$, $B_{l,m}$, $C_{l,m}$, $D_{l,m}$) are determined using the following boundary conditions: (a) Φ must be finite everywhere except at a source, (b) Φ_{out} must asymptotically approach a spherically outgoing wave as $r \rightarrow \infty$, (c) the flux normal to the boundary must be continuous, i.e. $D_{out}\hat{r} \cdot \nabla \Phi_{out} = D_{in}\hat{r} \cdot \nabla \Phi_{in}$ where D_{out} (D_{in}) is the photon diffusion coefficient outside (inside) the sphere, and (d) the photon fluence must be continuous across the boundary, i.e. $\Phi_{in} = \Phi_{out}$ at $r = a$ [56, 82].

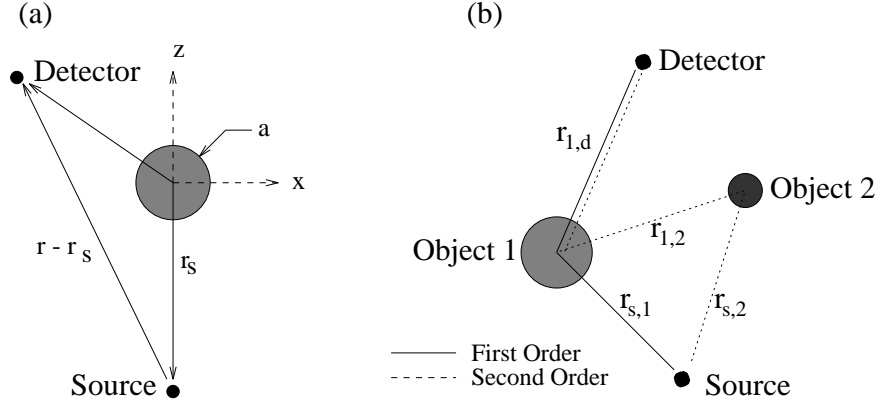


Figure 2.9: To solve the Helmholtz equation for a spherical boundary it is natural to use spherical coordinates with the origin at the center of the object (a). The source is positioned on the z-axis ($\theta_s = \pi$) to exploit the azimuthal symmetry of the problem, and the relevant distances between the source, object, and detector are indicated in the figure. Scattering from multiple objects is diagrammed in (b). The first and second order waves scattered from the first object are illustrated by the solid and dashed line respectively. The relevant distances are indicated in the diagram.

Considering these boundary conditions and using the orthogonality relation for the spherical harmonics [84], I find

$$A_{l,m} = -i \frac{v S_{AC} k^{out}}{D} h_l^{(1)}(k^{out} z_s) Y_{l,m}^*(\pi, 0) \left[\frac{D_{out} x j_l'(x) j_l(y) - D_{in} y j_l(x) j_l'(y)}{D_{out} x h_l^{(1)'}(x) j_l(y) - D_{in} y h_l^{(1)}(x) j_l'(y)} \right] , \quad (2.35)$$

$$B_{l,m} = i A_{l,m} , \quad (2.36)$$

$$C_{l,m} = -i \frac{v S_{AC} k^{out}}{D} h_l^{(1)}(k^{out} z_s) Y_{l,m}^*(\pi, 0) \left[\frac{D_{out} x h_l^{(1)}(x) j_l'(x) - D_{out} x h_l^{(1)'}(x) j_l(x)}{D_{out} x h_l^{(1)'}(x) j_l(y) - D_{in} y h_l^{(1)}(x) j_l'(y)} \right] , \quad (2.37)$$

$$D_{l,m} = 0 , \quad (2.38)$$

where $x = k^{out} a$, $y = k^{in} a$, $\mathbf{r}_s = (r = z_s, \theta = \pi, \phi = 0)$, and j_l' and $h_l^{(1)'} \equiv h_l^{(1)'}(x)$ are the first derivatives of the functions j_l and $h_l^{(1)}$ with respect to the argument. Placing the source on the z-axis exploits the azimuthal symmetry of the problem leading to $A_{l,m} = C_{l,m} = 0$ for $m \neq 0$. The distortion of the wave is entirely dependent on the parameters $k^{out} = k(\omega, \mu_s^{out}, \mu_a^{out})$, $k^{in} = k(\omega, \mu_s^{in}, \mu_a^{in})$, D_{out} , D_{in} , \mathbf{r}_s , and the object

radius a . In general the infinite sum for Φ_{out} converges, permitting the sum to be truncated after obtaining the desired precision. The proceeding calculations require no more than 20 terms in the series to obtain better than 10^{-5} precision, which far exceeds experimental precision. On a Sun Microsystems (Mountain View, CA) Sparc 2, Φ_{out} can be calculated 10-100 times per second (depending on the above mentioned parameters).

For the special case wherein the heterogeneity is a perfect absorber, I satisfy the zero partial flux boundary condition

$$\frac{1}{4}\Phi(\mathbf{r}) - \frac{D}{2v}\frac{\partial}{\partial r}\Phi(\mathbf{r}) = 0 \quad (2.39)$$

at $r = a$. Of course $\Phi_{in} = 0$. The solution in this case is

$$A_{l,m} = -i\frac{vS_{AC}k^{out}}{D}h_l^{(1)}(k^{out}z_s)Y_{l,m}^*(\pi, 0) \left[\frac{j_l(x) - \frac{2k^{out}}{3\mu'_s}j'_l(x)}{h_l^{(1)}(x) - \frac{2k^{out}}{3\mu'_s}h_l^{(1)\prime}(x)} \right] . \quad (2.40)$$

$$B_{l,m} = iA_{l,m} , \quad (2.41)$$

$$C_{l,m} = 0 , \quad (2.42)$$

$$D_{l,m} = 0 . \quad (2.43)$$

The analytic solutions enable us to estimate the measurement precision required to detect optical inhomogeneities. The required phase precision is determined from the position-dependent difference in phase between the incident wave and the distorted wave, while the required amplitude precision is found from the position-dependent ratio of $|\Phi_{out}|/|\Phi_{inc}|$. Contour plots of the phase difference and the amplitude ratio indicate the spatial positions which are most sensitive to the presence of the object as well as the required signal-to-noise ratio. Fig. 2.10 illustrates this spatially-dependent sensitivity for a perfectly absorbing sphere immersed in a medium with $\mu'_s = 10.0 \text{ cm}^{-1}$ and $\mu_a = 0.02 \text{ cm}^{-1}$. These plots show that 1.0° phase and 10.0% amplitude precision is sufficient for localization with measurements made in the shadow (within 4.0 cm of the object) of the 1.0 cm diameter absorber. This is well within the 0.1° phase and 0.1% amplitude precision available with current detectors. Localization of smaller

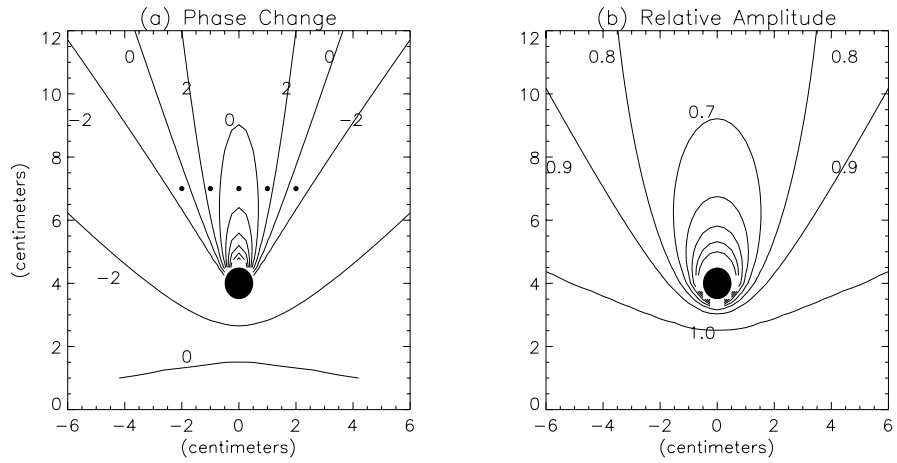


Figure 2.10: These sensitivity plots demonstrate the phase and amplitude resolution necessary to measure a DPDW distorted by a perfect absorber. Plotted in (a) is the phase difference between an incident wave and the wave distorted by a 1.0 cm diameter absorber. The ratio of the amplitude of the distorted wave with respect to the incident wave is plotted in (b). For these plots, the surrounding medium's optical characteristics are $\mu'_s=10 \text{ cm}^{-1}$ and $\mu_a=0.02 \text{ cm}^{-1}$, the modulation freq. is 200 MHz, and $v = 2.25 \cdot 10^{10} \text{ cm/s}$. The dots in (a) represent the locations where measurements were made in order to characterize the object.

absorbers will require better precision. A more detailed signal-to-noise analysis that reveals the limits to detecting, localizing, and characterizing is given in chapter 3.

2.5.2 Experimental Verification of the Analytic Solution

Two sets of experiments were performed, one to check the validity of the theory and the other to resolve object characteristics by fitting the theory to experimental data. In the first set of experiments, the object and source are fixed in the Intralipid with a separation z_s . The phase and amplitude of the distorted DPDW are measured by moving the detector to different points on a two-dimensional grid containing the source and the center of the object. These experimental results are then compared to the prediction of eq. (2.31) for the given object properties. In the second set of experiments, the properties of different spherical absorbers are found by fitting the theory to a measurement of the distorted wavefront along a line. This was accomplished by minimizing the least squares theoretical fit to the experimental data using the object position and radius as free parameters. The optical properties of the Intralipid were determined before each experiment through separate measurements of phase and amplitude of the DPDW propagating in the infinite homogeneous system [3, 21]. These quantities were used in the subsequent analysis.

The measurements indicate that the analytic theory accurately predicts the distortion of the DPDW. Furthermore, because of the close agreement, we are able to characterize a spherical absorber embedded in the turbid medium. These observations were not obvious *a priori* for one major reason: the theory is derived from the diffusion equation, but photon migration is better approximated by a transport equation. In fact, significant differences between the diffusion equation and the transport equation arise near sharp boundaries. As mentioned below, evidence of these differences have been detected.

The measured distortion of the DPDW by a perfectly absorbing sphere is shown in fig. 2.11 and compared to the predicted distortion. This comparison illustrates that the analytic solution shows good agreement with the experimental data.

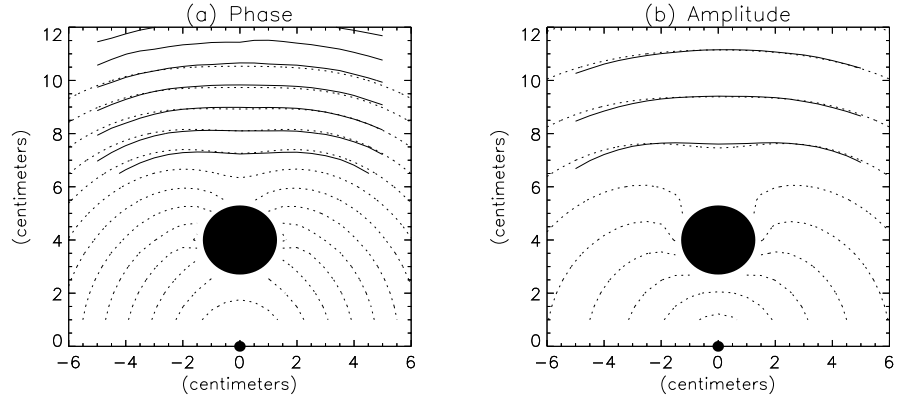


Figure 2.11: The experimental measurements (solid lines) of a DPDW distorted by a 1.3 cm radius perfect absorber are compared to the theoretical prediction (dotted lines) for the given experimental parameters. Phase contours are drawn every 20 degrees in (a), while the amplitude contours are drawn every $e^{-0.5}$. For this experiment, the optical properties of the surrounding medium were $\mu'_s=3.0 \text{ cm}^{-1}$ and $\mu_a=0.02 \text{ cm}^{-1}$, $f=200 \text{ MHz}$, and $v = 2.25 \cdot 10^{10} \text{ cm/s}$.

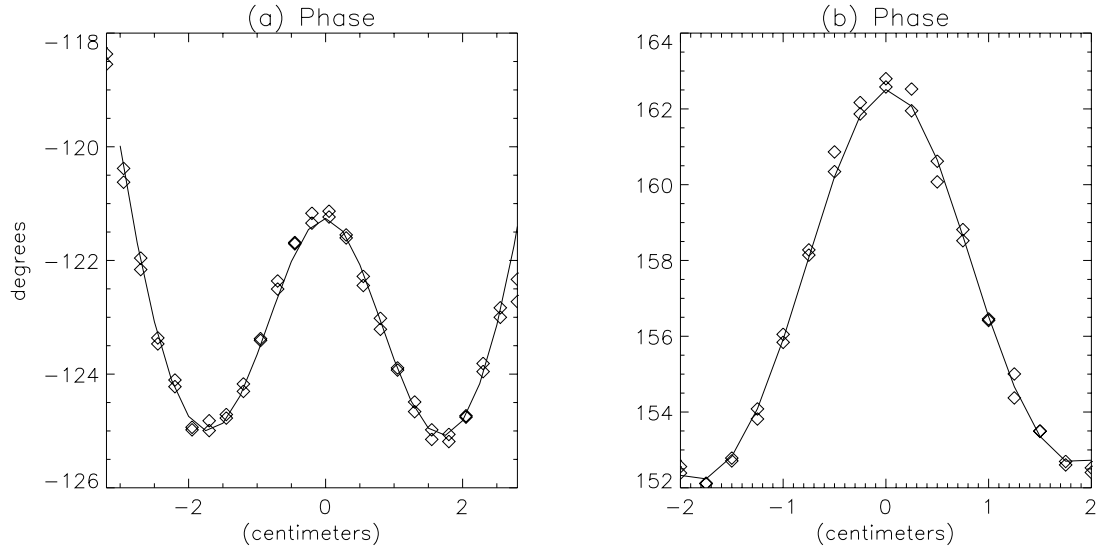


Figure 2.12: The fits to experiment C and G from table 2.1 are presented in (a) and (b) respectively. The experimental data (\diamond 's) are compared to the best fit (solid line). The experimental parameters are given in table 2.1.

Table 2.1: The results of fitting theory to a series of experimental observations of a DPDW scattered by an absorber are presented in this table. The absorber had a radius of $a_{exp} = 1.3$ cm and was positioned at $Z = 4.0$ cm, $X = 0.0$ cm, and $Y = 0.0$ cm. For each experiment, the detector was positioned at $Z_{detector}$ and scanned from $-2.0 < X < 2.0$. The experiments were performed in different concentrations of Intralipid for which the photon random walk step is given by l^* . In all experiments, $\mu_a = 0.02 \text{ cm}^{-1}$, $f = 200 \text{ MHz}$, and $v = 2.25 \cdot 10^{10} \text{ cm/s}$.

Exp.	$Z_{detector}$	Intralipid	$l^* = 1/\mu'_s$	Z_{fit}	X_{fit}	Y_{fit}	a_{fit}
	cm		cm	cm	cm	cm	cm
A	6.5	0.25%	0.60	3.87	-0.05	0.08	1.02
B	7.5	0.25%	0.60	4.08	-0.06	-0.56	1.04
C	6.5	0.50%	0.33	4.06	0.00	-0.13	1.12
D	7.5	0.50%	0.33	4.01	-0.02	0.08	1.15
E	6.5	0.75%	0.23	4.20	0.01	-0.07	1.15
F	7.5	0.75%	0.23	4.11	0.00	0.12	1.20
G	6.5	1.00%	0.18	4.12	0.02	0.00	1.22
H	7.5	1.00%	0.18	4.17	0.00	0.04	1.21

As an example of the utility of the analytic solution, a simple least-squares fitting algorithm was used to fit the analytic solution to the measurements of phase and amplitude of the DPDW to predict object size and location. Measurements were taken along lines parallel to those indicated in fig. 2.10a. The results of these experiments are presented in table 2.1. Fits for two of these experiments are shown in fig. 2.12.

The results in table 2.1 show that a fit to measurements made in the shadow of the object determines the x and y position of the absorber to an accuracy of ± 0.1 cm and the z position to ± 0.2 cm. Finally, the object radius was determined to within ± 0.3

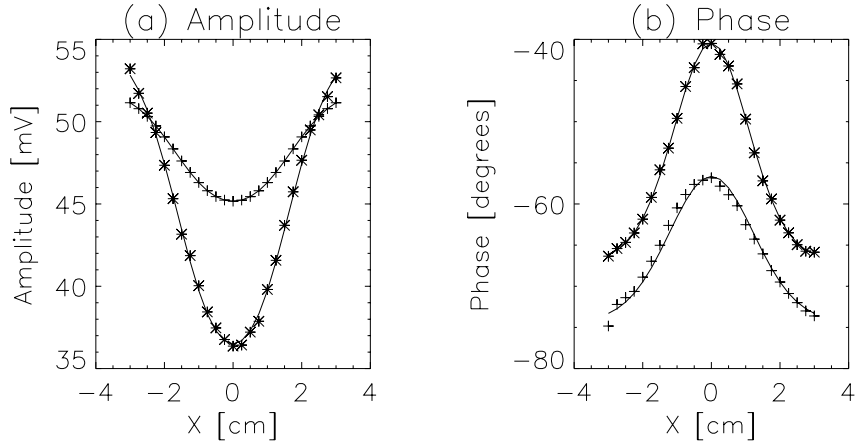


Figure 2.13: The fits to experiment C (+'s) and H (*'s) from table 2.2 for the scattering of DPDW's from purely scattering spheres. The experimental data are given by the symbols and the best fits by the solid lines. There is an arbitrary amplitude and phase difference between the two sets of data. The fits were made using the objects optical properties and initial source amplitude and phase as free parameters. The experimental parameters are given in table 2.2.

cm. With a decrease in the photon random walk step, the discrepancy between the determined radius and the known radius is seen to decrease. This trend is a result of applying the diffusion equation to a system with a sharp absorbing boundary.

To demonstrate that this least-squares fitting algorithm can be used to characterize the optical properties of spherical objects, I measured the amplitude and phase of DPDW's scattered by purely scattering objects. The objects were spheres of polystyrene resin with different concentrations of titanium-oxide (TiO_2). The method for casting these spheres is described in section 6.3. Measurements were taken along lines parallel to those indicated in fig. 2.10a with a 2.5 cm diameter object centered at $x=0$ and $y=4$ cm. The results of these experiments for spheres with different concentrations of TiO_2 are presented in table 2.2.

Fits for two of these experiments are shown in fig. 2.13. The fits agree well with the experimental data. Fits were made for spheres with eight different concentrations of TiO_2 and in all cases good agreement was found. The reduced scattering coefficient of

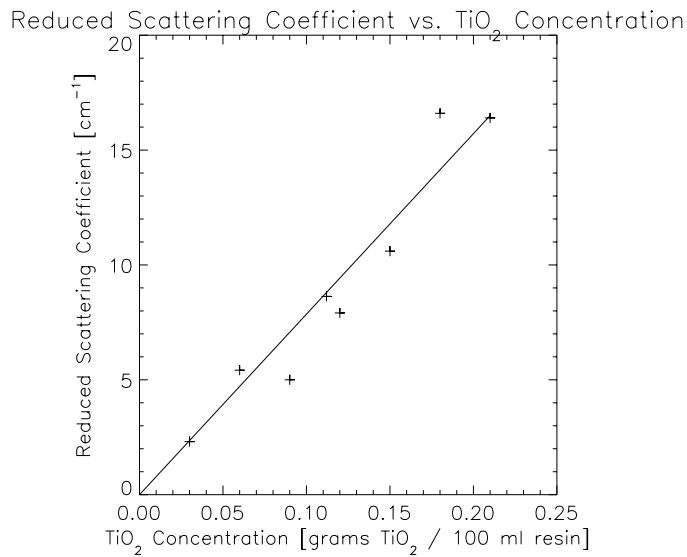


Figure 2.14: The best fits for the reduced scattering coefficients is graphed versus the TiO_2 concentration in the resin spheres. The expected linear relationship and zero intercept are observed.

the object is expected to increase linearly with the concentration of TiO_2 . The data in table 2.2 show this trend. A summary of the determined reduced scattering coefficient versus TiO_2 concentration is shown in fig. 2.14. Note that the relationship is linear and that the reduced scattering coefficient goes to zero as the TiO_2 concentration goes to zero.

2.5.3 Scattering from Multiple Objects

When the sample contains two or more spherical objects, the distorted wave is calculated by summing scattering events of different order. We first calculate the scattering of the incident wave from each object. This is the first order scattered wave. The first order scattered waves are incident on and consequently scattered by the surrounding objects resulting in second order scattered waves whose amplitude is smaller than the first order wave. For two spherical objects embedded in an infinite homogeneous

Table 2.2: Results for the fitted object reduced scattering coefficient versus different TiO_2 concentrations.

Exp	Background		TiO ₂ Concentration	Object $\mu'_s \text{ cm}^{-1}$
	$\mu'_s \text{ cm}^{-1}$	$\mu_a \text{ cm}^{-1}$	grams TiO ₂ / 100 ml Resin	
A	2.56	0.014	0.03	2.31
B	2.56	0.014	0.06	5.42
C	2.08	0.008	0.09	5.00
D	2.08	0.008	0.11	8.63
E	1.87	0.020	0.12	7.91
F	1.91	0.018	0.15	10.6
G	2.12	0.018	0.18	16.6
H	2.15	0.015	0.21	16.4

medium, the general solution is of the form

$$\Phi_{out} = \Phi_{inc} + \sum_{n=1}^{\infty} \left(\Phi_{scatt,1}^{(n)} + \Phi_{scatt,2}^{(n)} \right), \quad (2.44)$$

where $\Phi_{scatt,i}^{(n)}$ is the n^{th} order scattered wave from the i^{th} object (see fig. 2.9). While the first order waves ($\Phi_{scatt,i}^{(1)}$) are easily calculated using eq. (2.32), the second order waves ($\Phi_{scatt,i}^{(2)}$) require the solution of complex integral equations since the first order waves are not spherical. If the first order waves are spherical to a good approximation, then the second order waves can be computed analytically using the same procedure for calculating the first order scattered waves. The condition is only satisfied for small absorbing objects. In this regime we can check the significance of the second ordered scattered waves from the ratio of $\Phi_{scatt,i}^{(2)}$ to Φ_{inc} . This ratio indicates that $\Phi_{scatt,i}^{(2)}$ is negligible when

$$\left(\frac{v\delta\mu_{a,i}}{D_o} a_i^3 \right) \left(\frac{v\delta\mu_{a,j}}{D_o} a_j^3 \right) \frac{r_{sd}}{r_{si}r_{ij}r_{jd}} \exp(ik(r_{si} + r_{ij} + r_{jd} - r_{sd})) \ll 1, \quad (2.45)$$

where i and j denote the different objects (see fig. 2.9) and $\delta\mu_{a,i}$ is the difference in the absorption coefficient between the i^{th} object and the background.

2.5.4 Semi-Infinite Media

In medical imaging, measurements are typically made by placing the source and detector on the scalp or surface of the breast. Treating such a system as infinite is obviously incorrect and will lead to discrepancies between theory and experiment. Planar boundaries between diffusive and non-diffusive media can be modeled by requiring $\Phi_{out} = 0$ on an extrapolated zero boundary a distance $z_o = 2/(3\mu'_s)$ from the actual boundary (some investigators use $z_o = 0.7104/3\mu'_s$), away from the diffusive medium [4, 76, 78, 79]. Multiple planar boundaries can be modeled by employing additional extrapolated zero boundary conditions. To first order, the extrapolated zero amplitude boundary condition is satisfied by placing an image source of negative amplitude at the position of the actual source reflected about the extrapolated

zero boundary. The photon fluence is then calculated by superimposing the DPDW's generated by the two sources and their respective scattered waves. In general, one must also consider an image of the scattered waves to ensure that Φ_{out} equals zero on the extrapolated zero boundary. These images then create waves that scatter off the object *ad infinitum*.

2.5.5 General Heterogeneous Media

In biological media the optical inhomogeneities will have arbitrary shapes. It is not possible to find analytic solutions for general heterogeneous media. We must therefore resort to numerical techniques. There are many approaches to numerically solving the diffusion equation for spatially varying optical properties, including finite difference, finite element, and perturbative methods. Here I present a short review of perturbative methods.

With a perturbative method the signal reaching the detector is considered to be a superposition of the DPDW that travelled through a homogeneous system, plus the first order scattering of DPDW's from optical inhomogeneities, plus the second order, etc. The optical properties of the background/homogeneous medium are usually taken to be the average or most common optical properties. One generally divides the region of interest (i.e. the region containing the inhomogeneity) into voxels. The first order scattered DPDW is then the scattering of the incident DPDW from each voxel. If the optical properties of the voxel are the same as the background then no wave is scattered from that voxel. The voxels are chosen to be small enough so that the scattered DPDW can be linearized, that is the amplitude of the scattered wave is linearly proportional to the change in the absorption coefficient and the change in the reduced scattering coefficient.

One way to derive the linearized scattered DPDW is to take the limiting form of Φ_{scatt} (eq. (2.33)) for small radius spheres. To leading order in $k^{out}a$ and $k^{in}a$

$$\Phi_{scatt}(\mathbf{r}_s, \mathbf{r}, \mathbf{r}_d) = v S_{AC} \frac{\exp(ik|\mathbf{r}_s - \mathbf{r}|)}{4\pi D_{out}|\mathbf{r}_s - \mathbf{r}|} \frac{\exp(ik|\mathbf{r} - \mathbf{r}_d|)}{4\pi |\mathbf{r} - \mathbf{r}_d|} \left[\frac{4\pi a^3}{3} \right]$$

$$\left\{ \frac{-v\delta\mu_a(\mathbf{r})}{D_{out}} + \left[ik - \frac{1}{|\mathbf{r}_s - \mathbf{r}|} \right] \left[ik - \frac{1}{|\mathbf{r} - \mathbf{r}_d|} \right] \left[\frac{-3\delta\mu'_s(\mathbf{r})\cos\theta}{3\mu'_{s,out} + 2\delta\mu'_s(\mathbf{r})} \right] \right\} . \quad (2.46)$$

Here, $\delta\mu_a = \mu_{a,in} - \mu_{a,out}$ is the difference in the absorption coefficient of the voxel and background, $\delta\mu'_s = \mu'_{s,in} - \mu'_{s,out}$ is the difference in the reduced scattering coefficient, $k = k_{out}$, and θ is the angle between the line joining the source to the voxel and the line joining the detector to the voxel. The volume for a sphere of radius a appears in eq. (2.46). If the voxel is not a sphere then the $4\pi a^3/3$ must be replaced by the actual volume of the voxel.

$\Phi_{scatt}(\mathbf{r}_s, \mathbf{r}, \mathbf{r}_d)$ is linearized by assuming that $\delta\mu'_s(\mathbf{r}) \ll \mu'_s$. The first order scattered wave reaching the detector is found by summing the contributions from each voxel. When $\Phi_{scatt}(\mathbf{r}_s, \mathbf{r}, \mathbf{r}_d)$ is linearized then a matrix equation can be written for the first order scattered wave $\Phi_{scatt}^{(1)}$. The matrix equation is

$$\begin{aligned} \begin{pmatrix} \Phi_{scatt}^{(1)}(\mathbf{r}_{s,1}, \mathbf{r}_{d,1}) \\ \Phi_{scatt}^{(1)}(\mathbf{r}_{s,2}, \mathbf{r}_{d,2}) \\ \vdots \\ \Phi_{scatt}^{(1)}(\mathbf{r}_{s,n}, \mathbf{r}_{d,n}) \end{pmatrix} &= \begin{pmatrix} M_{1,1} & M_{1,2} & \cdots & M_{1,m} \\ M_{2,1} & M_{2,2} & \cdots & M_{2,m} \\ \vdots & \vdots & & \vdots \\ M_{n,1} & M_{n,2} & \cdots & M_{n,m} \end{pmatrix} \begin{pmatrix} \delta\mu_{a,1} \\ \delta\mu_{a,2} \\ \vdots \\ \delta\mu_{a,m} \end{pmatrix} \\ &+ \begin{pmatrix} N_{1,1} & N_{1,2} & \cdots & N_{1,m} \\ N_{2,1} & N_{2,2} & \cdots & N_{2,m} \\ \vdots & \vdots & & \vdots \\ N_{n,1} & N_{n,2} & \cdots & N_{n,m} \end{pmatrix} \begin{pmatrix} \delta\mu'_{s,1} \\ \delta\mu'_{s,2} \\ \vdots \\ \delta\mu'_{s,m} \end{pmatrix}. \quad (2.47) \end{aligned}$$

$\Phi_{scatt}^{(1)}(\mathbf{r}_{s,i}, \mathbf{r}_{d,i})$ is the first order scattered wave for the i^{th} source-detector pair, $\delta\mu_{a,j}$ and $\delta\mu'_{s,j}$ are respectively the change in the absorption and reduced scattering coefficients of voxel j relative to the background. The elements of matrix M and matrix N are given by the linearized version of eq. (2.46). Specifically,

$$M_{i,j} = v S_{AC} \frac{\exp(ik|\mathbf{r}_{s,i} - \mathbf{r}_j|)}{4\pi D_{out} |\mathbf{r}_{s,i} - \mathbf{r}_j|} \frac{\exp(ik|\mathbf{r}_j - \mathbf{r}_{d,i}|)}{4\pi |\mathbf{r}_j - \mathbf{r}_{d,i}|} \left[\frac{4\pi a^3}{3} \right] \left[\frac{-v}{D_{out}} \right], \quad (2.48)$$

and

$$N_{i,j} = v S_{AC} \frac{\exp(ik|\mathbf{r}_{s,i} - \mathbf{r}_j|)}{4\pi D_{out} |\mathbf{r}_{s,i} - \mathbf{r}_j|} \frac{\exp(ik|\mathbf{r}_j - \mathbf{r}_{d,i}|)}{4\pi |\mathbf{r}_j - \mathbf{r}_{d,i}|} \left[\frac{4\pi a^3}{3} \right] \\ \left[ik - \frac{1}{|\mathbf{r}_{s,i} - \mathbf{r}_j|} \right] \left[ik - \frac{1}{|\mathbf{r}_j - \mathbf{r}_{d,i}|} \right] \left[\frac{\cos \theta_{i,j}}{\mu'_{s,out}} \right], \quad (2.49)$$

where \mathbf{r}_j is the position of the j^{th} voxel and $\mathbf{r}_{s,i}$ and $\mathbf{r}_{d,i}$ are the position of the i^{th} source and detector respectively.

This same matrix equation can be found directly from the heterogeneous diffusion equation. When the optical properties are spatially varying then the photon diffusion equation is

$$-\nabla D(\mathbf{r}) \cdot \nabla \Phi(\mathbf{r}) - D(\mathbf{r}) \nabla^2 \Phi(\mathbf{r}) + v \mu_a(\mathbf{r}) \Phi(\mathbf{r}) - i\omega \Phi(\mathbf{r}) = v S_0(\mathbf{r}). \quad (2.50)$$

Separating the spatially constant terms to the left-hand side and the spatially varying terms to the right-hand side we get

$$\nabla^2 \Phi(\mathbf{r}) - \frac{v \mu_{a,o}}{D_o} \Phi(\mathbf{r}) + i \frac{\omega}{D_o} \Phi(\mathbf{r}) = \\ - \frac{v}{D(\mathbf{r})} S_0(\mathbf{r}) + \frac{1}{\mu'_{s,o}} \nabla \delta \mu'_s(\mathbf{r}) \cdot \nabla \Phi(\mathbf{r}) + \frac{v \delta \mu_a(\mathbf{r})}{D_o} \Phi(\mathbf{r}) + 3 \left(\mu_{a,o} - i \frac{\omega}{v} \right) \delta \mu'_s \Phi(\mathbf{r}). \quad (2.51)$$

The solution to this equation is, after integrating $\nabla \delta \mu'_s(\mathbf{r}) \cdot \nabla \Phi(\mathbf{r})$ by parts and recognizing that $\nabla^2 \Phi^{(0)} = k_o^2 \Phi^{(0)}$,

$$\Phi(\mathbf{r}) = \frac{v S_o \exp(ik_o |\mathbf{r} - \mathbf{r}_s|)}{4\pi D_o |\mathbf{r} - \mathbf{r}_s|} + \int \left[-\frac{v \delta \mu_a(\mathbf{r}')}{D_o} \Phi(\mathbf{r}') G(\mathbf{r}', \mathbf{r}) \right. \\ \left. + \frac{\delta \mu'_s(\mathbf{r}')}{\mu'_{s,o}} \nabla \Phi(\mathbf{r}') \cdot \nabla G(\mathbf{r}', \mathbf{r}) \right] d\mathbf{r}' . \quad (2.52)$$

This equation is usually solved perturbatively by assuming that $\Phi = \Phi^{(0)} + \Phi^{(1)} + \Phi^{(2)} + \dots$. This is known as the Born approximation. Substituting this perturbative expansion into eq. (2.52) and collecting terms of like order, we obtain

$$\Phi^{(0)}(\mathbf{r}_s, \mathbf{r}_d) = \frac{v S_o \exp(ik_o |\mathbf{r}_d - \mathbf{r}_s|)}{4\pi D_o |\mathbf{r}_d - \mathbf{r}_s|}$$

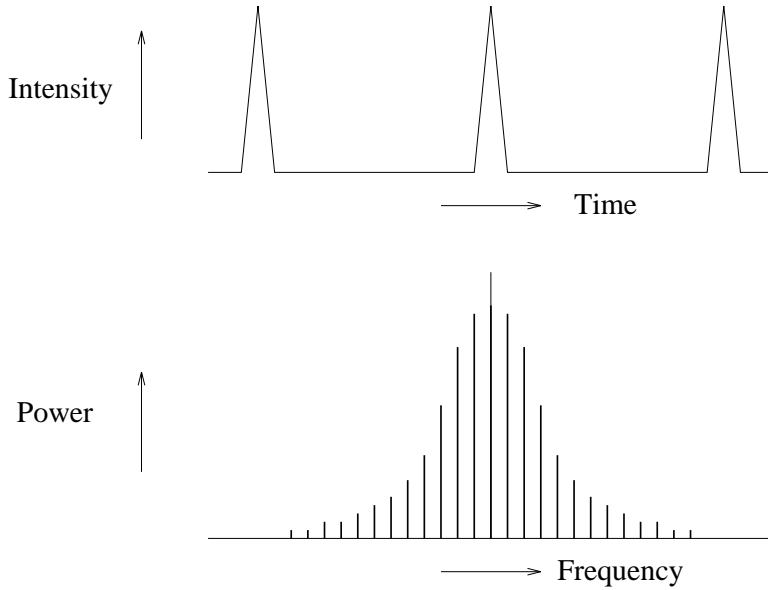


Figure 2.15: A drawing of a pulse-train from a mode-locked laser and the corresponding Fourier expansion.

$$\Phi^{(1)}(\mathbf{r}_s, \mathbf{r}_d) = \int \left[\frac{-v\delta\mu_a(\mathbf{r})}{D_o} \Phi^{(0)}(\mathbf{r}_s, \mathbf{r}) G(\mathbf{r}, \mathbf{r}_d) + \frac{\delta D(\mathbf{r})}{D_o} \nabla \Phi^{(0)}(\mathbf{r}_s, \mathbf{r}) \cdot \nabla G(\mathbf{r}, \mathbf{r}_d) \right] d\mathbf{r}. \quad (2.53)$$

This equation for the first order scattered wave (first Born approximation) is identical to the equation that we obtained by summing the limiting form of the analytic solution over all voxels.

2.6 Time-Domain Measurements

The DPDW scattering theory is easily extended to the time domain. A pulse-train of light propagating in a turbid media can be thought of as a superposition of many DPDW's with different modulation frequencies (see fig. 2.15). Thus, a time resolved measurement of the propagation of a light pulse is an easy way to determine the frequency response of the system [85]. To calculate the response to a pulse of light, we simply compute the scattering due to each DPDW in parallel.

I computed the temporal evolution of a light pulse with width $\tau=10$ ps and period $T=1.0\ \mu\text{s}$ in an infinite medium with different size perfect absorbers. The results indicate that the measured photon fluence decreases as a result of an absorber but that the decay rate of the fluence is relatively unaffected by its presence. These results are consistent with the experimental observations of Liu *et al.* [86].

2.7 Photon Migration within the P_3 Approximation

At optical wavelengths between 600 and 900 nm, the absorption of photons in the body is generally small compared to the corresponding scattering rate. Thus a major condition for the validity of the diffusion approximation is satisfied. The criteria is sometimes violated in hematomas, liver, and other regions with large concentrations of blood where photon absorption is large. A more accurate model of photon transport is required to describe and analyze photon migration through these systems. This section presents the P_3 solution of the transport equation [87, 88], which is a more accurate approximation for photon transport than the diffusion approximation. I demonstrate the advantages and disadvantages of the P_3 approximation for analyzing highly absorbing systems. I find that the P_3 approximation, in general, permits a more accurate determination of the reduced scattering, μ'_s , and absorption, μ_a , coefficients for highly absorbing systems (i.e. $\mu_a/\mu'_s > 0.1$) or systems probed at modulation frequencies in excess of 2 to 3 GHz. In systems with highly anisotropic scattering (i.e. $\langle \cos \theta \rangle \sim 1$), determination of the reduced scattering coefficient using the P_3 approximation gives values comparable to results obtained within the diffusion (P_1) approximation.

2.7.1 P_3 Theory

The transport equation was presented in section 2.1 (eq. (2.1)) along with a description of the P_N approximation method. Here, I present the solution of the P_3 approximation and discuss the limits in which the P_3 approximation reduces to the diffusion

approximation. The P_2 equations are not solved because of inconsistencies that arise at boundaries [55].

Expanding the radiance $L(\mathbf{r}, \hat{\Omega}, t)$, phase function $f(\hat{\Omega}, \hat{\Omega}')$, and source $S(\mathbf{r}, \hat{\Omega}, t)$ terms of the transport equation (eq. (2.1)) in spherical harmonics and evaluating the integral over $d\hat{\Omega}'$; the transport equation is rewritten as

$$\sum_{l,m} \left[\frac{1}{v} \frac{\partial \phi_{l,m}}{\partial t} + \nabla \cdot \phi_{l,m} \hat{\Omega} + \mu_t^{(l)} \phi_{l,m} - q_{l,m} \right] Y_{l,m}(\hat{\Omega}) = 0 , \quad (2.54)$$

where $\mu_t^{(l)} = \mu_s(1 - g_l) + \mu_a$ (note $\mu_t^{(0)} = \mu_a$). g_l is the coefficient for the l^{th} moment of the normalized phase function. For the Henyey-Greenstein phase function, $g_l = g^l$ where g is the average cosine of the scattering angle (see appendix B). When the photon scattering is anisotropic then $\mu_t^{(l+1)} > \mu_t^{(l)}$.

Next, we multiply eq. (2.54) by $Y_{\alpha,\beta}(\hat{\Omega})$ and integrate over $\hat{\Omega}$. Using the orthogonality relations for the spherical harmonics, we obtain an infinite set of coupled linear differential equations for $\phi_{l,m}$ that agree with Kaltenbach and Kaschke [87]. See appendix A for these calculations. Within the P_3 approximation, the moments greater than $l = 3$ are ignored, i.e. we set $\phi_{l,m} = 0$ for $l > 3$. By considering higher moments of the radiance, the P_3 approximation should be more accurate than the diffusion approximation. However, the P_3 approximation will break down as the anisotropy of the radiance is increased by increasing photon absorption and/or the DPDW modulation frequency.

Working in the frequency domain (i.e. $\partial/\partial t \rightarrow -i\omega$), the equation for $\phi_{0,0}$ in a homogeneous medium is

$$\left[9\nabla^4 + \beta\nabla^2 + \gamma \right] \phi_{0,0}(\mathbf{r}, \omega) = Wq_{0,0}(\mathbf{r}, \omega) + Xq_{1,0}(\mathbf{r}, \omega) + Yq_{2,0}(\mathbf{r}, \omega) + Zq_{3,0}(\mathbf{r}, \omega) , \quad (2.55)$$

where

$$\beta = 90 \frac{\omega^2}{v^2} + i \frac{\omega}{v} \left(55\mu_a + 27\mu_t^{(1)} + 35\mu_t^{(2)} + 63\mu_t^{(3)} \right) - \left(27\mu_a\mu_t^{(1)} + 28\mu_a\mu_t^{(3)} + 35\mu_t^{(2)}\mu_t^{(3)} \right) \quad (2.56)$$

$$\gamma = 105 \left(-i \frac{\omega}{v} + \mu_a \right) \left(-i \frac{\omega}{v} + \mu_t^{(1)} \right) \left(-i \frac{\omega}{v} + \mu_t^{(2)} \right) \left(-i \frac{\omega}{v} + \mu_t^{(3)} \right) , \quad (2.57)$$

and the right-hand-side of eq. (2.55) contains the moments of the source distribution. The coefficients W , X , Y , and Z are given in section A.1.2 by eq. (A.34), eq. (A.35), eq. (A.36), and eq. (A.37) respectively.

Let's assume that the source is an isotropic point source such that $q_{l,0} = 0$ for $l > 0$. For an infinite medium, the solution of eq. (2.55) is of the form

$$\phi_{0,0} \propto \frac{1}{4\pi r} \exp(ik_{p3}r) , \quad (2.58)$$

where k_{p3} is given by

$$k_{p3}^2 = \frac{\beta \pm \sqrt{\beta^2 - 36\gamma}}{18} . \quad (2.59)$$

Here I concentrate on the negative root. The positive root contributes to the solution only within a few mean free paths of the source. This solution has been discussed previously [88], particularly with regards to the positive root and the appropriate boundary conditions for semi-infinite media.

For typical parameters where the diffusion approximation is known to be valid, $|36\gamma/\beta^2| \ll 1$. For example, using $\mu_s = 100.0 \text{ cm}^{-1}$, $\mu_a = 0.1 \text{ cm}^{-1}$, $g = 0.9$, and $\omega = 0$, we see that $36\gamma/\beta^2 = 0.005$. Eq. (2.59) can then be expanded to first order, giving

$$k_{p3}^2 = \frac{\beta}{18} \left(1 - \sqrt{1 - \frac{36\gamma}{\beta^2}} \right) \approx \frac{\gamma}{\beta} \approx 3\mu_t^{(1)}(-\mu_a + i\frac{\omega}{v}) = k_{diff}^2 . \quad (2.60)$$

This is the well known wavenumber solution from the diffusion equation (see eq. (2.14) [21]). In the regime where the diffusion approximation is known to be valid, eq. (2.56) and eq. (2.57) can be approximated as

$$\beta = -35\mu_t^{(2)}\mu_t^{(3)} \quad (2.61)$$

$$\gamma = 105(-i\frac{\omega}{v} + \mu_a)\mu_t^{(1)}\mu_t^{(2)}\mu_t^{(3)} . \quad (2.62)$$

Thus, for these parameters, the P_3 solution reduces to the diffusion solution, indicating that the diffusion equation is valid when $|36\gamma/\beta^2| \ll 1$, i.e.

$$\left| \frac{108}{35} \left(\mu_a - i\frac{\omega}{v} \right) \frac{\mu_t^{(1)}}{\mu_t^{(2)}\mu_t^{(3)}} \right| \ll 1 . \quad (2.63)$$

For systems that do not satisfy this condition, it is believed that the full solution of the P_3 equation would more accurately approximate photon transport through the system. Furthermore, from this condition, we see that the limits of validity of the diffusion equation can be checked by: (1) increasing μ_a relative to μ_s , (2) increasing ω/v relative to μ_s , and (3) decreasing the scattering anisotropy factor while holding μ'_s constant.

2.7.2 Comparison of P_3 and Diffusion Theories

To test the usefulness of the P_3 approximation compared to the diffusion approximation, I first generated data for known parameters using a Monte Carlo computer code for photon transport in an infinite, homogeneous system. The code is explained in section 6.1.2 and supplied in appendix C. The Monte Carlo code was used to find the temporal response to a pulse of light injected into a homogeneous, infinite medium for various optical properties and scattering anisotropies. I then used the generated data to compare diffusion theory and P_3 as a function of μ_a , the modulation frequency ω (by Fourier transforming the data) and the scattering anisotropy. The comparison was made by fitting amplitude and phase data versus the source-detector separation using the P_3 solution and diffusion solution to find μ'_s and μ_a . Source-detector separations ranging from 2.0 to 4.0 cm, in steps of 0.2 cm, were used.

Fig. 2.16 displays the optical properties determined from the Monte Carlo data using the P_3 approximation and the diffusion approximation versus the known absorption coefficient of the medium. Results are plotted for data generated with two different anisotropy factors. All results in fig. 2.16 are for a modulation frequency of 390 MHz. The analysis based on the P_3 approximation is significantly better than diffusion theory at determining the correct μ'_s when the scattering is isotropic, i.e. $g = 0$, and the absorption coefficient exceeds 10% of the known reduced scattering coefficient. A similar difference is observed for the determined absorption coefficient. For anisotropic scattering ($g = 0.9$), we see that in finding μ'_s the P_3 approximation is not as good as the diffusion approximation when $\mu_a/\mu'_s < 0.2$, although P_3 still en-

ables a more accurate determination of μ_a . This is most likely a result of a premature truncation of the spherical harmonic expansion of the phase function in arriving at the P_3 theory. In diffusion theory the anisotropy is implicitly contained in the reduced scattering coefficient, while in the P_3 theory the anisotropy is expressed explicitly. Modifying the P_3 theory with the δ -E(4) approximation discussed by Star [88] may improve the determination of μ'_s . Basically, within the δ -E(4) approximation, a delta function is added to spherical harmonics expansion of the phase function (eq. (2.6)) to compensate for the truncation.

To investigate the accuracy of the diffusion approximation and the P_3 approximation for high modulation frequencies, I used Monte Carlo data for a system with $\mu'_s = 10.0 \text{ cm}^{-1}$ and $\mu_a = 0.50 \text{ cm}^{-1}$ and calculated the optical properties using both approximations for frequency components ranging from 0 to 6 GHz. The results are plotted in fig. 2.17 for a system with isotropic scattering (fig. 2.17 a and b) and anisotropic scattering with $g = 0.9$ (fig. 2.17 c and d). In the case of isotropic scattering, the P_3 approximation is in general more accurate than diffusion theory, although diffusion theory is accurate to 5% for modulation frequencies less than 4 GHz. For anisotropic scattering, however, μ'_s is more accurately determined by diffusion theory up to 6 GHz, while P_3 is superior for determining μ_a . Similar trends are observed for different absorption coefficients.

2.8 Summary

We have seen that the migration of photons in highly scattering media can be treated by the photon diffusion equation. For an intensity modulated source, the diffusion equation predicts a coherent photon density waves that propagate spherically outwards from the source, and this has been observed. Although microscopically the photons are individually following a random walk, macroscopically they produce a coherent intensity wave. The properties of this intensity wave can be understood using conventional optics. This was demonstrated experimentally with the refraction of DPDW's

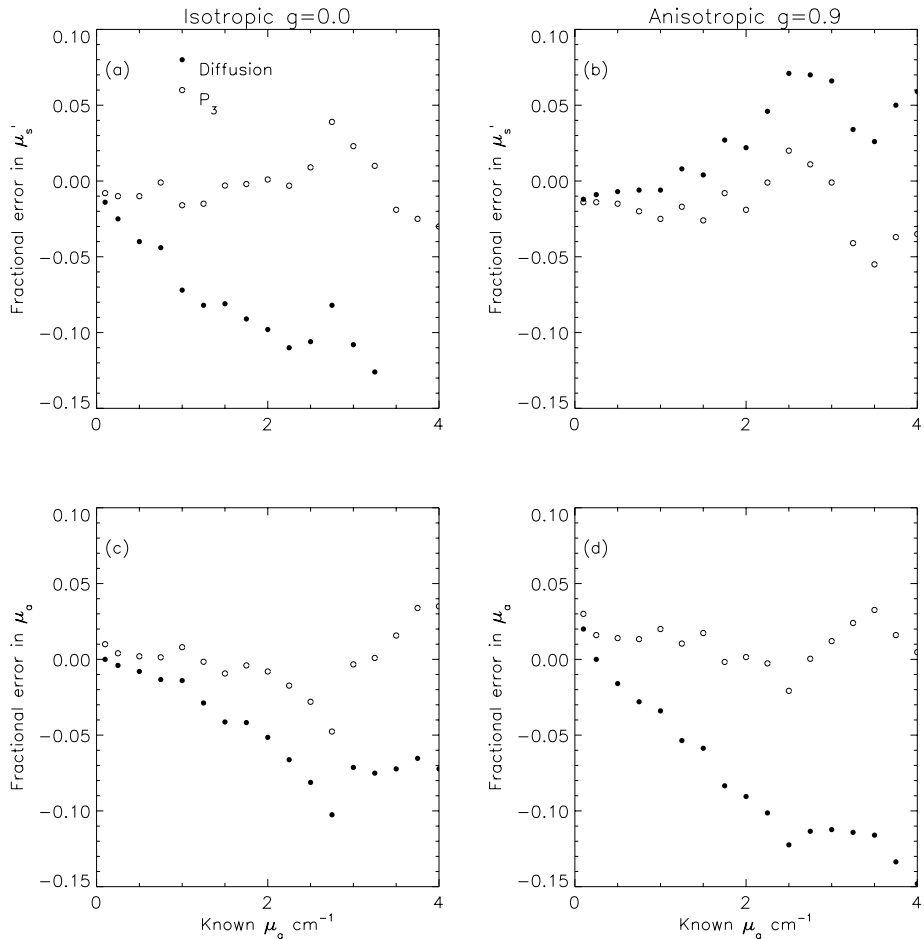


Figure 2.16: A comparison of diffusion theory (closed circles) and the P_3 approximation (open circles) for finding the scattering (top) and absorption (bottom) properties of an infinite system is presented as a function of the known absorption coefficient of the medium (μ'_s was fixed at 10.0 cm^{-1}). The results for isotropic scattering are presented in (a) and (b), and the anisotropic results are given in (c) and (d).

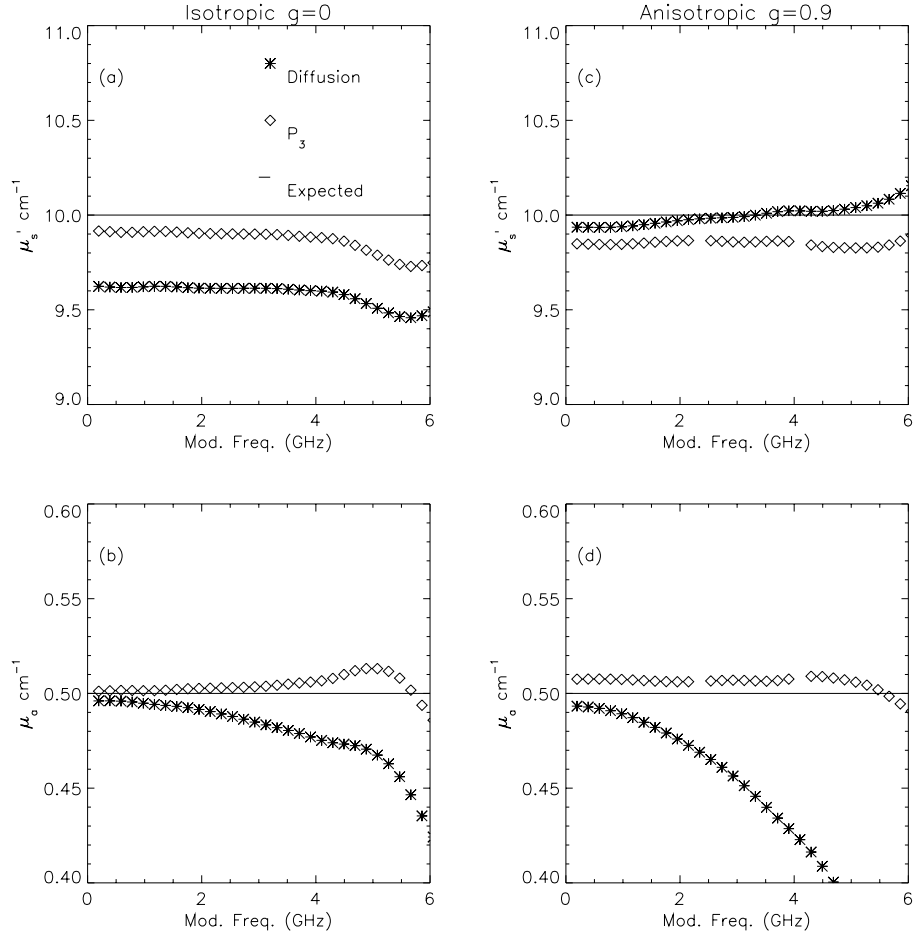


Figure 2.17: Optical properties determined using diffusion theory (stars) and P_3 (diamonds) are compared with the known optical properties (solid line) as a function of the modulation frequency. The results for isotropic scattering are presented in (a) and (b), and the anisotropic results are given in (c) and (d).

at a planar interface between two different scattering media, and the refraction, diffraction, and scattering by spherical inhomogeneities. Interestingly, the scattering is accurately modeled by an analytic solution of the Helmholtz equation and is analogous to a scalar version of Mie Theory for the scattering of electromagnetic waves from dielectric spheres. Experimental observations demonstrate that this solution can be used in conjunction with a simple imaging algorithm to characterize spherical objects. Finally we looked at higher order approximations to the transport equation, specifically the P_3 approximation, and found that the applicability of DPDW's could be extended to probe highly absorbing media such as liver and hematomas.

Chapter 3

Practical Limits to the Detection, Localization, and Characterization of Optical Inhomogeneities with Diffuse Photon Density Waves

In the previous chapter I demonstrated various physical properties of diffuse photon density waves (DPDW's), and showed that DPDW's are perturbed by the presence of optical inhomogeneities and that by measuring the perturbation of a DPDW it is possible to detect, localize, and characterize the inhomogeneities. It is desirable to establish fundamental limits for the detection, localization, and characterization of optical inhomogeneities in order to assess the degree with which diffusing photons can be effectively used to provide physiological information about tissues. An understanding of these limiting factors will lead to the optimization of medical optical imaging prototypes.

Since measurements are made in the near-field (i.e. within one DPDW wavelength of the source) the usual diffraction criteria are inadequate for resolution determinations. In the near-field, resolution is intimately related to the signal-to-noise ratio of the measurement. The resolving power of DPDW's has been studied within this context by comparing the amplitude of the spatial frequencies with the noise level [89]. Additionally, the resolving power of pulse-time measurements has been examined using temporal point spread functions [90, 91, 92, 93, 94]. No analysis, however, has been made that focuses on limitations for the detection, localization, and characterization of optical inhomogeneities with DPDW's.

This chapter presents such an analysis. The signals are calculated using the analytic model for the scattering of DPDW's discussed in section 2.5 [29, 30, 31]. Two different noise models are considered: shot-noise and random errors due to positional uncertainty of the source and detector. My analysis indicates that uncertainties in source, detector, and sample position limits detection to millimeter size objects, and full optical characterization to centimeter size objects. I show how small improvements can be made by optimizing the measurement geometry and source modulation frequency. I find that modulation frequencies less than 500 MHz are optimal for detection and characterization. For higher modulation frequencies the noise threshold increases with the modulation frequency more than the relevant signal. In addition, I show that spectral measurements (i.e. using DPDW information at several source modulation frequencies) enhance the characterization of scattering objects but not absorbing objects. Schemes for optimizing measurement protocols for clinically relevant systems are discussed.

3.1 The Models

In order to determine the limits for detection and characterization of localized heterogeneities, I utilize exact models. A spherical inhomogeneity embedded in an otherwise homogeneous turbid medium is used as the standard system (see fig. 3.1) for assessing the limits. The turbid medium is an infinite slab of finite thickness. Measurements are made in transmission mode at a single photon wavelength. For an ideal experimental system, the signal-to-noise ratio is shot-noise limited and thus scales with the square-root of the number of photons detected. However, there are other sources of random error that exceed shot-noise, such as the positional uncertainty of the source and detector relative to the sample. I consider these effects in the following sections.

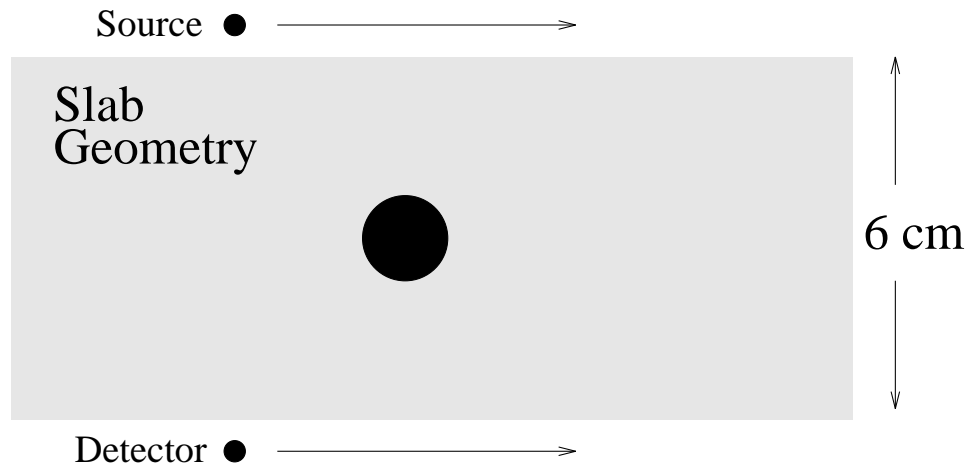


Figure 3.1: Diffuse Photon Density Waves are generated by injecting light from a sinusoidally modulated source into a turbid medium. The 3 mW, 780 nm source is modulated at 200 MHz. The turbid medium is 6.0 cm thick with a reduced scattering coefficient, μ'_s , of 10.0 cm^{-1} and $\mu_a = 0.05 \text{ cm}^{-1}$. A spherical object is embedded in the middle of the slab. Light is collected and delivered to a photo-multiplier tube via an optical fiber with an aperture of 0.4 cm. For the simulations, the source and detector are scanned together along the boundary, or the source is held fixed close to the object and the detector is scanned. Two different objects are studied; an absorbing object with $\mu'_{s,in} = 10.0 \text{ cm}^{-1}$ and $\mu_{a,in} = 0.15 \text{ cm}^{-1}$ and a scattering object with $\mu'_{s,in} = 15.0 \text{ cm}^{-1}$ and $\mu_{a,in} = 0.05 \text{ cm}^{-1}$. Other parameters are considered as indicated in the text.

3.1.1 Analytic Solution for the Signal

To calculate the signal resulting from the inhomogeneity in fig. 3.1, I use the analytic solution for the scattering of the DPDW's discussed in chapter 2.5 [29, 30, 31]. This method is exact provided that the diffusion approximation to the transport equation is valid. The analytic solution reveals that the measured DPDW outside the object is simply a superposition of the incident diffuse photon density wave plus the diffusive wave scattered from the object, i.e.

$$\Phi(\mathbf{r}_s, \mathbf{r}_d) = v S_{AC} \frac{\exp(ik_{out}|\mathbf{r}_s - \mathbf{r}_d|)}{4\pi D_{out}|\mathbf{r}_s - \mathbf{r}_d|} + \sum_{l=0}^{\infty} A_l h_l^{(1)}(k_{out} r_d) Y_l^0(\hat{\Omega}_d) . \quad (3.1)$$

Here, the position of the source (detector) is denoted by \mathbf{r}_s (\mathbf{r}_d) and the object is centered at the origin. S is the modulation amplitude of the source in photons per second. k_{out} is the wavenumber of the DPDW outside the object and is given by $k_{out}^2 = \frac{-v\mu_{a,out}+i\omega}{D_{out}}$, where v is the speed of light in the medium, $D_{out} = v/(3\mu'_{s,out})$ is the photon diffusion coefficient, $\mu'_{s,out}$ is the reduced scattering coefficient and $\mu_{a,out}$ is the absorption coefficient of the background medium, and $\omega = 2\pi f$ is the angular frequency of the DPDW (f denotes the modulation frequency). For the scattered wave, $h_l^{(1)}(x)$ are Hankel functions of the first kind and $Y_l^0(\hat{\Omega})$ are the spherical harmonics with the azimuthal index equal to zero since the source is taken to be on the z-axis and the object is at the origin (i.e. the system has azimuthal symmetry). The scattered wave is written as a series of partial-waves or multipole moments where the amplitude of each partial wave is given by the scattering amplitude A_l (see eq. (2.35)).

In general, the scattering amplitudes, A_l , depend on the diameter of the spherical object, the optical properties of the object and the background medium, and the source modulation frequency. Detection and characterization of the optical inhomogeneities depend on the magnitude of the different partial-waves or moments of the scattered DPDW. The most important moments of the scattered wave are the monopole ($\Phi_{sc}^{l=0}$), dipole ($\Phi_{sc}^{l=1}$), and quadrupole ($\Phi_{sc}^{l=2}$). To leading order in $k_{out}a$ and $k_{in}a$, assuming $|k_{out}a| \ll 1$ and $|k_{in}a| \ll 1$ (where k_{in} is the DPDW wavenumber inside the spherical

object and a is the radius of the object) these moments are

$$\Phi_{sc}^{l=0} = v S_{AC} \frac{\exp(ikr_s)}{4\pi D_{out} r_s} \frac{\exp(ikr_d)}{4\pi r_d} \left[\frac{4\pi a^3}{3} \right] \left[\frac{-v\delta\mu_a}{D_{out}} \right], \quad (3.2)$$

$$\Phi_{sc}^{l=1} = v S_{AC} \frac{\exp(ikr_s)}{4\pi D_{out} r_s} \frac{\exp(ikr_d)}{4\pi r_d} \left[ik - \frac{1}{r_s} \right] \left[ik - \frac{1}{r_d} \right] \left[\frac{4\pi a^3}{3} \right] \left[\frac{-3 \cos \theta \delta\mu'_s}{3\mu'_{s,out} + 2\delta\mu'_s} \right], \quad (3.3)$$

$$\begin{aligned} \Phi_{sc}^{l=2} = & v S_{AC} \frac{\exp(ikr_s)}{4\pi D_{out} r_s} \frac{\exp(ikr_d)}{4\pi r_d} \left[k^2 + \frac{3ik}{r_s} - \frac{3}{r_s^2} \right] \left[k^2 + \frac{3ik}{r_d} - \frac{3}{r_d^2} \right] \left[3 \cos^2 \theta - 1 \right] \\ & \left[\frac{4\pi a^5}{45} \right] \left[\frac{\delta\mu'_s}{5\mu'_{s,out} + 3\delta\mu'_s} \right]. \end{aligned} \quad (3.4)$$

Here, $\delta\mu_a = \mu_{a,in} - \mu_{a,out}$ is the difference in the absorption coefficient of the object and background, $\delta\mu'_s = \mu'_{s,in} - \mu'_{s,out}$ is the difference in the reduced scattering coefficient, $k = k_{out}$, and θ is the angle between the z-axis and the line joining the detector to the object center. To leading order $\Phi_{sc}^{l=0}$ depends only on $\delta\mu_a$ and $\Phi_{sc}^{l=1}$ and $\Phi_{sc}^{l=2}$ depend only on $\delta\mu'_s$. We have to look at higher order terms for the Φ_{sc}^l to see dependences on the other optical properties.

For an object that has the same scattering properties as the background, but different absorption properties, the signal is derived to leading order from the monopole term and scales as $a^3\delta\mu_a$. Thus, to leading order one can only reconstruct the product $a^3\delta\mu_a$ and cannot simultaneously determine the diameter and absorption coefficient of the object. When the monopole is the only detectable moment, a small, highly absorbing object cannot be distinguished from a larger, less absorbing object. The dipole and quadrupole moments have a different functional dependence on a and $\delta\mu_a$ and thus the object can be characterized, in principle, when both the monopole and either the dipole or the quadrupole moments are detectable.

The results are similar for an object with a pure scattering change. In that case, the dominate term is the dipole moment which depends on the product of a^3 and $\delta\mu'_s$. The size and scattering coefficient of a scattering object, therefore, cannot be simultaneously characterized unless the dipole and quadrupole moments are detectable. Generally, the detectability of the different moments of the scattered DPDW depends on the characteristics of the object and the noise in the measurements.

3.1.2 Noise Models

For an ideal experimental system the uncertainty in the measured amplitude and phase of the DPDW is given by shot-noise. Shot-noise is defined as the square-root of the number of photons detected. In practice, however, the uncertainty in the DPDW amplitude and phase is not dominated by shot-noise but is also affected by uncertainty in the position of the source and detector relative to one another and relative to the sample (see fig. 3.2). There are two different types of positional uncertainty. They are: 1) random errors associated with the incorrect positioning of the source and detector such that the actual distance of the source and detector with respect to each other and with respect to a reference point exhibits a normal distribution about the expected value, and 2) random errors from small motions of the sample, e.g. due to breathing and the heart pulse. An important difference between these two sources of positional errors is that the second type can be reduced by integration of the signal over longer times while the first type, in principle, can only be reduced by repeated trials wherein the source and detector are actually repositioned. In our laboratory we have found (in an infinite homogeneous medium) that the positional uncertainty is the leading contributor to the uncertainty in the amplitude and phase of the DPDW. For a given source-detector pair, with a positional uncertainty σ_r , the fractional uncertainty in the amplitude, $\frac{\sigma_{AC}}{|\Phi(\mathbf{r}_s, \mathbf{r}_d)|}$, in an infinite medium is given by

$$\begin{aligned} \frac{\sigma_{AC}}{|\Phi(\mathbf{r}_s, \mathbf{r}_d)|} &= \left[\text{Im}(k) + \frac{1}{|\mathbf{r}_s - \mathbf{r}_d|} \right] \sigma_r \\ &= \left[\sqrt{\frac{3}{2}} \sqrt{\mu_a \mu'_s} \left(\sqrt{1 + \left(\frac{\omega}{v \mu_a} \right)^2} - 1 \right)^{\frac{1}{2}} + \frac{1}{|\mathbf{r}_s - \mathbf{r}_d|} \right] \sigma_r , \end{aligned} \quad (3.5)$$

and the uncertainty in the phase in radians, σ_θ , in an infinite medium is given by

$$\begin{aligned} \sigma_\theta &= \text{Re}(k) \sigma_r \\ &= \sqrt{\frac{3}{2}} \sqrt{\mu_a \mu'_s} \left(\sqrt{1 + \left(\frac{\omega}{v \mu_a} \right)^2} + 1 \right)^{\frac{1}{2}} \sigma_r . \end{aligned} \quad (3.6)$$

$|\Phi(\mathbf{r}_s, \mathbf{r}_d)|$ is the amplitude of the detected DPDW, $\text{Im}(k)$ is the imaginary part of the DPDW wavenumber, and $\text{Re}(k)$ is the real part of the DPDW wavenumber. The noise in the amplitude decreases with increasing attenuation length of the DPDW. The noise in the phase decreases with increasing wavelength of the DPDW. Thus, a variation of system parameters which result in a decrease in the DPDW attenuation length and wavelength will increase the noise due to source-detector positional uncertainties. We have verified this relation with the equipment in our lab which has a positional uncertainty of 0.1 mm. To do so, we repeatably measured the amplitude and phase of the DPDW in an infinite medium at various source-detector separations and compared the measured uncertainties with those calculated using eq. (3.5) and eq. (3.6). This process was then repeated for systems with different optical properties and in all cases good agreement was observed. Eq. (3.5) and eq. (3.6) are a reasonable approximation of the amplitude and phase uncertainties that arise due to positional uncertainties in semi-infinite and slab geometries. For semi-infinite and slab geometries I do not write down the exact equation for the uncertainties. Calculations of the change in amplitude and phase for small displacements of the source and detector for such geometries show that the uncertainties are well approximated by eq. (3.5) and eq. (3.6).

An estimation of the magnitude of shot-noise and noise from positional errors indicates the significance of positional uncertainties. I estimate a clinically relevant shot-noise using a 3 mW light source with 100% modulation, a detector with a collection area of 0.1 cm^2 , a quantum efficiency of 1%, and the experimental system depicted in fig. 3.1. With these parameters, shot-noise gives a fractional error of 9×10^{-4} in the wave amplitude for a one second integration time (the phase noise is 9×10^{-4} radians or $\sim 0.05^\circ$). For a positional uncertainty of $10 \mu\text{m}$ in either the source or the detector, the fractional error in the amplitude is 2×10^{-3} and the phase noise is 0.03° . If the uncertainty is in the position of both the source and detector then the noise threshold is multiplied by $\sqrt{2}$. For a typical clinical situation the noise produced from positional uncertainties in the source and detector is comparable to shot-noise.

Achieving a positional certainty of $10 \mu\text{m}$ in the clinic is a daunting task consid-

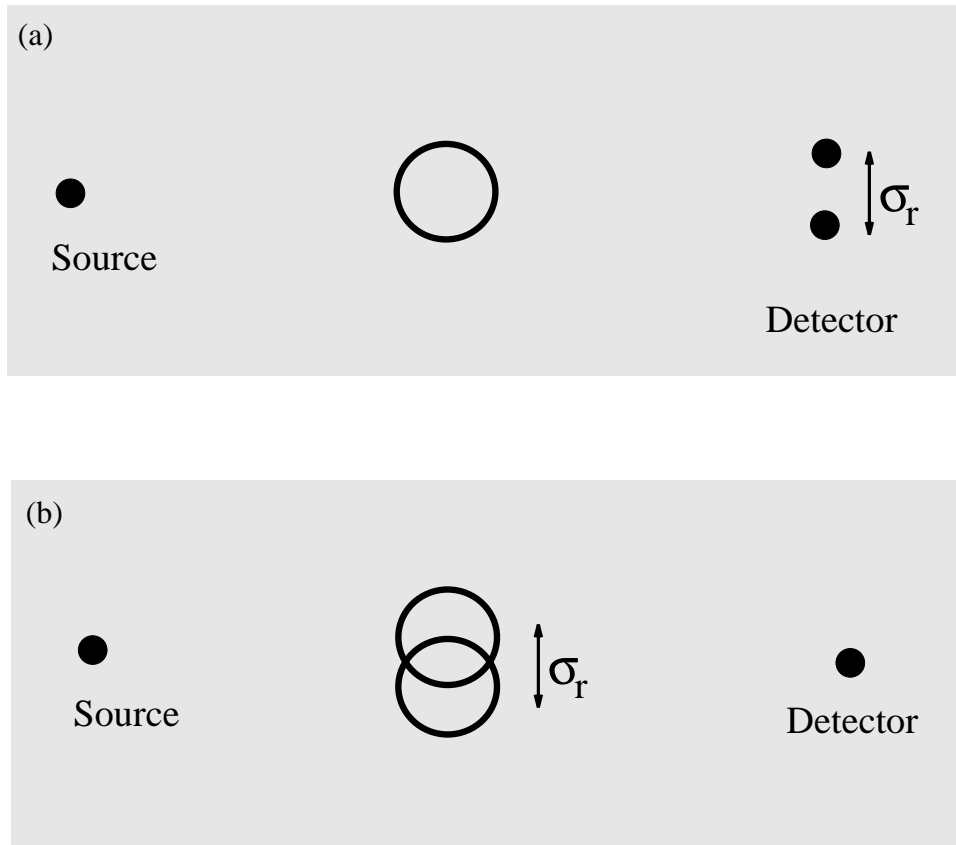


Figure 3.2: Errors from positional uncertainty can arise from an inaccurate positioning of the source and detector relative to each other (as depicted in (a)) and/or relative to the sample under study (as shown in (b)). These errors are random unless no vibrations are present and no realignment of the source and detector are made for multiple measurements. In a clinical environment vibrations will be present due to breathing and the heart beat. In case (a) and (b) σ_r is reduced by making repeated measurements. Positional uncertainties induced by sample vibrations of type (b) are reduced by longer integration times.

ering the motional artifacts arising from the respiration and pulse of the subjects. A more realistic positional uncertainty of $100 \mu\text{m}$ will result in a 2% uncertainty in the amplitude and 0.3° degree uncertainty in the phase. These results are for a best case scenario and are based on the shot-noise arising under the above described conditions and the additional noise arising from a positional uncertainty of $10 \mu\text{m}$. These two types of noise will be reduced by the \sqrt{N} where N is the number of independent measurements averaged to obtain a single value for the amplitude and the phase.

3.2 Description of Simulations

All results in this chapter for the detection and characterization of optical inhomogeneities using DPDW's are based on analytic calculations of the distorted DPDW with appropriate levels of random noise. The sample is an infinite slab, 6 cm thick (~ 60 random walk steps thick) which is homogeneous except for a spherical heterogeneity centered between the input and output planes of the slab. Measurements are made in transmission mode, i.e. the source is on one side of the slab and the detector is on the other side. Two types of spherical objects are considered: an absorbing object which has the same scattering coefficient as the background, and a scattering object which has the same absorption coefficient as the background.

To study the limits for detection and localization of these objects, the source and detector are scanned together along the surface of the slab. The perturbation to the amplitude and phase of the DPDW by the object can be described, respectively, by the ratio of the amplitudes with and without the object and the difference in the phase with and without the object.

In Section 3.3 the detectability of the object is found by comparing this perturbation with the noise level. If the perturbation is greater than the noise level, the object is deemed detectable. A large portion of parameter space is studied by varying the background optical properties, the object optical properties, and the DPDW modulation frequency. Note that at each detector position the signal is integrated for

1 second and measured once. Shot-noise can be reduced by increasing the integration time while the noise due to positional errors can be reduced by averaging repeated measurements in which the source and detector are physically repositioned. If the positional errors are due to movement of the sample, then the noise is also reduced by increasing the integration time.

The ultimate clinical applications of these probes may depend on our capabilities for object characterization. For example, to specify tumor size and malignancy or brain bleed maturity, it is likely that the size and optical properties of the detectable optical inhomogeneity will need to be characterized. In section 3.4 limits to object characterization are studied by first calculating the perturbed DPDW and then estimating the uncertainty with which the object's size and optical properties can be determined by means of a chi-squared fitting procedure to the analytic solution. The perturbed DPDW is first calculated using the analytic solution and then appropriate noise is added. "Measurements" are made with the source fixed at a position closest to the object at $x=0$ and $z=0$, and the detector scanned from $x=-2.0$ to 2.0 cm in steps of 0.20 cm at $z=6.0$ cm. A total of 42 independent measurements are obtained (21 amplitude and 21 phase measurements). In all studies the DPDW modulation frequency is 200 MHz. The noise added in these measurements is that given by the shot-noise for a 3 mW source and the noise from random positional uncertainties of $10 \mu\text{m}$ as described in section 3.1.2. Thus the noise used in the simulations is approximately 0.3% in the amplitude and 0.08° phase.

The fitting procedure is based on minimizing the chi-square difference between the measured DPDW profile and the analytic solution by varying the object's diameter and optical properties. This procedure is a best case scenario since we assume the background optical properties as well as the position and shape of the object. In practice more general imaging methods must be used that do not assume that the shape of the object is known. My results therefore represent the best one can possibly do in terms of characterization for a specific set of measurements. For a given noise level, the uncertainty in the estimated properties is found using the chi-squared method

described by Bevington [95]. In essence, the uncertainty of a fit parameter is found by varying the parameter until the chi-square value increases by one from the value at the global minimum. Theoretically, the uncertainty determined in this way is equivalent to the uncertainty that would be found from multiple experiments.

The chi-square difference function to be minimized is

$$\chi^2(\mu'_s, \mu_a, a) = \sum_{i=1}^N \frac{\left[|\Phi_{\text{exp}}^i(\mathbf{r}_s^i, \mathbf{r}_d^i)| - |\Phi_{\text{anal}}^i(\mathbf{r}_s^i, \mathbf{r}_d^i, \mu'_{s,in}, \mu_{a,in}, a)| \right]^2}{\sigma_{AC}^{i2}} + \frac{\left[\text{Arg}[\Phi_{\text{exp}}^i(\mathbf{r}_s^i, \mathbf{r}_d^i)] - \text{Arg}[\Phi_{\text{anal}}^i(\mathbf{r}_s^i, \mathbf{r}_d^i, \mu'_{s,in}, \mu_{a,in}, a)] \right]^2}{\sigma_\theta^{i2}}. \quad (3.7)$$

Here, the sum is over all measurements, \mathbf{r}_s^i and \mathbf{r}_d^i are the position of the source and detector for the i^{th} measurement, $\Phi_{\text{exp}}^i(\mathbf{r}_s^i, \mathbf{r}_d^i)$ is the experimental photon fluence for this pair, and $\Phi_{\text{anal}}^i(\mathbf{r}_s^i, \mathbf{r}_d^i, \mu'_{s,in}, \mu_{a,in}, a)$ is the fluence obtained from the analytic solution (eq. (3.1)) using the optical characteristics of the object (i.e. $\mu'_{s,in}$, $\mu_{a,in}$, and a). Recall that $\Phi_{\text{exp}}^i(\mathbf{r}_s^i, \mathbf{r}_d^i)$ is obtained by adding random noise to the analytic solution (eq. (3.1)). The vertical bars, $|\Phi|$, indicate the absolute value of the complex number and $\text{Arg}[\Phi]$ represents the phase of the complex number Φ .

The initial amplitude and phase of the source are known. Uncertainty in the amplitude and phase of the source introduces systematic errors, further complicating the characterization procedure. If such uncertainty is present, then the initial phase and amplitude of the source can also be used as free parameters in the χ^2 fit at the expense of increasing the uncertainty in the other fitting parameters.

3.3 Detection and Localization

Breast tumors and brain bleeds are optical inhomogeneities in the sense that their optical scattering and absorption properties are different than that of the surrounding media. An understanding of the detection limits of these inhomogeneities is important for designing optical screening techniques. An optical inhomogeneity is said to be

detectable if the perturbation to the detected amplitude or phase of the DPDW is larger than the noise threshold.

We can detect absorbing objects as small as 3 mm when the object absorption coefficient is a factor of 3 larger than the background. We can detect scattering objects as small as 4 mm when the object scattering coefficient is a factor of 1.5 larger than the background. The small absorbing objects are detectable because of perturbations to the amplitude of the DPDW, while scattering objects are detectable because of perturbations to the phase of the DPDW. The detectability of objects with different contrast is determined by the $a^3\delta\mu_a$ ($a^3\delta\mu'_s$) dependence of the leading order multipole moment of the DPDW scattered from an absorbing (scattering) object. Generally the detectability of an object is determined by the magnitude of $a^3\delta\mu_a$ or $a^3\delta\mu'_s$. For example, a 3 mm diameter absorber with $\delta\mu_a=0.10 \text{ cm}^{-1}$ is detectable, then a 1 mm object with $\delta\mu_a=2.7 \text{ cm}^{-1}$ is also detectable for the same system. This rule of thumb is discussed further in Section 3.6.

3.3.1 Detection of Absorbing Objects

Fig. 3.3 plots the change in the amplitude and phase of the DPDW due to a spherical absorber with $\mu_{a,in}=0.15 \text{ cm}^{-1}$ embedded in a system with $\mu'_{s,out}=10.0 \text{ cm}^{-1}$ and $\mu_{a,out}=0.05 \text{ cm}^{-1}$. Details of the system are described in fig. 3.1. Results are plotted for 1 mm, 2 mm, and 3 mm diameter absorbers. Given the previously discussed noise threshold, the absorber can be detected if its diameter is at least 3 mm. Note that the largest change in the signal occurs when the object lies directly between the source and detector. Thus if the object is detectable, its transverse position can be determined. By scanning the source and detector along three orthogonal axes, the central coordinates of a detectable object are easily determined. The certainty in the determined position of the object is in principle set by the accuracy in the position of the source and detector.

Fig. 3.4 presents contour plots of the smallest detectable absorber for a large portion of parameter space. Note that the noise levels depend on the factors that

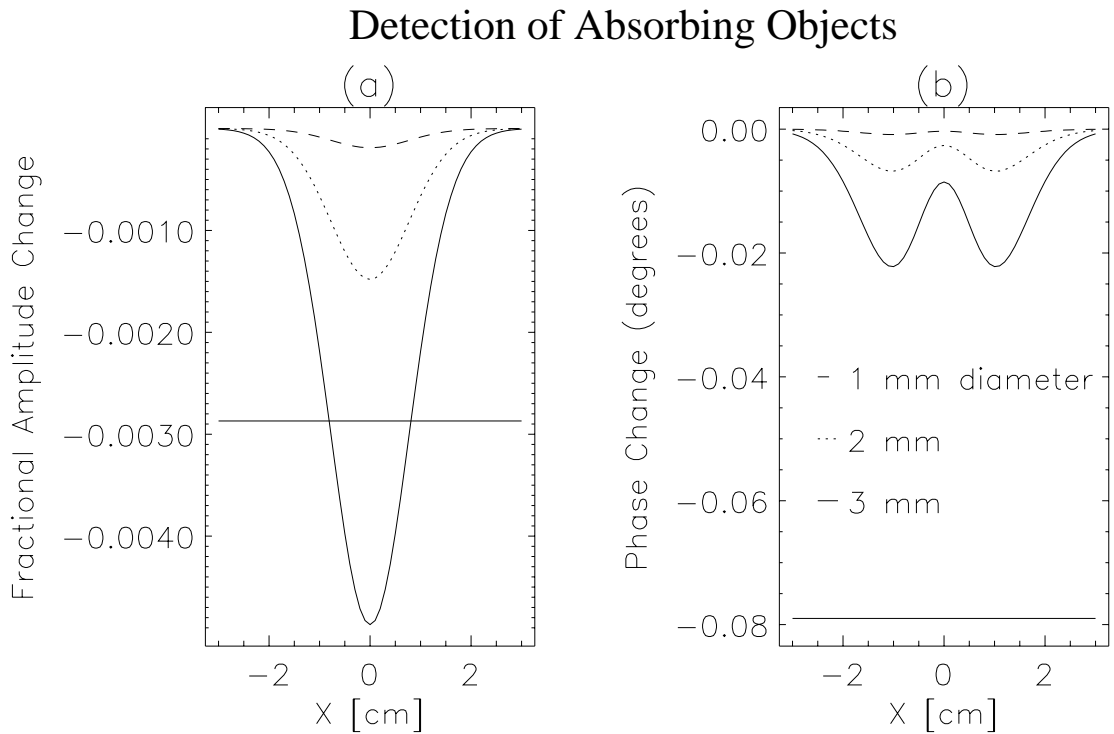


Figure 3.3: The fractional change in the amplitude and change in degrees of the phase due to the presence of the absorbing object is given in (a) and (b) respectively as a function of the lateral position of the source-detector. The system is described in the caption of fig. 3.1. Results are given for 1.0 mm (dashed line), 2.0 mm (dotted line), and 3.0 mm (solid line) diameter absorbers. The noise threshold is given by the solid horizontal line in (a) and (b). Note that the signal does not exceed the noise threshold unless the object's diameter is greater than or equal to 3.0 mm, and then it is only the change in the amplitude and not the phase that is detectable.

are being varied in these graphs and are therefore not fixed at the levels used in fig. 3.3. For example, with a 200 MHz modulation frequency with $\mu'_s=20.0 \text{ cm}^{-1}$ and $\mu_a=0.05 \text{ cm}^{-1}$, the fractional error in the amplitude is 0.7% and the phase error is 0.3°. With a 200 MHz modulation frequency with $\mu'_s=10.0 \text{ cm}^{-1}$ and $\mu_a=0.15 \text{ cm}^{-1}$, the fractional error in the amplitude is 1% and the phase error is 0.4°. Recall that with a 200 MHz modulation frequency with $\mu'_s=10.0 \text{ cm}^{-1}$ and $\mu_a=0.05 \text{ cm}^{-1}$, the fractional error in the amplitude is 0.3% and the phase error is 0.08° so that in fig. 3.4 the noise levels are varying by at least a factor of 5. The noise levels are still determined using a 1 second integration time.

In fig. 3.4a, the contours indicating the diameter of the smallest detectable absorber are drawn as a function of the background reduced scattering coefficient and the object absorption coefficient. The background absorption coefficient was kept fixed and the object reduced scattering coefficient was kept equal to the background reduced scattering coefficient. Clearly, as the object absorption coefficient increases, smaller objects become detectable. The background reduced scattering coefficient has little effect on absorber detectability indicating that the increasing noise, resulting from a larger $\mu'_{s,out}$, is balanced by an increasing signal. The noise increases because of reduced photon transmission through the slab with increased μ'_s . In fig. 3.4b, contours are drawn as functions of the background and object absorption coefficients while keeping the scattering coefficients constant. The detectability of absorbers diminishes as the background absorption coefficient rises because of an increase in shot-noise (due to increased photon absorption) and the decrease in the absorption contrast of the object. In fig. 3.4c, contours are given as a function of source modulation frequency and object absorption coefficient. Surprisingly, increasing the modulation frequency actually decreases the detectability of absorbers. This trend is observed because the noise increases more rapidly than the signal, as discussed further in section 3.5.2 and fig. 3.12.

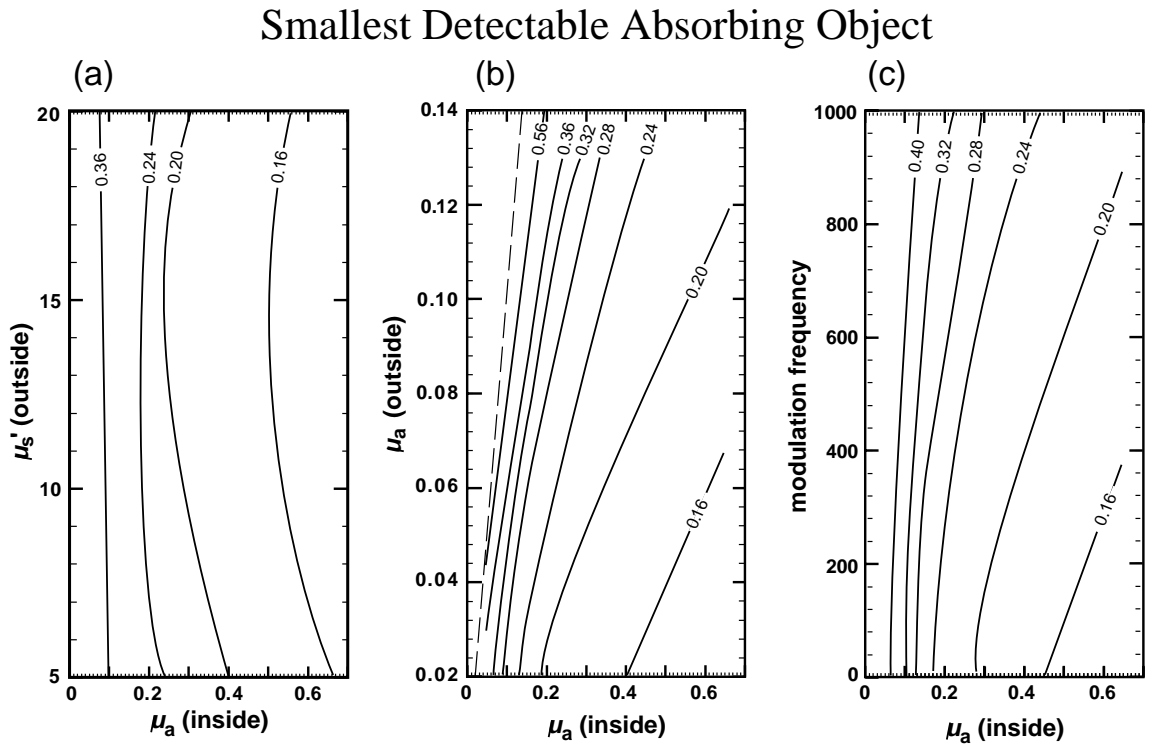


Figure 3.4: The diameter of the smallest detectable absorber is plotted as a function of (a) $\mu'_{s,out}$ and $\mu_{a,in}$, (b) $\mu_{a,out}$ and $\mu_{a,in}$, and (c) source modulation frequency and $\mu_{a,in}$. The contours indicate the diameter of the smallest detectable absorber in units of centimeters. The system and measurements are described in fig. 3.1. In (a), $f = 200$ MHz, $\mu_{a,out} = 0.05$ cm $^{-1}$, and $\mu'_{s,in} = \mu'_{s,out}$. In (b), $f = 200$ MHz and $\mu'_{s,out} = \mu'_{s,in} = 10.0$ cm $^{-1}$. In (c), $\mu'_{s,out} = \mu'_{s,in} = 10.0$ cm $^{-1}$ and $\mu_{a,out} = 0.05$ cm $^{-1}$. The noise levels are based on a positional uncertainty of 10 μm and a 1 second integration time. The dashed line in (b) indicates where $\mu_{a,out} = \mu_{a,in}$.

3.3.2 Detection of Scattering Objects

Fig. 3.5 graphs the relative change in the signal due to an object with a different reduced scattering coefficient than the background. From fig. 3.5 we see that a 0.4 cm diameter object with a 50% increase in μ'_s relative to the background is detectable. A small scattering object is detectable because the phase shift exceeds the noise threshold while a small absorbing object is detectable because of the relative change in the amplitude. It is because of this distinction that one can ultimately distinguish absorbing and scattering objects. Localization of a scattering object is straightforward since the largest change in the phase occurs when the object is directly between the source and detector.

Contour plots of the smallest detectable scattering object are presented in fig. 3.6. In fig. 3.6a, the smallest detectable object is plotted as a function of background and object reduced scattering coefficient. These results corroborate our expectations that smaller scatterers can be detected when the scattering contrast is increased. In fig. 3.6b, results are plotted as a function of background absorption coefficient and object scattering coefficient. The object absorption coefficient is kept the same as the background. The background absorption coefficient has little effect on the detectability of scattering objects except when the scattering contrast is large. In fig. 3.6c, results are plotted as a function of source modulation frequency and object scattering coefficient. The detectability of the scattering object is relatively unaffected by increasing the modulation frequency, indicating that the noise and signal are increasing at the same rate. In contrast, for the absorbing object, the detectability decreased because the noise increased more than the signal.

3.4 Characterization

After a tumor or brain bleed has been detected and localized, we can then derive information about the inhomogeneity's physical and physiological state by characterizing its size and optical properties. As seen in figs. 3.3 and 3.5 the amplitude and

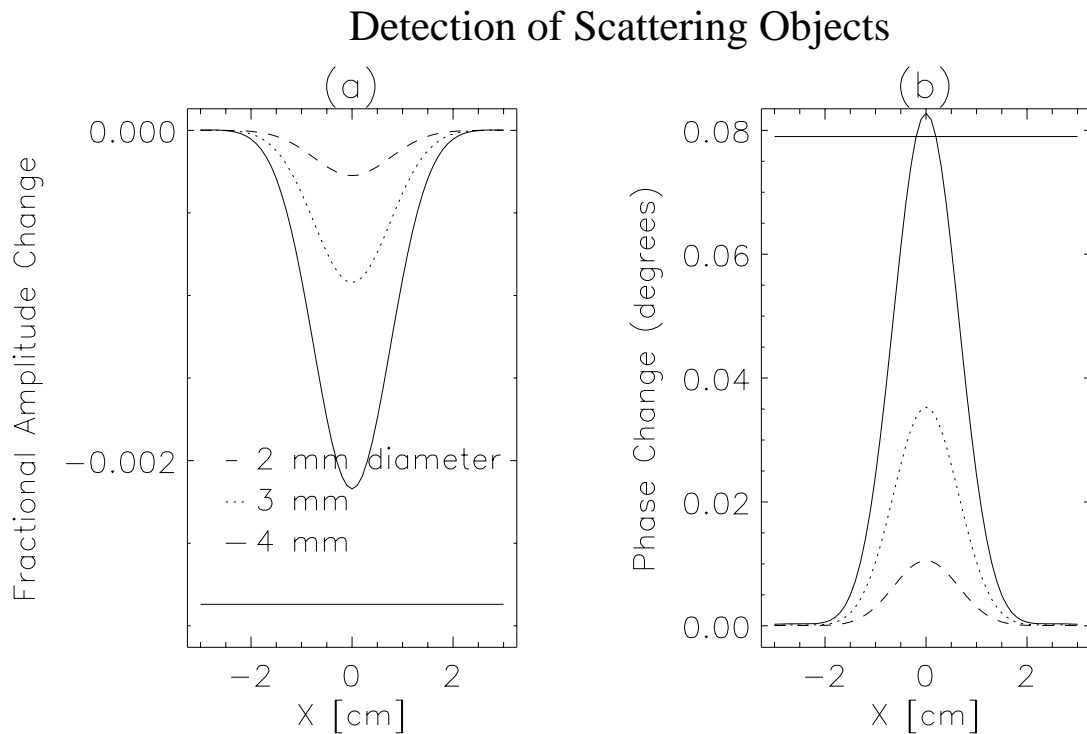


Figure 3.5: The fractional change in the amplitude and change in degrees of the phase due to the scattering object is given in (a) and (b) respectively as a function of the lateral position of the source-detector. The solid line corresponds to a 0.4 cm diameter object, while the dotted and dashed lines correspond to a 0.3 cm and 0.2 cm diameter object respectively. System parameters are described in the caption of fig. 3.1. The noise threshold is given by the solid horizontal line and is 0.3% for the amplitude change and 0.08 degrees phase.

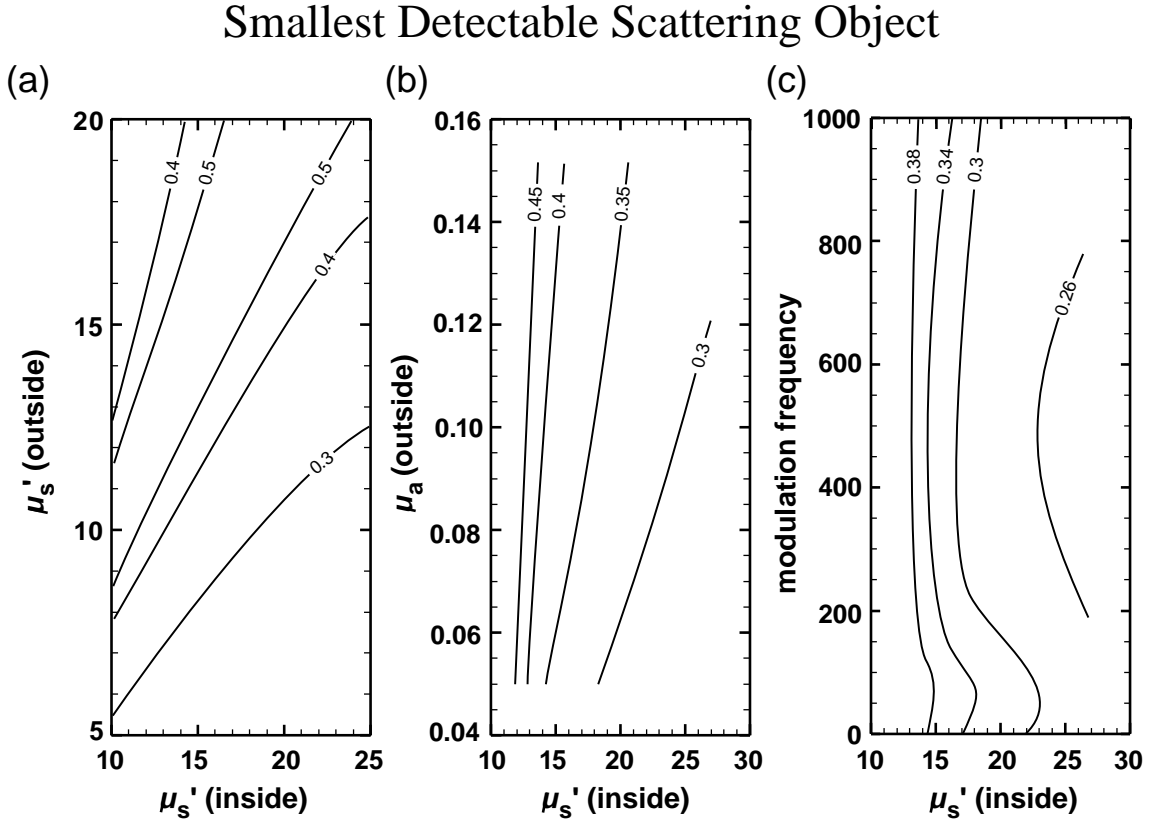


Figure 3.6: The diameter of the smallest detectable scatterer is plotted as a function of (a) $\mu_{s,out}'$ and $\mu_{s,in}'$, (b) $\mu_{a,out}$ and $\mu_{s,in}$, and (c) source modulation frequency and $\mu_{s,in}$. The contours indicate the diameter of the smallest detectable scatterer in units of centimeters. The system and measurements are described in fig. 3.1. In (a), $f = 200$ MHz and $\mu_{a,out} = \mu_{a,in} = 0.05 \text{ cm}^{-1}$. In (b), $f = 200$ MHz, $\mu_{s,out}' = 10.0 \text{ cm}^{-1}$, and $\mu_{a,out} = \mu_{a,in}$. In (c), $\mu_{s,in}' = 10.0 \text{ cm}^{-1}$ and $\mu_{a,out} = \mu_{a,in} = 0.05 \text{ cm}^{-1}$. The noise levels are based on a positional uncertainty of 10 μm and a 1 second integration time.

phase profile of a distorted DPDW is sensitive to the size of the inhomogeneity as well as the optical properties. Thus, in principle, the characteristics of an inhomogeneity can be determined from the profile of the distorted DPDW. However, in contrast to localization, the size and optical properties cannot be determined directly. We must rely on indirect methods, such as image reconstruction techniques or best fits to analytic solutions for the measured DPDW profile, in order to deduce this information. As described in the experimental section (section 3.2), I use chi-squared fitting techniques to fit for the size and optical properties of the optical inhomogeneity.

3.4.1 Characterization of Absorbing Objects

First I consider simultaneous characterization of the diameter and absorption coefficient of an absorbing object embedded in the center of a 6 cm thick slab (see fig. 3.1). The scattering coefficient of the object is the same as the background, and the detector is scanned from $x=-2.0$ to 2.0 cm in steps of 0.2 cm while the source is fixed nearest the object at $x=0$. Fig. 3.7 presents contour plots of the fractional uncertainty of the object's diameter and absorption coefficient. Three different contour plots are given: in fig. 3.7a,b results are given versus object diameter and absorption coefficient ($\mu'_{s,out} = \mu'_{s,in} = 10.0 \text{ cm}^{-1}$, $\mu_{a,out} = 0.05 \text{ cm}^{-1}$, and $f = 200 \text{ MHz}$). In fig. 3.7c,d results are given versus background reduced scattering coefficient and object absorption coefficient ($\mu'_{s,in} = \mu'_{s,out}$, $\mu_{a,out} = 0.05 \text{ cm}^{-1}$, diameter=1.2 cm, and $f = 200 \text{ MHz}$). In fig. 3.7e,f results are given versus background absorption coefficient and object absorption coefficient ($\mu'_{s,out} = \mu'_{s,in} = 10.0 \text{ cm}^{-1}$, diameter=1.2 cm, and $f = 200 \text{ MHz}$). The system is described in more detail in fig. 3.1. These three contour plots reveal the variation in fractional uncertainty over a large sampling of the parameter space. The magnitude of the uncertainty depends on the total number of measurements that are considered in the χ^2 fit and in general decreases as the square-root of the number of measurements. For the parameter space considered in fig. 3.7, we see that given 21 measurements of the phase and amplitude (for a total of 42 independent measurements), the absorbing object can be accurately characterized when its diameter

exceeds 0.8 cm. Here a 20% uncertainty is considered to be accurate.

The contour plots versus the object's diameter and absorption coefficient (fig. 3.7-a,b) show that the uncertainties diminish rapidly as the diameter increases and slowly as the absorption coefficient is increased. The slower decrease in the uncertainties for larger absorption coefficients results from saturation of the signal. In general the error bar for the diameter is symmetric about the mean value while the error bar for the absorption coefficient of the object is asymmetric. The asymmetry results from the saturation of the signal for larger absorption coefficients. Thus the upper error is always larger than the lower error. The difference is usually within 20%. In all contour plots I plot the average of the lower and upper fractional uncertainties.

From the contour plots versus the background reduced scattering coefficient and the object absorption coefficient (fig. 3.7c,d), we see a similar dependence on the absorption coefficient of the object and that the uncertainties initially decrease and then increase as $\mu'_{s,out}$ increases. The explanation for this is that as $\mu'_{s,out}$ increases, the DPDW wavelength decreases, and as the ratio between the DPDW wavelength and the object diameter gets smaller, the fractional perturbation to the signal increases. Therefore we would expect the uncertainties in the fitting parameters to decrease. However, the noise from positional errors is also increasing because the DPDW wavelength is decreasing. In addition, the shot-noise is increasing because of the reduced transmission through the slab as μ'_s is increased. For the conditons in fig. 3.7c,d, the interplay between the increasing signal and increasing noise is such that the uncertainties first decrease and then increase.

From the contour plots versus the background absorption coefficient and the object absorption coefficient (fig. 3.7e,f), we see that the uncertainties increase as the background absorption coefficient is increased, and they decrease as the object absorption coefficient is increased. There are two factors contributing to the dependence on the background absorption coefficient: first, more light absorption leads to an increase in shot noise, and second, the decrease in the absorption contrast of the object results in a smaller perturbation to the DPDW.

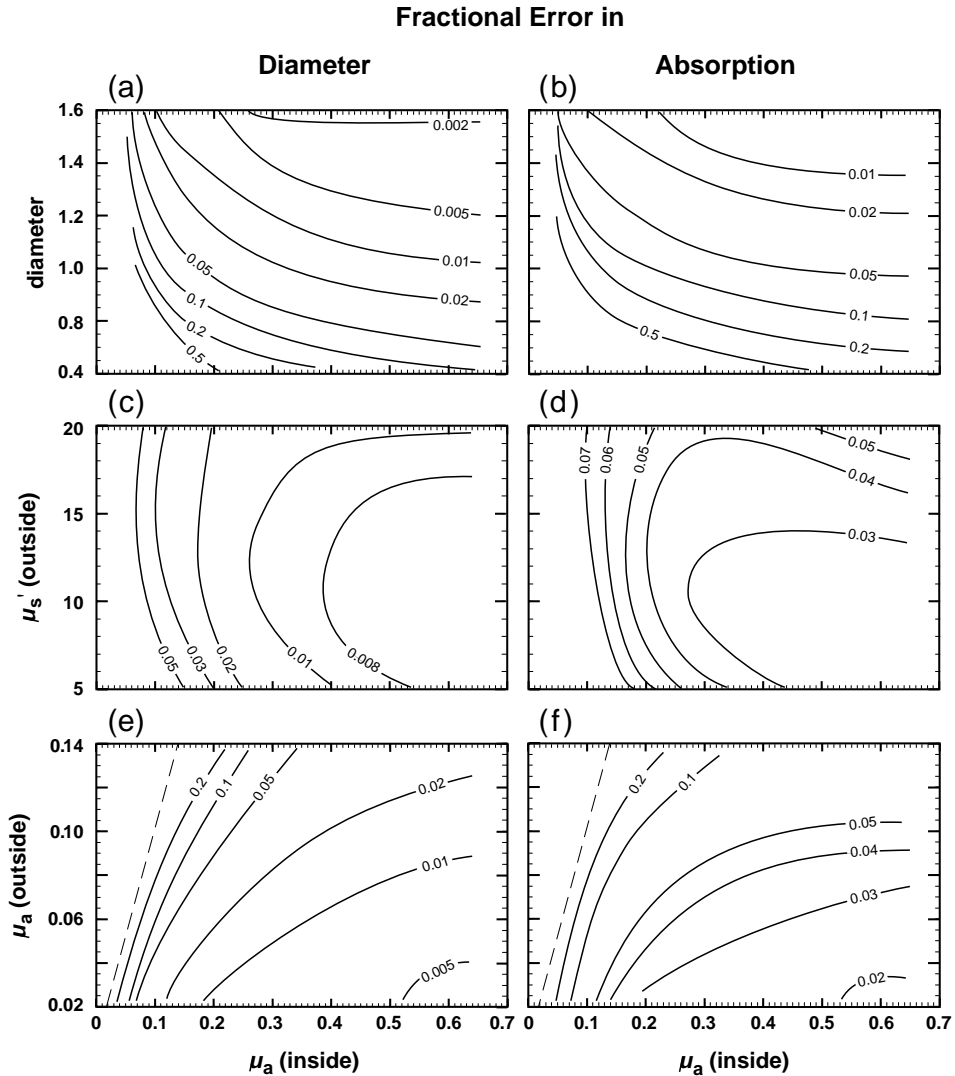


Figure 3.7: The fractional uncertainty in the object diameter (a,c,e) and object absorption coefficient (b,d,f) are plotted in contour plots for a large range of parameter space. The labels on the contours indicate the fractional uncertainty. In (a) and (b) uncertainties are plotted versus the diameter and absorption coefficient of the object. In (c) and (d) the background scattering coefficient and object absorption coefficient are varied. In (e) and (f) the background absorption coefficient and object absorption coefficient are varied. The dashed lines in (e) and (f) indicate where $\mu_a(\text{outside}) = \mu_a(\text{inside})$.

Although a 0.3 cm diameter absorber can be detected and localized, the absorber cannot be characterized accurately unless its diameter is greater than ~ 0.8 cm. This result was obtained using 21 measurements of amplitude and phase. As discussed in section 3.1.1, this difference between object detection and characterization arises from the functional form of the different moments of the scattered DPDW. Fig. 3.8 plots the contribution of the monopole, dipole, and quadrupole moments of the scattered DPDW to the total signal versus the diameter of the absorbing object. That is, I plot the amplitude and phase of

$$\frac{\Phi_{sc}^{(l)}}{\Phi_{inc}} . \quad (3.8)$$

Note that this quantity accounts for the perturbation of each moment to the incident DPDW. If this perturbation is greater than the noise threshold, the given moment of the scattered wave is detectable. The noise threshold is also indicated in the figure.

In order to detect the object it is only necessary for the monopole term to exceed the noise threshold. This occurs when the object's diameter is ≥ 0.3 cm, which agrees with the previous observation in fig. 3.3. The dipole moment does not exceed the noise threshold until the diameter is ≥ 0.8 cm. For absorber diameters ≥ 0.8 cm the monopole and dipole moments of the scattered wave are detectable and thus, in principle, the absorber is characterizable. The results in fig. 3.7 indicate that the absorber can be accurately characterized when the diameter exceeds 0.8 cm. Recall that the uncertainty in the object parameters decrease with the square root of the number of measurements and thus accurate characterization of smaller objects is possible by increasing the number of measurements. This may give an experimenter an improvement of 0.3 cm if, for example, 400 measurements are made of the scattered DPDW over the same spatial region as the 40 measurements. This 0.3 cm improvement is estimated from fig. 3.8; if the number of measurements is increased by a factor of ten then the uncertainty will decrease by approximately a factor of three. Thus, from fig. 3.8 we see that the monopole and dipole contributions exceed the noise threshold when the diameter of the absorber exceeds 0.5 cm.

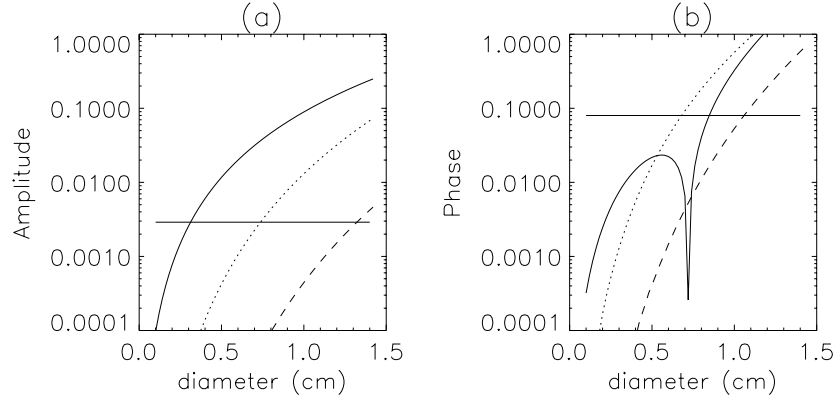


Figure 3.8: The amplitude (a) and phase (b) contribution of the monopole (solid line), dipole (dotted line), and quadrupole (dashed line) moments of the scattered wave to the incident wave is graphed versus the diameter of the absorbing object. The noise threshold is depicted by the horizontal line at 2.9×10^{-3} for the amplitude and 8×10^{-2} for the phase. When the monopole term exceeds the noise threshold at 0.3 cm, then the absorber is detectable. However, the diameter and absorption coefficient of the absorber can not be simultaneously determined until the monopole and dipole terms are detectable. This is the case for diameters greater than 0.8 cm.

3.4.2 Characterization of Scattering Objects

Here I consider the simultaneous characterization of the diameter and scattering coefficient of a scattering object embedded in the center of a 6 cm thick slab (see fig. 3.1). The absorption coefficient of the object is the same as the background, and the detector is scanned from $x=-2.0$ to 2.0 cm in steps of 0.2 cm while the source is fixed nearest the object at $x=0$. Fig. 3.9 presents contour plots of the fractional uncertainty of the object's diameter and scattering coefficient. Three different contour plots are given: in fig. 3.9a,b results are given versus object diameter and scattering coefficient ($\mu'_{s,out} = 10.0 \text{ cm}^{-1}$, $\mu_{a,out} = \mu_{a,in} = 0.05 \text{ cm}^{-1}$, and $f = 200 \text{ MHz}$). In fig. 3.9c,d results are given versus background reduced scattering coefficient and object reduced scattering coefficient ($\mu_{a,out} = \mu_{a,in} = 0.05 \text{ cm}^{-1}$, diameter=1.2 cm, and $f = 200 \text{ MHz}$). In fig. 3.9e,f results are given versus background absorption coefficient and object reduced scattering coefficient ($\mu'_{s,out} = 10.0 \text{ cm}^{-1}$, $\mu_{a,out} = \mu_{a,in}$,

diameter=1.2 cm, and $f = 200$ MHz). The system is described in more detail in fig. 3.1. By plotting these three contour plots we see the variation in the fractional uncertainty over a large sampling of the parameter space. The magnitude of the uncertainty depends on the total number of measurements that are considered in the χ^2 fit and in general decreases as the square-root of the number of measurements. For the parameter space considered in fig. 3.9, we see that, given 21 measurements of the phase and amplitude (for a total of 42 independent measurements), the scattering object can be accurately characterized when its diameter exceeds 0.8 cm. The exact value depends on the scattering coefficient of the object. Again an uncertainty less than 20% is considered accurate.

From the contour plots versus the object's diameter and scattering coefficient (fig. 3.9a,b), we see that the uncertainties diminish rapidly as the diameter increases and slowly as the reduced scattering coefficient is increased. The slower decrease in the uncertainties for larger scattering coefficients results from saturation of the signal and the leading order $a^3\delta\mu'_s$ dependence of the scattered wave. Note that in general the error bar for the diameter is symmetric about the mean value while the error bar for the scattering coefficient of the object is asymmetric. The asymmetry results from the saturation of the signal for larger scattering coefficients and thus the upper error is always larger than the lower error. The difference is usually within 20%. In all contour plots I plot the average of the lower and upper fractional uncertainties.

From the contour plots versus the background reduced scattering coefficient and the object reduced scattering coefficient (fig. 3.9c,d), we first see that the object cannot be characterized when the scattering contrast is smaller than 40%. Interestingly, the fractional uncertainty changes more with a change in the background scattering coefficient than with a change in the object scattering coefficient. One might expect that the uncertainty depends only on the difference in the scattering coefficients in which case changes in the fractional uncertainty would be symmetric with respect to changes in the scattering coefficient of the background and the object. The observed asymmetry results from the noise's dependence on the background reduced scattering

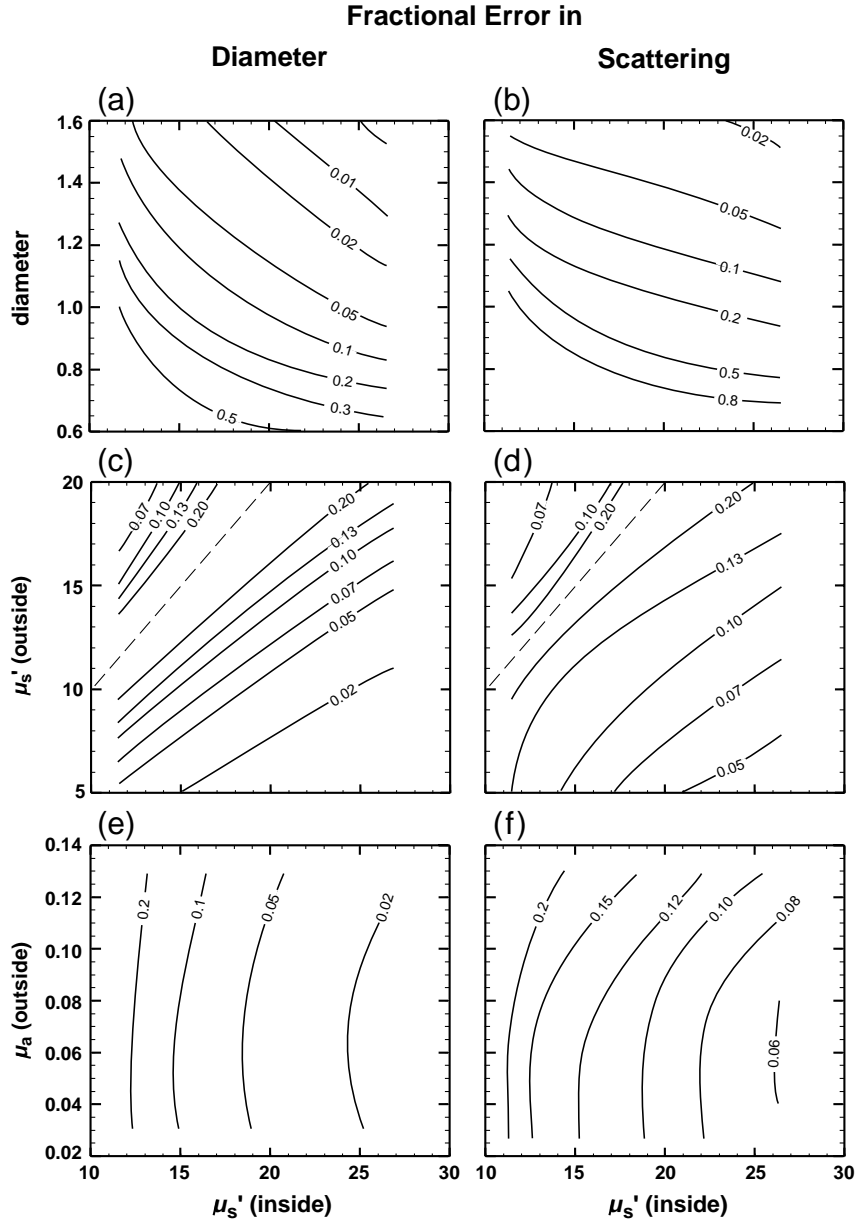


Figure 3.9: The fractional uncertainty in the object diameter (a,c,e) and object scattering coefficient (b,d,f) are plotted in contour plots. The labels on the contours indicate the fractional uncertainty. In (a) and (b) uncertainties are plotted versus the diameter and scattering coefficient of the object. In (c) and (d) the background scattering coefficient and object scattering coefficient are varied. In (e) and (f) the background absorption coefficient and object scattering coefficient are varied. The dashed line in (c) and (d) indicates where μ_s' (outside) = μ_s' (inside).

coefficient. As the background reduced scattering coefficient is increased, the noise also increases because of the reduced transmission of light through the slab (shot-noise) and the decrease in the DPDW wavelength.

From the contour plots versus the background absorption coefficient and the object reduced scattering coefficient (fig. 3.9e,f), we see that the uncertainties increase slightly with an increase in the absorption coefficient and decrease with an increase in the object reduced scattering coefficient. These trends are simply due to the increased shot-noise from increasing the background absorption coefficient and the increased signal from increasing the object reduced scattering coefficient.

Although a 0.4 cm diameter scatterer can be detected and localized, the scatterer cannot be characterized accurately unless its diameter is greater than 0.8 cm. As discussed earlier, this difference between object detection and characterization arises from the functional form of the different moments of the scattered DPDW.

3.5 Optimizing the Experimental Design

Improvements in detecting and characterizing optical inhomogeneities are generally achieved by increasing the signal relative to the noise. The noise threshold can be reduced by making multiple measurements or by integrating the signal longer and reducing shot-noise and positional error due to sample motions. These noise reduction techniques reduce the noise by the square-root of the number of measurements or the square-root of time. The magnitude of the perturbation can be increased by increasing the modulation frequency. Increasing the modulation frequency decreases the DPDW wavelength which in turn results in a larger scattering amplitude, particularly for the higher moments. However, increasing the modulation frequency will increase the shot-noise, as a result of the reduced DPDW amplitude for the same source-detector separation, and increase the uncertainty due to positional errors, as a result of the reduced DPDW wavelength. In the following subsections I investigate the interplay between these various factors.

3.5.1 Optimizing Measurement Geometry

To determine what role the position of the source and detector play in characterizing an object, I repeated the characterization simulation for two different measurement geometries. First the effect of fixing the source closest to the object at $x = 0$ and scanning the detector from $x=-3.0$ to 3.0 cm in steps of 0.30 cm was examined. The fractional uncertainty in the diameter and absorption coefficient for this set of measurements is graphed in fig. 3.10 along with the previous result obtained from scanning the detector from $x=-2.0$ to 2.0 cm in steps of 0.20 cm. These results indicate that the characterization accuracy is decreased when the range over which the detector is scanned is increased while keeping the number of measurements constant. The second measurement geometry was chosen to examine the effect of scanning the source and detector together from $x=-3.0$ to 3.0 cm. For comparison, these results are also plotted in fig. 3.10. The characterization accuracy is decreased further when the source and detector are scanned together. From fig. 3.10 we see that the measurement geometry is optimized for object characterization by keeping the source and detector near the absorbing object. This result applies to scattering objects as well.

These observations are easily understood within the context of the moments analysis. Fig. 3.11 graphs the contribution of each moment to the total signal (eq. (3.8)) versus the transverse position of the detector. Results are plotted for two cases: 1) the source is scanned with the detector and 2) the source is fixed at $x=0$. The moments are calculated for a 1.0 cm diameter absorber. From fig. 3.11 we see that, overall, the moments make a larger contribution to the scattered wave when the source is fixed near the object. In particular, the perturbation is larger for transverse displacements of the detector from $x=0$ and therefore it is detectable for a greater number of measurements. By concentrating the measurements where the perturbation is strongest, we are increasing the average signal-to-noise ratio resulting in a more accurate determination of an object's characteristics.

This result suggests that the most accurate characterization will arise from all measurements coming from the source and detector fixed nearest the object. This

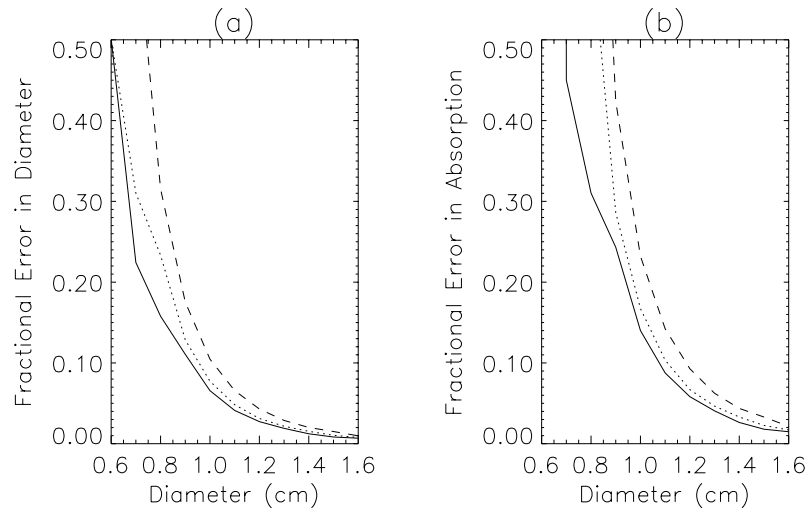


Figure 3.10: The fractional uncertainty for (a) the object diameter and (b) object absorption coefficient are plotted versus the known object diameter for different sets of measurements. The solid line corresponds to the set of measurements presented in fig. 3.7, that is the detector is scanned from $x=-2.0$ to 2.0 cm while the source is fixed at $x=0$. The dotted line corresponds to keeping the source fixed at $x=0$ and scanning the detector from $x=-3.0$ to 3.0 cm, while for the dashed line the source and detector were scanned together from $x=-3.0$ to 3.0 cm. In all cases 21 independent measurements of the phase and amplitude were obtained at even intervals over the range of the scan. The system parameters are described in fig. 3.1.

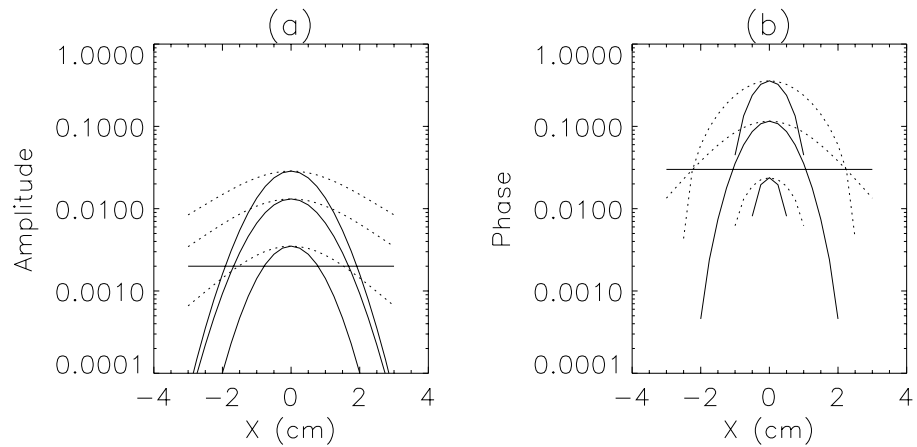


Figure 3.11: The amplitude (a) and phase (b) contribution of the monopole, dipole, and quadrupole moments of the scattered wave to the incident wave is graphed versus the lateral position of the detector. The source was scanned with the detectors for the solid line and fixed at $x=0$ for the dashed lines. At $x=0$ the top, middle, and bottom pair of solid and dashed lines correspond respectively to the contributions of the monopole, dipole, and quadrupole moments. The noise threshold is depicted by the horizontal line at 2×10^{-3} for the amplitude and 3×10^{-2} for the phase. When the source is fixed at $x=0$, i.e. near the object, the signal is larger, permitting an accurate characterization of smaller objects.

is indeed the case when there are only two unknowns, e.g. diameter and absorption coefficient. That is, the amplitude and phase from one source-detector pair provides sufficient information to determine two unknowns. However, if there are more than two unknowns (e.g. initial amplitude and phase of the source, object shape, and/or object position in addition to the diameter and absorption coefficient of the object), then the additional information provided from a spatially distributed set of source-detector pairs is required.

Usually the initial amplitude and phase of the source and the shape of the object will not be known accurately, and therefore measurements from a spatially distributed set of source-detector pairs is optimal. The signal to noise comparison in fig. 3.11 indicates which measurements provide information about the optical inhomogeneity and therefore provides an approach for designing an optimal measurement geometry.

3.5.2 Optimal Modulation Frequency

Comparing signal-to-noise ratios for different DPDW modulation frequencies, we can determine the optimal frequency for detecting and characterizing different objects. Fig. 3.12a,b plots the change in the signal due to each moment relative to the incident wave (eq. 3.8) as a function of modulation frequency for an absorbing object. Although the magnitude of each moment is increasing with frequency, each moment's perturbation of the signal is not necessarily increasing because of interference between the moment and the incident wave. In fact, as is seen in fig. 3.12a,b, at 2200 MHz the quadrupole moment effects no phase shift and at 300 MHz the quadrupole moment effects no amplitude change. These nulls in general do not decrease the ability to characterize an object because a null in either the amplitude or phase is compensated by a large signal in the phase or amplitude respectively. On the other hand, the frequency at which these nulls occur depends on the characteristics of the object and therefore they may be exploited to improve object characterization. A similar idea has been suggested by Yao *et al.* [96].

The shot-noise and positional error as a function of modulation frequency are plot-

ted in fig. 3.12c and d. They exhibit an increase with modulation frequency as expected. For the model system, the shot-noise exceeds the positional noise at frequencies larger than 800 MHz. The crossover point for the amplitude noise occurs because the amplitude of the DPDW is decreasing exponentially as approximately the square-root of the modulation frequency. Thus the fractional error due to shot-noise is increasing exponentially. On the other hand, the fractional error due to positional uncertainty is increasing approximately with the square-root of the modulation frequency. Because of the rapid increase in noise with modulation frequency, measurements at high modulation frequencies are undesirable. Likewise, measurements at low modulation frequencies are undesirable because of the small perturbations.

To determine the optimal frequency for detection and characterization, I calculate the signal-to-noise ratio for the monopole, dipole, and quadrupole moments. These results are plotted in fig. 3.12e and f. The best signal to noise is obtained around 0 MHz. Although the signal-to-noise ratio is smaller at higher modulation frequencies, it is possible to accurately characterize a 1.0 cm diameter absorber at 2.0 GHz, because the monopole and dipole perturbations still exceeds the noise threshold.

Similar results were also obtained for the scattering objects (see fig. 3.13). The main difference is that the best signal-to-noise ratio for scattering objects is obtained around 500 MHz.

Modulation frequencies between 0 and 500 MHz are appropriate when considering the characterization of single objects embedded in otherwise homogeneous systems. If multiple objects are present and resolution becomes an issue, then measurements at higher modulation frequencies are desirable. By resolution I mean the ability to distinguish signals that originate from different sources, e.g. the waves scattered from two distinct objects. Resolution improves with higher modulation frequencies because the DPDW wavelength decreases and we gain sensitivity to smaller length scales. The analytic techniques presented here permit us to determine the maximum modulation frequencies that provide useful information, but they do not provide a simple framework for analyzing the resolving power of DPDW's. The reader is referred

to Pattanayak [89] for a discussion on the resolving power of DPDW's.

3.5.3 Utilizing Spectral Information

It has been suggested that measurements of the amplitude and phase of diffuse photon density waves at several modulation frequencies may be used to enhance sensitivity to the optical properties of a turbid medium [3]. I have investigated this possibility by comparing fractional uncertainties obtained with three different source-detector configurations. The three configurations are: 1) modulation frequency held constant at 200 MHz, 2) modulation frequency scanned from 0 to 1000 MHz in steps of 200 MHz, and 3) modulation frequency scanned from 0 to 1000 MHz in steps of 100 MHz. In each of the three cases, the source was held fixed closest to the object and the detector was scanned from $x = -2.0$ to 2.0 cm in steps of 0.2 cm. Also, for each case the total number of independent measurements was kept constant at 210 measurements of amplitude and phase (i.e. at each position 10 measurements were made of amplitude and phase). In this way, any observed improvement in the characterization of the object can be attributed to spectral measurements rather than an overall increase in the number of measurements. In case (1) this required making 10 measurements at 200 MHz at each spatial position, while in case (2) 2 measurements were made at each frequency and each spatial position.

Fig. 3.14a,b plots the fractional uncertainty in the diameter and absorption coefficient of an absorbing object versus the diameter of the object for the three different source-detector configurations. No improvement is observed in the fractional uncertainty of the diameter or the absorption coefficient. On the other hand, for a scattering object a decrease in the fractional uncertainty of μ'_s is observed when measurements are made over a range of modulation frequencies (see fig. 3.14c,d). Spectral measurements thus enhance the characterization of scattering objects as well as providing a means of distinguishing scattering from absorbing objects.

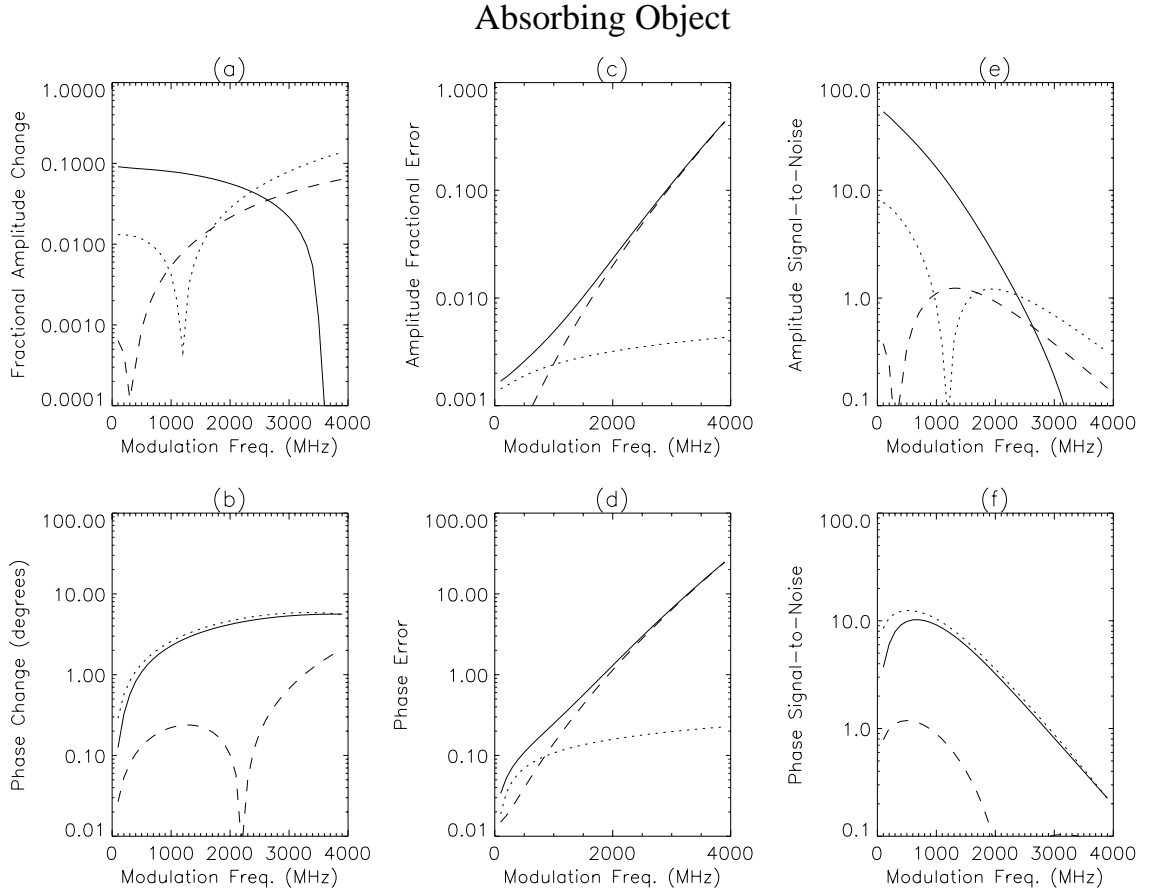


Figure 3.12: The contribution of the monopole (solid line), dipole (dotted line), and quadrupole (dashed line) moments of the scattered wave to the amplitude (a) and phase (b) of the total wave is plotted versus the modulation frequency of the source. The source and detector are separated by 6.0 cm with a 1.0 cm diameter absorbing object centered between them. The optical properties of the object are given in fig. 3.1. The noise in the amplitude and phase is given in (c) and (d) respectively. The dotted (dashed) line corresponds to the positional (shot) noise. The solid line is the combination of positional and shot noise. The signal to noise ratio for amplitude and phase is given respectively in (e) and (f) for the monopole (solid line), dipole (dotted line), and quadrupole (dashed line) moments.

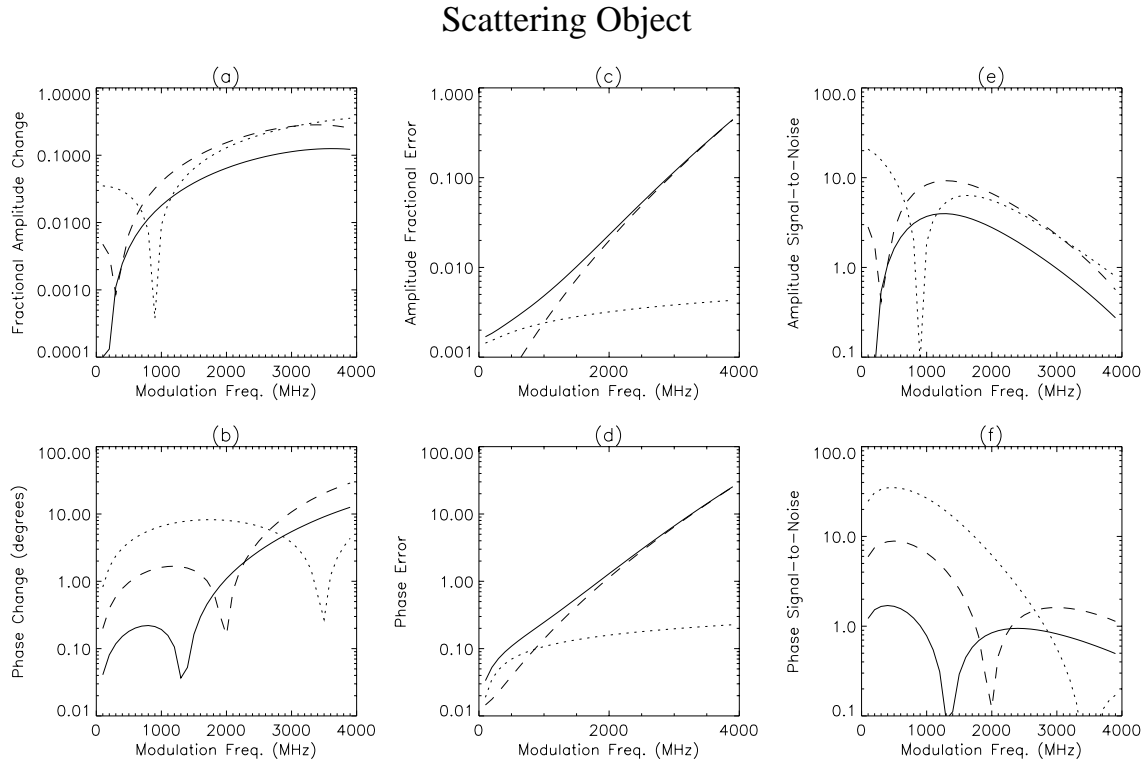


Figure 3.13: The contribution of the monopole (solid line), dipole (dotted line), and quadrupole (dashed line) moments of the scattered wave to the amplitude (a) and phase (b) of the total wave is plotted versus the modulation frequency of the source. The source and detector are separated by 6.0 cm with a 1.0 cm diameter scattering object centered between them. The optical properties of the object are given in fig. 3.1. The noise in the amplitude and phase is given in (c) and (d) respectively. The dotted (dashed) line corresponds to the positional (shot) noise. The solid line is the combination of positional and shot noise. The signal to noise ratio for amplitude and phase is given respectively in (e) and (f) for the monopole (solid line), dipole (dotted line), and quadrupole (dashed line) moments..

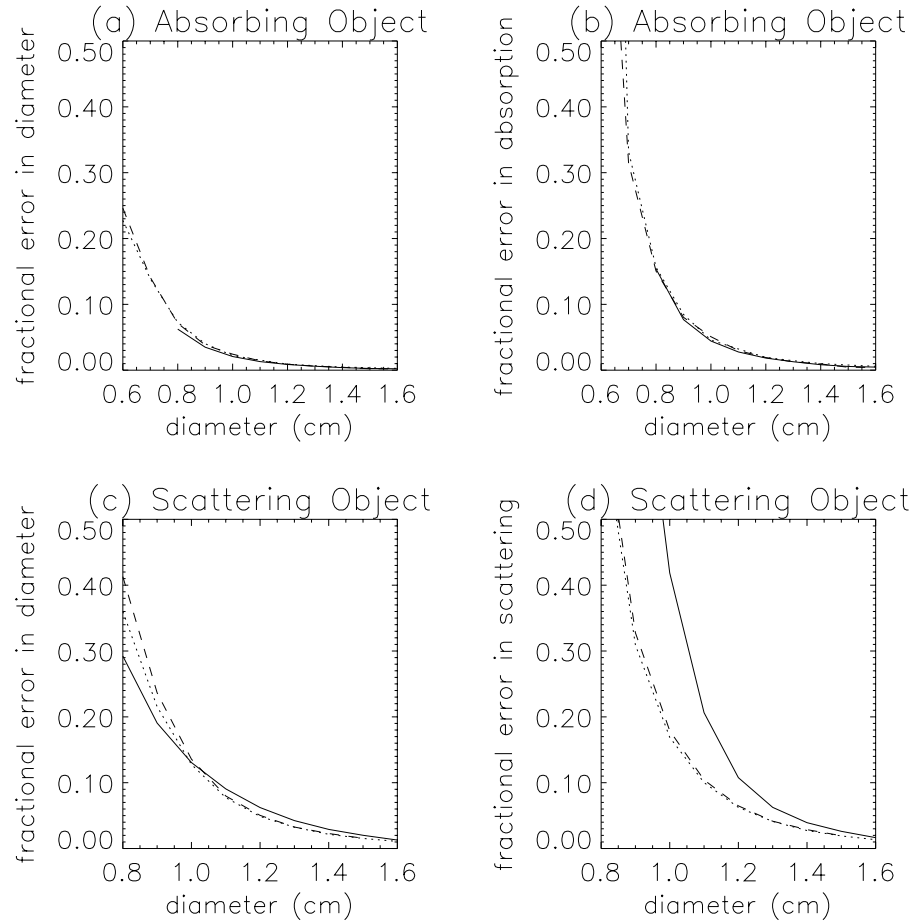


Figure 3.14: The fractional uncertainty in the diameter and absorption coefficient of an absorbing object are given in (a) and (b) respectively versus the diameter of the object. In (c) and (d) the fractional uncertainties are given for a scattering object. Results are given for three different source detector configurations. In all configurations the source was held fixed closest to the object at $x=0$ and the detector was scanned from $x=-2.0$ to 2.0 cm in steps of 0.2 cm. The solid lines corresponds to a modulation frequency of 200 MHz with 10 measurements made at each position. The dotted line results from the modulation frequency scanned from 0 to 1000 MHz in steps of 200 MHz with 2 measurements at each position. Finally, the dashed lines corresponds to 1 measurement at each position with the frequency scanned from 0 to 1000 MHz in steps of 100 MHz. Note that the spectral measurements improve the characterization of the scattering coefficient of the scattering object but do not enhance the characterization of the absorbing object.

3.5.4 Measurements at Multiple Optical Wavelengths

It is reasonable to expect that measurements at multiple optical wavelengths will improve our ability to characterize optical inhomogeneities. I will show that this additional information does not improve our ability to characterize the size and optical properties of inhomogeneities.

Consider two sets of measurements made on the same sample: one at optical wavelength λ_1 and the other at optical wavelength λ_2 . For each set we can independently characterize the size and absorption coefficient of the object. Assuming that a common chromophore is the dominant absorber at the two optical wavelengths, then the size of the characterized absorber should be the same for each set. Thus, instead of having four unknowns ($a(\lambda_1)$, $\mu_a(\lambda_1)$, $a(\lambda_2)$, and $\mu_a(\lambda_2)$), we only have three, and three parameters can be characterized more accurately than four.

This argument may sound reasonable, but we have to be careful. It is true that the uncertainties in the three parameters will be smaller than the uncertainties determined for the four parameters when the two data sets are characterized independently. However, will the uncertainties be any smaller than if all measurements were made at a single wavelength? Let's say that each data set has N measurements. In the first case we are using N measurements to get $a(\lambda_1)$ and $\mu_a(\lambda_1)$ and N measurements to get $a(\lambda_2)$ and $\mu_a(\lambda_2)$. In the second case we are using $2N$ measurements to determine a , $\mu_a(\lambda_1)$, and $\mu_a(\lambda_2)$. We would do better to use $2N$ measurements to find just two parameters, a and $\mu_a(\lambda_1)$.

What if we knew the absorption spectrum of the dominant chromophore at λ_1 and λ_2 ? In this case there would only be two unknowns since $\mu_a(\lambda_1)$ and $\mu_a(\lambda_2)$ would have a known proportionality C . This might lead to improved characterization. To see if this is possible we must consider the extended minima (or valleys) of the chi-squared surfaces for the different data sets. For a two dimensional chi-square function, there is a valley which indicates the relation between systematic deviations in the two fitting parameters. The valley for fitting $a(\lambda_1)$ and $\mu_a(\lambda_1)$ may look like curve 1 in fig. 3.15. This curve tells us what the deviation in a will be if we know the deviation

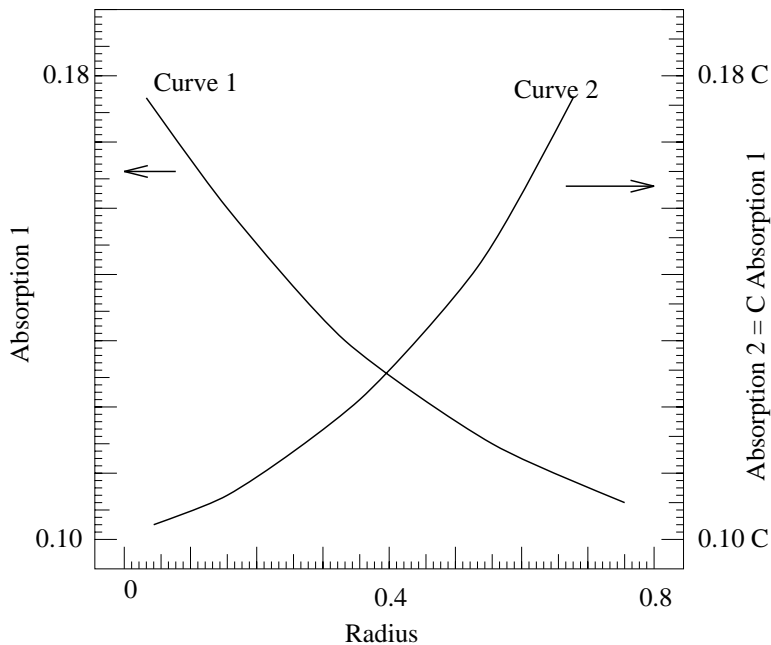


Figure 3.15: Possible chi-squared valleys for a two parameter fit for the object radius and absorption coefficient at two different optical wavelengths.

in μ_a and vice versa. For repeated measurements of the λ_1 data set, the determined a and μ_a values will always appear on curve 1. For λ_2 the valley may look like curve 2 in fig. 3.15. Curve 1 and curve 2 intersect at the correct values for the object parameters. If we fit both data sets simultaneously with the constraint that $a(\lambda_2) = a(\lambda_1)$ and $\mu_a(\lambda_2) = C\mu_a(\lambda_1)$ then the fitting parameters will be drawn towards the intersection point of the two curves, decreasing the uncertainty. If the valleys nearly overlap, then the fitting parameters will not be strongly drawn towards the intersection point. Improved characterization is possible only if the different curves have significantly different slopes near the intersection point.

Valleys for three spherical objects with different absorption coefficients but the same radius are shown in fig. 3.16. The dotted, dashed, and dot-dashed lines were derived from simulations for 5 mm diameter absorbers with absorption coefficients of 0.15, 0.45, and 0.75 cm^{-1} , respectively, relative to the background coefficient of 0.05 cm^{-1} . The other system parameters are indicated in fig. 3.1. These valleys

nearly overlap and therefore we cannot use multiple optical wavelengths to improve object characterization. Even if the curves were more perpendicular, uncertainties associated with the dominant chromophore assumption would reduce any gains in object characterization.

3.6 Summary

The interaction between DPDW's and optical inhomogeneities provides a straightforward way of detecting and localizing inhomogeneities and a means for characterizing the size and optical properties of the inhomogeneity. If no noise were present in the measurements then our ability to characterize these objects would only be limited by the validity of the model used for the analysis. Here, I have used an exact analytic model for the scattering of DPDW's from spherical inhomogeneities which is based on the diffusion approximation to the photon transport equation. This model is valid on length scales larger than the photon random walk step, $1/\mu'_s$, which is around 1 mm for tissue. Unfortunately noise is always present, and, as we have seen, it diminishes our ability to characterize inhomogeneities.

Detecting and locating inhomogeneities is possible if the perturbation of the incident DPDW, the signal (see eq. (3.8)), is greater than the noise threshold. The results presented here demonstrated that 3 mm diameter objects are detectable for realistic parameters. For small absorbing objects the signal is dominated by the monopole moment, while for small scattering objects the signal is dominated by the dipole and quadrupole moments. For transmission measurements, the strongest signal occurs when the object is directly between the source and detector and therefore a detectable object is easily located. Changing the modulation frequency does not greatly change the detectability of absorbing or scattering objects except at high frequencies where the signal is obscured by shot-noise (see figs. 3.4, 3.6, 3.12, and 3.13). The detectability of objects with different optical properties embedded in the same system as described in fig. 3.1 can be determined from the leading order form of the moments of

the scattered DPDW (see eqs. (3.2-3.4)). For instance, the leading order signal from a small absorbing object is proportional to $a^3\delta\mu_a$. This product, $a^3\delta\mu_a$, indicates how much larger a less absorbing object must be or how much smaller a more absorbing object can be in order for it to still be detectable. In particular, the product shows that the size of a detectable object scales as $\delta\mu_a^{-1/3}$. For example, given that an object with $\delta\mu_a=0.1 \text{ cm}^{-1}$ is detectable if $a > 0.3 \text{ cm}$, then an object with $\delta\mu_a = 0.05 \text{ cm}^{-1}$ is detectable if $a > 0.38 \text{ mm}$.

Characterizing the size and optical properties of an object is not as straightforward because an indirect method is required, e.g. chi-squared fitting, to determine the parameters from measurements of the distorted DPDW. Furthermore, it is necessary for more than one moment of the scattered DPDW to perturb the signal by a detectable amount in order to distinguish the contributions from the object's size and optical properties. To determine the size and either the absorption or scattering coefficient of an object, it is necessary for two moments to be detectable (i.e. two unknowns and two equations). Likewise, to accurately determine three parameters, it is necessary for at least three moments to be detectable. Because of these additional requirements, inhomogeneities cannot be accurately characterized unless they are 1 cm or larger in diameter for realistic parameters.

I have demonstrated that the measurement geometry can be optimized in order to characterize smaller objects. The only useful measurements are those for which the perturbation is detectable. Therefore, for transmission through a slab geometry it is best to make measurements with the source closest to the object and the detector scanned near the point of closest approach to the object or vice-versa. I have also demonstrated that 0 MHz is the optimal frequency for detecting and characterizing absorbing objects. Scattering objects are best detected and characterized with modulation frequencies near 500 MHz. Characterization of scattering objects is further optimized using measurements at several modulation frequencies.

Still smaller objects can be characterized if there is a priori knowledge of the size or optical properties of the object. For example, knowledge of the structural properties

of the system obtained from a CAT scan or MRI affords an accurate determination of the optical properties of tumors smaller than 1 cm. By reducing the number of unknowns, accurate tumor characterization becomes feasible with the detection of fewer multipole moments. If we know the size of an absorbing or scattering object, then the optical contrast can be determined as long as the contribution from a single moment is detectable. Likewise if the optical contrast is known and the size is sought. Thus, with prior knowledge it is possible to accurately characterize detectable objects, i.e. objects on the order of 3 mm in diameter. Any uncertainty in the priorly known quantity will result in a systematic error in the determined quantity. For example, if the size of the object is measured using MRI to be 5 mm and it is actually 4 mm, then the reconstructed absorption coefficient will be systematically reduced by 50%. The systematic deviation in the absorption (scattering) coefficient of an absorbing (scattering) object due to an incorrect previous determination of the size is described by the universal curve presented in fig. 3.16. The solid line derives from the $a^3\delta\mu_a$ ($a^3\delta\mu'_s$) dependence of the dominate contribution to the scattered wave from an absorbing (scattering) object and indicates that an overestimation of the size results in an underestimation of the optical parameter and vice versa. The dotted, dashed, and dot-dashed lines were derived from simulations for 5 mm diameter absorbers with absorption coefficients of 0.15, 0.45, and 0.75 cm^{-1} , respectively, relative to the background coefficient of 0.05 cm^{-1} . The observed deviation from the universal curve (solid line) arises from the increased importance of higher order multipole moments. This deviation is small and thus the universal curve serves as a good rule of thumb. Note that this result is valid for objects of general shape by replacing a^3 with the volume of the object.

The limits discussed here for detecting and characterizing optical inhomogeneities with diffuse photon density waves are based on ideal systems where the noise is governed by shot-noise and positional errors. The results should thus be viewed as a best case scenario. In the clinical environment, other sources of noise are expected to exist that will further complicate the accurate characterization of optical inhomogeneities. For instance, the intrinsic fluctuations of a biological sample about its average

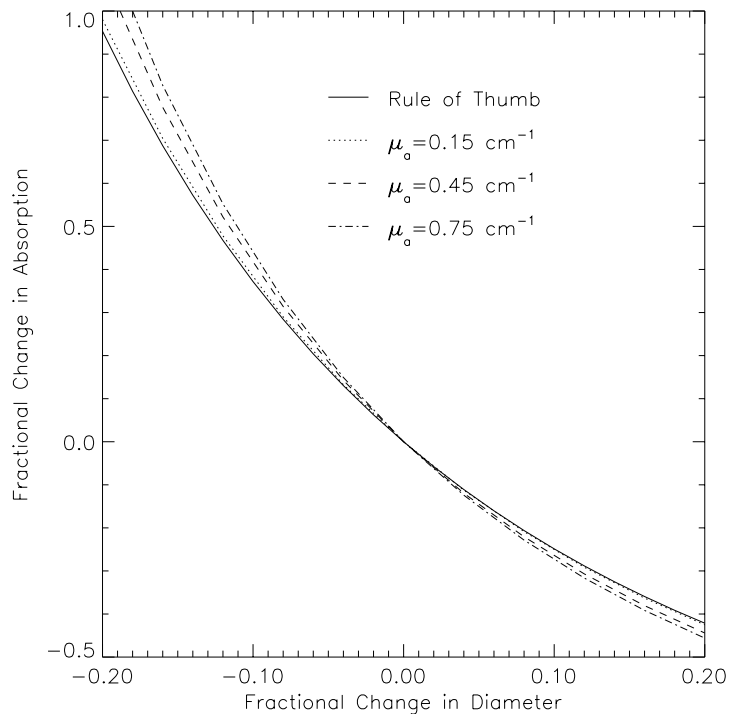


Figure 3.16: The fractional deviation in the optical parameter versus the fractional deviation in the diameter is graphed. The optical parameter represents either the absorption coefficient or scattering coefficient.

background value causes amplitude and phase shifts. If the intrinsic heterogeneity is not considered in imaging algorithms, then the corresponding signal fluctuations are essentially noise. Quantification of the intrinsic heterogeneity of different biological samples is necessary to determine if this type of noise is significant. Another source of systematic noise is the discrepancy between diffusion models and experiment. A discrepancy between models and experiment of 1% amplitude and a few degrees phase is not uncommon, especially at higher modulation frequencies. Further investigation is required to determine the effect of this systematic noise on optical imaging.

Chapter 4

Correlation Diffusion

4.1 Introduction

In the previous two chapters I discussed the properties of diffuse photon density waves (DPDW's) and the use of these intensity waves to probe turbid media for variations in optical properties. In this chapter I show that diffusing photons can also be used to probe the dynamical properties of turbid media. Information about the dynamics is obtained from the Doppler broadening of the laser linewidth as it migrates through the medium. The broadening of the linewidth manifests itself in the intensity fluctuations of spatially coherent speckles of scattered light. On the other-hand, DPDW's manifest themselves in the average intensity of scattered light.

Although the physics for probing the dynamical properties is different, I demonstrate a theoretical model for speckle fluctuations that is completely analogous to photon diffusion. The similarity in the mathematical form of the models suggests that the observed properties of DPDW's should also be observed for speckle fluctuations.

The theoretical basis for this work dates back to the late 1960's with the development of quasi-elastic light scattering theory (QELS) for optically dilute dynamical systems which scatter light no more than once. Extensions to highly scattering systems was made in the 1980's in various guises by Bonner and Nossal [46], Pine *et al.* [48], MacKintosh and John [49], Maret and Wolf [50], and Vol'kov and Romanov [51]. The analogy of correlation transport to photon transport was first made by Ackerson

et al. [57, 58] in the 1990's in order to better understand the behavior of correlation functions in the regime between single scattering and multiple scattering.

In section 4.2 I review these theories and develop a diffusion theory for predicting speckle fluctuations. The advantage of the correlation diffusion theory over previous theories is the ease with which predictions can be made for turbid media with spatially varying dynamical and optical properties. In the final sections of this chapter, I present experimental and Monte Carlo results which demonstrate the accuracy of the correlation diffusion model for various systems. In the next chapter I present two biomedical applications for this work.

4.2 Theory

When a beam of laser light with uniform intensity is incident on a rough surface, the reflection of the beam will not have a uniform intensity but will instead be composed of many bright and dark spots. These spots are called speckles and are illustrated by fig. 4.1. The complex intensity profile arises because light is reflected in many different directions from the rough surface and thus photons that have traveled different path lengths interfere constructively and destructively at the detector. The same happens for light that has migrated through a turbid solid sample. That is, the photons exit the sample traveling in different directions and different path lengths and thus interfere constructively and destructively at the detector. If the rough surface moves or scattering particles in the turbid medium are moving, the speckle pattern will then fluctuate in time. The time scale of the intensity fluctuations depends on the motion of the surface and scattering particles.

For the turbid medium, the time scale of speckle intensity fluctuations depends on the number of interactions that detected photons have had with moving scattering particles. This section briefly reviews the theory for temporal field autocorrelation functions of light scattered from optically dilute systems such that photons scatter no more than once before being detected. I then discuss the extension of single scat-

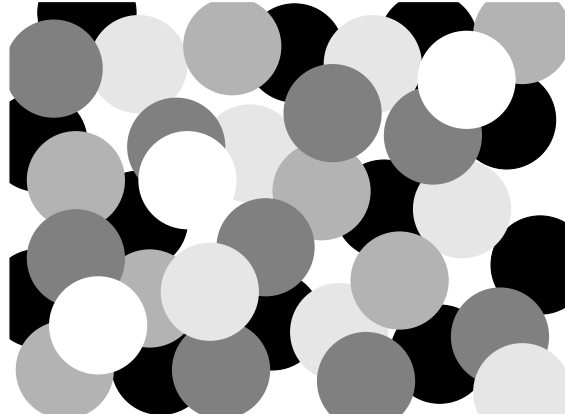


Figure 4.1: An illustration of a speckle pattern. The light regions correspond to regions of strong light intensity, and the dark regions correspond to regions of little intensity.

tering theory to systems which highly scatter light. After a brief review of diffusing wave spectroscopy, I describe in detail a new and more general method based on the transport/diffusion of correlation in optically dense systems.

4.2.1 Single Scattering

Consider the system depicted in fig. 4.2. A beam of coherent light is incident on a dilute suspension of identical scattering particles. The light scattered by an angle θ is detected by a photo-detector. The electric field reaching the detector is a superposition of all the scattered electric fields,

$$\begin{aligned}
 E &= E_o F(q) \sum_{n=1}^N \exp(i\mathbf{k}_{in} \cdot \mathbf{r}_n) \exp(i\mathbf{k}_{out} \cdot (\mathbf{R}_d - \mathbf{r}_n)) \\
 &= E_o F(q) \exp(i\mathbf{k}_{out} \cdot \mathbf{R}_d) \sum_{n=1}^N \exp(-i\mathbf{q} \cdot \mathbf{r}_n) .
 \end{aligned} \tag{4.1}$$

Here, E is the electric field reaching the detector at position \mathbf{R}_d , E_o is the amplitude of the incident field, and $F(q)$ is the form factor for light to receive a moment transfer of $\mathbf{q} = \mathbf{k}_{\text{out}} - \mathbf{k}_{\text{in}}$ where \mathbf{k}_{out} and \mathbf{k}_{in} are the output and input wavevectors respectively and $|\mathbf{q}| = 2k_o \sin \theta/2$ where $k_o = |k_{in}| = |k_{out}|$. For simplicity I neglect polarization effects and assume randomly positioned and oriented scatterers. Under these conditions the scattering differential cross-section is only dependent on the magnitude of \mathbf{q} . The summation is over the N particles in the scattering volume and \mathbf{r}_n is the position of each particle. We see from eq. (4.1) that the phase of each scattered wave depends on the momentum transfer (i.e. scattering angle) and the position of the particle. In a disordered system, the particles are randomly distributed resulting in random constructive and destructive interference at the detector. Displacing a single particle changes the interference and thus the intensity reaching the detector.

For particles which are undergoing random relative motion, e.g. Brownian motion, the phases of the individual scattered waves are changing randomly, independently from the other scattered waves. The intensity at the detector will thus fluctuate. The time scale of the intensity fluctuations is given by the rate at which the phase of the scattered waves is changing and thus depends on the motion of the scattering particles and the momentum transfer. Therefore, the intensity fluctuations are more rapid at larger scattering angles and for faster moving particles.

By monitoring the intensity fluctuations it is possible to derive information about the motion of the scattering particles. There are two standard approaches. One entails analysis of the power spectrum of the detected signal, i.e.

$$S(\omega) = \int dt I^2(t) \cos(\omega t) . \quad (4.2)$$

The other uses the unnormalized temporal autocorrelation of the intensity,

$$G_2(\tau) = \langle I(t)I(t + \tau) \rangle . \quad (4.3)$$

$I(t)$ is the intensity at time t and the $\langle \dots \rangle$ denotes an ensemble average. For an ergodic system, an ensemble average is equivalent to a time average and thus $G_2(\tau)$ can be

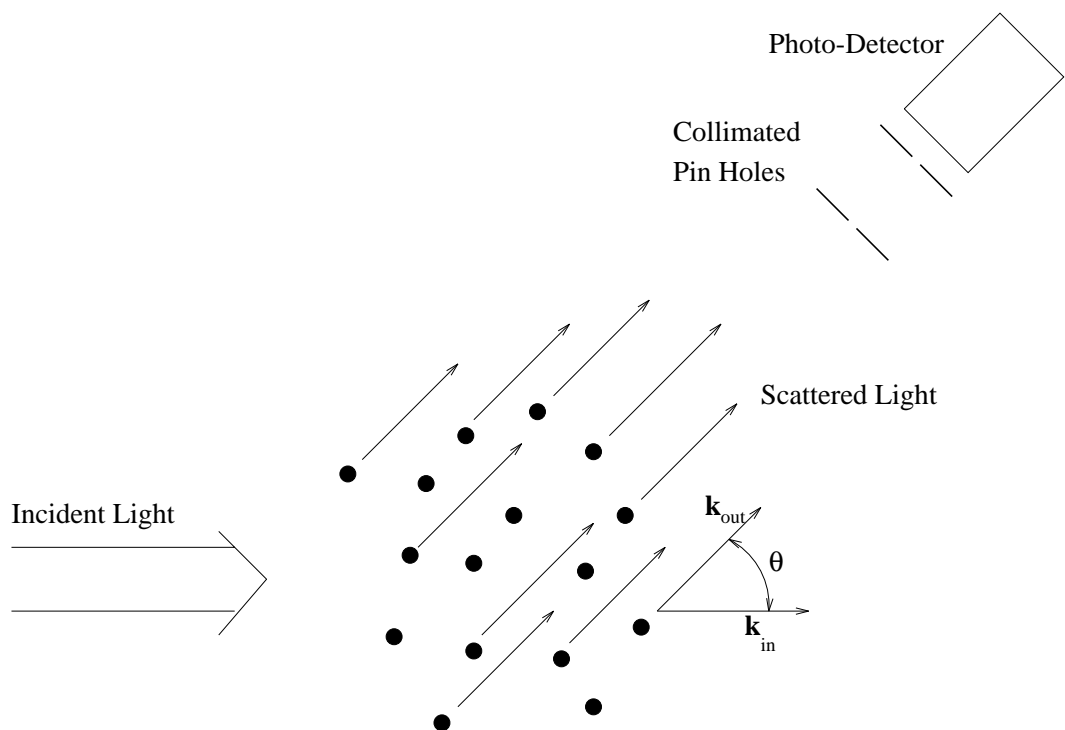


Figure 4.2: Light is incident on a dilute suspension of scatterers. The suspension is dilute enough such that photons are scattered no more than once. Light that is scattered by an angle θ is collimated by two pin-holes and monitored with a photo-detector.

obtained by a temporal average of the correlation function. The two methods are related as discussed [46, 52, 97, 98]. The exact relationship states that the intensity power spectrum and field correlation function form a Fourier transform pair [46, 98, 99, 100], i.e.

$$S(\omega) = \frac{\langle I \rangle^2}{2\pi} \int_{-\infty}^{\infty} \cos(\omega\tau) [g_2(\tau) - 1] d\tau , \quad (4.4)$$

where $g_2(\tau) = G_2(\tau)/\langle I \rangle^2$ is the normalized temporal intensity correlation function and $\langle I \rangle$ is the average intensity.

I focus on the temporal correlation method. Instead of calculating the temporal intensity autocorrelation function, $G_2(\tau)$, the standard approach is to derive the temporal field correlation function, $G_1(\tau) = \langle E(0)E^*(\tau) \rangle$, and note that the two are related by the Siegert relation [48, 50, 100]

$$G_2(\tau) = \langle I \rangle^2 + \beta |G_1(\tau)|^2 , \quad (4.5)$$

where $\langle I \rangle$ is the ensemble averaged intensity. β is a parameter which depends on the number of speckles detected and the coherence length and stability of the laser. β thus depends on the experimental setup. For an ideal experimental setup $\beta = 1$. See [101, 102] for more discussion on β .

The normalized temporal field correlation function is

$$g_1(\tau) = \frac{\langle E(0)E^*(\tau) \rangle}{\langle |E(0)|^2 \rangle} , \quad (4.6)$$

Using eq. (4.1) for the scattered electric field and noting that the cross terms resulting in eq. (4.6) average to zero when particle motions are uncorrelated, we find

$$g_1(\tau) = \langle \exp(i\mathbf{q} \cdot \Delta\mathbf{r}(\tau)) \rangle . \quad (4.7)$$

$\Delta\mathbf{r}(\tau) = \mathbf{r}(\tau) - \mathbf{r}(0)$ is the displacement of a particle in time τ and the average is over $\Delta\mathbf{r}(\tau)$ weighted by the appropriate distribution. In the case of Brownian motion, the average is weighted by [36]

$$P(\Delta\mathbf{r}(\tau)) = \frac{1}{(4\pi D_B \tau)^{3/2}} \exp\left(-\frac{|\Delta\mathbf{r}(\tau)|^2}{4D_B \tau}\right) , \quad (4.8)$$

where $P(\Delta\mathbf{r}(\tau))$ is the probability of a particle being displaced a distance $\Delta\mathbf{r}$ in a time τ . Calculating the weighted average, eq. (4.7) becomes

$$g_1(\tau) = \exp\left(-\frac{1}{6}q^2\langle\Delta r^2(\tau)\rangle\right). \quad (4.9)$$

$\langle\Delta r^2(\tau)\rangle = 6D_B\tau$ is the mean squared displacement of the scattering particles in time t where D_B is the Brownian diffusion coefficient. The correlation function thus decays exponentially with a decay time on the order of the amount of time it takes a scattering particle to move a wavelength of light. That is, the time scale of the intensity fluctuations is on the order of the time it takes a particle to move one light wavelength (q^{-1}).

The decay of $g_1(\tau)$ for systems with random flow can also be calculated. In this case $\Delta\mathbf{r}(\tau) = \mathbf{V}\tau$ and the average is over the velocity distribution. For an isotropic, Gaussian velocity distribution, the correlation function still decays as eq. (4.9) but $\langle\Delta\mathbf{r}(\tau)^2\rangle = \langle\Delta V^2\rangle\tau^2$ where $\langle\Delta V^2\rangle$ is the mean square velocity. A Gaussian speed distribution is assumed [103]. Shear flow and turbulence have also been studied [40, 41, 42, 43, 104].

4.2.2 Multiple Scattering - Diffusing Wave Spectroscopy

When the concentration of scattering particles is increased, light is scattered many times before it exits the system (see fig. 4.3). The photons reaching the detector have followed various trajectories of differing path lengths. Under these conditions the correlation function can be calculated using the framework of diffusing wave spectroscopy (DWS). Considering only those photons which have scattered N times before detection, the normalized field correlation function has the form

$$\begin{aligned} g_1^{(N)}(\tau) &= \left\langle \exp\left(i\sum_{n=1}^N \mathbf{q}_n \cdot \Delta\mathbf{r}_n\right) \right\rangle_{q,\Delta\mathbf{r}} \\ &= \langle \exp(i\mathbf{q} \cdot \Delta\mathbf{r}) \rangle_{q,\Delta\mathbf{r}}^N \\ &= \left\langle \exp\left(-\frac{1}{6}q^2\langle\Delta r^2(\tau)\rangle\right) \right\rangle_q^N \end{aligned}$$

$$= \exp\left(-\frac{1}{6}\langle q^2 \rangle \langle \Delta r^2(\tau) \rangle s/l\right). \quad (4.10)$$

On the first line the sum appears in the argument of the exponent to account for the phase shift accumulated from each scattering event. The $\langle \dots \rangle$ denotes an average over the momentum transfer and particle displacement. The average over the scattering angle (momentum transfer) is necessary because it is not constrained as it was in the single scattering experiment. The second line is derived assuming that successive scattering events and neighboring particle motions are uncorrelated. These assumptions are valid in a disordered system with no particle-particle interactions. Some care must be taken when particle motions are correlated. The third line results from the ensemble average over the particle displacement where $\langle \Delta r^2(\tau) \rangle$ is the mean square displacement of the scattering particles (see section 4.2.1). The mean-square displacement has been assumed to be isotropic. This is the case with Brownian motion and random flow, but not directional flows. We next bring the q -average inside the argument of the exponential via a first order cumulant expansion. This approximation is valid as long as $\frac{1}{6}q^2 \langle \Delta r^2(\tau) \rangle \ll 1$. Finally we assume that there have been many scattering events in which case N is well approximated by s/l where s is the path length and $l = 1/\mu_s$ is the scattering length.

The average over the momentum transfer is weighted by the normalized differential cross section. That is

$$\begin{aligned} \langle q^2 \rangle &= \int_0^\pi f(\cos \theta) q^2 d(\cos \theta) \\ &= 4k_o^2 \left\langle \sin^2 \frac{\theta}{2} \right\rangle \\ &= 2k_o^2 [1 - \langle \cos \theta \rangle] \\ &= 2k_o^2 \frac{l}{l^*}. \end{aligned} \quad (4.11)$$

Here $f(\cos \theta)$ is the normalized form factor and $q^2 = 4k_o^2 \sin^2(\theta/2)$. Using the similarity relation discussed in section 2.1 we see that $l/l^* = 1 - \langle \cos \theta \rangle$, where $l^* = 1/\mu'_s$ is the photon random walk step length and the average over $\cos \theta$ is also weighted by the normalized differential cross-section, we see that $\langle q^2 \rangle = 2k_o^2 l/l^*$. Therefore,

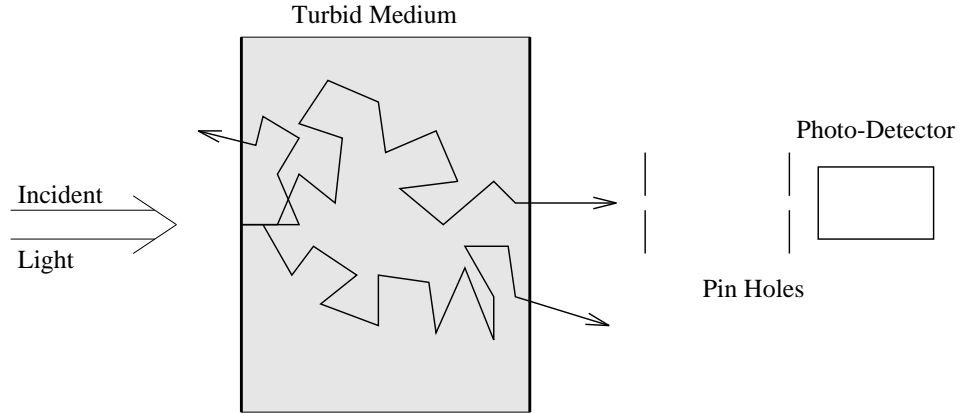


Figure 4.3: Light is incident on a concentrated suspension of scatterers. Photons on average are scattered many times before exiting the system. A single speckle of transmitted light is imaged with pin holes (or gathered by a single-mode fiber) and monitored with a photo-detector.

the normalized field correlation function of light that has migrated a path length s through a highly scattering system is given by

$$g_1^{(N)}(\tau) = \exp\left(-\frac{1}{3}k_o^2 \langle \Delta r^2(\tau) \rangle \frac{s}{l^*}\right). \quad (4.12)$$

Eq. (4.12) has the same form as the single scattering result, eq. (4.9), except the decay rate is multiplied by the number of random walk steps in the medium, s/l^* , and k_o appears instead of q because there is no longer a single scattering angle in the problem. The correlation function for trajectories of longer length will decay more quickly, permitting the motion of scattering particles to be probed on ever shorter time scales.

The validity of eq. (4.12) has been verified directly by Yodh *et al.* [105] using a pulsed laser and gating the broadened response to select photon path lengths of a specific length. A summary of their experimental results is shown in fig. 4.4. They measured the correlation function for photon path lengths between 7 cm and 13 cm through a 2.0 mm thick 30% suspension of $0.460 \mu\text{m}$ polystyrene spheres. In the inset of fig. 4.4 they demonstrate the single exponential decay of the correlation function for two different path lengths. Fig. 4.4 shows that the decay rate increases linearly with

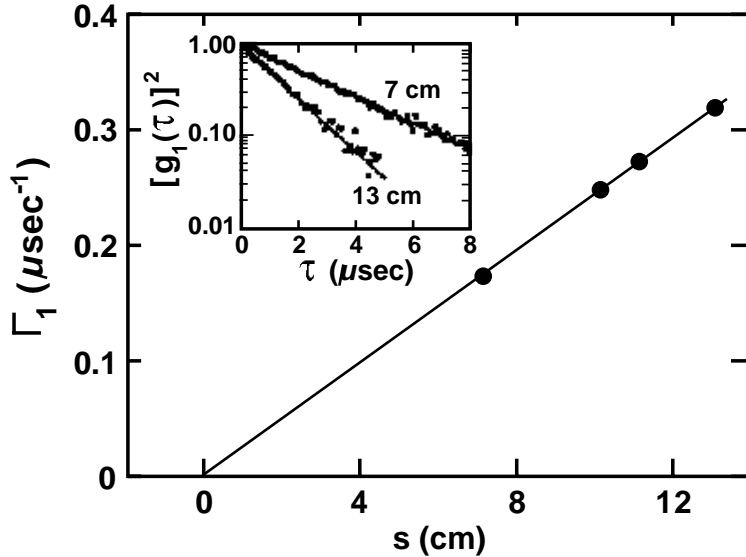


Figure 4.4: The decay rate for the correlation function increases linearly with the photon path length. The correlation function measured for photon path lengths of 7 cm and 13 cm is shown in the inset. The decay is log-linear as expected. Reproduced with permission from A. G. Yodh *et al.* Phys. Rev. B **42**, 4744 (1990) [105].

the path length as expected by eq. (4.12).

It is not always convenient to use a pulsed laser and gating techniques to pick out photons which have traveled a specific path length through the sample. Generally, a continuous wave laser is used to illuminate the sample and the full distribution of path lengths contributes to the decay of the correlation function. Under these conditions, the field correlation function is given by

$$g_1(\tau) = \int_0^\infty P(s) \exp\left(-\frac{1}{3}k_o^2 \langle \Delta r^2(\tau) \rangle \frac{s}{l^*}\right) ds , \quad (4.13)$$

where $P(s)$ is the normalized distribution of path lengths. This relation is valid given the assumption that the laser coherence length is much longer than the width of the photon path length distribution [102]. When the scattering length is much smaller than the dimensions of the sample and the absorption length, the path length distribution is found from the photon diffusion equation. For a point source and point detector in

an infinite medium, $P(s)$ is

$$P(s) = \sqrt{\frac{vr_{sd}^2}{4\pi D}} \exp\left(\sqrt{\frac{v\mu_a r_{sd}^2}{D}}\right) s^{-3/2} \exp\left(-\frac{vr_{sd}^2}{4Ds}\right) \exp(-\mu_a s) . \quad (4.14)$$

Here r_{sd} is the separation between the source and detector. Using the photon diffusion approximation to calculate $P(s)$, $g_1(\tau)$ has been calculated for various geometries including semi-infinite and slab [106]. The solution for an infinite medium with a point source is

$$g_1(\tau) = \exp\left(-\sqrt{k_o^2 \langle \Delta r^2(\tau) \rangle + 3\mu_a l^*} \frac{r_{sd}}{l^*}\right) . \quad (4.15)$$

With no photon-absorption, the correlation function still decays as a single exponential but as the $\sqrt{\langle \Delta r^2(\tau) \rangle}$ instead of as $\langle \Delta r^2(\tau) \rangle$. Photon absorption reduces the contribution of long path length photons and thus suppresses the decay at early correlation times. $g_1(\tau)$ has been verified experimentally for absorption free media by Pine *et al.* [106] and for absorbing media by Tamura and co-workers [107, 108].

For a semi-infinite medium with a collimated point source and a point detector, the distribution of photon path lengths is found using the method of images to satisfy the semi-infinite boundary condition (see section 2.3). The photon path length distribution is

$$P(s) = \left[\sqrt{\frac{4\pi D}{vr_1^2}} \exp\left(-\sqrt{\frac{v\mu_a r_1^2}{D}}\right) - \sqrt{\frac{4\pi D}{vr_2^2}} \exp\left(-\sqrt{\frac{v\mu_a r_2^2}{D}}\right) \right]^{-1} s^{-3/2} \left[\exp\left(-\frac{vr_1^2}{4Ds}\right) - \exp\left(-\frac{vr_2^2}{4Ds}\right) \right] \exp(-\mu_a s) . \quad (4.16)$$

The distance from the real source to the detector is $r_1 = (\rho^2 + l^{*2})^{1/2}$ where ρ is the separation between the source and detector on the surface and l^* is the distance inside the medium where the collimated source becomes diffuse. The distance between the image source and the detector is $r_2 = (\rho^2 + (l^* + 2z_b)^2)^{1/2}$ where z_b is the extrapolation distance to the imaging boundary as determined by the mismatch in the indices of

refraction (see section 2.3). With this $P(s)$ the field correlation function is

$$g_1(\tau) = \frac{\exp\left(-\sqrt{k_o^2 \langle \Delta r^2(\tau) \rangle + 3\mu_a l^*} \frac{r_1}{l^*}\right) - \exp\left(-\sqrt{k_o^2 \langle \Delta r^2(\tau) \rangle + 3\mu_a l^*} \frac{r_2}{l^*}\right)}{\exp\left(-\sqrt{3\mu_a l^*} \frac{r_1}{l^*}\right) - \exp\left(-\sqrt{3\mu_a l^*} \frac{r_2}{l^*}\right)}. \quad (4.17)$$

Other important geometries include plane wave transmission through a slab and diffuse backscattering of a plane wave. These solutions are discussed by Pine *et al.* [106]. For plane wave transmission through a slab

$$g_1(\tau) = \frac{\left(\frac{L}{l^*} + \frac{4}{3}\right) \sqrt{6D_B k_o^2 \tau}}{\left(1 + \frac{8}{3}D_B k_o^2 \tau\right) \sinh\left[\frac{L}{l^*} \sqrt{6D_B k_o^2 \tau}\right] + \frac{4}{3} \sqrt{6D_B k_o^2 \tau} \cosh\left[\frac{L}{l^*} \sqrt{6D_B k_o^2 \tau}\right]}, \quad (4.18)$$

where L is the thickness of the slab. For backscattering of a plane wave from a slab

$$g_1(\tau) = \frac{\sinh\left[\sqrt{6D_B k_o^2 \tau} \left(\frac{L}{l^*} - 1\right)\right] + \frac{2}{3} \sqrt{6D_B k_o^2 \tau} \cosh\left[\sqrt{6D_B k_o^2 \tau} \left(\frac{L}{l^*} - 1\right)\right]}{\left(1 + \frac{8}{3}D_B k_o^2 \tau\right) \sinh\left[\frac{L}{l^*} \sqrt{6D_B k_o^2 \tau}\right] + \frac{4}{3} \sqrt{6D_B k_o^2 \tau} \cosh\left[\frac{L}{l^*} \sqrt{6D_B k_o^2 \tau}\right]}. \quad (4.19)$$

For a slab of infinite thickness, eq. (4.19) becomes

$$g_1(\tau) = \frac{\exp\left[-\sqrt{6D_B k_o^2 \tau}\right]}{1 + \frac{2}{3} \sqrt{6D_B k_o^2 \tau}}. \quad (4.20)$$

To summarize, within the framework of diffusing wave spectroscopy, the decay of $g_1(\tau)$ is found by first considering photon trajectories of a given length through the sample and calculating the average phase fluctuations by averaging over the particle displacements and the momentum transfer per scattering event. The distribution of path lengths through the sample is then used to determine the overall decay of $g_1(\tau)$.

Similar equations for the field correlation function arising from highly scattering systems have been obtained using field theory. For discussions on the derivation using field theory see MacKintosh and John [49], Maret and Wolf [50], and Vol'kov and Romanov [51].

4.2.3 Correlation Transport and Correlation Diffusion

A different approach for finding $g_1(\tau)$ has been proposed by Ackerson *et al.* [57, 58] that does not rely on the assumptions made by DWS. This new approach treats the

transport of correlation through a scattering system much like the radiative transport equation [60, 83] treats the transport of photons. The difference between the correlation transport equation (CT) and the radiative transport equation (RT) is that the CT accumulates the decay of the correlation function for each scattering event. Since contributions to the decay of the correlation function arise from each scattering event from a moving particle, the CT is simply constructed by adding the single scattering correlation function to the term which accounts for photon scattering in the RT equation (eq. (2.1)). This term accounts for all scattering events. The correlation transport equation is thus [57, 58]

$$\nabla \cdot G_1^T(\mathbf{r}, \hat{\Omega}, \tau) \hat{\Omega} + \mu_t G_1^T(\mathbf{r}, \hat{\Omega}, \tau) = \mu_s \int G_1^T(\mathbf{r}, \hat{\Omega}', \tau) g_1^s(\hat{\Omega}, \hat{\Omega}', \tau) f(\hat{\Omega}, \hat{\Omega}') d\hat{\Omega}' + S(\mathbf{r}, \hat{\Omega}). \quad (4.21)$$

Here, $G_1^T(\mathbf{r}, \hat{\Omega}, \tau)$ is the unnormalized temporal field correlation function which is a function of position \mathbf{r} , direction $\hat{\Omega}$, and correlation time τ . The scattering and absorption coefficients are respectively μ_s and μ_a , and $\mu_t = \mu_s + \mu_a$. $g_1^s(\hat{\Omega}, \hat{\Omega}', \tau)$ is the normalized temporal field correlation function for single scattering. $f(\hat{\Omega}, \hat{\Omega}')$ is the normalized differential scattering cross-section. $S(\mathbf{r}, \hat{\Omega})$ is the light source distribution. The scattering coefficient is the reciprocal of the scattering length, $\mu_s = 1/l$, and the absorption coefficient is the reciprocal of the absorption length, $\mu_a = 1/l_a$. The time dependence (not to be confused with correlation time) has been left out of the equation since I only consider measurements with CW sources and systems in equilibrium (i.e. steady state). The time dependence can be included by adding a time-derivative of $G_1^T(\mathbf{r}, \hat{\Omega}, \tau)$ (i.e. $v^{-1} \frac{\partial}{\partial t} G_1^T(\mathbf{r}, \hat{\Omega}, \tau, t)$) to the left-hand side of eq. (4.21) and letting $G_1^T(\mathbf{r}, \hat{\Omega}, \tau) \rightarrow G_1^T(\mathbf{r}, \hat{\Omega}, \tau, t)$.

At zero correlation time, $\tau = 0$, there has been no decorrelation and the CT equation reduces to the RT equation. This equivalence arises because the unnormalized field correlation function at $\tau = 0$ is just the ensemble averaged intensity, which is the quantity determined by the RT equation.

The CT equation provides a means for considering the intermediate regime between single scattering systems and systems through which light diffuses. Furthermore, in

the limit of single scattering, it reduces to the standard single scattering correlation function discussed in section 4.2.1 and, as I will discuss, solutions in the photon diffusion regime are the same as obtained from DWS (see section 4.2.2). The CT equation is useful because its validity ranges from single scattering to multiple scattering systems, does not require the assumptions made within DWS, and affords a straight-forward approach to considering systems with spatially-varying optical and dynamical properties. A drawback to the CT equation is the difficulty in obtaining analytical and numerical solutions. The RT equation is plagued by the same problem. Because of the similarity between the CT equation and the RT equation we should be able to apply the same approximation methods to the CT equation as we applied to the RT equation.

Using the standard diffusion approximation the CT equation reduces to the following correlation diffusion equation (see appendix A):

$$\left(D_\gamma \nabla^2 - v\mu_a - \frac{1}{3}v\mu'_s k_o^2 \langle \Delta r^2(\tau) \rangle \right) G_1(\mathbf{r}, \tau) = -vS(\mathbf{r}) . \quad (4.22)$$

Here, $D_\gamma = v/(3\mu'_s)$ is the photon diffusion coefficient, v is the speed of light in the medium, and $\mu'_s = \mu_s(1 - \langle \cos \theta \rangle) = 1/l^*$ is the reduced scattering coefficient. Recall that for Brownian motion $\langle \Delta r^2(\tau) \rangle = 6D_B\tau$ and for random flow $\langle \Delta r^2(\tau) \rangle = \langle \Delta V^2 \rangle \tau^2$.

To obtain the correlation diffusion equation it is necessary to assume that the photons are diffusing and that the scattering phase function, $f(\hat{\Omega}, \hat{\Omega}')$, and the single scattering correlation function, $g_1^s(\hat{\Omega}, \hat{\Omega}', \tau)$, only depend on the scattering angle $\hat{\Omega} \cdot \hat{\Omega}'$, and that $k_o^2 \langle \Delta r^2(\tau) \rangle \ll 1$. The photon diffusion assumption is valid if the photon random walk step length is smaller than the dimensions of the sample and the photon absorption length. The scattering angle assumption (i.e. $\hat{\Omega} \cdot \hat{\Omega}'$) is valid for systems with randomly oriented scatterers and isotropic dynamics (e.g. Brownian motion and random flow). The short time assumption requires the correlation time τ to be much smaller than the time it takes a scatterer to move a wavelength of light. When the photon wavelength is 514 nm and the dynamics are Brownian motion with $D_B = 1 \times 10^{-8} \text{ cm}^2 \text{s}^{-1}$, then the short time assumption requires $\tau \ll 1 \times 10^{-3} \text{ s}$. The

breakdown of this approximation is explored in section 4.4. In an infinite, homogeneous system the breakdown of this approximation is observable at 225 μs and is independent of the photon absorption coefficient. The deviation increases with source-detector separation and reduced scattering coefficient. For a source-detector separation of 1 cm the deviation is 20% and increases to 100% for a 2 cm source-detector separation.

Eq. (4.22) can be recast as a Helmholtz equation for the field correlation function, i.e.

$$\left(\nabla^2 + K^2(\tau)\right)G_1(\mathbf{r}, \tau) = -\frac{vS}{D_\gamma}\delta^3(\mathbf{r} - \mathbf{r}_s), \quad (4.23)$$

where $K^2(\tau) = -v\left(\mu_a + \frac{1}{3}\mu'_s k_o^2 \langle \Delta r^2(\tau) \rangle\right)/D_\gamma$. Here I have taken the light source to be point like, i.e. CW, and located at position \mathbf{r}_s . Note that $\frac{1}{3}\mu'_s k_o^2 \langle \Delta r^2(\tau) \rangle$ is a loss term similar to μ_a . While μ_a represents losses due to photon absorption, $\frac{1}{3}\mu'_s k_o^2 \langle \Delta r^2(\tau) \rangle$ represents the “absorption” of correlation due to dynamic processes. When $\tau = 0$ there is no dynamic absorption and eq. (4.23) reduces to the steady-state photon diffusion equation (eq. (2.12)).

For an infinite, homogeneous system with no photon absorption (i.e. $\mu_a = 0$), the solution to eq. (4.23) has the well known form

$$G_1(\mathbf{r}, \tau) = \frac{vS \exp\left(-\sqrt{\mu'_s k_o^2 \langle \Delta r^2(\tau) \rangle} |\mathbf{r} - \mathbf{r}_s|\right)}{4\pi D_\gamma |\mathbf{r} - \mathbf{r}_s|}. \quad (4.24)$$

This same solution has been derived within the context of DWS [48, 50], and from the scalar wave equation for the electric field propagating in a medium with a fluctuating dielectric constant [49, 109]. In contrast to these two approaches, the correlation diffusion equation provides a simple framework for considering turbid media with large scale spatially varying dynamics and optical properties.

With some difficulty, such systems can be considered with diffusing-wave spectroscopy. I have considered this and found that diffusing-wave spectroscopy requires the computation of complicated integrations of photon dwell times in localized voxels convolved with a volume integral. On the other hand, the correlation diffusion equation requires the solution of a simple differential equation. Because the correlation

diffusion equation is analogous to the photon diffusion equation, we can apply all of the techniques developed for photon diffusion to correlation diffusion. In the next few sections I demonstrate the “scattering” of correlation from dynamical inhomogeneities as well as tomographic reconstructions of the spatially varying dynamical properties of turbid media.

4.2.4 Ergodicity

The samples that I study experimentally are not ergodic, that is the time-averaged measurements are not equivalent to the ensemble-average computed by the various photon correlation spectroscopy theories. Ultimately this situation arises whenever the sample has static and dynamic scattering components. This presents a problem when measuring the temporal intensity correlation function $g_2(\tau)$ but is not a problem if one is measuring the temporal field correlation function $g_1(\tau)$ directly. To see the origin of the problem, it is necessary to begin with the electric field emerging from a non-ergodic system and derive $g_1(\tau)$ and $g_2(\tau)$.

The following discussion assumes that the non-ergodic system is highly scattering and comprises two components, a static, non-ergodic component and a dynamic, ergodic component. The extension to dynamic but non-ergodic systems is relatively straightforward but not relevant to this dissertation. Discussions of such systems can be found in [110, 111].

The electric field reaching the detector is a superposition of photons that have migrated through the static region without scattering from moving particles and photons that have scattered at least once from a moving (dynamic) particle. I refer to these two different types of photons as “constant” and “fluctuating.” Thus,

$$E(t) = E_c(t) + E_f(t) \quad (4.25)$$

where

$$E_c(t) = \sum_{i=1}^{N_c} \varepsilon_c^i(t) \quad (4.26)$$

is the constant electric field reaching the detector and

$$E_f(t) = \sum_{i=1}^{N_f} \varepsilon_f^i(t) \quad (4.27)$$

is the fluctuating electric field reaching the detector. The sum for $E_c(t)$ is over the number of photon trajectories (N_c) that travel only in the static region between the source and detector, where $\varepsilon_c^i(t)$ is the field for the i^{th} photon trajectory. The sum for $E_f(t)$ is over the number of photon trajectories (N_f) that sample the dynamic region between the source and detector, where $\varepsilon_f^i(t)$ is the field for the i^{th} photon trajectory.

With these definitions, the temporal electric field correlation function is

$$\begin{aligned} g_1(\tau) &= \frac{\langle E(t)E^*(t+\tau) \rangle_t}{\langle |E|^2 \rangle_t} \\ &= \frac{\langle E_c(t)E_c^*(t+\tau) \rangle_t + \langle E_f(t)E_f^*(t+\tau) \rangle_t}{I_c + \langle I_f \rangle + \langle E_c(t)E_f^*(t) \rangle_t + \langle E_f(t)E_c^*(t) \rangle_t} \\ &\quad + \frac{\langle E_c(t)E_f^*(t+\tau) \rangle_t + \langle E_f(t)E_c^*(t+\tau) \rangle_t}{I_c + \langle I_f \rangle + \langle E_c(t)E_f^*(t) \rangle_t + \langle E_f(t)E_c^*(t) \rangle_t} \\ &= \left[\frac{I_c + \langle I_f \rangle g_{1,f}(\tau)}{I_c + \langle I_f \rangle} \right]. \end{aligned} \quad (4.28)$$

The $\langle \dots \rangle_t$ denotes a time average. E_c does not fluctuate in time and thus the intensity $I_c = \langle E_c(t)E_c^*(t+\tau) \rangle_t$ is constant. $E_f(t)$ does fluctuate in time so that $\langle I_f \rangle = \langle E_f(t)E_f^*(t) \rangle_t$ is the time-averaged fluctuating intensity and $g_{1,f}(\tau)$ is the temporal field correlation function of $E_f(t)$ (this decays from 1 to 0). The terms in the numerator on the third line in eq. (4.28) average to zero because the phases of the constant and fluctuating photon trajectories are uncorrelated. Likewise, the third and fourth terms in the denominator on the second and third lines average to zero.

Eq. (4.28) is the field correlation function which we calculate using the correlation diffusion equation. If more than one speckle is imaged with the collection optics then a coherence parameter $\sqrt{\beta}$ enters to reduce the observed decay of $g_1(\tau)$. Under these less than ideal conditions the measured correlation function is

$$g_1(\tau) = \left[\frac{I_c + \sqrt{\beta} \langle I_f \rangle g_{1,f}(\tau)}{I_c + \langle I_f \rangle} \right]. \quad (4.29)$$

The factor $\sqrt{\beta}$ is easily removed from $g_1(\tau)$. The field correlation function is expected to decay from 1 and plateau at a value of $B = I_c/(I_c + \langle I_f \rangle)$. The less than ideal experimental conditions will result in $g_1(\tau)$ decaying from a value less than 1 to B . In non-ideal conditions, the total decay will be $\sqrt{\beta} A = \sqrt{\beta} \langle I_f \rangle / (I_c + \langle I_f \rangle)$, when it was expected to be A . $A + B = 1$, and B is found from the value of $g_1(\tau)$ as $\tau \rightarrow \infty$. We can thus obtain the correct field correlation function using

$$g_1^{\text{Correct}}(\tau) = (1 - B) \frac{g_1^{\text{Measured}}(\tau) - B}{g_1^{\text{Measured}}(\tau = 0) - B} + B . \quad (4.30)$$

As we will see, problems arise when measuring $g_2(\tau)$ because the value of B and A cannot be determined.

Deriving the explicit form for the temporal intensity correlation function is a little more involved. In this case

$$\begin{aligned} G_2(\tau) &= \langle I(t)I(t + \tau) \rangle_t \\ &= \langle E(t)E^*(t)E(t + \tau)E^*(t + \tau) \rangle_t \\ &= I_c^2 + I_c(t) \langle I_f \rangle + E_c(t)E_c^*(t + \tau) \langle E_f^*(t)E_f(t + \tau) \rangle_t \\ &\quad + E_c^*(t)E_c(t + \tau) \langle E_f(t)E_f^*(t + \tau) \rangle_t + \langle I_f \rangle I_c(\tau) \\ &\quad + \langle E_f(t)E_f^*(t)E_f(t + \tau)E_f^*(t + \tau) \rangle . \end{aligned} \quad (4.31)$$

The product on the first line of eq. (4.31) results in 16 terms, 10 of which average to zero. The remaining 6 terms are given on the 3rd, 4th, and 5th lines. Although E_c and I_c are independent of time, the argument is given to indicate the origin of the different terms. The 3rd and 4th terms are the heterodyne terms arising from the beating of E_c with $E_f(t)$, i.e.

$$E_c(t)E_c^*(t + \tau) \langle E_f^*(t)E_f(t + \tau) \rangle_t = E_c^*(t)E_c(t + \tau) \langle E_f(t)E_f^*(t + \tau) \rangle_t = I_c \langle I_f \rangle g_{1,f}(\tau) . \quad (4.32)$$

The 6th term is more complicated. The summations over different trajectories giving rise to $E_f(t)$ (eq. (4.27)) must be included and the time-average of the products

of the different trajectories must be considered. The 6th term is thus

$$\begin{aligned}
\langle E_f(t)E_f^*(t)E_f(t+\tau)E_f^*(t+\tau) \rangle_t &= \sum_{i,j,k,l=1}^{N_f} \langle \varepsilon_f^i(t)\varepsilon_f^{j*}(t)\varepsilon_f^k(t+\tau)\varepsilon_f^{l*}(t+\tau) \rangle_t \\
&= \sum_{i=j=k=l=1}^{N_f} \langle \varepsilon_f^i(t)\varepsilon_f^{j*}(t)\varepsilon_f^k(t+\tau)\varepsilon_f^{l*}(t+\tau) \rangle_t \\
&\quad + \sum_{i=j=1,k=l=1,i \neq k}^{N_f} \langle \varepsilon_f^i(t)\varepsilon_f^{j*}(t)\varepsilon_f^k(t+\tau)\varepsilon_f^{l*}(t+\tau) \rangle_t \\
&= \langle I_f \rangle^2 + \langle I_f \rangle^2 \left[\frac{N_f^2 - N_f}{N_f^2} \right] |g_{1,f}(\tau)|^2 \\
&\approx \langle I_f \rangle^2 + \langle I_f \rangle^2 |g_{1,f}(\tau)|^2 . \tag{4.33}
\end{aligned}$$

The first term, $\langle I_f \rangle^2$, derives from the N_f , $i = j$ terms multiplied by the N_f , $k = l$ terms. The second term results from $i = l$ and $j = k$, excluding the N_f terms where $i = j = k = l$. The reasonable assumption $N_f \ll N_f^2$ is made. The other combinations of i , j , k , and l average to zero because the phases are uncorrelated.

The temporal intensity correlation function for the described non-ergodic system is thus

$$g_2(\tau) = 1 + \frac{2\sqrt{\beta} I_c \langle I_f \rangle |g_{1,f}(\tau)| + \beta \langle I_f \rangle^2 |g_{1,f}(\tau)|^2}{(I_c + \langle I_f \rangle)^2} . \tag{4.34}$$

This correlation function has a heterodyne term, $2I_c \langle I_f \rangle |g_{1,f}(\tau)|$, and a homodyne term, $\langle I_f \rangle^2 |g_{1,f}(\tau)|^2$. I have included the coherence factor β which depends on the number of speckles averaged and the laser coherence length. When measuring a single speckle created by a stable, long coherence length laser, then $\beta = 1$. Unfortunately, experimentally, β usually varies between 0 and 1 and must be measured. It is safe to assume that β will remain constant for measurements made on different speckles since β only depends on the laser and detection optics. However I_c will vary, changing the relative importance of the homodyne and heterodyne terms.

The standard method to obtain the field correlation function (that which we calculate) from the intensity correlation function (that which we measure) is to use the Siegert relation

$$g_2(\tau) = 1 + \beta |g_1(\tau)|^2 . \tag{4.35}$$

This method does not work when the system is non-ergodic. If we determine $g_1(\tau)$ from the measured $g_2(\tau)$ (eq. (4.34)) using eq. (4.35) then we find that

$$g_1(\tau) = \left[\frac{2\sqrt{\beta}I_c \langle I_f \rangle |g_{1,f}(\tau)| + \beta \langle I_f \rangle^2 |g_{1,f}(\tau)|^2}{2\sqrt{\beta} I_c \langle I_f \rangle + \beta \langle I_f \rangle^2} \right]^{1/2}. \quad (4.36)$$

Not only is this different than what we calculate (eq. (4.28)), but many different $g_1(\tau)$'s could be measured for the same system by changing the experimental setup and thus changing β and/or by imaging a different speckle and thus changing I_c . Even if β were known (say $\beta = 1$), this method would not produce the correct field correlation function. Furthermore, $g_1(\tau)$ determined in this way decays from 1 to 0 when it should decay from 1 to B .

The standard approach for obtaining $g_1(\tau)$ from $g_2(\tau)$ thus does not apply to non-ergodic systems. Another approach has been suggested by Joosten *et al.* [112]. Their approach is to make the measurement on a speckle where the intensity is the ensemble-averaged intensity. The fluctuating part of the correlation function is then correct and the correct correlation function is obtained by adding a constant to $g_2(\tau)$ so that it decays from 2 to a value greater than 1 instead of decaying from a value less than 2 to 1. Assuming $\beta = 1$ then the value added to $g_2(\tau)$ is just B^2 , such that

$$\begin{aligned} g_2(\tau) &= 1 + \frac{\beta I_c^2 + 2\sqrt{\beta} I_c \langle I_f \rangle |g_{1,f}(\tau)| + \beta \langle I_f \rangle^2 |g_{1,f}(\tau)|^2}{(I_c + \langle I_f \rangle)^2} \\ &= 1 + \beta \frac{(I_c + \langle I_f \rangle |g_{1,f}(\tau)|)^2}{(I_c + \langle I_f \rangle)^2}. \end{aligned} \quad (4.37)$$

The correct $g_1(\tau)$ can then be calculated using the Siegert relation (eq. (4.35)). The disadvantage of this method is that β must be known and the measurement must be made on an appropriate speckle. It is possible to determine β using an ergodic system but experience will show that for a fixed source and detection system that β can vary by up to 10% over the course of a few minutes. Furthermore, collecting light from a specific speckle emanating from a turbid medium for more than a few seconds requires extreme measures to isolate the system from mechanical vibrations. Joosten's *et al* method is therefore not practical if an accuracy better than 10% is desired.

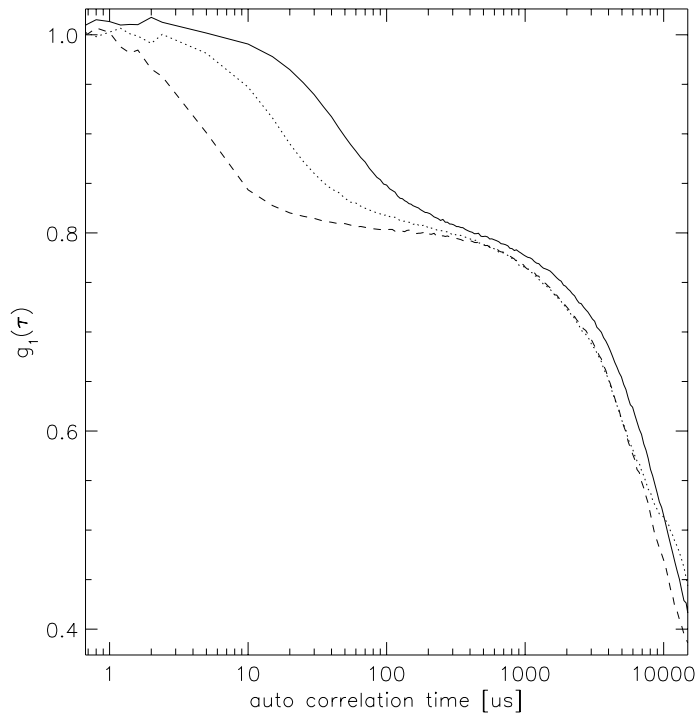


Figure 4.5: The ensemble average correlation function from a non-ergodic turbid medium is shown. The medium is a solid, highly scattering slab with a cylindrical vein through which a highly scattering colloid flows. The early τ decay corresponds to the flow dynamics while the long τ decay results from the ensemble averaging. The three curves come from three different flow speeds, the solid/dotted/dashed lines correspond to flow speeds of $0.08/0.24/0.88 \text{ cm s}^{-1}$ respectively. The early τ decay rate increases with the flow speed. The longer τ decay depends only on the rate of ensemble averaging, which is held constant. The intermediate plateau reveals the relative magnitudes of $\langle I_c \rangle$ and $\langle I_f \rangle$ and tells us what fraction of the detected photons have sampled the dynamic region. This is independent of the flow speed as expected.

In general, for a non-ergodic system, from a measurement of $g_2(\tau)$ it is not possible to independently determine I_c , $\langle I_f \rangle$, and β . Therefore the proper temporal electric field correlation function cannot be determined. In order to obtain the proper correlation function I ensemble average during the acquisition of the intensity correlation function. This method has been described in detail by Xue *et al.* [110]. The technique for ensemble averaging that I use is explained in section 6.2. Basically, the idea is to move the detector from speckle to speckle during the course of the measurement. In this way, $E_c(t)$ will fluctuate on a time scale given by the motion of the detector from speckle to speckle. Eq. (4.31) thus becomes

$$\begin{aligned} G_2(\tau) &= \langle E_c(t)E_c^*(t)E_c(t+\tau)E_c^*(t+\tau) \rangle + \langle E_c(t)E_c^*(t+\tau) \rangle \langle E_f^*(t)E_f(t+\tau) \rangle \\ &\quad + \langle E_c^*(t)E_c(t+\tau) \rangle \langle E_f(t)E_f^*(t+\tau) \rangle + 2\langle I_f \rangle \langle I_c \rangle \\ &\quad + \langle E_f(t)E_f^*(t)E_f(t+\tau)E_f^*(t+\tau) \rangle \\ &= (\langle I_c \rangle + \langle I_f \rangle)^2 + \beta(\langle I_c \rangle |g_{1,c}(\tau)| + \langle I_f \rangle |g_{1,f}(\tau)|)^2 , \end{aligned} \quad (4.38)$$

where $\langle I_c \rangle$ is the average intensity of the constant component of the speckles, $g_{1,c}(\tau)$ is the correlation function of the fluctuating $E_c(t)$, and all $\langle \dots \rangle$ are time averages. The normalized intensity correlation function is thus

$$g_2(\tau) = 1 + \beta \frac{(\langle I_c \rangle |g_{1,c}(\tau)| + \langle I_f \rangle |g_{1,f}(\tau)|)^2}{(\langle I_c \rangle + \langle I_f \rangle)^2} . \quad (4.39)$$

$g_{1,c}(\tau)$ decays in a log-linear fashion on a time scale that is proportional to the amount of time it takes to move the detector from one speckle to the next [111]. If the decay time of $g_{1,c}(\tau)$ is much longer than that of $g_{1,f}(\tau)$ then the measured correlation function will look like that shown in fig. 4.5 and the fluctuations due to sample dynamics are easily separated from ensemble averaging fluctuations. The correlation function at early times when $g_{1,c}(\tau) \approx 1$ is then

$$g_2(\tau) = 1 + \beta \frac{(\langle I_c \rangle + \langle I_f \rangle |g_{1,f}(\tau)|)^2}{(I_c + \langle I_f \rangle)^2} , \quad (4.40)$$

and from the Siegert relation [48, 50, 100]

$$g_2(\tau) = 1 + \beta |g_1(\tau)|^2 \quad (4.41)$$

we find that

$$g_1(\tau) = \frac{(\langle I_c \rangle + \langle I_f \rangle |g_{1,f}(\tau)|)}{(\langle I_c \rangle + \langle I_f \rangle)} . \quad (4.42)$$

This is exactly the temporal field correlation function which we calculate with the correlation diffusion theory. There is no need to separate $\langle I_f \rangle |g_{1,f}(\tau)|$ from $\langle I_c \rangle$. From the plateau in the correlation function that occurs when $g_{1,f}(\tau) \ll 1$ it is possible to determine $\langle I_c \rangle$ and thus $\langle I_f \rangle$ and $|g_{1,f}(\tau)|$. However, for comparisons with solutions of the correlation diffusion equation it is not necessary to make this separation, it is only necessary that $g_{1,c}(\tau) \approx 1$ for the temporal region of interest.

4.3 Experimental Results

4.3.1 Validity of Diffusion Equation for Media with Spatially Varying Brownian Motion

This section compares experimental and theoretical results to verify the validity of the correlation diffusion equation for turbid media with spatially varying dynamical and optical properties. The experiments are performed on a turbid slab which is static and homogeneous except for a spherical region which is dynamic. Dynamic regions with different magnitudes of Brownian motion and different scattering coefficients are considered.

Before discussing the experiment I briefly review the solution to eq. (4.22) for a medium which is homogeneous except for a spherical region (with radius a) characterized by different optical and dynamical properties than the surrounding medium. The spherical region can also be characterized by different optical properties. The analytic solution of the correlation diffusion equation for this system reveals that the measured correlation function outside the sphere can be interpreted as a superposition of the incident correlation plus a term which accounts for the “scattering” of the correlation

from the sphere, i.e.

$$G_1^{out}(\mathbf{r}_s, \mathbf{r}_d, \tau) = \frac{S \exp(iK^{out}(\tau)|\mathbf{r}_d - \mathbf{r}_s|)}{4\pi D_\gamma |\mathbf{r}_d - \mathbf{r}_s|} + \sum_{l=0}^{\infty} A_l h_l^{(1)}(K^{out}(\tau)\mathbf{r}_d) Y_l^0(\theta, \phi). \quad (4.43)$$

Here, $h_l^{(1)}$ are Hankel functions of the first kind and $Y_l^0(\theta, \phi)$ are spherical harmonics. The sphere is centered on the origin, and the source is placed on the z-axis to exploit azimuthal symmetry. The coefficient A_l is the scattering amplitude of the l^{th} partial wave and is found by matching the appropriate boundary conditions on the surface of the sphere. The boundary conditions are similar to that for the photon diffusion equation discussed in section 2.5. Specifically, the correlation must be continuous across the boundary as well as the net flux normal to the boundary, i.e. $G_1^{out}(a, \tau) = G_1^{in}(a, \tau)$ and $-D_\gamma^{out} \hat{r} \cdot \nabla G_1^{out}(\mathbf{r}, \tau)|_{r=a} = -D_\gamma^{in} \hat{r} \cdot \nabla G_1^{in}(\mathbf{r}, \tau)|_{r=a}$ on the surface of the sphere. $G_1^{in}(\mathbf{r}, \tau)$ is the correlation function inside the spherical object and \hat{r} is the normal vector to the sphere. Applying these boundary conditions, we find

$$A_l = \frac{-ivSK^{out}}{D_\gamma^{out}} h_l^{(1)}(K^{out}z_s) Y_l^{0*}(\pi, 0) \left[\frac{D_\gamma^{out} x j'_l(x) j_l(y) - D_\gamma^{in} y j_l(x) j'_l(y)}{D_\gamma^{out} x h_l^{(1)'}(x) j_l(y) - D_\gamma^{in} y h_l^{(1)}(x) j'_l(y)} \right], \quad (4.44)$$

where j_l are the spherical Bessel functions of the first kind, $x = K^{out}a$, $y = K^{in}a$, a is the radius of the sphere, \mathbf{r}_s is the position of the source, and j'_l and $h_l^{(1)'} \equiv h_l^{(1)''}$ are the first derivatives of the functions j_l and $h_l^{(1)}$ with respect to the argument. This solution has been discussed in detail for DPDW's in section 2.5 [29, 30]. By viewing the perturbation of temporal correlation as a scattering process, simple algorithms adapted from scattering theory can be applied to reconstruct images of spatially varying dynamics in turbid media.

I demonstrate the scattering of temporal correlation by a dynamical inhomogeneity in an experiment shown in fig. 4.6. In this experiment, the temporal intensity correlation function is measured in remission from a semi-infinite, highly-scattering, solid slab of TiO₂ suspended in resin ($D_B = 0$). The slab contains a spherical cavity filled with a turbid, fluctuating suspension of 0.296 μm polystyrene balls ($D_B = 1.5 \times 10^{-8} \text{ cm}^2 \text{s}^{-1}$). The measured temporal intensity correlation function, $g_2(\tau)$, for three different source detector separations is presented in fig. 4.7. $g_2(\tau)$ is plotted for the system with no

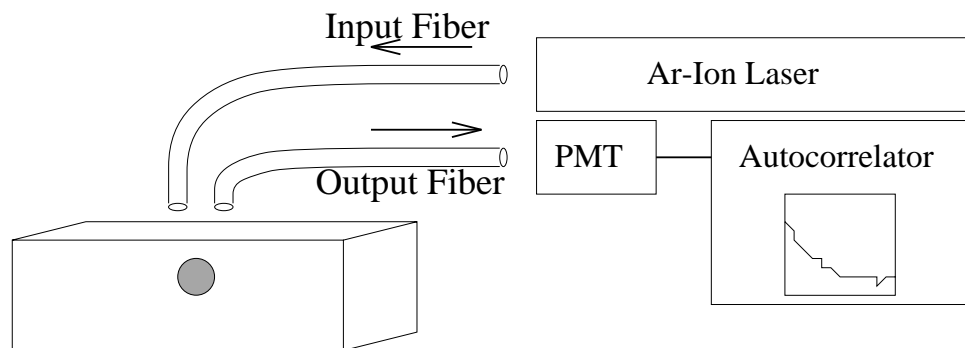


Figure 4.6: The 514 nm line from an argon ion laser (operated at 2.0 W with an etalon) is coupled into a multi-mode fiber optic cable and delivered to the surface of a solid slab of TiO_2 suspended in resin. The slab has dimensions of 15x15x8 cm. A spherical cavity with a diameter of 2.5 cm is located 1.8 cm below the center of the upper surface. The cavity is filled with a 0.2% suspension of 0.296 μm diameter polystyrene spheres at 25 °C resulting in $\mu'_s = 6.67 \text{ cm}^{-1}$, $\mu_a = 0.002 \text{ cm}^{-1}$, and $D_B = 1.5 \times 10^{-8} \text{ cm}^2\text{s}^{-1}$. For the solid, $\mu'_s = 4.55 \text{ cm}^{-1}$ and $\mu_a = 0.002 \text{ cm}^{-1}$. A single-mode fiber collects light at a known position and delivers it to a photo-multiplier tube (PMT), whose output enters a digital autocorrelator to obtain the temporal intensity correlation function. The temporal intensity correlation function is related to the temporal field correlation function by the Siegert relation [100, 48, 50]. The fibers can be moved to any position on the sample surface.

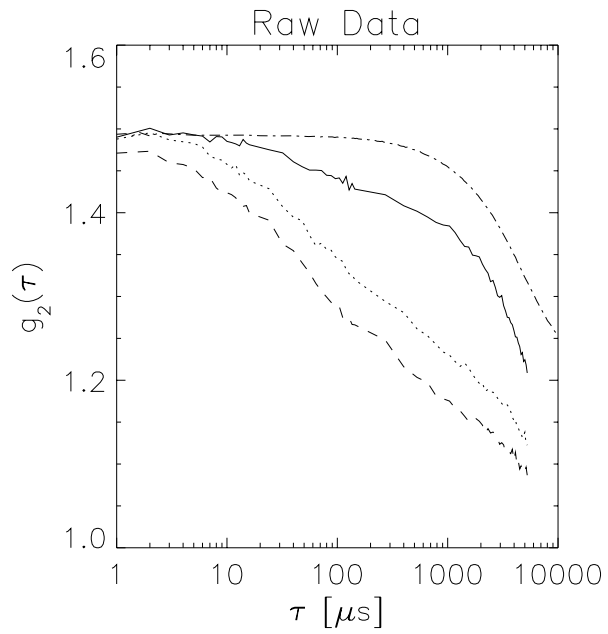


Figure 4.7: Experimental measurements of the temporal intensity autocorrelation function for three different source-detector pairs with a colloid present and one source-detector position without the colloid. The dot-dashed line illustrates the decay of the correlation function due to ensemble averaging (i.e. no colloid is present). This decay is independent of source-detector position. The dashed, dotted, and solid lines correspond to $g_2(\tau)$ measured with a colloid in the cavity and source-detector positions respectively at 1, 2, and 3 as indicated in fig. 4.8.

Brownian motion (i.e. no colloid is present) to illustrate the time scale introduced by ensemble averaging. From the raw data we see that $\beta \approx 0.5$, as expected, since we are using a single-mode fiber that propagates the two orthogonal polarizations. We also observe the short time decay of the correlation function due to Brownian motion and the long time decay due to ensemble averaging. The decay due to ensemble averaging is significant for $\tau > 300 \mu\text{s}$ and is not dependent on source-detector position or separation.

Fig. 4.8 plots the decay of the normalized temporal field correlation function, $g_1(\tau)$, obtained from $g_2(\tau)$ and compares these results to theoretical predictions based on eq. (4.43). The expected trend is observed. When the source and detector are closer to the dynamical region, there is more decay in the correlation function and the rate of decay is greater. Here the largest fraction of detected photons have sampled the dynamical region and on average have had more scattering events in the dynamical region. The agreement between experiment and theory is NOT good. In order to get good agreement the Brownian diffusion coefficient must be reduced by a factor of 3 to 4. For the theoretical results presented in fig. 4.8, $D_B = 3.77 \times 10^{-9} \text{ cm}^2\text{s}^{-1}$ which is a factor of ~ 4 smaller than the expected $D_B = 1.5 \times 10^{-8} \text{ cm}^2\text{s}^{-1}$. The cause of this discrepancy is discussed below.

Although quantitative agreement is not observed, qualitative agreement is observed. Correlation functions were measured for different reduced scattering coefficients and Brownian diffusion coefficients for the dynamical region. Fig. 4.9 plots the measured correlation functions for different μ'_s compared with theory. Three different concentrations of $0.813 \mu\text{m}$ diameter polystyrene microspheres were used to obtain reduced scattering coefficients of 3.5, 4.5, and 9.0 cm^{-1} for the dynamical region. The rest of the system is the same as the previous experiment (see fig. 4.6). Using the Brownian diffusion coefficient as a free parameter to fit the theory to experiment, good agreement was obtained. In all cases the Brownian diffusion coefficient had to be reduced by a factor of ~ 3 . For $0.813 \mu\text{m}$ diameter polystyrene microspheres the expected D_B is $5.46 \times 10^{-9} \text{ cm}^2\text{s}^{-1}$. For $\mu'_s = 3.5, 4.5$, and 9.0 cm^{-1} the fits for D_B where

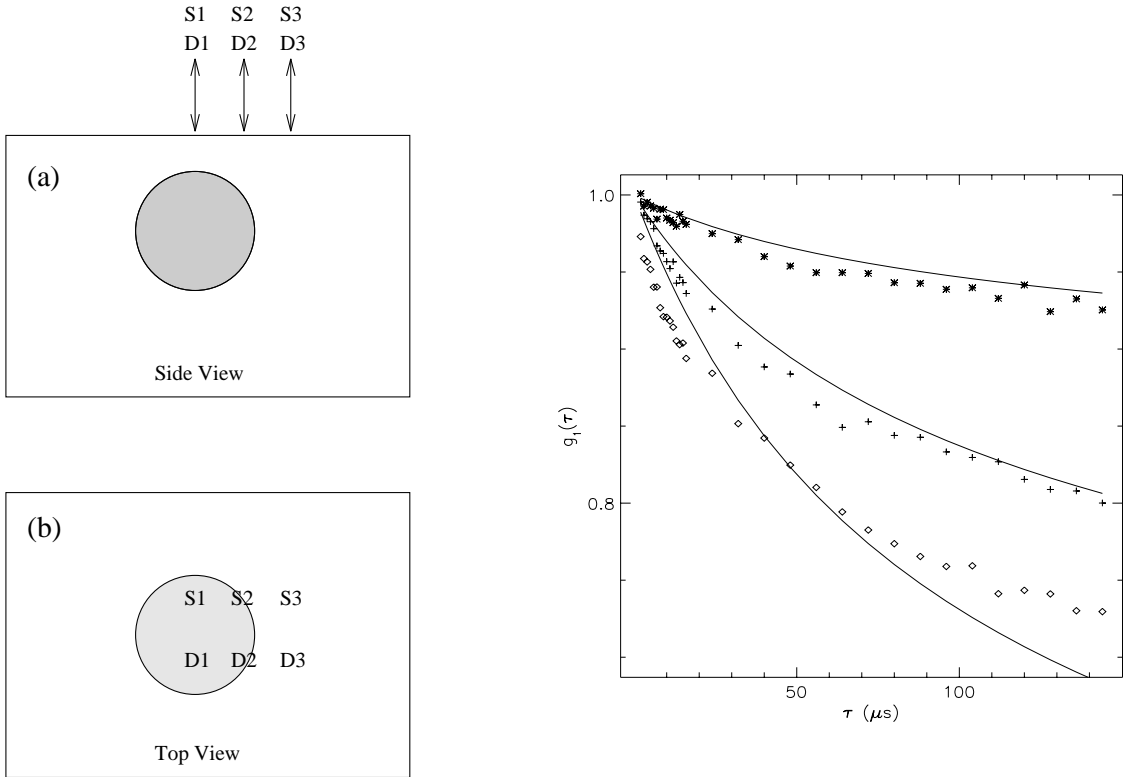


Figure 4.8: Experimental measurements of the normalized temporal field autocorrelation function for three different source-detector pairs are compared with theory. The geometry is illustrated in (a) and (b). With respect to an x-y coordinate system whose origin lies directly above the center of the spherical cavity, the source-detector axis was aligned parallel to the y-axis with the source at $y=1.0$ cm and the detector at $y=-0.75$ cm. Keeping the source-detector separation fixed at 1.75 cm, measurements were made at $x=0.0$ cm, 1.0 cm, and 2.0 cm, and are indicated by the \diamond 's, +'s, and *'s respectively. The uncertainty for these measurements is 3% and arises from uncertainty in the position of the source and detector. The solid line was calculated using the known experimental parameters with D_B as a free parameter (see fig. 4.6). Note larger and more rapid decays are observed when the source and detector are nearest the dynamic sphere.

2.21×10^{-9} , 2.14×10^{-9} , and $1.78 \times 10^{-9} \text{ cm}^2\text{s}^{-1}$ respectively.

Correlation functions for different Brownian diffusion coefficients are plotted in fig. 4.10. Different D_B were obtained by using monodisperse polystyrene microspheres with diameters of $0.137 \mu\text{m}$, $0.300 \mu\text{m}$, and $0.813 \mu\text{m}$. The concentrations were varied to keep $\mu'_s = 4.5 \text{ cm}^{-1}$. Once again good agreement between experiment and theory was observed by using a smaller D_B in the theory. The relative values for the fitted D_B agree with that of the experimental D_B . The expected values of D_B were 3.28×10^{-8} , 1.50×10^{-8} , and $5.46 \times 10^{-9} \text{ cm}^2\text{s}^{-1}$ respectively for the $0.137 \mu\text{m}$, $0.300 \mu\text{m}$, and $0.813 \mu\text{m}$ diameter polyballs. The fitted values for D_B were 1.49×10^{-8} , 8.21×10^{-9} , and $2.71 \times 10^{-9} \text{ cm}^2\text{s}^{-1}$.

I believe the observed disagreement in the Brownian diffusion coefficient results from mismatches in the indices of refraction at the resin/air and resin/colloid interfaces. In an early analysis [94] the semi-infinite boundary condition was solved incorrectly, but fortuitously resulted in better agreement. In that case [94], the point source was not placed a distance of $l^* = 1/\mu'_s$ away from the collimated source along the source axis as in the usual treatment of a collimated source [76], but rather at the collimated source position. Furthermore, the image source (to satisfy the extrapolated boundary condition for index mismatched media) was positioned as if the real source had been extended into the medium. This treatment resulted in quantitative agreement between theory and experiment.

The high sensitivity to the treatment of the semi-infinite boundary conditions renders this experimental setup inappropriate for rigorously validating the correlation diffusion equation for systems with spatially varying dynamical and optical properties. In the next section I compare the theory with Monte Carlo results for infinite media with spherical inhomogeneities and obtain quantitative agreement. The agreement supports the view that correlation “scatters” from spatial variations of the particle diffusion coefficient ($D_B(\mathbf{r})$), the absorption ($\mu_a(\mathbf{r})$), and the reduced scattering coefficient ($\mu'_s(\mathbf{r})$).

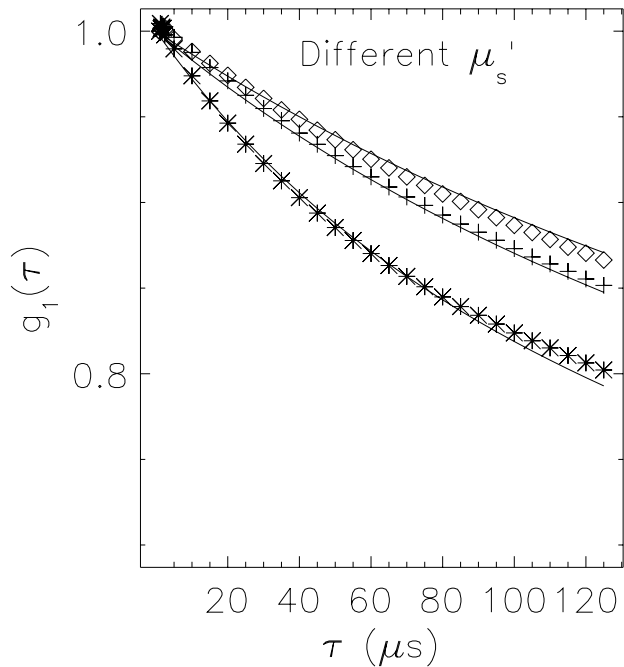


Figure 4.9: Experimental measurements of the normalized field correlation function for a dynamical region with three different μ'_s are plotted. The source and detector were separated by 1.5 cm and centered over the position of the sphere. The \diamond 's, +'s, and *'s correspond to $\mu'_s = 3.5, 4.5$, and 9.0 cm^{-1} respectively. The solid line was calculated using the known experimental parameters with D_B as a free parameter.

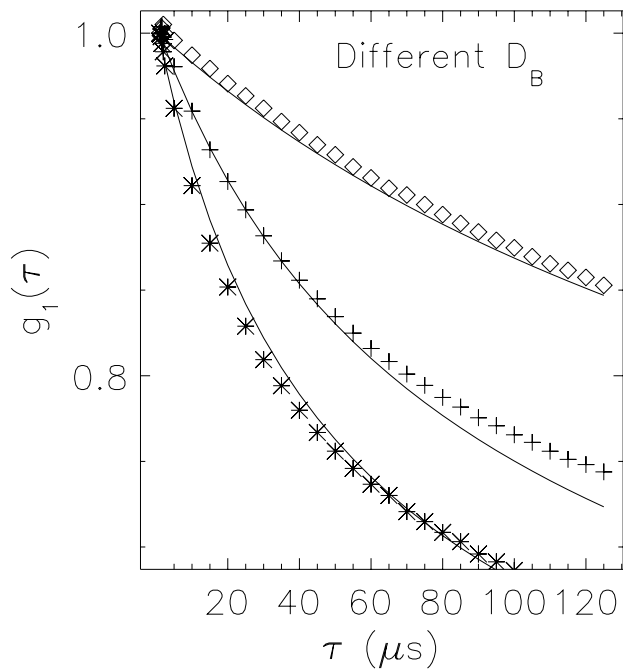


Figure 4.10: Experimental measurements of the normalized field correlation function for a dynamical region with three different D_B are plotted. The source and detector were separated by 1.5 cm and centered over the position of the sphere. The \diamond 's, $+$'s, and $*$'s correspond to $a = 0.813, 0.300$, and $0.137 \mu\text{m}$ respectively. The solid line was calculated using the known experimental parameters with D_B as a free parameter.

4.3.2 Imaging Media with Spatially Varying Brownian Motion

Since the perturbation of correlation by inhomogeneities can be viewed as a scattering process, one can readily envision the application of tomographic algorithms for the reconstruction of images of spatially varying dynamics [13]. I have investigated this possibility. I use an inversion algorithm, one of several possible schemes [13, 113], which is based on a solution to the correlation diffusion equation, eq. (4.22), generalized to include spatially varying dynamics, $D_B(\mathbf{r}) = D_{B,o} + \delta D_B(\mathbf{r})$, absorption, $\mu_a(\mathbf{r}) = \mu_{a,o} + \delta\mu_a(\mathbf{r})$, and scattering, $\mu'_s(\mathbf{r}) = \mu'_{s,o} + \delta\mu'_s(\mathbf{r})$ and $D_\gamma(\mathbf{r}) = D_{\gamma,o} + \delta D_\gamma(\mathbf{r})$. $D_{B,o}$, $\mu'_{s,o}$, and $\mu_{a,o}$ are the spatially uniform background characteristics. $\delta\mu_a(\mathbf{r})$ is the spatial variation in the absorption coefficient, $\delta\mu'_s(\mathbf{r})$ is the spatial variation in the reduced scattering coefficient, $\delta D_\gamma(\mathbf{r})$ is the spatial variation in the photon diffusion coefficient, and $\delta D_B(\mathbf{r})$ represents the spatial variation in the particle diffusion coefficient relative to the background value.

The correlation diffuse equation with spatially varying optical and dynamical properties is

$$\begin{aligned} \nabla^2 G_1(\mathbf{r}_s, \mathbf{r}, \tau) - \frac{v\mu_{a,o}}{D_{\gamma,o}} G_1(\mathbf{r}_s, \mathbf{r}, \tau) - \frac{2v\mu'_s k_o^2 D_{B,o} \tau}{D_{\gamma,o}} G_1(\mathbf{r}_s, \mathbf{r}, \tau) = \\ - \frac{v}{D_\gamma(\mathbf{r})} S_o \delta(\mathbf{r}_s - \mathbf{r}) + \frac{1}{\mu'_{s,o}} \nabla \delta\mu'_s(\mathbf{r}) \cdot \nabla G_1(\mathbf{r}_s, \mathbf{r}, \tau) + \frac{v\delta\mu_a(\mathbf{r})}{D_{\gamma,o}} G_1(\mathbf{r}_s, \mathbf{r}, \tau) \\ + \frac{2v\mu'_s k_o^2 \delta D_B(\mathbf{r}) \tau}{D_{\gamma,o}} G_1(\mathbf{r}_s, \mathbf{r}, \tau) + 3\mu_{a,o} \delta\mu'_s G_1(\mathbf{r}_s, \mathbf{r}, \tau). \end{aligned} \quad (4.45)$$

This equation can be solved using the first Born approximation as is described in section 2.5.5. We can also solve this equation using the Rytov approximation [113]. Within the Rytov approximation we assume that $G_1(\mathbf{r}_s, \mathbf{r}, \tau) = G_{1,o}(\mathbf{r}_s, \mathbf{r}, \tau) \exp(\Phi_s(\mathbf{r}_s, \mathbf{r}, \tau))$. Following the procedure described by Kak and Slaney [113] we obtain an integral equation relating $\Phi_s(\mathbf{r}_s, \mathbf{r}, \tau)$ to the spatial variation of the dynamical and optical properties, i.e.

$$\begin{aligned} \Phi_s(\mathbf{r}_s, \mathbf{r}_d, \tau) = - \frac{1}{G_1^o(\mathbf{r}_s, \mathbf{r}_d, \tau)} \int d^3 r' \left[\frac{2v\mu'_s k_o^2 \tau \delta D_B(\mathbf{r}')}{D_{\gamma,o}} H(\mathbf{r}', \mathbf{r}_d, \tau) G_1^o(\mathbf{r}_s, \mathbf{r}', \tau) \right. \\ \left. + \frac{v\delta\mu_a(\mathbf{r})}{D_{\gamma,o}} H(\mathbf{r}', \mathbf{r}_d, \tau) G_1^o(\mathbf{r}_s, \mathbf{r}', \tau) + \frac{\delta D_\gamma(\mathbf{r})}{D_{\gamma,o}} \nabla G_1^T(\mathbf{r}, \hat{\Omega}, \tau) {}^{(0)}_1(\mathbf{r}_s, \mathbf{r}) \cdot \nabla H(\mathbf{r}, \mathbf{r}_d) \right] \end{aligned} \quad (4.46)$$

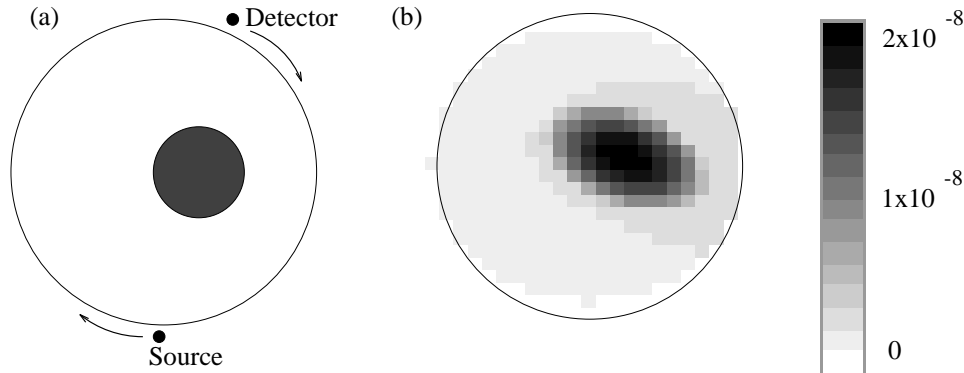


Figure 4.11: An image reconstructed from experimental measurements of the scattered correlation function is shown in (b). The system was a 4.6 cm diameter cylinder with $l^*=0.25$ cm, $\mu_a=0.002$ cm $^{-1}$, and $D_B=0$ (see illustration in (a)). A 1.3 cm diameter spherical cavity was centered at $x=0.7$ cm, $y=0$, and $z=0$ and filled with a colloid with $l^*=0.25$ cm, $\mu_a=0.002$ cm $^{-1}$, and $D_B=1.5 \times 10^{-8}$ cm 2 s $^{-1}$. A slice of the image at $z=0$ cm is presented in (b). The values of the reconstructed particle diffusion coefficients are indicated by the legend in units of cm 2 s $^{-1}$.

Here, $H(\mathbf{r}', \mathbf{r}_d, \tau)$ is the Green's function for the homogeneous correlation diffusion equation, $\delta\mu_a(\mathbf{r})$ is the spatial variation in the absorption coefficient, $\delta D_\gamma(\mathbf{r})$ is the spatial variation in the photon diffusion coefficient, and $\delta D_B(\mathbf{r})$ represents the spatial variation in the particle diffusion coefficient relative to the background value. The position of the source (detector) is \mathbf{r}_s (\mathbf{r}_d).

There are many techniques that can be employed to invert eq. (4.46) [13, 113]. All the methods are based on discretizing the integral equation and using measurements of $\Phi_s(\mathbf{r}_s, \mathbf{r}_d)$ with several different source-detector pairs to solve the coupled set of linear equations (see section 2.5.5). I use the Simultaneous Iterative Reconstruction Technique [113] to solve the coupled equations.

To demonstrate that the correlation diffusion equation can be used as the basis for a tomographic reconstruction algorithm, I took several measurements on a solid, highly-scattering sample that contained a spherical, dynamical region. The system was

a solid cylinder of TiO_2 suspended in resin. The cylinder was homogeneous except for a 1.3 cm diameter spherical cavity which was filled with an aqueous suspension of 0.296 μm polystyrene balls ($D_B = 1.5 \times 10^{-8} \text{ cm}^2\text{s}^{-1}$) and centered at $z=0$ (the z -axis is the axis of the cylinder). The optical properties of the colloid matched that of the solid so that we are only imaging variations in the dynamical properties. Measurements were made every 30° at the surface of the cylinder for $z=0$, 1, and 2 cm, with source-detector angular separations of 30° and 170° and correlation times of $\tau = 15, 25, 35, 45, 55, 65, 75$, and 85 μs . Except where the measurements were made, a highly reflective coating was applied to the surface so that the cylindrical medium could be treated as infinite. This approximation has been discussed by Haskell *et al.* [76] and its validity permits us to obtain accurate reconstructions of the dynamical properties.

The image of $D_B(\mathbf{r})$ in fig. 4.11 was reconstructed from ~ 600 measurements of the scattered correlation function, $\Phi_s(\mathbf{r}_s, \mathbf{r}_d, \tau)$, using 400 iterations of the Simultaneous Iterative Reconstruction Technique [113]. The $z=0$ slice of the image is shown in fig. 4.11b. From this image the center (in the x - y plane) of the dynamic region and the magnitude of the particle diffusion coefficient are determined. The center of the object in the image is within 2 mm of the actual center of the dynamic sphere. This discrepancy scales with the uncertainty in the position of the source and detector. The sphere diameter (~ 1.3 cm) and particle diffusion coefficient ($\sim 1.8 \times 10^{-8} \text{ cm}^2\text{s}^{-1}$) obtained from the imaging procedure also agree reasonably well with experimentally known parameters (1.3 cm and $1.5 \times 10^{-8} \text{ cm}^2\text{s}^{-1}$).

4.3.3 Validity of Diffusion Equation for Media with Spatially Varying Flow Properties

The experiments described thus far demonstrate the diffusion and scattering of correlation in turbid samples where the dynamics are governed by Brownian motion. The correlation diffusion equation can be modified to account for other dynamical processes. In the cases of random flow and shear flow the correlation diffusion equation

becomes

$$\left(D_\gamma \nabla^2 - v \mu_a - 2v \mu'_s D_B k_o^2 \tau - \frac{1}{3} v \mu'_s \langle \Delta V^2 \rangle k_o^2 \tau^2 - \frac{1}{15} v \mu'^{-1}_s \Gamma_{eff}^2 k_o^2 \tau^2 \right) G_1(\mathbf{r}, \tau) = -v S(\mathbf{r}). \quad (4.47)$$

The fourth and fifth terms on the left-hand side of eq. (4.47) arise from random and shear flows respectively. $\langle \Delta V^2 \rangle$ is the second moment of the particle speed distribution (assuming the velocity distribution is isotropic and Gaussian)[103, 46], and Γ_{eff} is the effective shear rate [104]. Notice that the “dynamical absorption” for flow in eq. (4.47) increases as τ^2 (compared to the τ increase for Brownian motion) because particles in flow fields travel ballistically; also D_B , $\langle \Delta V^2 \rangle$, and Γ_{eff} appear separately because the different dynamical processes are uncorrelated. The form of the “dynamical absorption” term for random flow is related to that for Brownian motion. Both are of the form $\frac{1}{3} v \mu'_s \langle \Delta r^2(\tau) \rangle$, where $\langle \Delta r^2(\tau) \rangle$ is the mean square displacement of a scattering particle. For Brownian motion $\langle \Delta r^2(\tau) \rangle = 6D_B\tau$, and for random flow $\langle \Delta r^2(\tau) \rangle = \langle \Delta V^2 \rangle \tau^2$. The derivation of the “dynamical absorption” term for shear flow is more complex and the reader is referred to Wu *et al.* [104] for a complete discussion.

Flow in turbid media is an interesting problem that has received some attention. In these measurements experimenters typically determine a correlation function that may be a compound of many decays representing a weighted average of flow within the sample. For example, Bonner and Nossal have developed an approach for measuring random blood flow in homogeneous tissue [46], Wu *et al.* have applied DWS to study uniform shear flow [104], and Bicout and co-workers have applied DWS to study inhomogeneous flow and turbulence [114, 115, 116, 117]. In all cases, *a priori* knowledge of the flow is used in the analyses. The application of correlation diffusion imaging will further clarify information about heterogeneous flows in turbid media.

I conducted experiments to examine the correlation signal arising from a solid highly scattering medium with a single cylindrical vein containing a highly scattering liquid under Poiseuille flow. The experimental system is depicted in fig. 4.12. In this experiment, the correlation function is measured in remission from a semi-infinite,

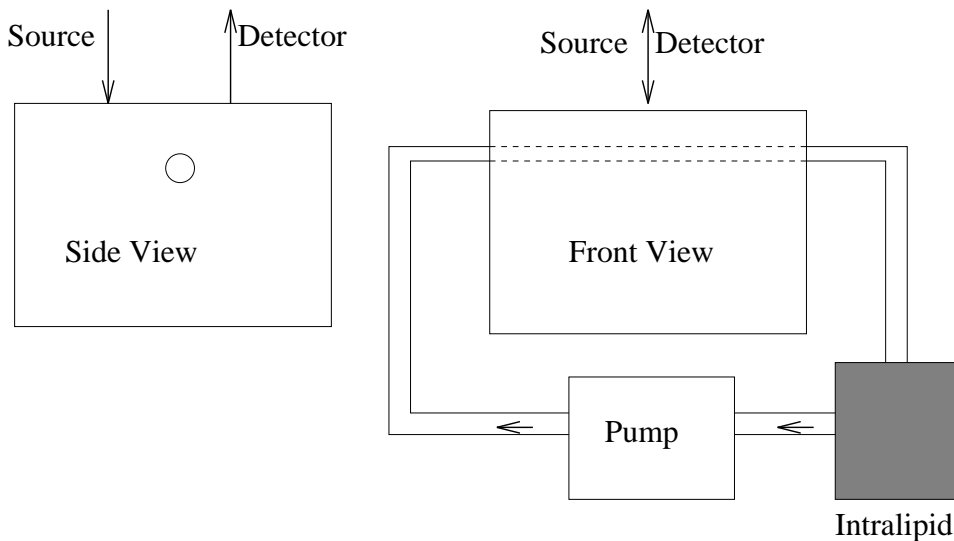


Figure 4.12: The experimental system is the same as described in fig. 4.6 except that the TiO_2 slab now has a 6 mm diameter cylindrical cavity instead of a spherical cavity. The cylindrical cavity is centered 13 mm below the surface of the slab and 0.5% Intralipid is pumped through the cavity at flow speeds of 0.442 cm s^{-1} , 0.884 cm s^{-1} , and 1.77 cm s^{-1} . For the solid, $\mu'_s = 4.0 \text{ cm}^{-1}$ and $\mu_a = 0.002 \text{ cm}^{-1}$. For the Intralipid, the optical properties are assumed to be the same as the TiO_2 . The correlation function is measured with the source and detector separated by 2.0 cm, i.e. the source is 1.0 cm to the left of the vein and the detector is 1.0 cm to the right.

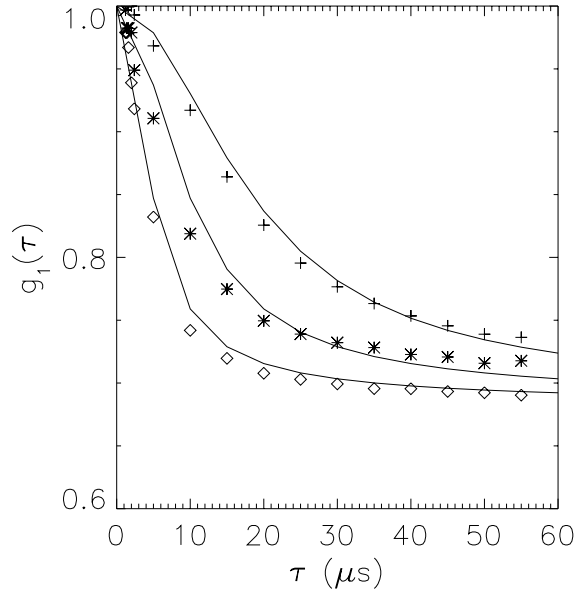


Figure 4.13: Experimental measurements of the normalized temporal field correlation function for three different flow speeds are compared with theory. Measurements for flow speeds of 0.442 cm s^{-1} , 0.884 cm s^{-1} , and 1.77 cm s^{-1} are indicated respectively by the '+'s, '*'s, and \diamond 's. The solid lines are calculated using the experimental parameters given in fig. 4.12 and effective shear rates of 3.0 s^{-1} , 6.0 s^{-1} , and 12.0 s^{-1} .

highly-scattering, solid slab of TiO_2 suspended in resin ($\Gamma_{eff} = 0$). A 0.5% solution of Intralipid [71] is pumped through the cylindrical vein in the slab with pump speeds of 0.442 cm s^{-1} , 0.884 cm s^{-1} , and 1.77 cm s^{-1} . The experimental results are shown by the symbols in fig. 4.13.

Measurements of the normalized temporal field correlation function were compared with the exact solution of correlation scattering from cylindrical inhomogeneities. The derivation of the analytic solution for a cylinder is similar to that for a sphere. Once again, the correlation is a superposition of the incident and scattered correlation, i.e. $G_1^{out} = G_1^o + G_1^{scatt}$. For a cylinder of infinite length, the solution for the scattered wave in cylindrical coordinates is [118]

$$G_1^{scatt}(r, \theta, z) = -\frac{vS}{2\pi^2 D_\gamma} \sum_{n=1}^{\infty} \int_0^{\infty} dp \cos(n\theta) \cos(pz)$$

$$\begin{aligned} & \times K_n(\sqrt{p^2 - (K^{out})^2} r) K_n(\sqrt{p^2 - (K^{out})^2} r_s) \\ & \times \left[\frac{D_\gamma^{out} x I'_n(x) I_n(y) - D_\gamma^{in} y I_n(x) I'_n(y)}{D_\gamma^{out} x K_n'(x) I_n(y) - D_\gamma^{in} y K_n(x) I_n'(y)} \right], \end{aligned} \quad (4.48)$$

where I_n and K_n are modified Bessel functions, $x = \sqrt{p^2 - (K^{out})^2} a$, $y = \sqrt{p^2 - (K^{in})^2} a$, and a is the radius of the cylinder. The solution has been simplified by taking the z-axis as the axis of the cylinder and assuming that the source is at $z = 0$ and $\theta = 0^\circ$.

The comparison between experiment (symbols) and theory (solid lines) shown in fig. 4.13 indicates a good agreement. The parameters used in the calculation, except for Γ_{eff} , were the known parameters. The effective shear rate, Γ_{eff} , was determined by fitting the analytic solution to the data with the constraint that Γ_{eff} had to scale linearly with the flow speed. The best fit to the data indicates that Γ_{eff} is approximately 6.8 cm^{-1} times the flow speed. Since the shear rate is given by the change in speed per unit length in the direction perpendicular to the flow, one might expect that the effective shear rate would be the flow speed divided by the radius of the vein. This simple calculation gives an effective shear rate that is a factor of two smaller than the measured Γ_{eff} . This difference is not yet understood, but could result from the mismatches in optical indices of refraction and sensitivity to the semi-infinite boundary condition.

4.4 Monte Carlo Simulations

This section presents the results of various Monte Carlo simulations of correlation diffusion. I used the results from Monte Carlo simulations to check the accuracy of the correlation diffusion equation when the accuracy of my experimental results was questionable or I did not have the experimental data. In many cases these simulations provide a signal-to-noise ratio that is difficult to achieve in the laboratory and therefore permit a more accurate test of the validity of the correlation diffusion theory.

I first present simulation results for an infinite, homogeneous system compared

with correlation diffusion theory. This comparison illustrates the behavior of the correlation function as different parameters are varied. Good agreement with diffusion theory is observed. I then present results for a system which is infinite, static, and homogeneous except for a spherical dynamic region. This system avoids the shortcomings of the experimental system used in the previous section. Results are compiled for a wide range of parameters and compared with correlation diffusion theory. The agreement is good indicating the robustness of the theory. I then present simulations for a two-component system with spatially uniform random flow in a spatially uniform static medium. This system models a capillary network in tissue. The comparison with correlation diffusion theory demonstrates that the homogeneous solution can be used as long as the dynamical term is weighted by

$$\frac{\mu'_s(\text{random flow component})}{\mu'_s(\text{random flow component}) + \mu'_s(\text{static component})} . \quad (4.49)$$

The Monte Carlo simulations for obtaining electric field temporal autocorrelation functions is described in appendix 6.2.2. Briefly, the approach is to histogram the accumulated momentum transfer of photons scattered from moving particles as they propagate through a system with spatially varying dynamics. That is, scattering events in a static medium do not contribute to the accumulated momentum transfer while scattering events in a dynamic medium do contribute. The contribution is proportional to the magnitude of the dynamics. In the simulation the momentum transfer is accumulated as a dimensionless variable that scales with k_o^2 . The histogram, when normalized, is just the momentum transfer probability distribution $P(Y)$. The correlation function can then be calculated with [119, 120]

$$g_1(\tau) = \int_0^\infty dY P(Y) \exp\left(-\frac{1}{3} Y k_o^2 \langle \Delta r^2(\tau) \rangle\right) . \quad (4.50)$$

$P(Y)$ is determined from the Monte Carlo simulation, k_o^2 is the wavenumber of light in the medium, and $\langle \Delta r^2(\tau) \rangle$ is determined by the dynamics of the system.

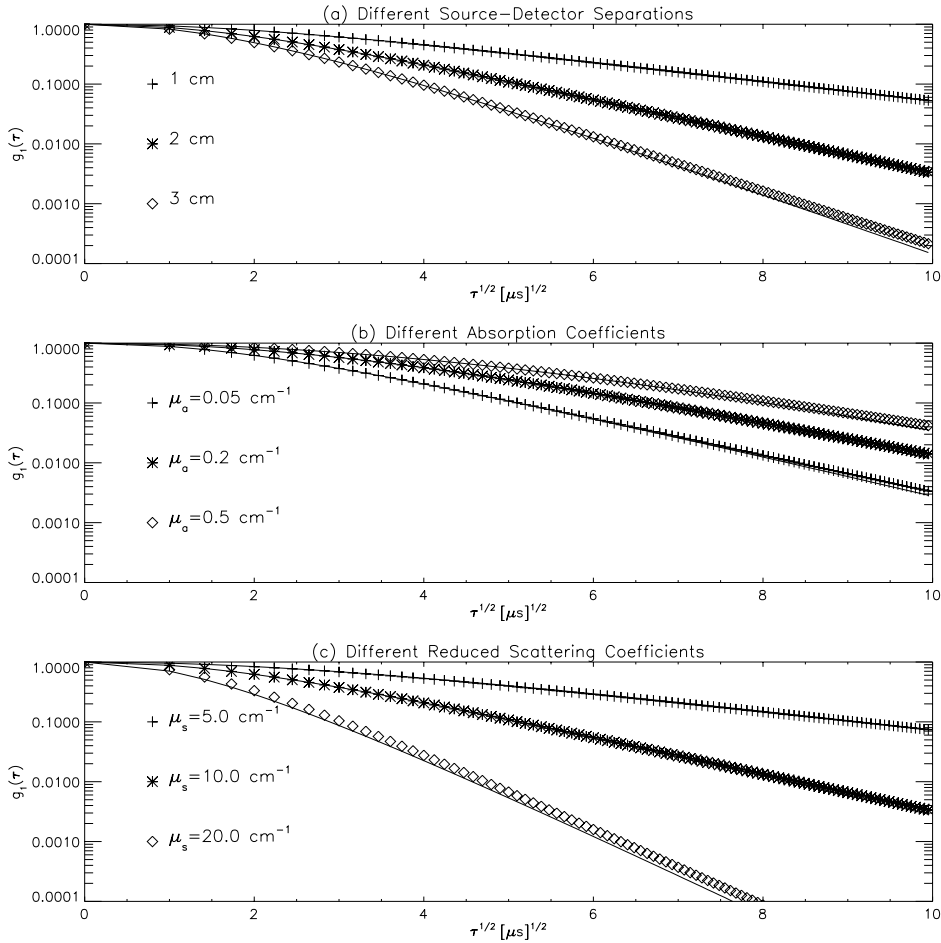


Figure 4.14: Monte Carlo simulations for correlation diffusion in a homogeneous medium are compared with theory for different (a) source-detector separations, (b) absorption coefficients, and (c) reduced scattering coefficients. Unless otherwise stated, the source-detector separation is 2.0 cm, $\mu'_s=10.0 \text{ cm}^{-1}$, $\mu_a=0.05 \text{ cm}^{-1}$, and $D_B = 1.0 \cdot 10^{-8} \text{ cm}^2\text{s}^{-1}$. The Monte Carlo results are given by the symbols. The solid lines are calculated from diffusion theory.

4.4.1 Homogeneous Media with Brownian Motion

Comparisons of eq. (4.13) with experimental measurements of absorption-free media has been made by Pine *et al.* [106]. Good agreement is found except in regimes where the photon diffusion approximation breaks down. Here, I compare solutions of the correlation diffusion equation with photon absorption to Monte Carlo simulations. In this case, the solution is

$$G_1(\mathbf{r}, \tau) = \frac{S \exp\left(-\sqrt{3\mu_a\mu'_s + 6\mu'^2_s D_B k_o^2 \tau} |\mathbf{r} - \mathbf{r}_s|\right)}{4\pi D_\gamma |\mathbf{r} - \mathbf{r}_s|}. \quad (4.51)$$

At early correlation times the behavior is governed by photon absorption and at later times it is governed by dynamical processes. The transition time is given by $\tau_c = \mu_a / (2\mu'_s D_B k_o^2)$. At shorter τ the correlation function will plateau while at longer τ it will decay exponentially as the square-root of τ with the same rate as if there were no photon absorption.

Fig. 4.14a plots the Monte Carlo results for different source-detector separations ρ . The optical and dynamical properties are held constant at $\mu'_s = 10.0 \text{ cm}^{-1}$, $\mu_a = 0.05 \text{ cm}^{-1}$, and $D_B = 1 \times 10^{-8} \text{ cm}^2 \text{s}^{-1}$. The decay rate of $g_1(\tau)$ increases linearly with ρ , as expected. Next, we see the plateau at early τ and that the transition time is independent of ρ . Finally, $g_1(\tau)$ calculated using correlation diffusion theory for the different source-detector separations is given by the solid lines. In all cases good agreement is observed.

Results for varying μ_a and μ'_s while keeping the source-detector separation fixed are given in fig. 4.14b and fig. 4.14c respectively. In fig. 4.14b we see that τ_c increases as the absorption coefficient is increased while the decay rate at $\tau > \tau_c$ is not changed. In fig. 4.14c we see that increasing the reduced scattering coefficient increases the decay rate of the correlation function and decreases τ_c . In all cases, good agreement with diffusion theory is observed.

Fig. 4.15 plots the same correlation functions plotted in fig. 4.14 for different source-detector separations, but the abscissa is extended from $100 \mu\text{s}$ to $400 \mu\text{s}$. At these longer correlation times the correlation diffusion equation is expected to break down

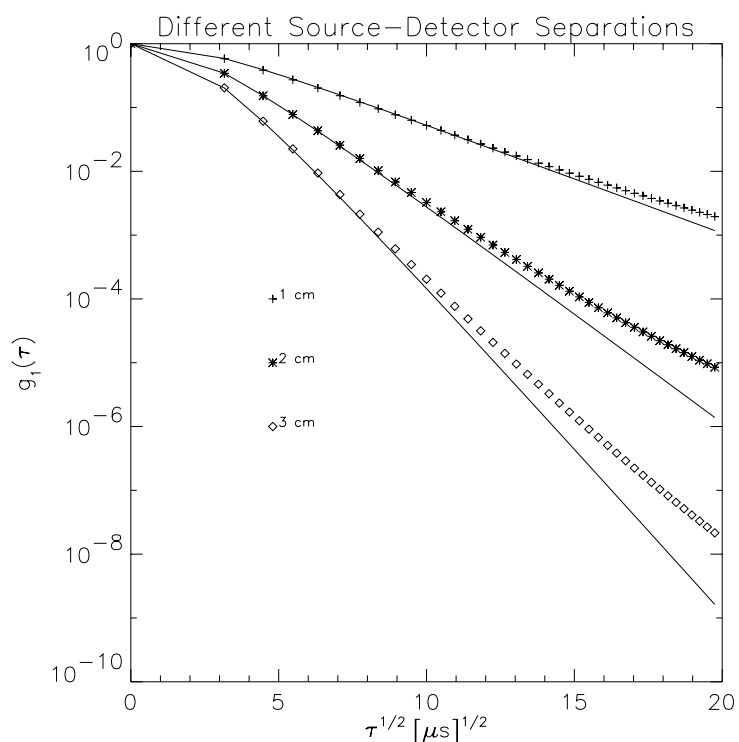


Figure 4.15: Monte Carlo simulations for correlation diffusion in a homogeneous medium are compared with theory for different source-detector separations. Monte Carlo results are given by the symbols. The solid lines are calculated from diffusion theory.

because of the approximation that $k_o^2 \langle \Delta r^2(\tau) \rangle \ll 1$. The results in fig. 4.15 indicate that the approximation is not valid when $k_o^2 \langle \Delta r^2(\tau) \rangle \geq 0.1$, that is, when $\tau \geq 225\mu s$. The magnitude of the deviation depends on the source-detector separation normalized by the photon random walk step length.

The behavior of the deviation is understood. At longer correlation times the decay results from shorter photon path lengths since the longer path lengths have a faster decay rate and no longer provide a significant contribution. For the shorter path lengths the photon diffusion approximation is not valid since the photons are not diffusing. Furthermore, the q average is not appropriate since there have been only a few scattering events, and in order for the photon to reach the detector, the scattering angles must be smaller than average. The smaller than average scattering angles results in the observed slower decay rate of the Monte Carlo simulations relative to diffusion theory.

4.4.2 Media with Spatially Varying Brownian Motion

Here I present Monte Carlo results to check the validity of the correlation diffusion equation for systems with spatially varying dynamical and optical properties. The system is infinite, static, and homogeneous except for a spherical region which is dynamic and may have different optical properties than the background. The homogeneous properties are $\mu'_s = 10.0 \text{ cm}^{-1}$, $\mu_a = 0.05 \text{ cm}^{-1}$, and $D_B = 0$ unless otherwise specified. For the sphere, $\mu'_s = 10.0 \text{ cm}^{-1}$, $\mu_a = 0.05 \text{ cm}^{-1}$, and $D_B = 1 \times 10^{-8} \text{ cm}^2 \text{s}^{-1}$ unless otherwise specified. Results are presented for the source-detector positions indicated in fig. 4.16.

Comparison of Monte Carlo results and correlation diffusion theory for a system with spatially varying dynamical properties but uniform optical properties are presented in fig. 4.17. Three different absorption coefficients are considered. In fig. 4.17a, b, and c the absorption coefficients are respectively $\mu_a = 0.02 \text{ cm}^{-1}$, $\mu_a = 0.05 \text{ cm}^{-1}$, and $\mu_a = 0.10 \text{ cm}^{-1}$. For each absorption coefficient, results are presented for the three detector positions. The Monte Carlo results are given by the symbols, and the solid

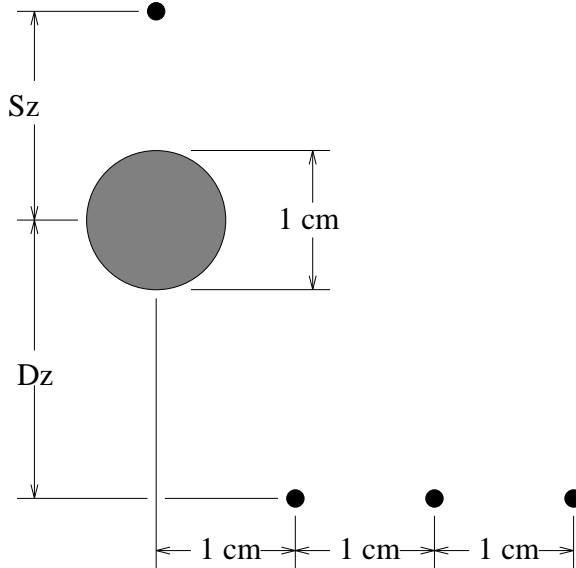


Figure 4.16: An isotropic point source is positioned S_z cm from the center of a spherical inhomogeneity. The sphere has a diameter of 1 cm. Detectors are positioned D_z cm away along the z-axis and displaced off of the z-axis at $\rho=1$, 2, and 3 cm.

lines indicate the prediction using correlation diffusion theory. The agreement is fairly good. Similar results are found for other Brownian diffusion coefficients; actually the results are the same, except that τ scales inversely with D_B .

The small discrepancies are most likely due to a significant fraction of the fluctuating photons having scattered from the dynamical region only a few times before detection. By fluctuating photons I mean those photons which have sampled the dynamic region as opposed to the static photons which have not seen the dynamic region. The distribution of the total momentum transfer with moving particles for the photons detected at $\rho=1.0$ cm is plotted in fig. 4.18 for $\mu_a = 0.05 \text{ cm}^{-1}$. The distribution has a discontinuity at $2k_o$ which is the maximum momentum transfer per scattering event. The diffusion approximation is NOT valid in the regime of a few scattering events. The contribution to $P(Y)$ for $Y < 2$ thus leads to the observed discrepancy. This was checked by noting a correlation between a reduction in the discrepancy with a reduction in the discontinuity for results which are not presented.

In fig. 4.19 I present results for a sphere with different μ_a and D_B than the back-

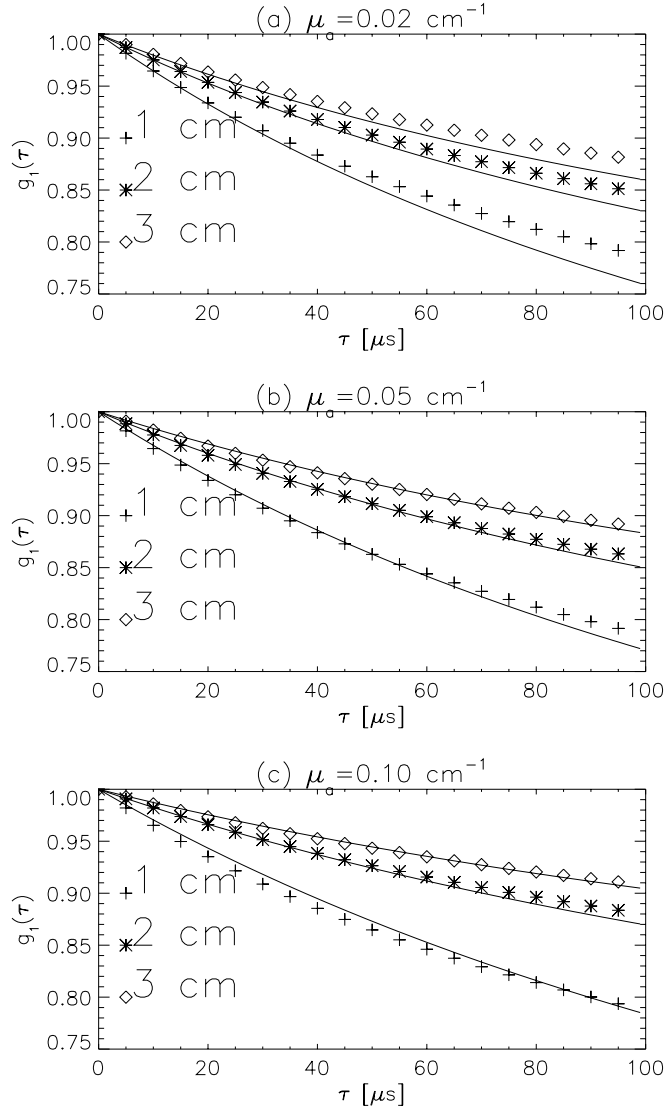


Figure 4.17: Monte Carlo results for the $g_1(\tau)$ (symbols) are compared with correlation diffusion theory (solid lines) for the system depicted in fig. 4.16. The optical properties are spatially uniform. In (a), (b), and (c) the absorption coefficient is respectively 0.02 cm^{-1} , 0.05 cm^{-1} , and 0.10 cm^{-1} . The ρ position of the detector is indicated in the legend. The source is at $Sz=1.0 \text{ cm}$ and the detector is at $Dz=1.0 \text{ cm}$.

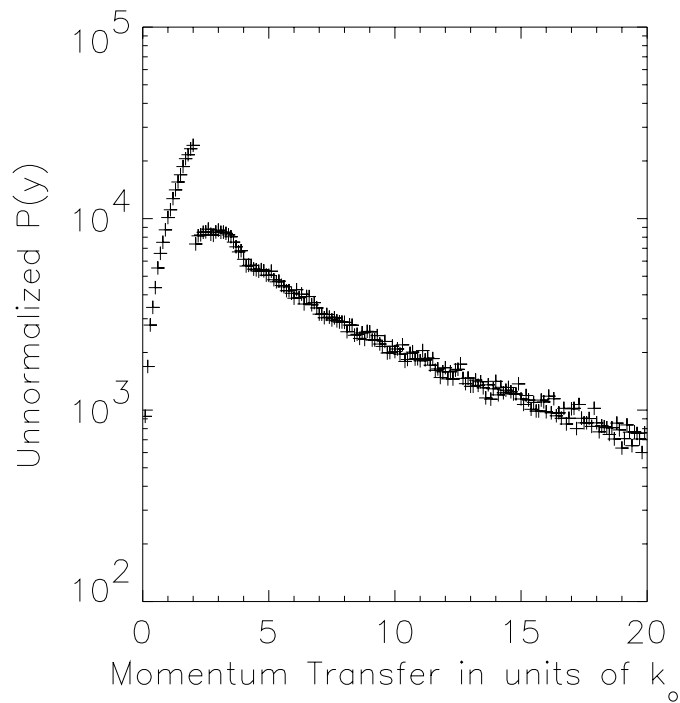


Figure 4.18: Distribution of the total momentum transfer from moving scatterers. The geometry of the system is depicted in fig. 4.16.

ground. For the background $D_B = 0$ while for the sphere $D_B=1\times 10^{-8}$. For the background $\mu_a = 0.05 \text{ cm}^{-1}$. For the results presented in fig. 4.19a, b, and c the object absorption coefficient is respectively $\mu_a = 0.02 \text{ cm}^{-1}$, $\mu_a = 0.05 \text{ cm}^{-1}$, and $\mu_a = 0.20 \text{ cm}^{-1}$. When the absorption coefficient of the object is the same as the background then the agreement between Monte Carlo and correlation diffusion is good. However the agreement is not as good when the absorption coefficient of the object is different than the background. This discrepancy results from the breakdown of the photon diffusion equation for systems with spatially varying optical properties. As observed in fig. 4.17 and fig. 4.18 there are many photons which only have a few scattering events in the sphere. The diffusion approximation overestimates the path lengths of these photons in the object. Thus when the absorption coefficient of the object is larger than the background, diffusion theory overestimates the number of absorbed photons, fewer fluctuating photons reach the detector, and the correlation function does not decay as much. For objects with smaller absorption coefficients, diffusion theory overestimates the amount of decay in the correlation function. These are the trends observed in fig. 4.19.

Fig. 4.20 presents results for a sphere with different μ'_s and D_B than the background. For the background $D_B = 0$ while for the sphere $D_B=1\times 10^{-8}$. For the background $\mu'_s = 10.0 \text{ cm}^{-1}$. For the results presented in fig. 4.20a, b, and c, the object reduced scattering coefficient is respectively $\mu'_s = 5.0 \text{ cm}^{-1}$, $\mu'_s = 10.0 \text{ cm}^{-1}$, and $\mu'_s = 15.0 \text{ cm}^{-1}$. When the reduced scattering coefficient of the object is the same as the background then the agreement between Monte Carlo and correlation diffusion is good. However the agreement is not as good when the reduced scattering coefficient of the object is different than the background. This discrepancy also results from the breakdown of the photon diffusion equation for systems with spatially varying optical properties.

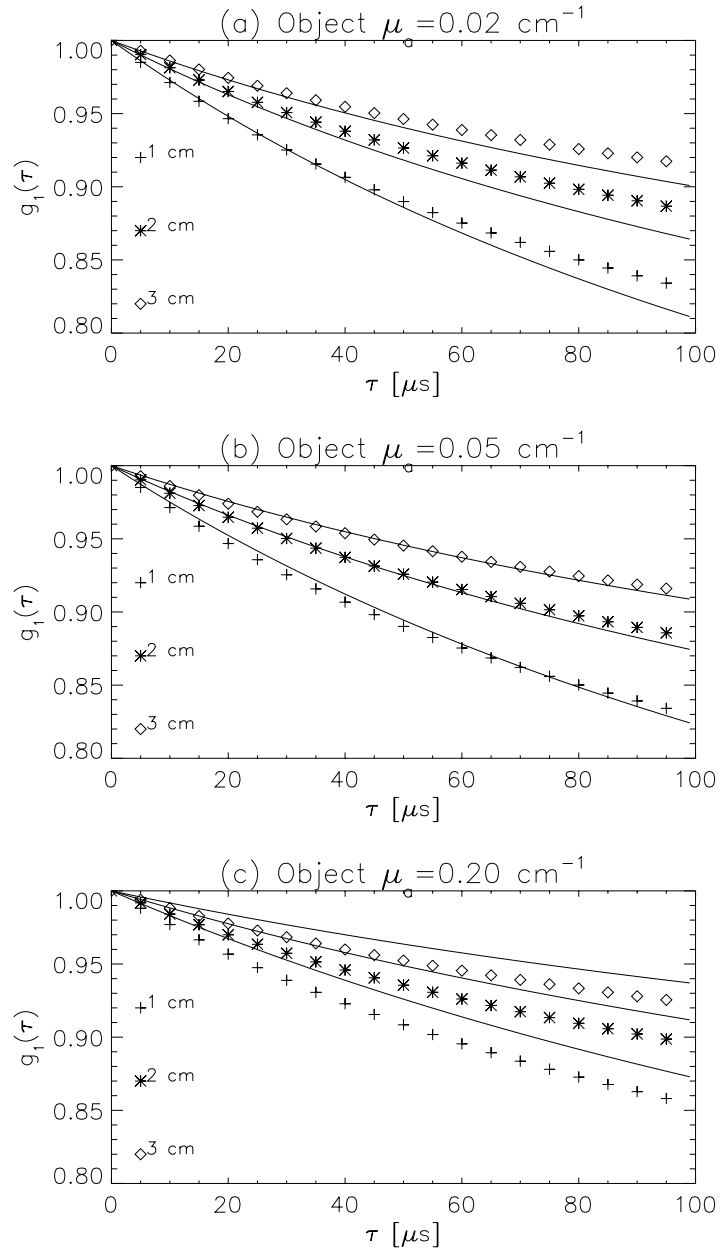


Figure 4.19: Monte Carlo results for $g_1(\tau)$ (symbols) are compared with correlation diffusion theory (lines) for the system depicted in fig. 4.16. In (a), (b), and (c) the object absorption coefficient is respectively 0.02 cm^{-1} , 0.05 cm^{-1} , and 0.20 cm^{-1} . The ρ position of the detector is indicated in the legend. The source is at $Sz=1.5 \text{ cm}$ and the detector is at $Dz=2.0 \text{ cm}$.

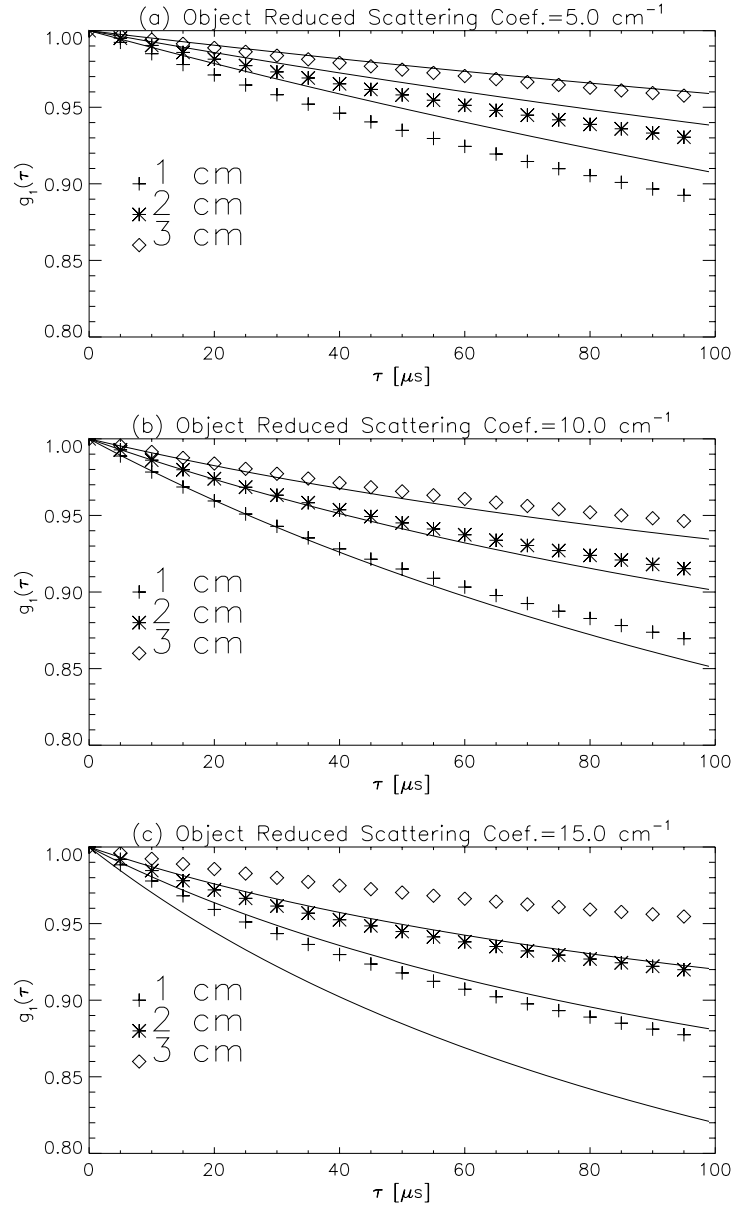


Figure 4.20: Monte Carlo results for $g_1(\tau)$ (symbols) are compared with correlation diffusion theory (lines) for the system depicted in fig. 4.16. In (a), (b), and (c) the object reduced scattering coefficient is respectively 5.0 cm^{-1} , 10.0 cm^{-1} , and 15.0 cm^{-1} . The ρ position of the detector is indicated in the legend. The source is at $Sz=2.0 \text{ cm}$ and the detector is at $Dz=2.0 \text{ cm}$.

4.4.3 Media with Random Flow

Tissue blood flow is a good example of a turbid medium with random flow. Capillary networks are generally randomly oriented on length scales set by the photon random walk step length. When the capillary flow is oriented, as it is in muscle, the photon generally scatters 10+ times between interactions with blood such that the photon's direction is randomized between blood interactions. Thus, the flow is effectively random. Tissue blood flow can be modeled as a two component system, the static tissue matrix and the randomly flowing blood. Monte Carlo results for this system are compared to correlation diffusion theory predictions.

Because the system is composed of two uniformly distributed components, it is necessary to modify the correlation diffusion equation to account for the volume fraction of blood. This is done by simply weighting the dynamical absorption term by the probability of scattering from a red blood cell, i.e.

$$\left(D_\gamma \nabla^2 - v \mu_a - \frac{1}{3} P_{\text{blood}} v \mu'_s k_o^2 \langle \Delta V^2 \rangle \tau^2 \right) G_1(\mathbf{r}, \tau) = -v S(\mathbf{r}) . \quad (4.52)$$

P_{blood} is the probability of scattering from a red blood cell and is given by

$$P_{\text{blood}} = \frac{\mu'_s(\text{blood})}{\mu'_s(\text{blood}) + \mu'_s(\text{static component})} . \quad (4.53)$$

The other optical parameters in eq. (4.52) account for the combined contribution from the tissue matrix and the blood.

A comparison of the Monte Carlo results and correlation diffusion theory is presented in fig. 4.21 for $P_{\text{blood}} = 0.1$. The optical properties are $\mu'_s = 10.0 \text{ cm}^{-1}$ and $\mu_a = 0.05 \text{ cm}^{-1}$. The mean square speed of the red blood cells is $\langle \Delta V^2 \rangle = 1.0 \text{ mm}^2 \text{s}^{-2}$. The agreement is quite good when $k_o^2 \langle \Delta V^2 \rangle \tau^2 \ll 1$ indicating that the diffusion theory can be used to quantify blood flow in particular and random flow in turbid media in general. The discrepancy observed for times greater than 25 μs arises from the $k_o^2 \langle \Delta V^2 \rangle \tau^2 \ll 1$ assumption (note that $[k_o^2 \langle \Delta V^2 \rangle]^{-1/2} = 61 \mu\text{s}$). Comparisons were made for other P_{blood} and in all cases good agreement was observed.

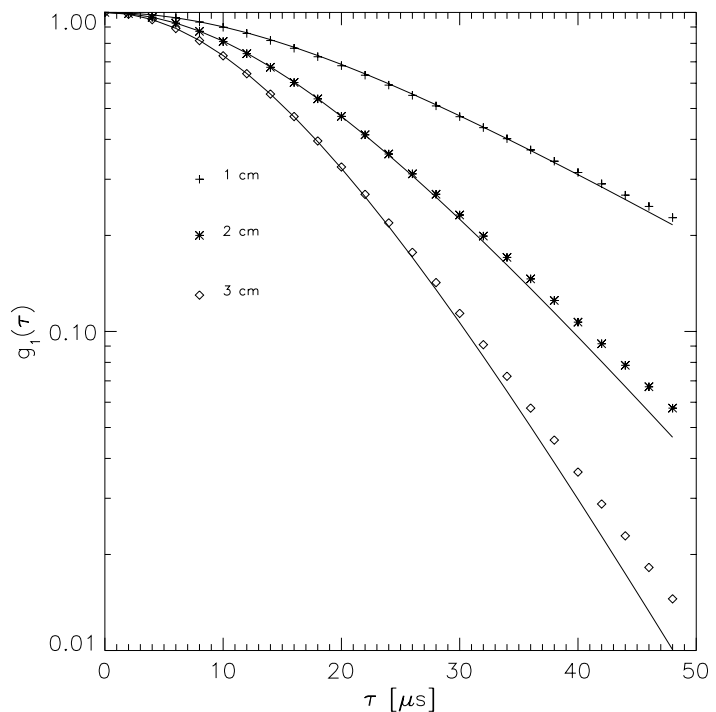


Figure 4.21: Comparison of Monte Carlo simulations and correlation diffusion theory for random flow in a static tissue-like matrix. The probability of scattering from a flow particle (blood) is 0.1.

4.5 Summary

I have shown that the transport of temporal electric field correlation through turbid media can be modeled using a diffusion equation and is thus completely analogous to photon diffusion. The properties of diffusing correlation are thus expected to be similar to the properties of photon diffusion presented in chapter 2. I demonstrated this experimentally by showing that the migration of correlation in a turbid medium with spatially varying dynamical and optical properties can be viewed as a macroscopic scattering of correlation “waves.” This concept was shown in the context of both forward and inverse problems. The inverse problem, otherwise known as image reconstruction methods, offers exciting possibilities for studying dynamical variations in heterogeneous turbid media. In biomedical optics, for example, this approach offers a simple framework for analyzing the complex signals obtained from fluid flow in the body. Two different biomedical applications are discussed in the next chapter.

Chapter 5

Biomedical Applications for Correlation Diffusion

5.1 Blood Flow Monitoring

Near-infrared spectroscopy (NIRS) has long been used to non-invasively measure pulse rate [8, 9, 10] and blood oxygenation [5, 6, 7, 10] and recently to measure blood flow [19, 121]. The advantage of NIRS over laser Doppler blood flowmetry (LDBF) to measure blood flow is that flow in larger volumes of tissue can be monitored. LDBF can only be used to interrogate mm^3 volumes of tissue whereas NIRS can interrogate 1 to 10 cm^3 volumes of tissue. LDBF is restricted to small volumes because quantitative information on blood flow is only available if detected photons have scattered from moving blood cells no more than once. LDBF can be used to quantify blood flow in larger volumes if the blood volume fraction (P_{blood} see eq. (4.53)) is known, however the signal-to-noise is generally prohibitively low for optode separations of 5 mm or larger. The signal-to-noise is limited by the maximum allowed tissue exposure to laser light. ANSI sets this maximum at 0.4 W cm^{-2} at 850 nm for exposures between 10 and 30,000 seconds [122]. NIRS is not restricted in this way since large aperture detectors can be used to collect more diffuse light. However, NIRS methods do make certain assumptions about metabolic activity during blood flow measurements.

After briefly reviewing the NIRS and LDBF methods for measuring blood flow and discussing their shortcomings, I demonstrate the use of correlation diffusion equation as a new tool for quantifying blood flow. This approach is only applicable in the

regime where there have been multiple scattering events from moving particles. As in the case of LDBF, the volume fraction of blood (i.e. P_{blood}) must be known and the signal-to-noise is prohibitively low for optode separations ≥ 5 mm. The advantage of using correlation diffusion analysis over LDBF is that blood flow variations on macroscopic (i.e. ≥ 1 mm) length scales can be quantitatively modeled. In this section I demonstrate the similarity of correlation diffusion to LDBF and in the next section I address the modeling of spatially varying flow.

The concept behind using light to monitor the pulse rate is quite simple. For red light (700-900 nm), the dominate absorber in the body is blood. During a heart beat, the local blood volume increases in the vascular system thus increasing the light absorption. By monitoring fluctuations in the intensity of light that diffuses through the tissue, one is effectively measuring the pulse rate.

Optical measurements of blood oxygen saturation is more sophisticated and relies on spectroscopic differences between oxy- and deoxy- hemoglobin. The absorption spectrum of $\sim 4\%$ hemoglobin is shown in fig. 5.1. Because of the isosbestic point at 800 nm it is possible to measure blood volume independent of oxygenation. The oxygenation is determined by differencing absorption measurements above and below 800 nm [12, 20]. For instance, the absorption coefficients at 780 nm (μ_a^{780}) and 850 nm (μ_a^{850}) are

$$\mu_a^{780} = \varepsilon_{Hb}^{780}[Hb] + \varepsilon_{HbO_2}^{780}[HbO_2], \quad (5.1)$$

$$\mu_a^{850} = \varepsilon_{Hb}^{850}[Hb] + \varepsilon_{HbO_2}^{850}[HbO_2], \quad (5.2)$$

where ε_{Hb}^{780} is the extinction coefficient of deoxy-hemoglobin at 780 nm, $\varepsilon_{HbO_2}^{780}$ is the extinction coefficient of oxy-hemoglobin at 780 nm, etc. The concentrations of deoxy- and oxy-hemoglobin are respectively $[Hb]$ and $[HbO_2]$. The oxygen saturation is given by

$$Y = \frac{[HbO_2]}{[Hb] + [HbO_2]}. \quad (5.3)$$

Solving eq. (5.1) and eq. (5.2) for $[Hb]$ and $[HbO_2]$ we find that the oxygen saturation

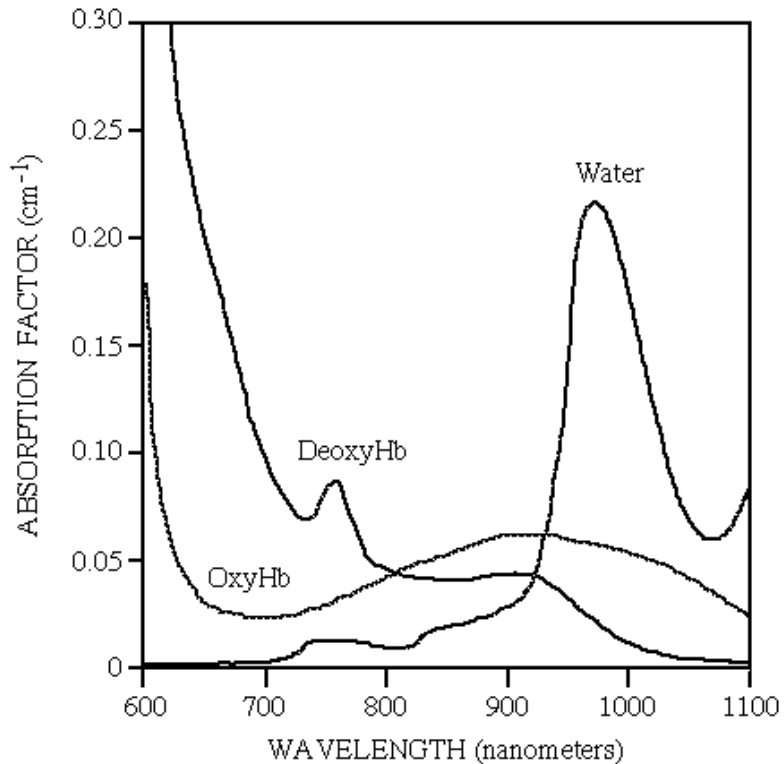


Figure 5.1: The absorption spectra of oxy- and deoxy- hemoglobin are given with that of water. The hemoglobin spectra are given for $\sim 4\%$ whole blood. The comparison with water absorption indicates the dominance of hemo-globin absorption in the near-infrared and water absorption in the infrared. Absorption due to other biologically relevant chromophores contributes less than 10% of that of hemoglobin and water in the displayed wavelength range.

of hemoglobin can be related to μ_a^{780} and μ_a^{850} , i.e.

$$Y = \frac{\mu_a^{850}\varepsilon_{\text{Hb}}^{780} - \mu_a^{780}\varepsilon_{\text{Hb}}^{850}}{\mu_a^{780}\varepsilon_{\Delta\text{Hb}}^{850} - \mu_a^{850}\varepsilon_{\Delta\text{Hb}}^{780}}, \quad (5.4)$$

where $\varepsilon_{\Delta\text{Hb}} = \varepsilon_{\text{HbO}_2} - \varepsilon_{\text{Hb}}$. This method for determining blood oxygen saturation is valid when oxy- and deoxy-hemoglobin are the dominant absorbers. If the absorption by other chromophores is important then the concentration of those other chromophores must also be considered.

NIRS measurements of blood flow derive from Fick's principle and use changes in oxyhemoglobin concentration as an intravascular tracer [19, 121]. Fick's principle states that the rate of accumulation of a tracer is equal to the difference in the rate of arrival and rate of departure of the tracer. If the tracer is oxyhemoglobin then Fick's principle is

$$\frac{\partial}{\partial t}[\text{HbO}_2] = F_{\text{Hb}} \left[[\text{HbO}_2]_+ - [\text{HbO}_2]_- \right], \quad (5.5)$$

where $[\text{HbO}_2]$ is the concentration of oxyhemoglobin, F_{Hb} is the flow of hemoglobin in units of per second, $[\text{HbO}_2]_+$ is the concentration of oxy-hemoglobin arriving, and $[\text{HbO}_2]_-$ is the concentration departing. If a sudden change in the arterial oxygen saturation occurs, the measurement is made before oxygenation change is observed in the venous efflux (i.e. $[\text{HbO}_2]_- = 0$), and during the course of the measurement there is no change in flow, then the hemoglobin flow can be found from

$$F_{\text{Hb}} = \frac{\Delta \text{SaO}_2(t)}{\int_0^t (\Delta \text{SaO}_2(t')) dt'}. \quad (5.6)$$

$\Delta \text{SaO}_2(t)$ is the total change in arterial blood oxygenation saturation at time t relative to a baseline measurement at $t = 0$ before the oxygen tracer is introduced. This quantity can be measured continuously using NIRS, assuming the venous oxygenation is constant. Sudden changes in arterial oxygenation can be induced by changing the oxygen-nitrogen mixture delivered to the subject through a ventilator, and thus eq. (5.6) suggests a straightforward method to measure arterial blood flow using NIRS.

This method has been used to measure arterial blood flow in the forearm [19] and in the brain [121]. The accuracy of the method has been checked by simultaneous

plethysmographic measurements [19]. Plethysmography is the determination of blood flow by measuring the volume increase in an organ during venous occlusion. This NIR method has been fairly successful in well-controlled situations. With the development of diffusing wave optical tomography [13] it may even permit tomographic imaging of flow.

However, the method does have shortcomings which prevent general applicability. First, this approach requires the subject to control his/her respiration either voluntarily or involuntarily through a respirator so that the oxy-hemoglobin tracer can be introduced. Second, the metabolic activity must be stable so that measured oxygen saturation changes can be ascribed to tracer accumulation. These two restrictions limit the conditions under which blood flow can be measured. Although generally ideal for bed-side monitoring, flow cannot be measured during subject activity (such as exercise) which may be required for the diagnosis of different vascular-related diseases. Furthermore, questions have been raised as to whether blood flow is perturbed by the varying blood oxygenation. Finally, independent measurements of flow and oxygenation cannot be correlated to obtain additional physiological information because of the required control of the oxygenation.

Laser Doppler blood flowmetry provides a different approach with different limitations. In laser Doppler blood flowmetry the Doppler shift of light that has scattered from moving particles is used to derive information about blood flow. This method does not place any restrictions on the subject. Therefore measurements can be made under any conditions. With LDBF, laser light is directed to the tissue, through which it scatters, occasionally scattering from a moving red blood cell. It then exits the tissue and is detected by a photo-detector. The beating of Doppler-shifted photons with other shifted and unshifted photons results in a fluctuating intensity at the detector. The power spectrum or temporal autocorrelation function of these fluctuations can be used to determine the flow.

The tissue matrix is static relative to the red blood cells and thus does not significantly contribute to any Doppler shift of the light frequency. The blood volume fraction

is generally smaller than 5% (excluding muscles, liver, and other highly perfused organs which can have a blood volume fraction of up to 20%). Thus photons experience Doppler-shifting events infrequently. If the optode separation is small (<2 mm) then detected photons have generally been Doppler-shifted no more than once. LDBF is thus similar to quasi-elastic light scattering except that the scattering angle of the Doppler scattering event is not known. Since more than 10^6 Doppler shifted photons are generally detected per second, the scattering angle is effectively an average over the differential cross section.

The major shortcoming of LDBF is the poor signal-to-noise ratio for optode separation greater than 5 mm. Once again, the signal-to-noise ratio is limited by the maximum laser exposure that tissue can endure. The lack of signal prevents the non-invasive determination of flow in deep tissues. Another disadvantage of LDBF is that the blood volume fraction (i.e. P_{blood}) must be known in order to quantify flow if multiple scattering events have occurred.

The correlation diffusion equation is the multiple scattering limit of LDBF except that the correlation diffusion equation provides a simple framework for considering systems with spatially varying flow and optical properties. To demonstrate the similarity of diffusing temporal correlation spectroscopy and LDBF, I used it to monitor blood flow in the arm during cuff ischemia. Cuff ischemia refers to the use of a pressure cuff to occlude blood flow in a limb thus preventing the delivery of oxygen to the limb. The measurements clearly show blood flow changes with cuff pressures, including the hyperemic overshoot after cuff release. The blood flow measurements are also correlated with changes in blood volume and blood oxygen saturation that were measured using NIRS. The NIRS and correlation measurements were obtained simultaneously.

The experimental system is diagrammed in fig. 5.2. A Ti:Sapphire laser was used to produce CW 800 nm light. The beam was coupled into a 200 μm multimode fiber ($\text{NA}=0.16$) and delivered to the subject's arm. Remission of the light was collected from the sample by a single-mode fiber in order to observe the intensity fluctuations

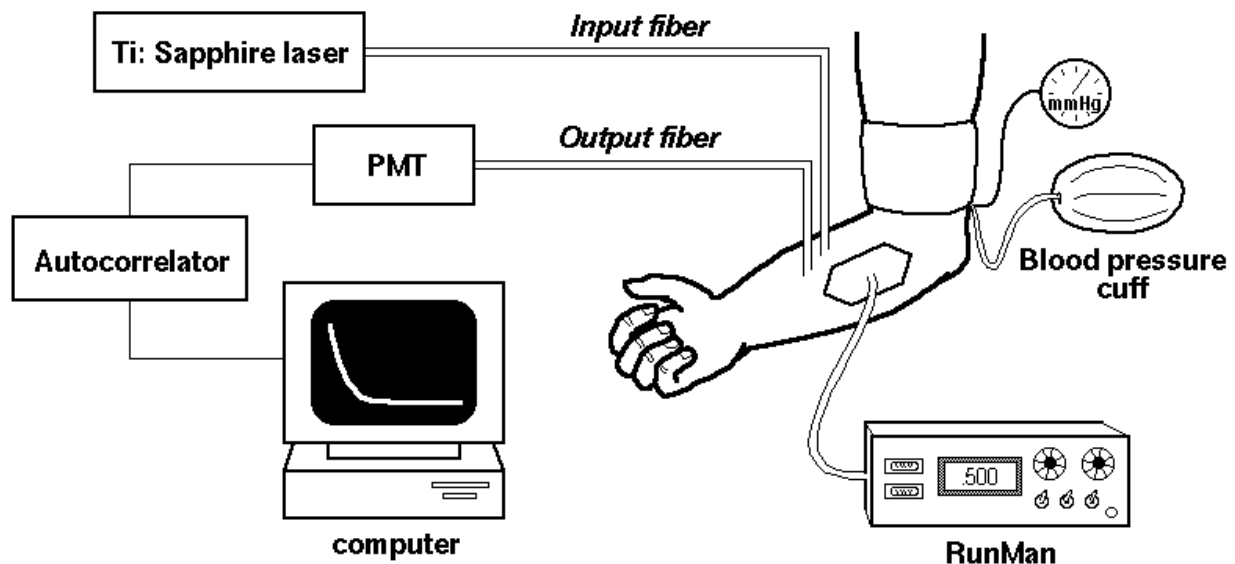


Figure 5.2: Setup for cuff ischemia experiments.

of a single speckle (or mode). The collected light is delivered to a photon-counting photo-multiplier tube (PMT), and the PMT signal is delivered to a digital temporal autocorrelator. Blood volume and oxygenation was measured using a Runman device (NIM Inc., Philadelphia, PA) to measure photon absorption at 760 nm and 850 nm [123]. Each correlation measurement was integrated for 3 minutes while blood volume and oxygenation measurements were gathered continuously. A baseline was measured for the first 18 minutes. The pressure was then quickly raised to 230 mm Hg to simultaneously occlude venous and arterial flow. The response was measured for 12 minutes. The pressure was then released in intervals over the next 15 minutes and measurements made until the flow, volume, and oxygenation returned to normal. These measurements are given in fig. 5.4.

Correlation functions measured during different cuff pressures are shown in fig. 5.3. The decay rate of the correlation function decreases as the cuff pressure is increased. There is a small decrease when the cuff pressure is increased to 50 mm Hg, a large decrease when the cuff pressure is increased to 100 mm Hg, and then a small decrease when the cuff pressure is increased to 150 mm Hg. The large change between

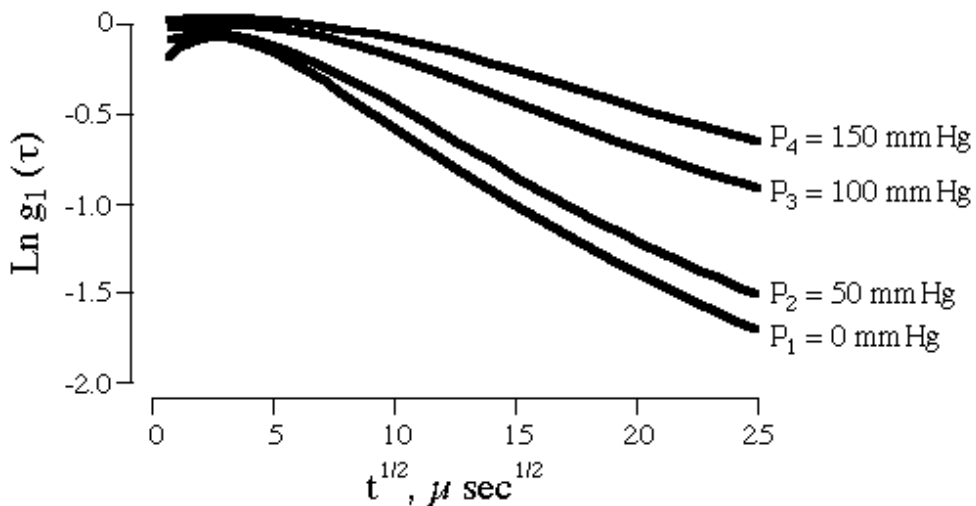


Figure 5.3: The correlation function measured with cuff pressures ranging from 0 mm Hg to 200 mm Hg.

50 mm Hg and 100 mm Hg results from venous occlusion.

During the baseline measurements presented in fig. 5.4, the blood flow, volume, and deoxygenation were found to be constant. During venous and arterial occlusion, the volume did not change but the deoxygenation increased while the flow rapidly decreased. No change in blood volume occurs because blood flow has been abruptly halted, as indicated by the change in flow. The deoxygenation of the blood increases (corresponding to a decrease in oxygenation) because of oxygen delivery to and metabolism by the surrounding cells. When the arteries are opened by dropping the pressure below 150 mm Hg, a significant increase in the blood volume is observed because the arteries are able to deliver more blood to the arm, but at the same time the blood cannot leave because the venous pathways are still occluded. The delivery of fresh blood is also indicated by the drop in blood deoxygenation as well as the increase in blood flow. As the pressure is dropped further the blood volume drops a little because of incomplete venous occlusion allowing blood to leak back to the heart. This notion of leakage is supported by the measured flow increasing as the pressure is decreased. Under normal circumstances the veins remain occluded and the blood volume and flow rate remain fixed until the pressure drops below 80 mm Hg. The observed leakage is

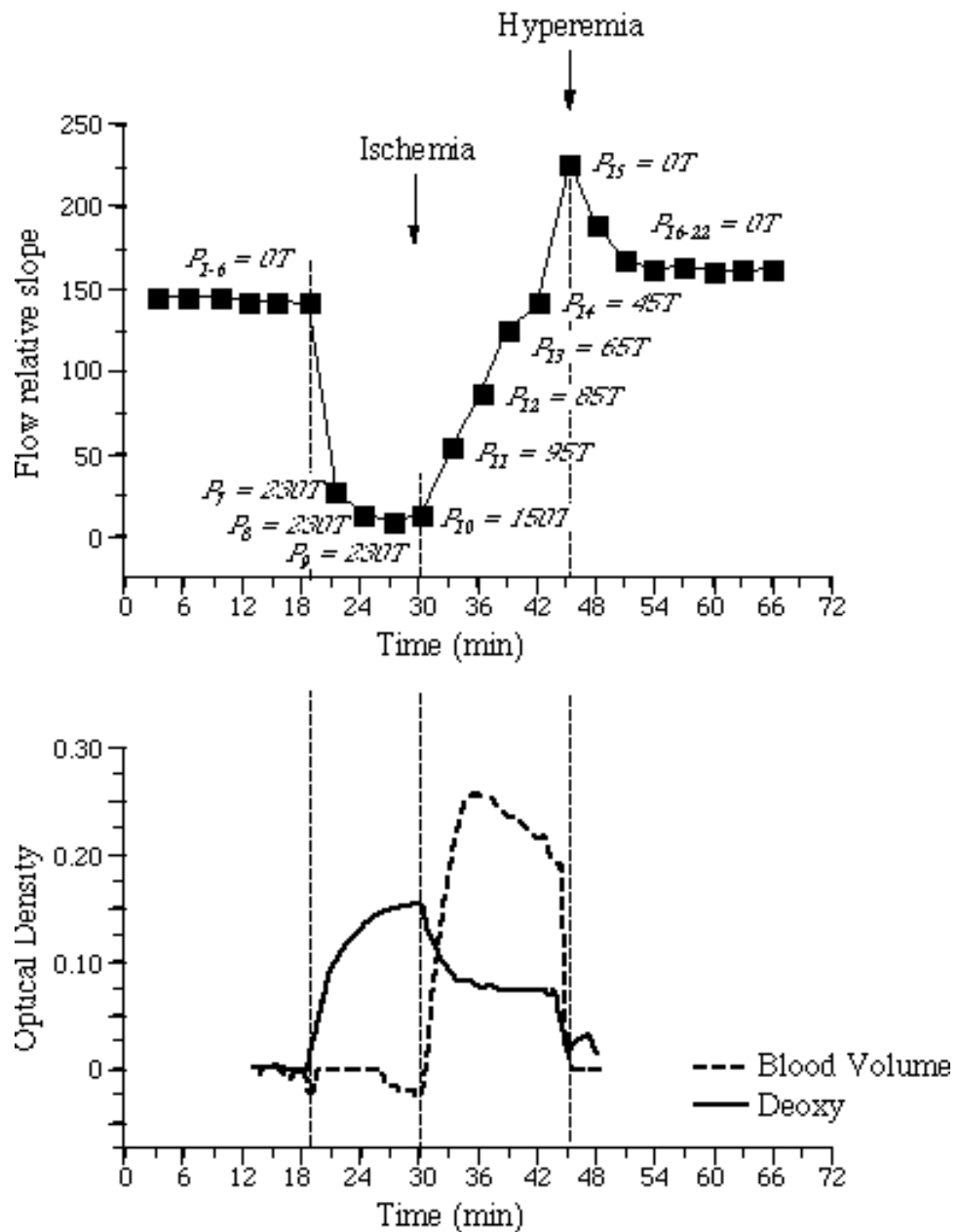


Figure 5.4: The measured decay rate of the correlation function for different cuff pressures applied continuously over an hour is graphed in the top figure. The blood volume and deoxygenation were measured simultaneously and are graphed in the bottom figure.

perhaps a result of our subject's high blood pressure. When the pressure is dropped to zero the blood volume and oxygenation is seen to return to normal but the blood flow first increases above the baseline because of a hyperemic response.

Similar observations have been made using laser Doppler blood flowmetry [124, 125, 126]. In the next section I show how the correlation diffusion spectroscopy can be used to quantify heterogeneous flow.

5.2 Burn Diagnosis

The non-invasive determination of the depth of severe burns has been a tantalizing problem for several years. A robust solution would offer medical practitioners a valuable tool for diagnosing and treating severe burns. Burned tissue is essentially a turbid medium with spatially varying dynamics, i.e. light is multiply scattered by the tissue and layers of burned tissue are characterized by a lack of blood flow, that is, blood flow ceases in severely burned tissue. The dynamical properties of turbid media can be probed by monitoring the temporal fluctuations of the intensities of different speckles emanating from the turbid media. Generally, information on a system's dynamics is obtained from the temporal autocorrelation function of these fluctuations [37, 127, 128]. In chapter 4 I showed that the correlation diffusion equation accurately predicts the temporal correlation function for turbid systems with spatially varying dynamics and that the dynamical properties of such systems can be imaged using reconstruction algorithms based on the correlation diffusion equation [94]. In this section I investigate the sensitivity of temporal field correlation measurements to burn thickness and the applicability of the correlation diffusion equation to absolute determination of burn thickness. Measurements on burn phantoms indicate that $100 \mu\text{m}$ sensitivity is obtainable and that the correlation diffusion equation predicts the observed correlation function fairly well. These positive results motivated animal studies at the Wellman Institute. Our measurements of various burns on a living pig confirm that $100 \mu\text{m}$ sensitivity is achievable.

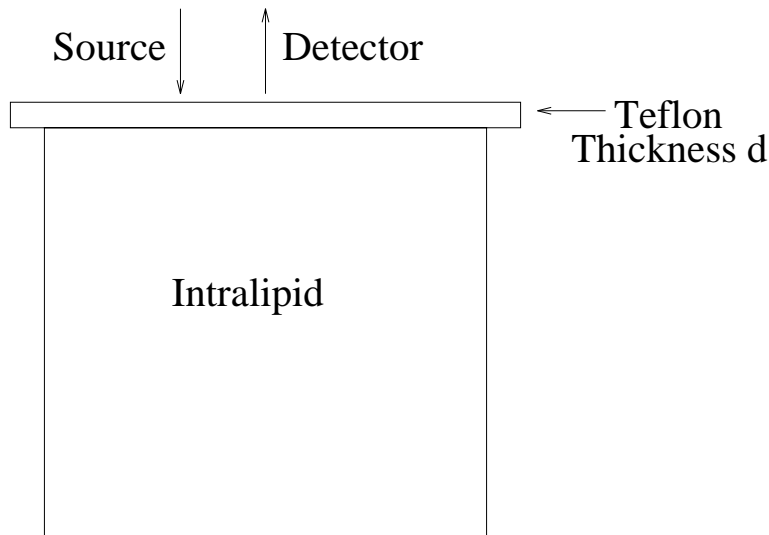


Figure 5.5: Schematic of the burn phantom.

5.2.1 Experiments on Phantoms

The burn phantom is drawn in fig. 5.5. It consists of a layer of teflon resting on a solution of Intralipid. The teflon mimics tissue that has been severely burned in that the teflon scatters light and the scattering particles are static. The Intralipid simulates the scattering and dynamical properties of the healthy tissue underlying the burned tissue. For the teflon $\mu'_s=79 \text{ cm}^{-1}$ and μ_a is negligibly small. A 3.75% solution of Intralipid was used for which $\mu'_s=55 \text{ cm}^{-1}$ and μ_a is negligibly small. For both the teflon and Intralipid solution the absorption was taken to be 0.002 cm^{-1} . The effective Brownian diffusion coefficient of the globules in the Intralipid solution is approximately $10^{-8} \text{ cm}^2\text{s}^{-1}$, as determined from the mean diameter of $0.4 \mu\text{m}$ for the globules. Thicknesses of teflon ranging from 0.132 mm to 0.802 mm are used in the experiments to mimic burns of different depths.

The experimental apparatus for probing the dynamical properties of this burn phantom is diagrammed in fig. 5.6. Two different lasers are used, the 514 nm line of an argon ion laser and a helium-neon laser. The laser is coupled into a multi-mode optical fiber (core diameter $200 \mu\text{m}$). This fiber delivers the light to the phantom. Several single mode fibers are positioned with the source fiber to collect light at

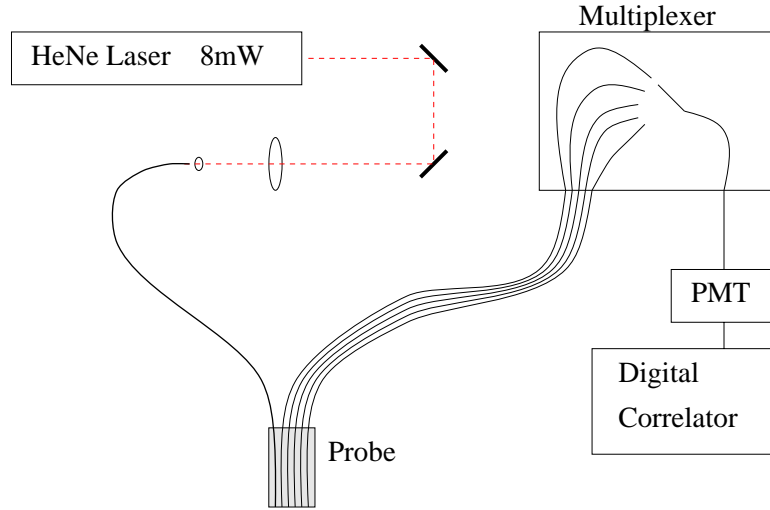


Figure 5.6: Schematic of the experimental setup. Details are given in the text.

distances of 0.2 mm to 2.4 mm from the source. The light collected with the single mode fibers is then delivered to a photon-counting photo-multiplier tube (PMT) and analyzed using a digital temporal autocorrelator. In the experiments presented here, approximately 1 mW of light is incident on the sample and the signal is integrated for 3 minutes. Higher powers are avoided to prevent pulse pile up, i.e. the photon count rate is already at the upper end of the linear response for the PMT. The multi-mode fiber has a numerical aperture of 0.365 and the single mode fibers are designed for 820 nm light. A better signal-to-noise ratio is obtainable by reducing the numerical aperture of the source fiber and using single mode fibers for 514 nm light.

The normalized field correlation function measured for different source-detector separations on the burn phantom with a teflon thickness of 0.65 mm is graphed in fig. 5.7. The decay of the correlation function arises from the dephasing of photons that have traveled different path lengths through the sample. Long path lengths contribute to the decay of the correlation function at short times while short path lengths dominate at long times. For an infinite homogeneous system where the dynamics are governed by Brownian motion, the correlation function decays exponentially as the square-root of the correlation time. This decay would appear as a straight line in fig. 5.7. The

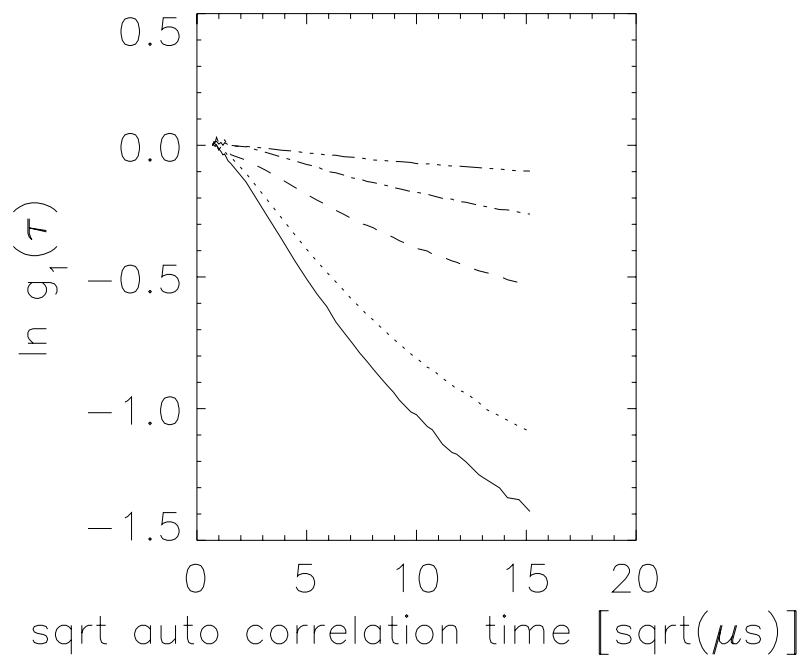


Figure 5.7: The natural log of the normalized field correlation function is plotted versus the square-root of the correlation time for different source-detector separations. The teflon sheet is 0.65 mm. The solid line is for a separation of 2.0 mm and the other lines in order of decreasing slope come from separations of 1.8, 1.2, 0.8, and 0.4 mm.

decay is the same for semi-infinite homogeneous systems except at short times where the decay is inhibited by the loss of long path length photon trajectories. The data presented in fig. 5.7 is nearly linear between 10 and 130 μs . The deviation from linearity at longer times arises from the teflon layer. Specifically, the decay at longer times comes from photons that have traveled short path lengths. In the burn phantom, the short path length photons dwell mostly in the static teflon layer, thus inhibiting the decay of the correlation function.

In addition to the deviation from linearity, the rate of decay in the “linear” region is also perturbed by the presence of the static layer. Fig. 5.8 plots the normalized field temporal correlation function for different teflon thicknesses with a source-detector separation of 1.2 mm. A significant difference is observed in the rates of decay for different teflon thicknesses. Fig. 5.8 indicates that these correlation measurements are sensitive to changes in the teflon thickness smaller than 100 μm .

To summarize the data for all teflon thicknesses and source-detector separations, I plot the slope of the correlation function in the linear region versus source-detector separation for different thicknesses, fig. 5.9a, and versus thickness for different separations, fig. 5.9b. In all cases, the linear region is taken to be between 5 μs and 130 μs .

First consider the slope as a function of source-detector separation for different thicknesses, fig. 5.9a. When no static layer is present, both theory and experiment (not shown) demonstrate that the slope of the correlation function grows linearly with source-detector separation. As seen in fig. 5.9a, the slope *does not* grow linearly with ρ when a static layer of sufficient thickness is present. However when the static layer is sufficiently small (in this case, when $d=0.132$ mm), the slope is observed to increase linearly with ρ . This observed behavior is expected. Photons in general spend a negligible amount of time in the static layer when its thickness is small. The static layer is thus effectively not there and we observe that the slope increases linearly with ρ . For thicker static layers however, photons spend a significant amount of time in the static layer and thus the correlation function does not decay as rapidly. As the source-

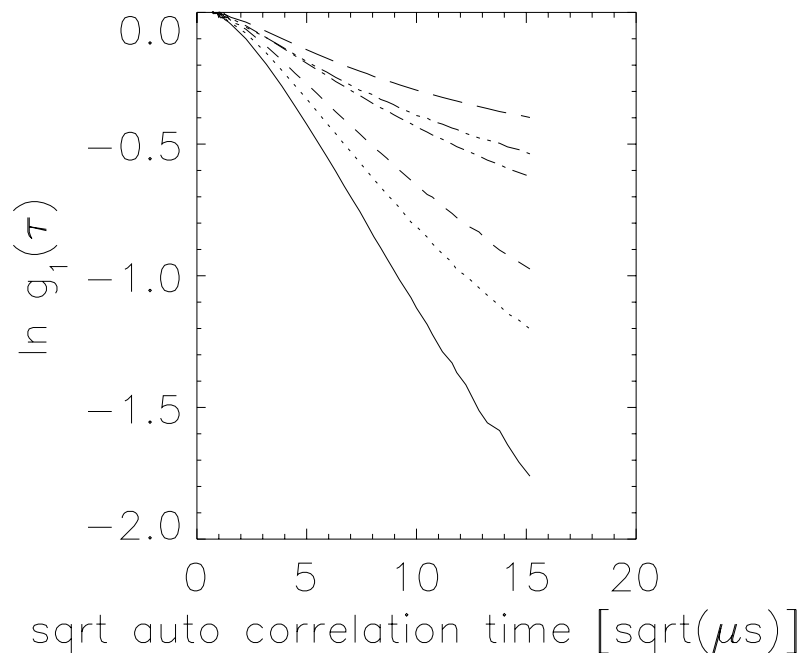


Figure 5.8: The natural log of the normalized field correlation function is plotted versus the square-root of the correlation time for different teflon thicknesses. The source-detector separation was held fixed at 1.2 mm. The solid line is for a thickness of 0.132 mm. The other lines in order of decreasing slope are for thicknesses of 0.258, 0.408, 0.517, 0.650, and 0.802 mm.

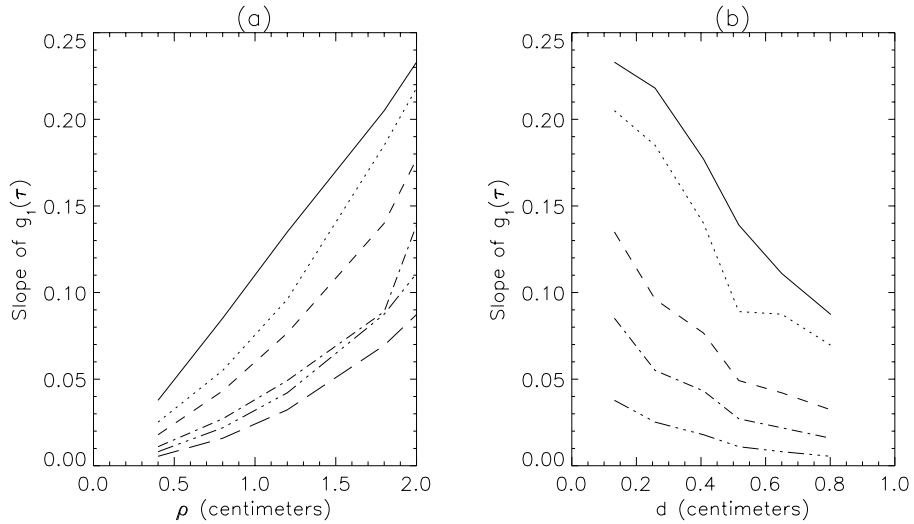


Figure 5.9: Slopes of the experimental data in the nearly linear region between 10 and 130 μs are given versus source-detector separation and teflon thickness. In (a) the slope is plotted versus separation for different thicknesses. The solid line corresponds to a thickness of 0.132 mm, and the other lines moving from the solid line are for thicknesses of 0.258, 0.408, 0.517, 0.650, and 0.802 mm. In (b) the slope is plotted versus teflon thickness for different separations. The solid line corresponds to a separation of 2.0 mm. The other lines, moving from the solid line, are for separations of 1.8, 1.2, 0.8, and 0.4 mm.

detector separation is increased, the photons are spending a smaller percentage of the time in the static layer and thus the slope is seen to increase faster than linear. For larger source-detector separations the slopes are expected to asymptotically approach the value expected for a system with no static layer. This is observed for separations greater than 10 mm when using teflon sheets less than 1 mm thick (not shown).

The slope versus thickness is plotted in fig. 5.9b for different ρ . This graph indicates that the slope decreases rapidly over a short range of thicknesses and that the center of this range depends on the source-detector separation. At smaller thicknesses the slope flattens (as seen for $\rho=2.0$ mm) because the photons dwell mostly in the dynamical region. The slope also flattens at larger thicknesses (as seen for $\rho=0.4, 0.8, \text{ and } 1.2$ mm) since the photons are then spending most of the time in the static region.

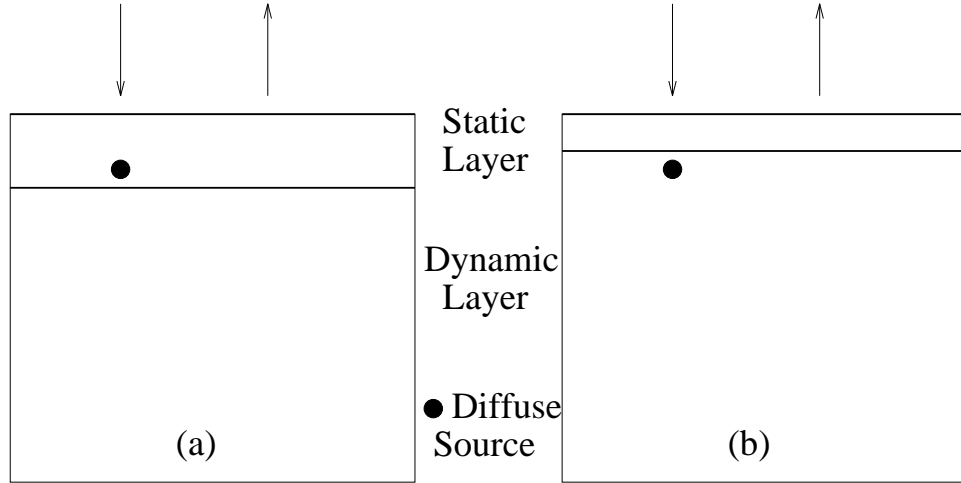


Figure 5.10: (a) and (b) illustrate two possible cases to be considered when obtaining an analytic solution of the diffusion equation for layered media. A collimated source is generally treated as a point diffuse source extended a distance of l^* into the medium. In (a) the thickness of the static layer is greater than l^* . In (b) the thickness of the static layer is smaller than l^* .

The rapid change in the slope occurs when the photons are evenly sampling both regions.

These measurements can be modeled with a solution of the correlation diffusion equation for the system depicted in fig. 5.5. As a reminder the correlation diffusion equation is

$$\left(-D_\gamma \nabla^2 + v\mu_a + 2\mu'_s v D_B k_o^2 \tau \right) G_1(\mathbf{r}, \tau) = v S(\mathbf{r}) . \quad (5.7)$$

Here $G_1(\mathbf{r}, \tau) = \langle E(\mathbf{r}, t) E^*(\mathbf{r}, t + \tau) \rangle$ is the unnormalized temporal electric field auto-correlation function at the position \mathbf{r} within the sample, $D_\gamma = v/(3\mu'_s)$ is the photon diffusion coefficient within the sample, μ'_s is the reduced scattering coefficient, μ_a is the absorption coefficient, and v is the speed of light in the medium. The $\langle \dots \rangle$ denote an ensemble average or, in the case of an ergodic system, an average over time t . D_B is the particle diffusion coefficient within the medium, k_o is the wavenumber of the light in the medium, and τ is the correlation time. The source light distribution is given by $S(\mathbf{r})$.

To solve the diffusion equation, I approximate the collimated source as an isotropic

point source displaced a distance $z_o = 1/\mu'_s$ into the medium along the axis of the collimated source. I also use the approximate extrapolated-zero boundary condition instead of the exact zero-flux boundary condition (partial flux in the case of an index mismatch). For the extrapolated-zero boundary condition, the field correlation is taken to be zero at $z = z_b = -2/(3\mu'_s)$, where the physical boundary is at $z = 0$. The diffusion equation must be solved for two cases: 1) when the point source is in the static layer, and 2) when the point source is displaced into the dynamic region (see fig. 5.10). In the first case, $G_1(\mathbf{r}, \tau)$ measured on the surface of the static layer a distance ρ from the source is given by

$$G_1(\mathbf{r}, \tau) = \frac{\exp(-k_1(\tau)\sqrt{\rho^2 + z_o^2})}{4\pi\sqrt{\rho^2 + z_o^2}} - \frac{\exp(-k_1(\tau)\sqrt{\rho^2 + (z_o + 2z_b)^2})}{4\pi\sqrt{\rho^2 + (z_o + 2z_b)^2}} + \int_0^\infty \lambda d\lambda A(\lambda) J_0(\lambda\rho) \frac{\sin(\sqrt{k_1^2(\tau) - \lambda^2}(z + z_b))}{\sqrt{k_1^2(\tau) - \lambda^2}}. \quad (5.8)$$

Here $k_1^2(\tau) = v^{(1)}\mu_a^{(1)}/D_\gamma^{(1)}$ is the correlation “wavenumber” in the static layer, $J_0(x)$ is a cylindrical Bessel function, and $A(\lambda)$ is a constant that depends on the thickness of the static layer and the properties of the dynamical medium. This constant is

$$A(\lambda) = -[\exp(iX(\lambda)(d - z_o)) - \exp(iX(\lambda)(d + 2z_b + z_o))] \frac{D_\gamma^{(2)}Y(\lambda) - D_\gamma^{(1)}X(\lambda)}{D_\gamma^{(1)}X(\lambda)\cos[X(\lambda)(d + z_b)] - iD_\gamma^{(2)}Y(\lambda)\sin[X(\lambda)(d + z_b)]}, \quad (5.9)$$

$X(\lambda) = \sqrt{k_1^2(\tau) - \lambda^2}$ and $Y(\lambda) = \sqrt{k_2^2(\tau) - \lambda^2}$ where $k_2(\tau) = (v^{(2)}\mu_a^{(2)} + 2v\mu_s'^{(2)}D_B k_o^2 \tau)/D_\gamma^{(2)}$ is the correlation “wavenumber” in the dynamical medium.

The solution for the second case is

$$G_1(\mathbf{r}, \tau) = \frac{\int_0^\infty \lambda d\lambda J_0(\lambda\rho) - 2iD_\gamma^{(2)} \exp(iY(\lambda)(z_o - d)) \sin(X(\lambda)z_b)}{D_\gamma^{(1)}X(\lambda)\cos[X(\lambda)(d + z_b)] - iD_\gamma^{(2)}Y(\lambda)\sin[X(\lambda)(d + z_b)]}. \quad (5.10)$$

Comparisons between experiment and diffusion theory are made in fig. 5.11. The parameters used in the calculation are given in the text discussing fig. 5.5. The

agreement between experiment and theory, although not perfect, is pretty good and certainly captures the trend as a function of source-detector separation and static layer thickness. It is interesting to note that the agreement is better at larger thicknesses where the diffusion theory is expected to be more valid in the static layer. The larger disagreement at smaller thicknesses is most likely a result of the breakdown of the diffusion approximation in the small static layer. In this regime, comparison with a solution of the correlation transport equation [57, 58] would be more appropriate.

As seen from figs. 5.9a and b, measurements of the temporal field correlation function are sensitive to variations of less than 100 μm in the teflon thickness. Furthermore, there is a correspondence between the thickness of the “burn” and the slope of the correlation function versus the source-detector separation (see fig. 5.9a). Burn thickness can thus, in principle, be determined from correlation measurements with an accuracy of better than 100 μm . However, an accurate determination depends on the established correspondence which, in general, is a function of the optical and dynamical properties of the burned tissue. It is thus important to investigate, numerically and experimentally, the dependence of the curves in fig. 5.9a on the optical and dynamical properties. For instance, we might find that a ratio of the slope of the correlation function measured on the burn to that measured over healthy tissue is relatively independent of the optical properties.

Fig. 5.9b suggests that these measurements would be suitable in a feedback loop for controlling an automatic laser ablation system. By first choosing a large source-detector separation such that the sensitivity of the slope of the correlation function to the burn depth is optimized, we can observe the preliminary layers of necrotic tissue being removed. As the burn thickness is decreased, smaller and smaller source-detector separations are monitored to maintain optimal sensitivity. For correlation measurements to be effective in a feedback system, a decent signal must be obtainable in a second. The measurements presented here were integrated for 3 minutes to obtain the best signal-to-noise ratio for presentation purposes. In fact, a sufficient signal-to-noise ratio is achieved after only a few seconds for the parameters used in the phantom

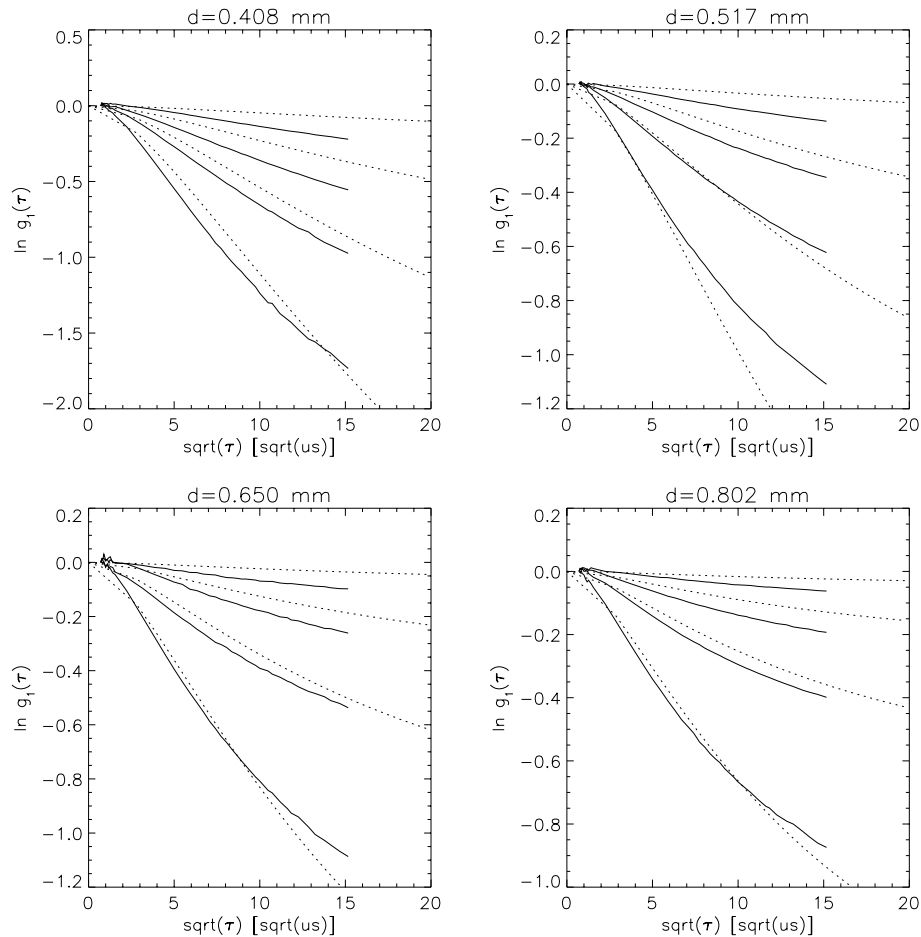


Figure 5.11: Comparisons between the experimental data and that predicted by theory for different thicknesses and separations are given. Each graph shows the results for a particular thickness of teflon. The solid lines are the experimental data and the dotted lines are theoretical. Results for separations of 0.4, 0.8, 1.2, and 1.8 mm are given.

trials. As mentioned, a better signal-to-noise ratio can be achieved by optimizing the fiber optics. In addition, since the photon count rate is so high, analog measurements of the correlation function may be possible. Analog measurements provide a higher duty cycle and thus a better signal-to-noise ratio.

The reduced scattering coefficient of the teflon and Intralipid is approximately 80 cm^{-1} and 50 cm^{-1} respectively. The reduced scattering coefficient for tissue is around 10 cm^{-1} . The absorption of tissue is $\sim 0.05 \text{ cm}^{-1}$. Measurements on tissue may not significantly alter the conclusions, but the accuracy of the correlation diffusion equation on the length scales of interest will be jeopardized because of the smaller reduced scattering coefficient.

The agreement between the correlation diffusion theory and the experimental results is encouraging. This theory will permit measurements of burn thickness to be quantified.

5.2.2 Clinical Work

After verifying with measurements on phantoms that photon correlation techniques are sensitive to differences in thickness of $100 \mu\text{m}$ and that the correlation diffusion equation (eq. (4.22)) can be used to model the correlation function, my next step was to apply the technique clinically. The clinical work was done with Norm Nishioka and Kevin Schomacker at the Wellman Institute in Boston. We used their pig burn model for the clinical trials [129].

This work was made possible by an Army grant to develop and investigate the efficacy of a laser debridement system. Debridement refers to the removal of dead tissue. Their debridement system is operational and is currently being tested with pigs since the skin of pigs closely resembles that of humans. As part of the Army grant, the Wellman Institute has been investigating possible optical feedback techniques for controlling the debridement. The idea is to use an optical technique to identify severely burned tissue and then provide feedback during the debridement process to determine when the severely burned tissue has been completely removed. Diffuse reflectance

Table 5.1: Burn depths were assessed from biopsied tissue using a LDH stain (lactate dehydrogenase). LDH is a vital stain, therefore it will not stain cells which are deadened by the burn.

Duration of Burn (sec)	Burn Depth (μm)
3	60-100 (epidermal)
5	400-500
7	500-600
12	1500-2000
20	2100-2200

[130, 131], fluorescence indicators of blood flow [132, 133], laser doppler [134, 135], and speckle visibility [136] techniques are being considered for this project.

To probe burn depth, we used the same experimental system that I used in the phantom studies (see fig. 5.12). The pig was anesthetized and stabilized on an operating table in an operating suite at the Wellman Institute. Burns were administered using 2 inch square metal blocks brought to 100 °C by boiling water. Burn thickness was controlled by applying the metal block to the skin for a duration of 1 to 20 seconds. For our study, five different burns were examined. The duration and depth of each burn is provided in table 5.1. I measured the correlation function on each burn for source-detector separations ranging from 0.2 mm to 2.4 mm. Measurements were made 48 hours after the administering of the burn.

Prior to burning the tissue, measurements were made at various positions on the skin to determine a baseline. Also, baselines were periodically measured on healthy tissue between measurements of the burned tissue. A set of preburn measurements at a single site is shown in fig. 5.13. Here we see the single exponential decay of the correlation function, and that the decay rate increases linearly with the source-detector

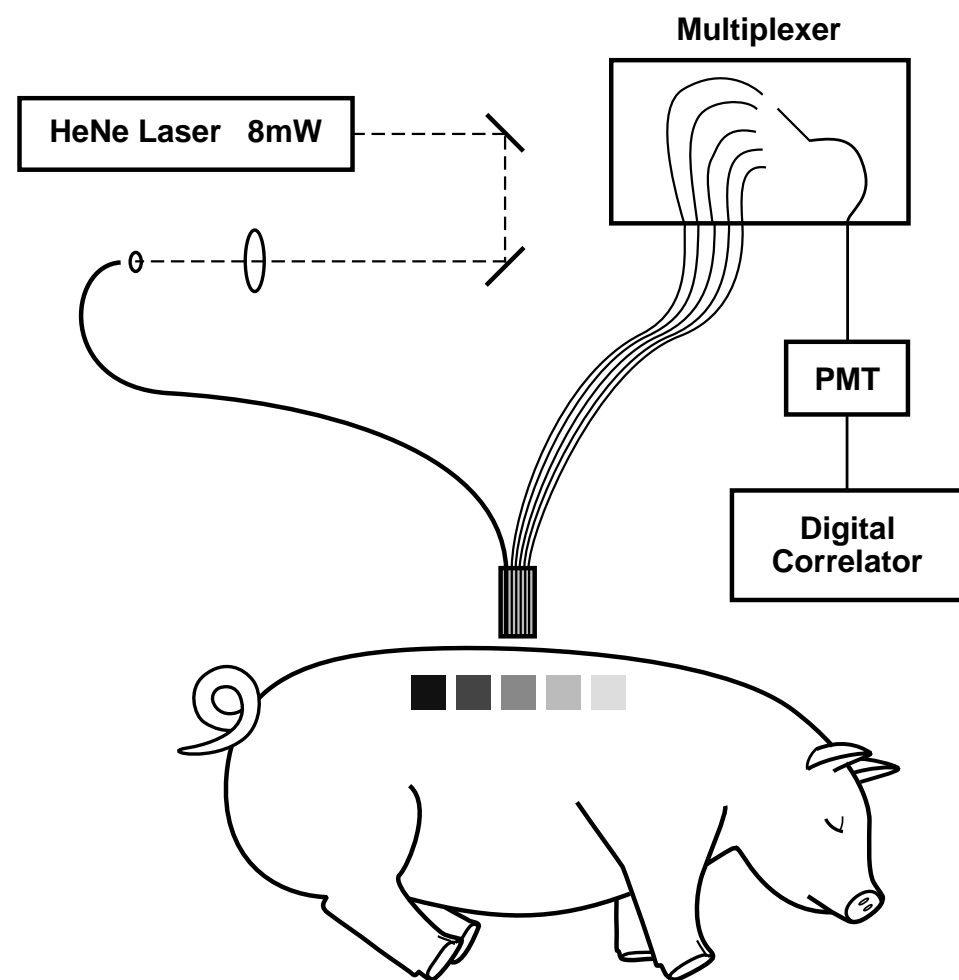


Figure 5.12: Experimental setup for the pig experiments. The shaded areas on the pig indicate burns of various depths.

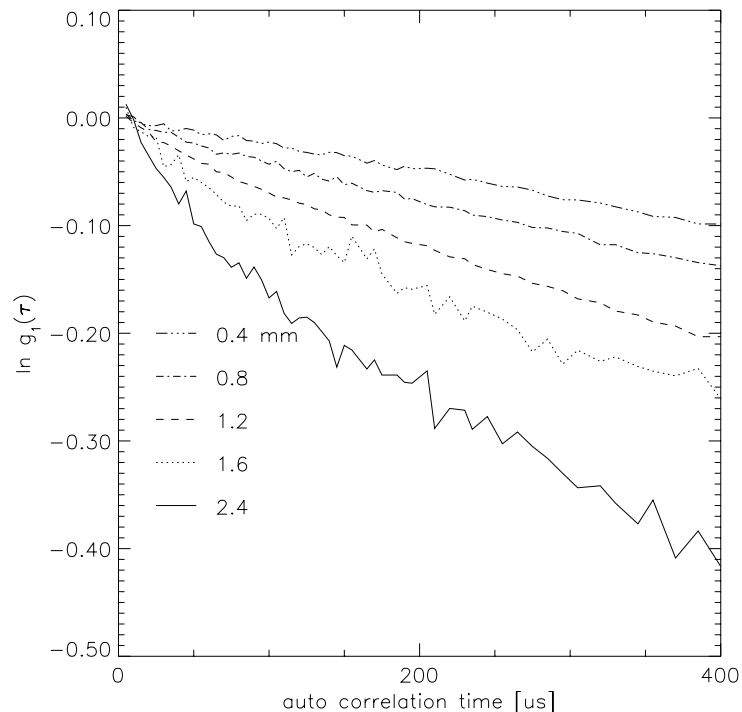


Figure 5.13: Correlation functions at a preburn site for different source-detector separations is presented. The separations are indicated in the legend.

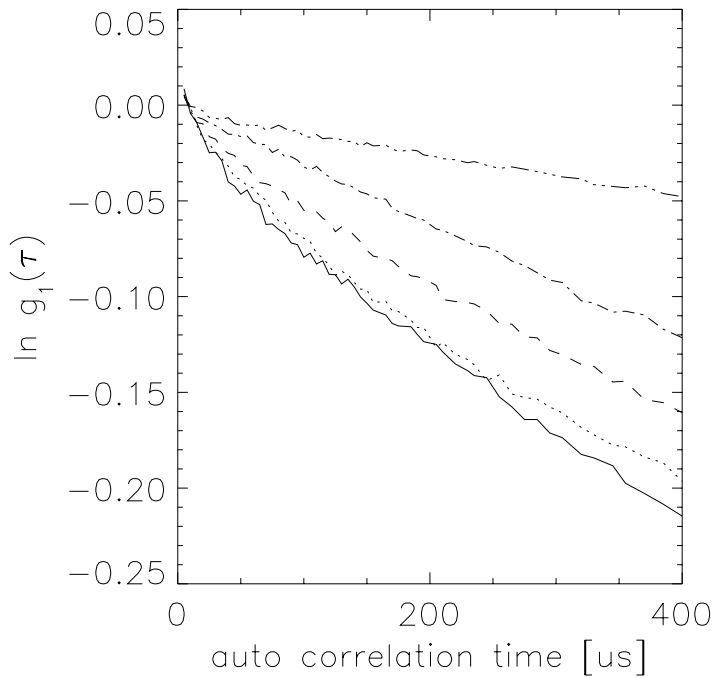


Figure 5.14: The temporal field correlation functions obtained from the 48 hour old burns for a source-detector separation of $800 \mu\text{m}$ are plotted. The correlation functions for the 3 s (solid line), 5 s (dotted line), 7 s (dashed line), 12 s (dot-dash line), and the 20 s (dot-dot-dot-dash line) burns are presented.

separation.

Fig. 5.14 plots the temporal field correlation functions obtained from the 48 hour old burns for a source-detector separation of $800 \mu\text{m}$. As expected, the decay rate of the correlation function decreases as the burn thickness increases. These data indicate that the 5, 7, 12, and 20 second burns are easily distinguished. To summarize the data for all source-detector separations, I determined the decay rate of the correlation function for $0 < \tau < 100 \mu\text{s}$ by fitting a line to the data, and plot the decay rate as a function of source-detector separation for different burns. These results are given in fig. 5.15 and indicate that it is possible to distinguish burns that vary in thickness by only $100 \mu\text{m}$. The behavior of the decay rate is expected. For shallow burns,

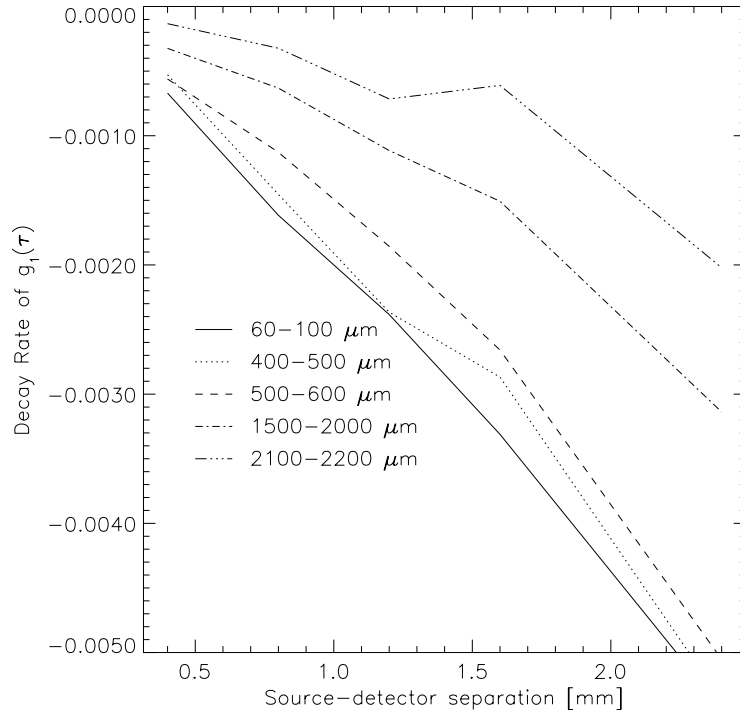


Figure 5.15: The decay rate of the correlation function versus source-detector separation is graphed for different burns. The burn depths are indicated in the legend.

the decay rate increases linearly with the source-detector separation as observed for healthy tissue and expected for a homogeneous system, i.e. the shallow burn does not perturb the correlation function. However, for deeper burns, the decay rate decreases and no longer increases linearly with the source-detector separation.

Our results from this clinical study are encouraging in that they verify that correlation measurements can be used to distinguish burns with thicknesses that vary by 100 μm . More research is needed to quantify the burn thickness from the raw data. The quantification will require knowledge of the optical and dynamical properties of the burn. It should be possible to determine these quantities from the correlation measurements and from diffuse reflectance measurements in the time-domain and/or frequency domain (see chapter 2). This quantification may be simplified by comparing correlation functions between burned and healthy tissue. A ratio of such measurements

may be insensitive to blood flow, thus reducing the number of unknowns in the determination of the burn depth. Finally, the behavior of the burns during the first few hours must be studied more carefully to determine if correlation techniques can be used to diagnose the severity of young burns. To be a suitable diagnostic tool, our technique must be able to characterize burns during the first day, preferably within the first six hours. This research is in progress.

Chapter 6

Experimental Methods

This chapter describes the two different techniques utilized in this dissertation for observing the behavior of diffusing photons in turbid media. In the first, I measure the average intensity and phase of light generated by an intensity modulated source and investigate the properties of the photon density as it diffuses through highly scattering media. Media with and without spatially varying optical properties are considered. In the second, I indirectly measure the temporal fluctuations of diffuse electric fields emanating from highly scattering media. From the time scale of the temporal fluctuations it is possible to derive information about the dynamical properties of the scattering media. Media with spatially varying dynamical and optical properties are considered.

6.1 Measuring Diffuse Photon Density Waves

When photons are introduced into a highly scattering medium, they undergo a random walk. Some photons will scatter only a few times before exiting the system while others will experience a thousand or more scattering events. The average number of scatter events for an infinite homogeneous medium is estimated as $(r/l^*)^2$ where r is the source-detector separation and l^* is the photon random walk step. When the source of photons is intensity modulated at a frequency f , then the photon fluence in the medium will also modulate with a frequency f . This modulation in the photon fluence can be thought as a traveling wave propagating outwards from the source and

is referred to as a diffuse photon density wave (DPDW) [3, 21, 22, 23, 68].

6.1.1 Experimental

The experimental apparatus for generating and detecting these DPDW's is depicted in fig. 6.1. The random medium used to multiply scatter the photons is usually a liquid called Intralipid. Intralipid is an emulsion of water and soy bean fat used for intravenous feeding of hospitalized patients. It is a polydisperse suspension of particles with an average diameter of $\sim 0.4 \mu\text{m}$, but a relatively wide range of sizes (i.e. from $\sim 0.1 \mu\text{m}$ to $\sim 1.1 \mu\text{m}$). The optical properties of Intralipid have been described by others [72, 73, 74]. We purchase our Intralipid from the supply room at the University of Pennsylvania. Other researchers obtain their Intralipid for free by accepting the spoils that are discarded by hospitals. By changing the solution concentration, it is possible to vary the light diffusion coefficient of the medium. The photon random walk step l^* , often referred to as the photon transport mean free path, is about 0.2 cm at 800 nm for a solution of 0.5% Intralipid by volume.

Polystyrene microspheres in suspension are often used as a turbid medium. They can be purchased from Seradyne and Bang Labs. These microspheres are mono-disperse and well characterized so that the scattering lengths can be calculated. We prefer Intralipid over polystyrene because of the price; \$20 per pint compared to \$10 per milliliter. We generally measure the optical properties using our optical technique and therefore don't require the well characterized microspheres. The disadvantage with Intralipid is that it spoils after a few days, much like milk, and it is a breeding ground for bacteria. Also since the scatterer is fat, the scattering properties are temperature dependent.

For the experiments described in chapters 2 and 3, a large tank (30 cm x 30 cm x 60 cm) is typically filled with an Intralipid solution. Source and detector optical fibers (~ 4 mm in diameter) are immersed in the solution at the same height above the tank floor. The fibers are pointed in orthogonal directions to minimize gradient systematics; specifically the detector fiber is perpendicular to the radial vector from

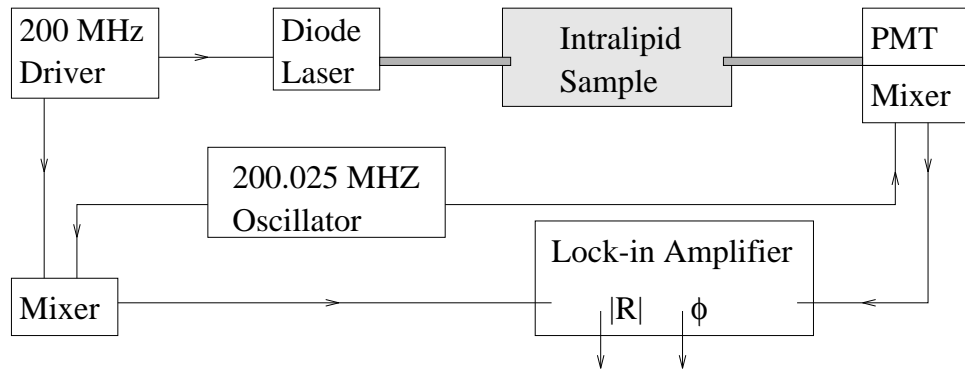


Figure 6.1: A known concentration of Intralipid solution fills a glass tank. The source is a diode laser that is amplitude modulated by a 200 MHz driver. Light is delivered into the sample through a source fiber, and picked up by a movable detector fiber. The fibers are pointed in orthogonal directions to minimize gradient systematics. The signal at the photomultiplier tube (PMT) is heterodyned down to 25 kHz (by modulating the second PMT dynode at 200.025 MHz), and then fed into a lock-in amplifier (Stanford, model #SRS-530). The 25 kHz lock-in reference signal is derived from the 200 MHz driver by standard mixing techniques. The two-phase lock-in amplifier provides amplitude ($|R|$) and phase (ϕ) output signals.

the source fiber.

The source light is derived from a 3 mW diode laser operating at 816 nm. The light is coupled into the source fiber by butting the fiber bundle up to the surface of the laser diode. The source fiber position in the tank is fixed.

Diffuse light is collected with the detector fiber which can be positioned anywhere in a plane parallel to the bottom of the tank by using a home-built translation stage driven by stepper motors (described below). The fiber delivers the collected light to a photo-multiplier tube (PMT). We use an R928 PMT from Hamamatsu. The PMT is modified to facilitate the phase and amplitude measurements. Basically the voltage at the second dynode is modulated at 200.025 MHz. Modified this way, the PMT acts both as a detector and a mixer. The PMT signal thus has a 400.025 MHz modulation and a 25 kHz modulation. We use a notch filter to pick out the 25 kHz signal. A 25 kHz reference is generated from the 200 MHz and 200.025 MHz oscillators by a mixer and low pass filter. The low frequency signals are then measured using

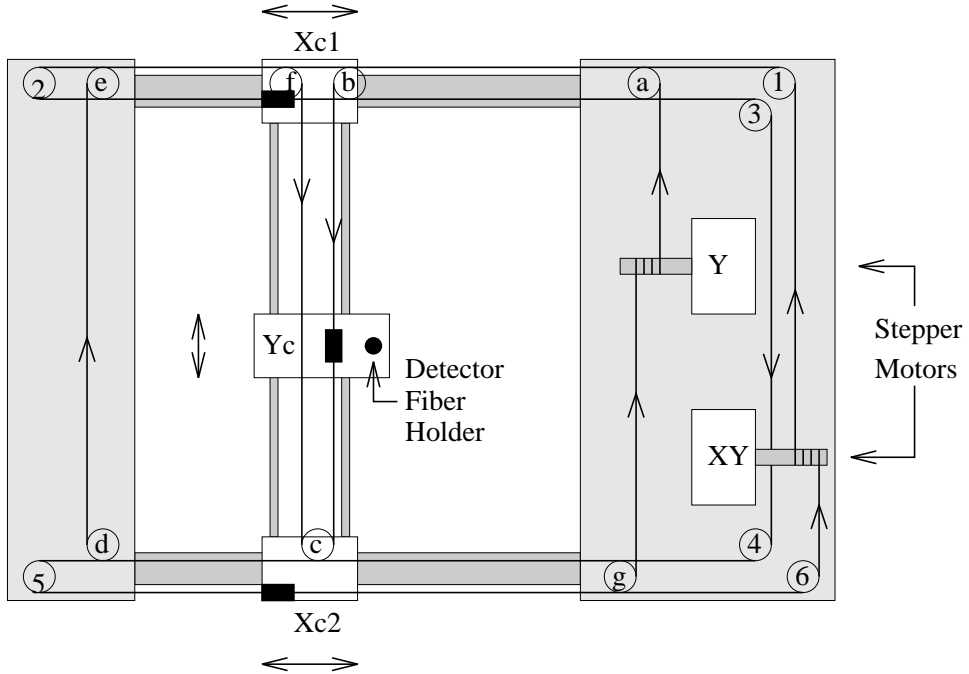


Figure 6.2: Home-made stepper motor-driven translation stage.

a lock-in amplifier (Stanford, model #SRS-530). The phase shift and AC amplitude of the detected light relative to the source are determined by the lock-in amplifier. The dynamic range of this apparatus is about 10^5 . Since the signal amplitude decays by more than $\exp(-2\pi)$ in one DPDW wavelength, the range of the experiments is limited to slightly more than one DPDW wavelength. Nevertheless it is possible to clearly distinguish the essential physical phenomena of diffuse photon density waves.

The stepper motor-driven translation stage is diagrammed in fig. 6.2. The x-axis carriages (Xc1 and Xc2) and the y-axis carriage (Yc) are moved by a wire and pulley system. The wire attached to the y-axis carriage (at the solid block) is drawn by the Y stepper motor. The wire attached to the x-axis carriages (at the solid blocks) is drawn by the XY stepper motor. Because of the wire configuration, the XY motor actually moves the Xc1, Xc2, and Yc carriages. The Y motor only moves the Yc carriage. The Y wire must have the designed configuration in order to permit full motion with a wire of constant length. From the XY motor the wire wraps the pulleys in the following order: 1, 2, 3, 4, 5, and 6. From the Y motor the wire wraps the

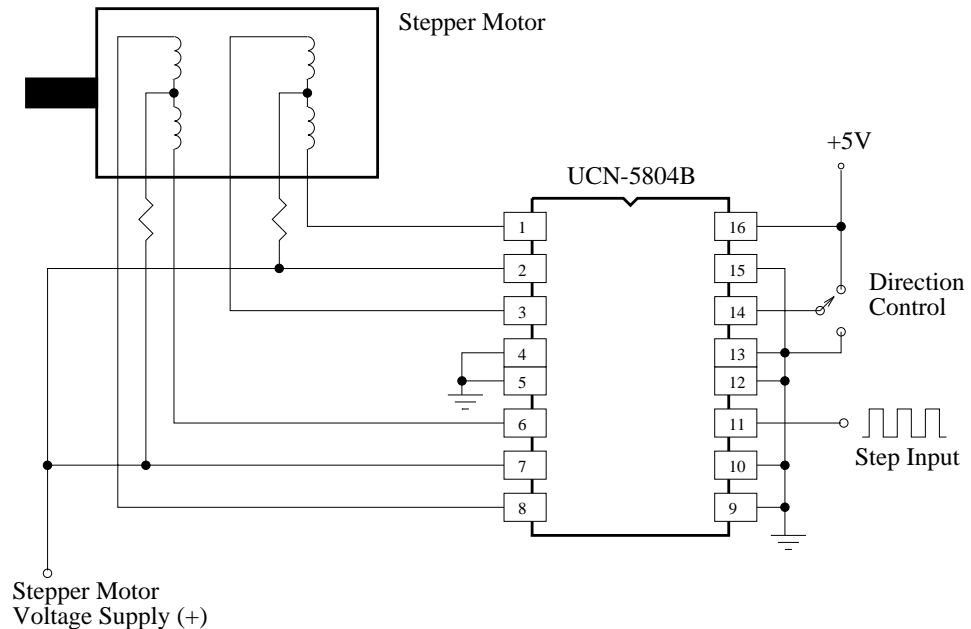


Figure 6.3: Circuit diagram for stepper motor controller. Pin 16 is the logic supply. Pin 15 is the output enable (when set high the chip turns off). Pin 14 is for direction control. Pin 11 is for step control. The chip number is UCN-5804B.

pulleys in the order: a, b, c, d, e, f, c, g. There are two pulleys in position c. All pulleys are on appropriate levels to keep wires from intersecting. The detector fiber is held in place by the Yc carriage.

We use 4-phase stepper motors with 200 steps per revolution. The motors are driven using a specially designed, inexpensive integrated circuit (Herbach and Rademan 1-800-848-8001, H&R # Q5029 \$9.95). A schematic of a simple circuit using this chip for controlling the motor is given in fig. 6.3. The chip requires TTL pulses to advance the motor one step and to control the step direction. These pulses are provided by the parallel port (LPT1) of an IBM clone PC. We use Q-basic to directly assigning values to the parallel port. The base address for LPT1 is 888 (decimal) and the Q-basic command for assigning a value to address 888 is `out 888,n` where `n` is a value between 0 and 255 (see table 6.1) and is the decimal value of the binary word represented at the base address by pins 2 through 9. For example, if you want pins 2 and 3 to be high and 4 through 9 to be low then `n` would be 00000011 in binary which

Table 6.1: Configuration of the parallel port on an IBM-clone PC. The numbers correspond to pins on the 25 pin D-shell parallel port connector. Logic is inverted for numbers with a bar. x means that the bit is not used. The base address for port LPT1 is 888 (decimal). Pins 18-25 are logic ground.

Address	MSB	\leftarrow								LSB	function
base	9	8	7	6	5	4	3	2			output
base + 1	$\overline{11}$	10	12	13	14	x	x	x			input
base + 2	x	x	x	0	$\overline{17}$	16	$\overline{14}$	$\overline{1}$			in/out

is 3 in decimal.

Experiments are performed in several different geometries and are discussed in chapter 2.

In section 2.2 measurements of the propagation of DPDW's in a homogeneous, approximately infinite medium are described. For these measurements, the phase shift and AC amplitude of the detected diffusive wave is measured with respect to the source at each point on a 0.5 cm square planar grid. The measurements are made sufficiently far from the edges of the tank such that the medium could be approximated as being infinite.

In section 2.4 measurements of the refraction and diffraction of DPDW's are described. Experiments include measurements of the refraction by a planar interface between different concentrations of Intralipid and the refraction and diffraction by spherical objects with different optical properties than the surrounding medium. The planar interface is created by a 2 mm thick sheet of acrylic which separated the two different solutions of Intralipid. The spherical objects are created by containing different concentrations of Intralipid and black ink in a 4.0 cm diameter glass bulb. The wall of the glass bulb is approximately 3 mm.

In section 2.5 measurements of the scattering of DPDW's from spherical objects is described. Perfectly absorbing spheres and spheres with different scattering coef-

ficients were measured. The perfectly absorbing spheres are wooden spheres from a hobby shop painted matte black. The scattering spheres are made by suspending titanium dioxide in casting resin and letting it cure in hemispherical molds. Titanium dioxide/resin phantoms have been described in detail by Firbank *et al.* [137, 138] and are briefly discussed in section 6.3.

6.1.2 Monte Carlo

In addition to experimental measurements of DPDW's, I use Monte Carlo simulations of migrating photons to analyze certain properties with a signal-to-noise ratio that is difficult to achieve in the laboratory. Simulations are performed for a point source in an infinite, homogeneous medium. Results are obtained for different source modulation frequencies and medium absorption coefficients. These simulations permit a detailed examination of the breakdown of the photon diffusion approximation and the validity of higher order transport approximations for large photon absorption coefficient and modulation frequencies (see section 2.7).

The Monte Carlo code that I developed comprises only 500 lines of C code, this includes components for spherical objects (see appendix C). The basic idea is to launch N photons into the medium at time $t = 0$ and histogram partial photon flux in radial and temporal channels. For my simulations N is typically 1 million to 10 million and the code takes ~ 2 hours to run on a Sun Sparc 10 Model 512 50MHz processor or a 75 MHz Pentium. Once the temporal response to a pulse is found, a fast Fourier transform of the result into the frequency domain is performed for analyzing the properties of diffuse photon density waves.

There are many techniques for propagating and histogramming photons within Monte Carlo calculations [67, 139, 140]. To keep the code simple I mimic the physical process as closely as possible instead of relying on reduction techniques that purport to increase statistics while reducing computation (see [67, 139, 140] for discussions of different reduction techniques). The algorithm is charted in fig. 6.4. To propagate a photon from one interaction event to the next, the program calculates a scattering

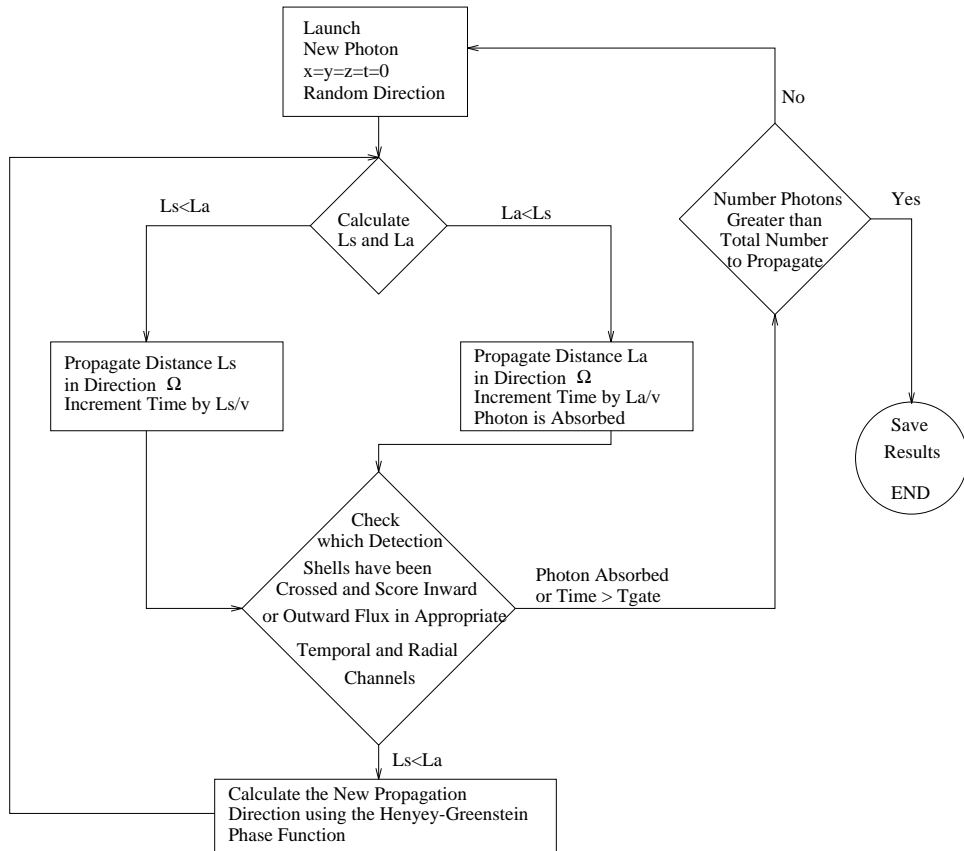


Figure 6.4: Flow chart for Monte Carlo simulations for a point source in infinite homogeneous medium.

length and an absorption length based on the exponential distributions derived from the scattering and absorption coefficients respectively. If the absorption length is shorter than the scattering length, then the photon is propagated the absorption length, scored if necessary, terminated, and a new photon is launched at time $t = 0$ from the source position. If the scattering length is shorter, then the photon is propagated the scattering length, scored if necessary, the scattering angle is calculated based on the Henyey-Greenstein phase function [139, 140, 141], and then a new scattering length and absorption length are calculated. Photon propagation continues until the photon is absorbed, escapes, or the time exceeds a maximum set by T_{gate} .

To exploit the spherical symmetry of the problem (the source is isotropic), spherical shell detectors are centered on the point source and the crossing of photons across each shell is scored in the appropriate temporal and radial channel. The width of each temporal channel is 20 ps. Inward and outward crossings are scored separately so that the Monte Carlo simulation can report the radial components of the photon flux. In this way we can obtain the photon fluence, $\Phi(r)$, and the net photon flux, $-D\nabla\Phi(r)$, from the data. For my analyses I use the photon fluence.

6.2 Photon Correlation Spectroscopy Techniques

Photons scattered by moving particles have their frequency Doppler-shifted by an amount proportional to the particle's speed, the photon's wavenumber, and the scattering angle. The frequency shifts are generally a very small fraction of the absolute frequency, typically ranging from 10^{-9} to 10^{-12} . These relatively small shifts are difficult to measure directly. Instead they are usually determined indirectly by measuring the beating of different frequencies as revealed in the fluctuating intensities of a single coherence area (i.e. speckle) of the scattering light. These fluctuations can be analyzed by looking at the power spectrum or temporal autocorrelation function of the fluctuations. I measure the temporal intensity autocorrelation function of the fluctuating speckles. This method is preferred over measuring the power spectrum for

two reasons. First, the correlation function is the quantity which is derived in the correlation diffusion equation (see chapter 4). Second, using digital correlators and photon counting techniques, it is possible to analyze smaller signals.

There is one major advantage of direct measurements. Indirect measurements of the Doppler broadening of the laser linewidth requires that single (or only a few) coherence areas of scatter light be detected. For systems which multiply scatter light, these coherence areas are on the order of $\sim 1 \mu\text{m}^2$. Small aperture light collectors are thus necessary, resulting in the collection of small numbers of photons. This is not the case for systems which scatter light no more than once since then the coherence area is then given by the laser beam size and coherence length. For direct measurements of Doppler broadening it is not necessary to collect light from a single coherence area and thus the number of photons collected can be increased by at least a factor of 10^3 . Low signal-to-noise ratio applications would benefit from the development of better filters for directly measuring these relatively small Dopper shifts.

6.2.1 Experimental

A schematic of the experimental apparatus for measuring the temporal intensity auto-correlation function (discussed in chapters 4 and 5) of a speckle's intensity fluctuations is presented in fig. 6.5. For the initial experiments, the 514 nm line of an Argon-ion laser (operating with an etalon) is used because of its long coherence length and strong power. In later human subject experiments, the 800 nm line of a Ti-Sapphire laser is used to coincide with the isosbestic point in the absorption spectra of oxy- and deoxy-hemoglobin. For the animal experiments, the 632 nm line of a HeNe laser is used because of its portability. In the future, it will be desirable to utilize laser diodes with stable, single longitudinal mode operation.

The laser beam is coupled into a multimode fiber using a fiber launch system purchased from Thor Labs (part # MDT612). Fibers with core diameters ranging from 50 to 200 μm and various numerical apertures (NA) are used. Generally, for large source-detector separations the diameter and NA are not critical, although

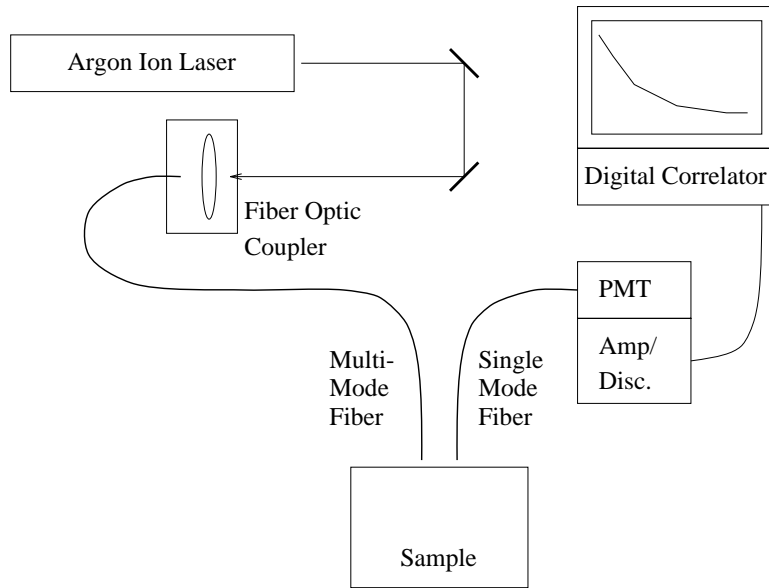


Figure 6.5: Experimental setup for photon correlation spectroscopy.

coupling with the laser beam is easier with large diameters and NA's. For the smaller source-detector separations used on the human subject and animal trials, it is best to use a small NA. This minimizes the divergence of the beam from the output of the fiber to the sample, thus reducing the possibility of detecting light that has reflected at the surface of the sample. For these measurements I use 200 μm core diameter fiber with an NA of 0.16 (Thor Labs FG-200-LAT).

Measurements are made on various samples with many source-detector separations. The source-detector positions are controlled by repositioning the source and detector fibers. Diffuse back reflection is measured from turbid, homogeneous, and solid slabs with either a spherical cavity containing a turbid colloid or a cylindrical vein through which a colloid is pumped. Transmission and reflection measurements are made on solid cylinders with spherical cavities. Human and animal subjects are also employed. These various samples are described in more detail in the appropriate chapters.

Single speckles of the diffuse light emanating from the sample are collected with a single mode fiber. I use different single mode fibers, all from Thor Labs. Basically it is best to use a single mode fiber designed for the wavelength of light to be detected.

Single mode fibers designed for short wavelengths will not propagate the desired longer wavelength thus killing the signal. Single mode fibers designed for longer wavelengths will pass many more modes (speckles) increasing the photon count rate but decreasing the relative magnitude of the fluctuations resulting in a decreased signal-to-noise ratio. This trade-off can be exploited if the photon count rate with the appropriate single mode fiber is near the dark current. The dark current is a constant noise source independent of the photon count rate and thus the signal-to-noise ratio decreases more than expected as the photon count rate approaches the dark current. In this case a better signal-to-noise ratio can be achieved by using a fiber for a longer photon wavelength which increases the photon count rate to a level such that the dark current is insignificant. To be more quantitative we must look at the relative trade-off between a significant dark current associated with the correct single mode fiber and the reduced relative magnitude of the fluctuations associated with using a single mode fiber for a longer wavelength.

A single mode fiber does not actually collect light from a single speckle but from a single spatial mode. Actually the single mode fiber propagates both polarizations so that it is really a dual mode fiber. The difference between observing a speckle and a mode is best demonstrated by comparing the measured correlation function for different distances between the single mode fiber and the sample. Because of the non-zero NA of the single mode fibers, the area from which light is collected increases with the distance between the sample and collecting fiber. The number of observed speckles increases with the collection area and thus the observed intensity fluctuations should decrease relative to the average intensity because of the averaging of uncorrelated, fluctuating speckles. In addition the average intensity should increase. However, the fluctuations are observed not to decrease and the average intensity remains constant. This result, perhaps surprising, arises because a single mode fiber projects the collected light onto a single spatial mode which by definition is coherent. The use of single mode fibers for observing speckles has been discussed by Ricka [142] and Van Keuren *et al.* [143].

The collected light is delivered to a photon counting photo-multiplier tube (Hamamatsu HC120). The dark count is less than 10 counts per second at room temperature. Smaller dark counts are achieved by cooling the PMT to 0°C. After-pulsing can occur for up to 100 ns and the response of the PMT is linear up to 200,000 counts per second. The signal from the PMT is amplified and then discriminated using an amplifier/discriminator package supplied by Brookhaven Instruments Corporation. The TTL signal from the discriminator goes to the digital correlator card housed in a 486 computer. The correlator is from Brookhaven Instruments Corporation (BI9000). To measure correlation functions faster than 200 ns it is necessary to cross-correlate the signal from two PMT's. This is best achieved by using a 50-50 fiber optic beam divider to split the beam between two PMT's and operate the digital correlator in cross-correlation mode.

Since the decay of the correlation function depends on the position of the source and detector relative to the dynamical regions of the sample, it is necessary to optimize the range of correlation times for which data is collected. It is important to choose the minimum correlation time to capture the early time decay. However it is not good to set this minimum arbitrarily low since smaller minimum correlation times reduce the signal-to-noise ratio. The maximum correlation time must be chosen so that the full decay, and thus the baseline, of the correlation function is recorded.

The samples used in my experiments are non-ergodic (a time average is not equal to an ensemble average). As described in the theory section on photon correlation spectroscopy and ergodicity (section 4.2.4), care must be taken with non-ergodic samples in order to obtain repeatable measurements. Basically, for non-ergodic samples each speckle has a constant component and a fluctuating component. The constant component is comprised of photons which have not scattered from any moving particles. The fluctuating component arises from the photons which have scattered from at least one moving particle. If we fix the source and compare speckles in a localized region some distance from the source, then we will see that the fluctuating component is the same from speckle to speckle (the ensemble average equals the time average) but

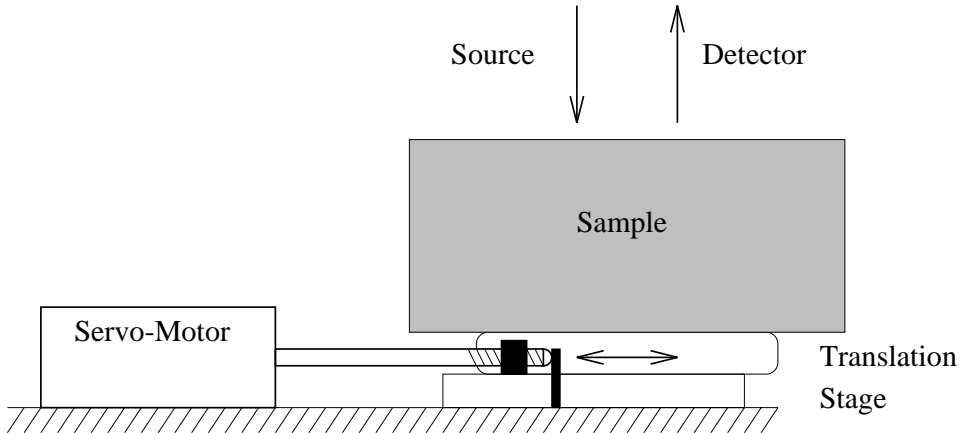


Figure 6.6: Setup for doing the ensemble average.

that the constant component differs (the ensemble average does not equal the time average). This variation in the constant component causes the measured temporal intensity correlation function to vary from speckle to speckle.

In order to measure the proper correlation function it is necessary to ensemble average the signal. I do this by moving the sample (or sometimes the source and detector) during the integration of a correlation function. In this way I measure an ensemble of constant components and thus obtain the desired ensemble average of the speckles' intensity. Moving of the sample affects the correlation function by increasing the observed intensity fluctuation. If the motion is slow enough then the decay of the correlation function due to moving the sample occurs on a time scale that is long compared to the time scale of interest. However, if we move the sample too fast then the ensemble averaging decay overlaps with the decay due to the internal dynamics.

A schematic of the system I use for moving the sample is shown in fig. 6.6. The sample is placed on a translation stage which is driven by a servo-motor. It is important to use a motor which moves smoothly. Stepper motors do not work well because their motion is jerky. This jerky motion results in fast intensity fluctuations which obscure the intensity fluctuations due to the internal dynamics. The speed of the servo-motor is set to move the sample approximately $50 \mu\text{m s}^{-1}$. It is important to ensemble average the signal in a localized area. If we average over too large of an area

then source-detector positions relative to objects in the sample are not well-defined and accurate comparisons with theory cannot be made. I use limit switches on the servo-motor to make it oscillate along a 400 μm path.

6.2.2 Monte Carlo

When the accuracy of my experimental results was questionable or I did not have the experimental data, I used the results from Monte Carlo simulations to check the accuracy of the correlation diffusion equation (see section 4.4). In many cases these simulations provide a signal-to-noise ratio that is difficult to achieve in the laboratory and therefore permit a more accurate test of the validity of the correlation diffusion theory. I run simulations for a point source in an infinite medium. Media with different dynamical properties are considered. I first gather data for a system with spatially uniform Brownian motion. The correlation diffusion equation is known to be valid for this system at short correlation times. Therefore, these first simulations worked as a test for the Monte Carlo code at early correlation times and to demonstrate the breakdown of the diffusion equation at long correlation times.

Next, I ran simulations for a homogeneous solid system containing a spherical region with scatterers undergoing Brownian motion. The optical properties of the spherical region are varied with respect to the background optical properties. These simulations are necessary to unravel systematic discrepancies between experimental data and correlation diffusion theory.

Finally, simulations are executed for a homogeneous system with different volume fractions of random flow. This is a model of tissue blood flow. All simulations are performed assuming isotropic scattering (i.e. $g = 0$).

The theoretical details pertinent to the Monte Carlo simulation are reviewed here. A complete discussion of deriving temporal electric field correlation functions ($g_1(\tau)$) is given in section 4.2. The correlation function of light that scatters once from a

dilute suspension of noninteracting uncorrelated particles is

$$g_1^s(\tau) = \exp\left(-\frac{1}{6}q^2 \langle \Delta r^2(\tau) \rangle\right), \quad (6.1)$$

where $\mathbf{q} = \mathbf{k}_{\text{out}} - \mathbf{k}_{\text{in}}$ is the momentum transfer imparted by the scattering event (see fig. 4.2) and $\langle \Delta r^2(\tau) \rangle$ is the mean square displacement of the scattering particles in time τ . The magnitude of the momentum transfer is $q = 2k_o \sin(\theta/2)$. When photons are multiply scattered by non-interacting uncorrelated particles, the correlation function is computed for a given photon path α with n uncorrelated scattering events as

$$g_1^{(\alpha)}(\tau) = \exp\left(-\frac{1}{6} \sum_{j=1}^n q_{\alpha,j}^2 \langle \Delta r^2(\tau) \rangle\right). \quad (6.2)$$

$q_{\alpha,j}$ is the momentum transfer experienced along path α at scattering site j .

The general procedure for considering multiple paths is to first relate the total dimensionless momentum transfer $Y = \sum_{j=1}^n q_{\alpha,j}^2 / 2k_o^2 = \sum_{j=1}^n (1 - \cos \theta_{\alpha,j})$ to the dimensionless path length $S = s/l^*$. Here s is the length of the photon trajectory through the sample and l^* is the photon random walk step length. For large n , Y is accurately approximated by the average over the scattering form factor and thus

$$Y \approx n \langle 1 - \cos \theta \rangle = \frac{nl}{l^*} = \frac{s}{l^*} = S. \quad (6.3)$$

Here $\langle \dots \rangle$ denotes the average over the scattering form factor and l is the photon scattering length which equals the photon random walk step length when the scattering is isotropic. Next the total correlation function is obtained from the weighted average of eq. (6.2) over the distribution of path lengths, i.e.

$$g_1(\tau) = \int_0^\infty P(S) \exp\left(k_o^2 \langle \Delta r^2(\tau) \rangle S/3\right) . \quad (6.4)$$

Although $P(S)$ can be determined using Monte Carlo simulations, it is usually found with the help of the photon diffusion equation.

This procedure has built into it two assumptions, the relation between Y and S and that $P(S)$ is accurately given by the photon diffusion equation. For the purposes of the Monte Carlo simulations it is desirable to take a different approach that doesn't

make these two assumptions. As suggested by Middleton and Fisher [120] and Durian [119], the total correlation function can be obtained from a weighted average over the total dimensionless momentum transfer experienced by all photon trajectories, i.e.

$$g_1(\tau) = \int_0^\infty P(Y) \exp\left(\frac{1}{3}Yk_o^2 \langle \Delta r^2(\tau) \rangle\right). \quad (6.5)$$

There are no assumptions in this formulation other than the standard noninteracting uncorrelated particles assumption. The drawback is that $P(Y)$ cannot be analytically calculated. However, Monte Carlo simulations provide a simple numerical approach to finding $P(Y)$ for different geometries. Such Monte Carlo simulations are described by Middleton and Fisher [120], Durian [119], and Koelink *et al.* [144].

The Monte Carlo simulation follows the trajectory of a photon using the algorithm described in section 6.1.2 with the addition that the dimensionless momentum transfer Y is incremented in dynamic regions. When the photon reaches a detector, the Y associated with that photon is scored in a $P(Y)$ histogram. After sufficient statistics have been accumulated for $P(Y)$ (typically 1 million to 10 million photons) $g_1(\tau)$ can then be calculated using eq. (6.5).

6.3 Making Resin Phantoms

Intralipid and India ink phantoms are often insufficient. Either a more permanent phantom is required or a system with spatially varying optical properties is desired. These properties are not available with Intralipid phantoms since Intralipid spoils after a few days (very much like milk) and, since it is a liquid, it is necessary to use a physical barrier that perturbs the light field to separate regions with different optical properties. Both of these limitations are overcome with polyester resin phantoms.

Polyester resin phantoms are solid and inert. The scattering and absorption coefficients of the solid can be controlled by mixing different amounts of scatterer (we use titanium-oxide) and dye to the liquid resin before the curing process. The resin can be formed into any shape using an appropriate mold. Optical heterogeneities can be

introduced before or after the curing process. The recipe for making a resin phantom follows.

6.3.1 Recipe for Resin Phantoms

Ingredients

- Polyester Resin (a.k.a. Castin Resin from Creative Wholesale (404)474-2110 \$25 per gallon)
- Catalyst (Creative Wholesale (404)474-2110 \$2)
- Titanium Oxide Powder (TiO_2 from Sigma Chemical Co. (800)325-3010 product # T8141 \$44.20 per kg)
- Dye (ICI plc, product name: Pro jet 900 NP)
- 100% Ethanol

Equipment

- Scale with 1 mg accuracy
- Test tube with a cap
- Sonicator
- Ventilation hood
- Disposable container for mixing resin, titanium oxide, and catalyst
- Molds

Procedure

Warning: all work with polyester resin should be done in a ventilation hood.

- Find an appropriate mold (molds are discussed below).
- Determine the desired value of μ'_s and μ_a for the phantom.
- Weigh 1 mg of TiO_2 powder for every 1 ml of polyester resin to obtain a μ'_s of $\sim 8 \text{ cm}^{-1}$. Put the weighed quantity into a test tube that can be capped.

- Weigh 20 mg of dye for every liter of resin to obtain a μ_a of $\sim 0.1 \text{ cm}^{-1}$. Put the weighed quantity with the TiO_2 .
- Add 100% ethanol to the TiO_2 and dye. Use a volume of ethanol that is 1% to 2% of the volume of resin to be used.
- Stir and then sonicate the mixture. Stir occasionally to re-suspend any clumps that settle to bottom. The mixture needs to be sonicated until the TiO_2 is completely suspended as well as the dye. This takes ~ 15 minutes.
- Pour the desired amount of resin into the mold or a mixing container if the mold is not appropriate for mixing.
- Pour the ethanol, TiO_2 , and dye mixture into the resin.
- Stir until uniform.
- Add catalyst to the resin mixture and stir well. For resin volumes greater than 500 ml use ~ 60 drops of catalyst per liter of resin. For smaller volumes you can use more catalyst, e.g. use 10-20 drops for 100 ml of resin.
- If the resin mixture is not yet in the mold then pour it into the mold.
- Let the sample cure for 12-24 hours in a ventilation hood.
- Remove solid resin sample from mold.
- Machine if desired.

6.3.2 Molds

It is important to choose the right mold for forming the resin sample. The mold has to be made of a material that will not react with resin as it is catalyzed. Furthermore, the mold has to have smooth surfaces so as to release the resin once it has hardened. In our lab, we have found that Tupperware containers, PVC, and teflon make good molds.

We use Tupperware when we want a semi-infinite medium with a flat interface and the shape of the sides and bottom is not important. The flat interface comes from the surface of the resin that is exposed to air. We use sheets of PVC to make rectangular molds when the shape of the edges is important. To make cylindrical molds we use PVC tubing. When making large samples, i.e. volumes greater than 1.5 liters, the resin tends to crack during the curing process. We have found that the large diameter PVC tubing reduces the risk of cracking over rectangular molds. Finally, we use teflon blocks for hemispherical molds to make spheres. The hemispherical molds are drilled in the teflon using ball end mills.

Sometimes it is desirable to make resin phantoms with spatially varying optical properties. There are a couple of techniques for doing so. One approach is to place a previously made solid resin object with different optical properties in the mold for the background medium before curing the background medium. This works well as long as care is taken to stabilize the inserted object and to remove any air bubbles that remain at the liquid-solid interface. Phantoms with capillary networks are easy to make by using teflon tubing in the mold to define the network. The tubes are then easy to remove after the resin has cured provided they don't form too many loops that greatly increase the resistance to being removed. Another approach is to machine the homogeneous phantom after the curing and then introduce media with different optical properties.

6.3.3 Machining

Hardened resin is a soft material that machines well in the lathe, mill, and drill press. Care must be taken with the band saw to prevent binding of the material with the blade. The age-old advice of cutting away small amounts of material, backing up, and repeating is sufficient for successfully using the band saw on hardened resin. I often use the lathe to flatten the face of a resin block or cylinder. I recommend removing no more than 0.020 inches of material per cut. Removing more material will result in divots. Some people prefer to use the mill to make a flat surface, but I find that the

lathe gives a smoother finish. In some instances, however, the sample is too large for the lathe and the mill must be used.

I next describe the technique for making resin samples with spherical cavities (see section 4.3.1). A block with cavity is made by first squaring off the faces of the block. Then I cut 2.2 cm of material off the top of the block, flatten the newly cut surfaces so that the smaller piece is 2.0 cm thick, use a 1 inch ball end mill to cut a hemisphere in the center of each of the two newly flattened surfaces, and drill a 3 mm filling hole through the thicker block to the hemisphere. Next I glue the two pieces together with resin and catalyst. It is necessary to use resin as the glue so as to match the indices of refraction between the two pieces. With other glues the interface is clearly visible indicating that light propagation is severely perturbed by the interface, whereas when using resin as the glue the interface disappears. Note that some glue will seep into the cavity. For this reason I let the glue cure so that gravity will cause seeping resin to flow into the filling hole. I can then remove this material by re-drilling the filling hole after the glue has cured.

A cylinder with a cavity is made in a similar way. First the cylinder is made smooth in the lathe. Then it is cut in half and the two faces are flattened in the lathe. A $\frac{1}{2}$ inch ball end mill is used to cut hemispheres into each piece, a 3 mm filling hole is drilled parallel to the axis of the cylinder, and the two pieces are glued together with resin.

6.3.4 **Warnings**

There are several mistakes that one can make that will ruin the sample. Here I list the ones that I know personally.

Use 100% ethanol to suspend the TiO_2 and dye. Water does not mix with resin, and TiO_2 has a high affinity for water. Therefore if the ethanol contains water, then the TiO_2 will preferentially suspend in the water and separate from the resin while the ethanol easily mixes with the resin. This suggests an interesting demonstration. Prepare identical samples except in one case use 95% ethanol and in the other use 100%.

Another interesting demonstration is to mix just water and resin. This produces a highly scattering emulsion that is stable for days if the volume fraction of water is small enough. Unfortunately this emulsion cannot be hardened.

Incomplete sonication of the TiO₂ and dye will result in an inhomogeneous sample. This warning holds especially for the TiO₂. The sonication breaks large aggregates of TiO₂ into submicron crystallites. Incomplete sonication will leave behind large aggregates which, when mixed with the resin, will quickly settle. In addition, after complete sonication, it is important not to shake or stir the ethanol/TiO₂ mixture since this often leads to aggregation. If the aggregation happens before you have added the TiO₂ to the resin then simply re-sonicate. Note that even under the best of circumstances that some settling of TiO₂ will occur during the curing process. I have not seen deviations in the scattering coefficient from the top of the sample to the bottom of the sample any greater than 10%. This deviation can be minimized by stirring the resin/TiO₂ and catalyst approximately 1 hour after the initial mixing of the resin and catalyst. The quoted optical properties of TiO₂ and dye in resin are only approximate. Therefore the properties should be measured optically once the sample has hardened.

Note that suspending the TiO₂ in the alcohol can be difficult. Add more alcohol if necessary but not more than 5% the volume of resin to be used. If too much ethanol is used then the resin will not harden but will instead become spongy.

We have had difficulty making polyester resin samples that were larger than 1.5 liters because of sample cracking during the curing process. This cracking occurs because the polyester resin has a large exothermic reaction with the catalyst which can result in significant volume changes. Firbank *et al.* have suggested using an epoxy resin which produces less heat during the curing process [138].

Finally, we have observed that x-rays will change the absorption coefficient of the resin. This was found accidentally when an x-ray was taken of a sample in the hospital.

Chapter 7

Summary

Diffusing photons can be used to detect, localize, and characterize optical and dynamical spatial inhomogeneities embedded in turbid media. Measurements of the intensity of diffuse photons reveals information about the optical properties of a system while speckle fluctuations carry information about the dynamical and optical properties. In this dissertation I have shown that simple diffusion theories can be used to accurately model the intensity signals and speckle correlation signals that diffuse through turbid media with spatially varying properties. This work is thus a unification of intensity and speckle probes of turbid media since the analogous theoretical models allow ideas and concepts developed for one probe to be easily applied to the other probe. I have also discussed possible biomedical applications for these techniques.

The photon diffusion equation has an interesting wave solution when the intensity of the light source is sinusoidally modulated. Under these conditions the diffusion equation reduces to a Helmholtz equation. For a point source in an infinite, homogeneous medium the solution is a scalar intensity wave that propagates spherically outwards from the source. The spherical wave has a complex wavenumber that depends on the optical properties and modulation frequency. This spherical wave has been observed and is called a diffuse photon density wave (DPDW).

The theoretical consequence of this solution is that we can neglect the details of the migration of individual photons and instead focus on the behavior of well understood classical, scalar waves. Classical wave theory indicates that waves refract at interfaces

between media with different optical properties (e.g. scattering and absorption in this case and refractive index in the case of ray optics) and are diffracted by absorbing objects.

I experimentally demonstrated the refraction and diffraction of diffuse photon density waves and showed that standard refraction and diffraction models agreed well with observations. I also showed that the interaction of diffuse photon density waves with localized optical inhomogeneities can be treated as a standard scattering problem whereby the wave detected outside of the object is a superposition of the incident and scattered waves. The scattering solution for diffuse photon density waves is analogous to a scalar version of the Mie scattering theory for electromagnetic waves and agrees well with experimental observation.

The photon diffusion equation is not valid if the absorption coefficient is larger than one tenth of the reduced scattering coefficient or if the DPDW modulation frequency approaches or exceeds the scattering frequency (i.e. $v\mu'_s$). I showed that higher order approximations to the radiative transport equation give better agreement with experimental observations under these conditions and that the solutions of these higher order approximations are still DPDW's, but with different functional forms for the wavenumber.

Because the scattering of diffuse photon density waves is understood, inverse scattering algorithms can be developed that permit optical inhomogeneities to be localized and characterized. Using realistic models for the intrinsic noise in a measurement, I performed a detailed signal-to-noise analysis which reveals the limits to the detection, localization, and characterization of optical inhomogeneities. I found that dominant sources of noise are shot noise and noise due to the uncertainties in the positions of the sources, detectors, and objects.

With best case estimates for these noise levels I found that optical inhomogeneities representing breast tumors (e.g. 300% contrast in absorption or 50% contrast in scattering) as small as 3 mm can be detected and localized, but that the size and optical properties of the "tumor" cannot be accurately characterized unless the

diameter exceeds 1 cm. This signal-to-noise analysis can be used to determine the optimal measurement geometry for object characterization, such as determining the best measurement positions and frequencies. The best modulation frequencies are between 0 and 500 MHz. Scattering objects are better characterized with measurements at multiple frequencies while no such gain is obtained for absorbing objects. Measurements close to the object give the strongest object signature, but a spatially distributed set of measurements is required for full characterization.

The optimal spatial extent for the measurements depends in a detailed way on the system parameters and is best determined for each specific case. With full optimization it is possible in a best case scenario to characterize tumors as small as ~ 7 mm embedded in 6 cm of breast tissue. Although this length scale cannot compete with magnetic resonance imaging (MRI) and x-ray mammography, it may still be clinically useful because of its potential for superior specification. Furthermore, there are applications for imaging large scale anomalies such as brain hematomas [15, 145, 146].

The correlation diffusion equation provides a simple framework for predicting and quantifying the speckle correlation functions that are measured on highly scattering systems with spatially varying dynamical and optical properties. Because the correlation diffusion equation is analogous to the photon diffusion equation, all concepts and ideas developed for DPDW's can be directly applied to the diffusion of correlation. I showed experimentally and with Monte Carlo simulations that the diffusion of correlation can be viewed as a correlation wave that propagates spherically outwards from the source and scatters from macroscopic spatial variations in dynamical and/or optical properties. I also demonstrated the utility of inverse scattering algorithms for reconstructing images of the spatially varying dynamical properties of a turbid media.

After laying the theoretical foundation for correlation diffusion, I illustrated its biomedical applicability with examples of monitoring blood flow and probing the depth of burned tissue. Combining diffuse photon and diffuse correlation methods to monitor non-invasively the behavior of blood during venous and arterial occlusion provides useful physiological information. In particular, we saw expected changes in blood

volume, blood oxygen saturation, and blood flow, including hyperemia, during different stages of venous and arterial occlusion. The combination allows us to monitor oxygen delivery and metabolism non-invasively. This technique may be useful for the diagnosis of various vascular diseases such as thrombosis. Correlation diffusion may be used to quantify the depth of severely burned tissue. I demonstrated this application on phantom systems and in the clinic using a pig model. My results indicate that burn thicknesses differing by 100 μm can be distinguished both in phantoms and in the clinic. Furthermore, I found that the correlation diffusion equation accurately predicts experimental measurements on a layered burn model. This suggests that an inversion algorithm could be developed to quantify burn depth clinically. The realization of this goal will require the combined use of diffuse correlation and diffuse photon probes.

In this dissertation I have given a complete account of the theory behind photon diffusion and correlation diffusion, aimed to convince my audience that these diffusion models are accurate for systems with spatially varying properties, and exemplify the application of these diffuse probes to clinical problems. There are bound to be numerous clinical and industrial applications that are yet to be discovered, and I hope that this work stimulates and aids their development.

Appendix A

P_N Approximation Method

I follow the P_N approximation to reduce the general transport equation to a diffusion equation. The method is simply to expand all angular dependent quantities in a spherical harmonic series and truncate the series at the N^{th} moment [54, 55, 56]. I first review the method for the photon transport equation and then apply it to the correlation transport equation.

A.1 Photon Transport Equation

The linear transport equation for photons propagating in media that scatter and absorb photons is [54, 55, 56]

$$\frac{1}{v} \frac{\partial L(\mathbf{r}, \hat{\Omega}, t)}{\partial t} + \nabla \cdot L(\mathbf{r}, \hat{\Omega}, t) \hat{\Omega} + \mu_t L(\mathbf{r}, \hat{\Omega}, t) = \mu_s \int L(\mathbf{r}, \hat{\Omega}', t) f(\hat{\Omega}, \hat{\Omega}') d\hat{\Omega}' + S(\mathbf{r}, \hat{\Omega}, t). \quad (\text{A.1})$$

This equation is described in detail in section 2.1. $L(\mathbf{r}, \hat{\Omega}, t)$ is the radiance at position \mathbf{r} , traveling in direction $\hat{\Omega}$, at time t , with units of $\text{W m}^{-2} \text{ sr}^{-1}$ (sr=steradian=unit solid angle). The normalized phase function is $f(\hat{\Omega}, \hat{\Omega}')$ which represents the probability of scattering into an angle $\hat{\Omega}'$ from angle $\hat{\Omega}$. v is the speed of light in the medium and $\mu_t = \mu_s + \mu_a$ is the transport coefficient where μ_s is the scattering coefficient and μ_a is the absorption coefficient. $S(\mathbf{r}, \hat{\Omega}, t)$ is the spatial and angular distribution of the

source with units of $\text{W m}^{-3} \text{sr}^{-1}$. The photon fluence is given by

$$\Phi(\mathbf{r}, t) = \int d\hat{\Omega} L(\mathbf{r}, \hat{\Omega}, t) , \quad (\text{A.2})$$

while the photon flux, or current density, is given by

$$\mathbf{J}(\mathbf{r}, t) = \int d\hat{\Omega} L(\mathbf{r}, \hat{\Omega}, t) \hat{\Omega} . \quad (\text{A.3})$$

Both the fluence and the flux have units of W m^{-2} .

Within the P_N approximation the radiance and source distribution are expanded as

$$L(\mathbf{r}, \hat{\Omega}, t) = \sum_{l=0}^N \sum_{m=-l}^l \phi_{l,m}(\mathbf{r}, t) Y_{l,m}(\hat{\Omega}) , \quad (\text{A.4})$$

and

$$S(\mathbf{r}, \hat{\Omega}, t) = \sum_{l=0}^N \sum_{m=-l}^l q_{l,m}(\mathbf{r}, t) Y_{l,m}(\hat{\Omega}) . \quad (\text{A.5})$$

The photon fluence $\Phi(\mathbf{r}, t)$ is given by $\phi_{0,0}$ (see eq. (A.19)) and the components of the flux $\mathbf{J}(\mathbf{r}, t)$ are given by $\phi_{1,m}$ (see eq. (A.20)). The $q_{l,m}(\mathbf{r}, t)$ are the amplitudes of the different angular moments of the source at position \mathbf{r} and time t .

For the phase function, we make the reasonable assumption that the probability amplitude is only dependent on the change in direction of the photon and thus

$$\begin{aligned} f(\hat{\Omega} \cdot \hat{\Omega}') &= \sum_{l=0}^{\infty} \frac{2l+1}{4\pi} g_l P_l(\hat{\Omega} \cdot \hat{\Omega}') \\ &= \sum_{l=0}^{\infty} \sum_{m=-l}^l g_l Y_{l,m}^*(\hat{\Omega}') Y_{l,m}(\hat{\Omega}) , \end{aligned} \quad (\text{A.6})$$

where $P_l(x)$ is a Legendre Polynomial and the second line is obtained using the angular addition rule [63]. The phase function is normalized and therefore $g_0 = 1$.

Substituting these expansions into the photon transport equation, eq. (A.1), we obtain

$$\begin{aligned} &\sum_{l=0}^N \sum_{m=-l}^l \left[\left[\frac{1}{v} \frac{\partial}{\partial t} + \hat{\Omega} \cdot \nabla + \mu_t \right] \phi_{l,m}(\mathbf{r}, t) Y_{l,m}(\hat{\Omega}) - q_{l,m} Y_{l,m}(\hat{\Omega}) \right. \\ &\quad \left. - \mu_s \int d\hat{\Omega}' \phi_{l,m}(\mathbf{r}, t) Y_{l,m}(\hat{\Omega}') \sum_{l'=0}^{\infty} \sum_{m'=-l}^l g_{l'} Y_{l',m'}^*(\hat{\Omega}') Y_{l',m'}(\hat{\Omega}) \right] = 0 . \end{aligned} \quad (\text{A.7})$$

Here $\mu_t = \mu_s + \mu_a$ is the transport coefficient. The integral over $\hat{\Omega}'$ is calculated using the orthogonality relation for the spherical harmonics, i.e.

$$\int d\hat{\Omega} Y_{l,m}(\hat{\Omega}) Y_{l',m'}^*(\hat{\Omega}) = \delta_{l,l'} \delta_{m,m'} . \quad (\text{A.8})$$

The transport equation then becomes

$$\sum_{l=0}^N \sum_{m=-l}^l \left[\left[\frac{1}{v} \frac{\partial}{\partial t} + \hat{\Omega} \cdot \nabla + \mu_t^{(l)} \right] \phi_{l,m}(\mathbf{r}, t) - q_{l,m} \right] Y_{l,m}(\hat{\Omega}) = 0 , \quad (\text{A.9})$$

where $\mu_t^{(l)} = \mu_s(1 - g_l) + \mu_a$ is the reduced transport coefficient.

Next, we multiply eq. (A.9) by $Y_{\alpha,\beta}^*(\hat{\Omega})$ and integrate over $\hat{\Omega}$. We can use the orthogonality relation for spherical harmonics (eq. (A.8)) on all the terms except the term with $\hat{\Omega} \cdot \nabla \phi_{l,m}(\mathbf{r}, t)$. The result is

$$\frac{1}{v} \frac{\partial}{\partial t} \phi_{\alpha,\beta} + \mu_t^{(\alpha)} \phi_{\alpha,\beta} + \sum_{l=0}^N \sum_{m=-l}^l \int d\hat{\Omega} \hat{\Omega} \cdot \nabla \phi_{l,m} Y_{l,m}(\hat{\Omega}) Y_{\alpha,\beta}^*(\hat{\Omega}) = q_{\alpha,\beta} . \quad (\text{A.10})$$

The \mathbf{r} and t dependence of $\phi_{l,m}$, and $q_{l,m}$ is assumed.

We now focus on the remaining integral. First take the dot product between $\hat{\Omega}$ and the gradient operator so that we have the components $\hat{\Omega}_x \frac{\partial}{\partial x}$, $\hat{\Omega}_y \frac{\partial}{\partial y}$, and $\hat{\Omega}_z \frac{\partial}{\partial z}$. The components of $\hat{\Omega} Y_{l,m}(\hat{\Omega})$ can be written in terms of spherical harmonics, specifically

$$\begin{aligned} \hat{\Omega}_x Y_{\alpha,\beta}^*(\hat{\Omega}) &= \sin \theta \cos \phi Y_{\alpha,\beta}^*(\hat{\Omega}) \\ &= -\frac{1}{2} \left[\frac{(\alpha + \beta + 1)(\alpha + \beta + 2)}{(2\alpha + 1)(2\alpha + 3)} \right]^{1/2} Y_{\alpha+1,\beta+1}^*(\hat{\Omega}) \\ &\quad + \frac{1}{2} \left[\frac{(\alpha - \beta)(\alpha - \beta - 1)}{(2\alpha - 1)(2\alpha + 1)} \right]^{1/2} Y_{\alpha-1,\beta+1}^*(\hat{\Omega}) \\ &\quad + \frac{1}{2} \left[\frac{(\alpha - \beta + 1)(\alpha - \beta + 2)}{(2\alpha + 1)(2\alpha + 3)} \right]^{1/2} Y_{\alpha+1,\beta-1}^*(\hat{\Omega}) \\ &\quad - \frac{1}{2} \left[\frac{(\alpha + \beta)(\alpha + \beta - 1)}{(2\alpha - 1)(2\alpha + 1)} \right]^{1/2} Y_{\alpha-1,\beta-1}^*(\hat{\Omega}) , \end{aligned} \quad (\text{A.11})$$

$$\begin{aligned} \hat{\Omega}_y Y_{\alpha,\beta}^*(\hat{\Omega}) &= \sin \theta \sin \phi Y_{\alpha,\beta}^*(\hat{\Omega}) \\ &= \frac{1}{2i} \left[\frac{(\alpha + \beta + 1)(\alpha + \beta + 2)}{(2\alpha + 1)(2\alpha + 3)} \right]^{1/2} Y_{\alpha+1,\beta+1}^*(\hat{\Omega}) \end{aligned}$$

$$\begin{aligned}
& -\frac{1}{2i} \left[\frac{(\alpha - \beta)(\alpha - \beta - 1)}{(2\alpha - 1)(2\alpha + 1)} \right]^{1/2} Y_{\alpha-1,\beta+1}^*(\hat{\Omega}) \\
& + \frac{1}{2i} \left[\frac{(\alpha - \beta + 1)(\alpha - \beta + 2)}{(2\alpha + 1)(2\alpha + 3)} \right]^{1/2} Y_{\alpha+1,\beta-1}^*(\hat{\Omega}) \\
& - \frac{1}{2i} \left[\frac{(\alpha + \beta)(\alpha + \beta - 1)}{(2\alpha - 1)(2\alpha + 1)} \right]^{1/2} Y_{\alpha-1,\beta-1}^*(\hat{\Omega}),
\end{aligned} \quad (\text{A.12})$$

$$\begin{aligned}
\hat{\Omega}_z Y_{\alpha,\beta}^*(\hat{\Omega}) &= \cos \theta Y_{\alpha,\beta}^*(\hat{\Omega}) \\
&= + \left[\frac{(\alpha - \beta + 1)(\alpha + \beta + 1)}{(2\alpha + 1)(2\alpha + 3)} \right]^{1/2} Y_{\alpha+1,\beta}^*(\hat{\Omega}) \\
&\quad + \left[\frac{(\alpha - \beta)(\alpha + \beta)}{(2\alpha - 1)(2\alpha + 1)} \right]^{1/2} Y_{\alpha-1,\beta}^*(\hat{\Omega}).
\end{aligned} \quad (\text{A.13})$$

$\hat{\Omega}$ is the direction of the photon where θ and ϕ are respectively the polar and azimuthal angles of the photon direction. These equations are derived with the help of the recurrence relations for associated Legendre polynomials using the Condon-Shortley phase convention. Refer to section 12.9 of Arfken [147] for more details. The book by Rose entitled *Elementary Theory on Angular Momentum* is also helpful [148].

Upon substituting eqs. (A.11)-(A.13) into eq. (A.10) the integral of three spherical harmonics becomes an integral of two spherical harmonics which is easily calculated using the orthogonality relation eq. (A.8). After straight-forward algebra the transport equation finally becomes

$$\begin{aligned}
\frac{1}{v} \frac{\partial}{\partial t} \phi_{\alpha,\beta} + \mu_t^{(\alpha)} \phi_{\alpha,\beta} &= \frac{1}{2} \sqrt{\frac{(\alpha + \beta + 2)(\alpha + \beta + 1)}{(2\alpha + 1)(2\alpha + 3)}} \left(\frac{\partial}{\partial x} + i \frac{\partial}{\partial y} \right) \phi_{\alpha+1,\beta+1} \\
&\quad + \frac{1}{2} \sqrt{\frac{(\alpha - \beta - 1)(\alpha - \beta)}{(2\alpha + 1)(2\alpha - 1)}} \left(\frac{\partial}{\partial x} + i \frac{\partial}{\partial y} \right) \phi_{\alpha-1,\beta+1} \\
&\quad + \frac{1}{2} \sqrt{\frac{(\alpha - \beta + 1)(\alpha - \beta + 2)}{(2\alpha + 1)(2\alpha + 3)}} \left(\frac{\partial}{\partial x} - i \frac{\partial}{\partial y} \right) \phi_{\alpha+1,\beta-1} \\
&\quad - \frac{1}{2} \sqrt{\frac{(\alpha + \beta)(\alpha + \beta - 1)}{(2\alpha + 1)(2\alpha - 1)}} \left(\frac{\partial}{\partial x} - i \frac{\partial}{\partial y} \right) \phi_{\alpha-1,\beta-1} \\
&\quad + \sqrt{\frac{(\alpha + \beta + 1)(\alpha - \beta + 1)}{(2\alpha + 1)(2\alpha + 3)}} \frac{\partial}{\partial z} \phi_{\alpha+1,\beta}
\end{aligned}$$

$$+ \sqrt{\frac{(\alpha + \beta)(\alpha - \beta)}{(2\alpha + 1)(2\alpha - 1)}} \frac{\partial}{\partial z} \phi_{\alpha-1,\beta} = q_{\alpha,\beta} . \quad (\text{A.14})$$

This is a coupled set of linear differential equations for $\phi_{\alpha,\beta}$. The P_N approximation is obtained by neglecting all $\phi_{\alpha,\beta}$ and g_α for $\alpha > N$.

A.1.1 P_1 and Diffusion Approximation

Within the P_1 approximation, the $\alpha = 0$ equation gives

$$\frac{1}{v} \frac{\partial}{\partial t} \phi_{0,0} + \mu_a \phi_{0,0} + \frac{1}{2} \sqrt{\frac{2}{3}} \left[\frac{\partial}{\partial x} - i \frac{\partial}{\partial y} \right] \phi_{1,-1} - \frac{1}{2} \sqrt{\frac{2}{3}} \left[\frac{\partial}{\partial x} + i \frac{\partial}{\partial y} \right] \phi_{1,1} + \sqrt{\frac{1}{3}} \frac{\partial}{\partial z} \phi_{1,0} = q_{0,0} , \quad (\text{A.15})$$

and the $\alpha = 1$ equations give

$$\frac{1}{v} \frac{\partial}{\partial t} \phi_{1,0} + \mu_t^{(1)} \phi_{1,0} + \sqrt{\frac{1}{3}} \frac{\partial}{\partial z} \phi_{0,0} = q_{1,0} , \quad (\text{A.16})$$

$$\frac{1}{v} \frac{\partial}{\partial t} \phi_{1,1} + \mu_t^{(1)} \phi_{1,1} - \frac{1}{2} \sqrt{\frac{2}{3}} \left[\frac{\partial}{\partial x} - i \frac{\partial}{\partial y} \right] \phi_{0,0} = q_{1,1} , \quad (\text{A.17})$$

$$\frac{1}{v} \frac{\partial}{\partial t} \phi_{1,-1} + \mu_t^{(1)} \phi_{1,-1} + \frac{1}{2} \sqrt{\frac{2}{3}} \left[\frac{\partial}{\partial x} + i \frac{\partial}{\partial y} \right] \phi_{0,0} = q_{1,-1} . \quad (\text{A.18})$$

We now transform $\phi_{0,0}$ and the $\phi_{1,m}$'s in eqs. (A.15)-(A.18) into the fluence $\Phi(\mathbf{r}, t)$ and net flux $\mathbf{J}(\mathbf{r}, t)$. The fluence is

$$\Phi(\mathbf{r}, t) = \int d\hat{\Omega} L(\mathbf{r}, \hat{\Omega}, t) = \sum_{l=0}^{\infty} \sum_{m=-l}^l \phi_{l,m} \int d\hat{\Omega} Y_{l,m}(\hat{\Omega}) = \sqrt{4\pi} \phi_{0,0} . \quad (\text{A.19})$$

The $\phi_{1,m}$'s can be gathered in appropriate linear combinations to give the components of the net flux \mathbf{J} . The appropriate linear combinations are obtained from the definition of the net flux (recall eq. (A.3)). They are

$$\begin{aligned} \mathbf{J}(\mathbf{r}, t) &= \int d\hat{\Omega} L(\mathbf{r}, \hat{\Omega}, t) \hat{\Omega} \\ &= \sum_{l=0}^{\infty} \sum_{m=-l}^l \phi_{l,m} \int d\hat{\Omega} [\sin \theta \cos \phi \hat{x} + \sin \theta \sin \phi \hat{y} + \cos \theta \hat{z}] Y_{l,m}(\hat{\Omega}) \end{aligned}$$

$$\begin{aligned}
&= \sqrt{\frac{4\pi}{3}} \sum_{l=0}^{\infty} \sum_{m=-l}^l \phi_{l,m} \int d\hat{\Omega} \left[\sqrt{\frac{1}{2}} (-Y_{1,1}^*(\hat{\Omega}) + Y_{1,-1}^*(\hat{\Omega})) \hat{x} \right. \\
&\quad - i \sqrt{\frac{1}{2}} (+Y_{1,1}^*(\hat{\Omega}) + Y_{1,-1}^*(\hat{\Omega})) \hat{y} \\
&\quad \left. + Y_{1,0}^*(\hat{\Omega}) \hat{z} \right] Y_{l,m}(\hat{\Omega}) \\
&= \sqrt{\frac{4\pi}{3}} \left[\sqrt{\frac{1}{2}} (-\phi_{1,1} + \phi_{1,-1}) \hat{x} - i \sqrt{\frac{1}{2}} (\phi_{1,1} + \phi_{1,-1}) \hat{y} + \phi_{1,0} \hat{z} \right]. \quad (\text{A.20})
\end{aligned}$$

Eqs. (A.15)-(A.18) are thus equivalent to

$$\frac{1}{v} \frac{\partial}{\partial t} \Phi(\mathbf{r}, t) + \mu_a \Phi(\mathbf{r}, t) + \nabla \cdot \mathbf{J}(\mathbf{r}, t) = S_0(\mathbf{r}, t), \quad (\text{A.21})$$

$$\frac{1}{v} \frac{\partial}{\partial t} \mathbf{J}(\mathbf{r}, t) + \mu_t^{(1)} \mathbf{J}(\mathbf{r}, t) + \frac{1}{3} \nabla \Phi(\mathbf{r}, t) = \mathbf{S}_1(\mathbf{r}, t). \quad (\text{A.22})$$

Here $S_0(\mathbf{r}, t)$ and $\mathbf{S}_1(\mathbf{r}, t)$ are respectively the monopole and dipole moments of the source at position \mathbf{r} and time t as defined in eq. (2.8).

Eq. (A.21) and eq. (A.22) constitute the P_1 approximation to the photon transport equation. The derivation of the diffusion equation from these equations is discussed in section 2.1 starting with eq. (2.9) and eq. (2.10), which correspond to eq. (A.21) and eq. (A.22) respectively.

A.1.2 P_3 Approximation

With the P_1 approximation we had four coupled differential equations to decouple. The P_3 approximation will give us 16 coupled differential equations. In general the P_N approximation will have $(N + 1)^2$ coupled differential equations. To simplify the derivation, we can approximate the one-dimensional transport equation, obtain a differential equation for the fluence, and then extend the one-dimensional result to three dimensions. In one-dimension we need only concern ourselves with the $m = 0$ equations and therefore the P_N approximation will have $N + 1$ coupled differential equations. This simplification works because the photon transport equation does not have a preferred direction, and thus all differential operators that appear in the P_N

equations will be symmetric under rotations (e.g. ∇^2 and ∇^4). We can thus transform the one-dimensional equation to a higher dimension equation by replacing $\frac{\partial^{2n}}{\partial z^{2n}}$ to ∇^{2n} where n is an integer and ∇ is the differential operator for the desired dimensional space. In three dimensions $\nabla = \frac{\partial}{\partial x}\hat{x} + \frac{\partial}{\partial y}\hat{y} + \frac{\partial}{\partial z}\hat{z}$. This simplification does not work if the optical properties are spatially varying. In this case, spatial derivatives of the optical properties appear that are not spherically symmetric.

In one dimension the $\alpha = 0$ equation is

$$\frac{1}{v} \frac{\partial}{\partial t} \phi_{0,0} + \mu_a \phi_{0,0} + \sqrt{\frac{1}{3}} \frac{\partial}{\partial z} \phi_{1,0} = q_{0,0} . \quad (\text{A.23})$$

The $\alpha = 1$ equation is

$$\frac{1}{v} \frac{\partial}{\partial t} \phi_{1,0} + \mu_t^{(1)} \phi_{1,0} + \sqrt{\frac{1}{3}} \frac{\partial}{\partial z} \phi_{0,0} + \sqrt{\frac{4}{15}} \frac{\partial}{\partial z} \phi_{2,0} = q_{1,0} . \quad (\text{A.24})$$

The $\alpha = 2$ equation is

$$\frac{1}{v} \frac{\partial}{\partial t} \phi_{2,0} + \mu_t^{(2)} \phi_{2,0} + \sqrt{\frac{4}{15}} \frac{\partial}{\partial z} \phi_{1,0} + \sqrt{\frac{9}{35}} \frac{\partial}{\partial z} \phi_{3,0} = q_{2,0} . \quad (\text{A.25})$$

The $\alpha = 3$ equation is

$$\frac{1}{v} \frac{\partial}{\partial t} \phi_{3,0} + \mu_t^{(3)} \phi_{3,0} + \sqrt{\frac{9}{35}} \frac{\partial}{\partial z} \phi_{2,0} = q_{3,0} . \quad (\text{A.26})$$

We can decouple these equations to find an equation for $\phi_{0,0}$ by back-substitution. First, re-write the equations as

$$\begin{aligned} A\phi_{0,0} + B\phi_{1,0} &= q_{0,0} \\ C\phi_{0,0} + D\phi_{1,0} + E\phi_{2,0} &= q_{1,0} \\ F\phi_{1,0} + G\phi_{2,0} + H\phi_{3,0} &= q_{2,0} \\ I\phi_{2,0} + J\phi_{3,0} &= q_{3,0} . \end{aligned} \quad (\text{A.27})$$

The coefficients A through J are given by eq. (A.23) through eq. (A.26). First multiply the third line by J , switch the order of J and H , and substitute for $J\phi_{3,0}$ from line

4. Transposing J and H is okay since we are assuming the optical properties are spatially uniform. The third line of eq. (A.27) becomes

$$\begin{aligned} JF\phi_{1,0} + JG\phi_{2,0} + HJ\phi_{3,0} &= Jq_{2,0} \\ JF\phi_{1,0} + JG\phi_{2,0} + Hq_{3,0} - HI\phi_{2,0} &= Jq_{2,0} \quad (\text{A.28}) \\ JF\phi_{1,0} + (JG - HI)\phi_{2,0} &= Jq_{2,0} - Hq_{3,0} \end{aligned}$$

Next, multiply the second line of eq. (A.27) by $(JG - HI)$, transpose $(JG - HI)$ and E , and substitute for $(JG - HI)\phi_{2,0}$ from the third line of eq. (A.28). The second line of eq. (A.27) becomes

$$\begin{aligned} (JG - HI)C\phi_{0,0} + (JG - HI)D\phi_{1,0} + E(JG - HI)\phi_{2,0} &= \\ (JG - HI)q_{1,0} \\ (JG - HI)C\phi_{0,0} + (JG - HI)D\phi_{1,0} + EJq_{2,0} - EHq_{3,0} - EJF\phi_{1,0} &= \quad (\text{A.29}) \\ (JG - HI)q_{1,0} \\ (JGC - HIC)\phi_{0,0} + (JGD - HID - EJF)\phi_{1,0} &= \\ (JG - HI)q_{1,0} - EJq_{2,0} + EHq_{3,0} \end{aligned}$$

Finally, multiply the first line of eq. (A.27) by $\mathcal{L} = (JGD - HID - EJF)$, transpose \mathcal{L} and B , and substitute for $\mathcal{L}\phi_{1,0}$ from the third line of eq. (A.29). The first line of

eq. (A.27) becomes

$$\begin{aligned}
& \mathcal{L}A\phi_{0,0} + B\mathcal{L}\phi_{1,0} = \\
& \quad \mathcal{L}q_{0,0} \\
& \mathcal{L}A\phi_{0,0} + (BJG - BHI)q_{1,0} - BEJq_{2,0} + BEHq_{3,0} - (BJGC - BHIC)\phi_{0,0} = \\
& \quad \mathcal{L}q_{0,0} \\
& (JGDA - HIDA - EJFA - BJGC + BHIC)\phi_{0,0} = \\
& (JGD - HID - EJF)q_{0,0} + (BHI - BJJG)q_{1,0} + BEJq_{2,0} - BEHq_{3,0}
\end{aligned} \tag{A.30}$$

Finally, replace the coefficients with their definitions from eq. (A.26), change $\frac{\partial^2}{\partial z^2}$ to ∇^2 and $\frac{\partial^4}{\partial z^4}$ to ∇^4 , and we obtain

$$\left[9\nabla^4 + \beta\nabla^2 + \gamma\right]\phi_{0,0}(\mathbf{r}, \omega) = Wq_{0,0}(\mathbf{r}, \omega) + Xq_{1,0}(\mathbf{r}, \omega) + Yq_{2,0}(\mathbf{r}, \omega) + Zq_{3,0}(\mathbf{r}, \omega), \tag{A.31}$$

where

$$\beta = 90\frac{\omega^2}{v^2} + i\frac{\omega}{v}\left(55\mu_a + 27\mu_t^{(1)} + 35\mu_t^{(2)} + 63\mu_t^{(3)}\right) - \left(27\mu_a\mu_t^{(1)} + 28\mu_a\mu_t^{(3)} + 35\mu_t^{(2)}\mu_t^{(3)}\right) \tag{A.32}$$

$$\gamma = 105\left(-i\frac{\omega}{v} + \mu_a\right)\left(-i\frac{\omega}{v} + \mu_t^{(1)}\right)\left(-i\frac{\omega}{v} + \mu_t^{(2)}\right)\left(-i\frac{\omega}{v} + \mu_t^{(3)}\right). \tag{A.33}$$

The right-hand-side of eq. (A.31) contains the moments of the source distribution where

$$\begin{aligned}
W &= 105\left(-i\frac{\omega}{v} + \mu_t^{(3)}\right)\left(-i\frac{\omega}{v} + \mu_t^{(2)}\right)\left(-i\frac{\omega}{v} + \mu_t^{(1)}\right) - 27\left(-i\frac{\omega}{v} + \mu_t^{(1)}\right)\nabla^2 \\
&\quad - 28\left(-i\frac{\omega}{v} + \mu_t^{(3)}\right)\nabla^2
\end{aligned} \tag{A.34}$$

$$X = 27\sqrt{\frac{1}{3}}\frac{\partial^3}{\partial z^3} - 105\sqrt{\frac{1}{3}}\left(-i\frac{\omega}{v} + \mu_t^{(3)}\right)\left(-i\frac{\omega}{v} + \mu_t^{(2)}\right)\frac{\partial}{\partial z} \tag{A.35}$$

$$Y = 105\sqrt{\frac{4}{45}}\left(-i\frac{\omega}{v} + \mu_t^{(3)}\right)\nabla^2 \tag{A.36}$$

$$Z = 105\sqrt{\frac{36}{3 \cdot 15 \cdot 35}}\frac{\partial^3}{\partial z^3} \tag{A.37}$$

Solutions to the P_3 equation and comparisons with the diffusion equation are made in section 2.7.

A.2 Correlation Transport Equation

The P_N approximation as described for the photon transport equation can be applied to the correlation transport equation with only a few modifications. The correlation transport equation is

$$\nabla \cdot G_1^T(\mathbf{r}, \hat{\Omega}, \tau) \hat{\Omega} + \mu_t G_1^T(\mathbf{r}, \hat{\Omega}, \tau) = \mu_s \int G_1^T(\mathbf{r}, \hat{\Omega}', \tau) g_1^s(\hat{\Omega}, \hat{\Omega}', \tau) f(\hat{\Omega}, \hat{\Omega}') d\hat{\Omega}' + S(\mathbf{r}, \hat{\Omega}). \quad (\text{A.38})$$

Here, $G_1^T(\mathbf{r}, \hat{\Omega}, \tau)$ is the unnormalized temporal field correlation function which is a function of position \mathbf{r} , direction $\hat{\Omega}$, and correlation time τ . The scattering and absorption coefficients are respectively μ_s and μ_a , and $\mu_t = \mu_s + \mu_a$ is the transport coefficient. Furthermore, $g_1^s(\hat{\Omega}, \hat{\Omega}', \tau)$ is the normalized temporal field correlation function for single scattering, $f(\hat{\Omega}, \hat{\Omega}')$ is the normalized differential cross-section, and $S(\mathbf{r}, \hat{\Omega})$ is the source distribution. The scattering coefficient is the reciprocal of the scattering length, $\mu_s = 1/l$, and the absorption coefficient is the reciprocal of the absorption length, $\mu_a = 1/l_a$. The time dependence (not to be confused with correlation time) has been left out of the equation since I am only considering measurements with CW sources. The time dependence can be included by adding a time-derivative of $G_1^T(\mathbf{r}, \hat{\Omega}, \tau)$ (i.e. $v^{-1} \frac{\partial}{\partial t} G_1^T(\mathbf{r}, \hat{\Omega}, \tau)$) to the left-hand side of eq. (A.38).

In analogy to photon transport, the correlation fluence is

$$G_1(\mathbf{r}, t) = \int d\hat{\Omega} G_1^T(\mathbf{r}, \hat{\Omega}, \tau), \quad (\text{A.39})$$

while the correlation flux is given by

$$\mathbf{J}_g(\mathbf{r}, t) = \int d\hat{\Omega} G_1^T(\mathbf{r}, \hat{\Omega}, \tau) \hat{\Omega}. \quad (\text{A.40})$$

The main difference between the correlation transport equation and the photon transport equation is the appearance of $g_1^s(\hat{\Omega}, \hat{\Omega}', \tau)$ in the integral, as discussed in

section 4.2.3. The appearance of this angular dependent quantity will result in integrals of three spherical harmonics which are handled in a fashion similar to the handling of $\hat{\Omega} \cdot \nabla \phi_{l,m}(\mathbf{r}, t)$ in the photon transport equation (see section A.1).

Within the P_N approximation $G_1^T(\mathbf{r}, \hat{\Omega}, \tau)$ and the source distribution are expanded as

$$G_1^T(\mathbf{r}, \hat{\Omega}, \tau) = \sum_{l=0}^N \sum_{m=-l}^l \Gamma_{l,m}(\mathbf{r}, \tau) Y_{l,m}(\hat{\Omega}) , \quad (\text{A.41})$$

and

$$S(\mathbf{r}, \hat{\Omega}) = \sum_{l=0}^N \sum_{m=-l}^l q_{l,m}(\mathbf{r}) Y_{l,m}(\hat{\Omega}) . \quad (\text{A.42})$$

For the phase function, we make the reasonable assumption that the amplitude is only dependent on the change in direction of the photon and thus

$$\begin{aligned} f(\hat{\Omega} \cdot \hat{\Omega}') &= \sum_{l=0}^{\infty} \frac{2l+1}{4\pi} g_l P_l(\hat{\Omega} \cdot \hat{\Omega}') \\ &= \sum_{l=0}^{\infty} \sum_{m=-l}^l g_l Y_{l,m}^*(\hat{\Omega}') Y_{l,m}(\hat{\Omega}) , \end{aligned} \quad (\text{A.43})$$

where P_l is a Legendre Polynomial and the second line is obtained using the angular addition rule [63]. The phase function is normalized and therefore $g_0 = 1$.

The single scattering temporal field correlation function is

$$g_1^s(\hat{\Omega}, \hat{\Omega}', \tau) = \exp\left(-\frac{1}{6}q^2 \langle \Delta r^2(\tau) \rangle\right) = \exp\left(-\frac{1}{3}k_o^2 \langle \Delta r^2(\tau) \rangle (1 - \hat{\Omega} \cdot \hat{\Omega}')\right) , \quad (\text{A.44})$$

where $\langle \Delta r^2(\tau) \rangle$ is the mean square displacement of the scattering particles and $q = 2k_o \sin(\theta/2)$ is the momentum transfer for the scattered photon where θ is the angle between $\hat{\Omega}$ and $\hat{\Omega}'$. For particles undergoing Brownian motion, $\langle \Delta r^2(\tau) \rangle = 6D_B\tau$ where D_B is the Brownian diffusion coefficient. When $\tau \ll (2D_B k_o^2)^{-1}$, then eq. (A.44) is Taylor expanded to

$$\begin{aligned} g_1^s(\hat{\Omega}, \hat{\Omega}', \tau) &= 1 - 2D_B k_o^2 \tau + 2D_B k_o^2 \tau (\hat{\Omega} \cdot \hat{\Omega}') \\ &= 1 - 2D_B k_o^2 \tau + 2D_B k_o^2 \tau \frac{4\pi}{3} \sum_{m=-1}^1 Y_{1,m}^*(\hat{\Omega}') Y_{1,m}(\hat{\Omega}) . \end{aligned} \quad (\text{A.45})$$

The second line is obtained using the angular addition rule [63]. Note that $(2D_B k_o^2)^{-1} \approx 10^{-3}$ s when $D_B = 1 \times 10^{-8}$ cm² s⁻¹ and the wavelength of light is 514 nm.

Substituting these expansions into the correlation transport equation, eq. (A.38), we obtain

$$\sum_{l=0}^N \sum_{m=-l}^l \left\{ \left[\hat{\Omega} \cdot \nabla + \mu_t \right] \Gamma_{l,m}(\mathbf{r}, \tau) Y_{l,m}(\hat{\Omega}) - q_{l,m} Y_{l,m}(\hat{\Omega}) \right. \\ \left. - \mu_s \int d\hat{\Omega}' \Gamma_{l,m}(\mathbf{r}, \tau) Y_{l,m}(\hat{\Omega}') \sum_{l'=0}^N \sum_{m'=-l}^l g_{l'} Y_{l',m'}^*(\hat{\Omega}') Y_{l',m'}(\hat{\Omega}) \right. \\ \left. \left[1 - 2D_B k_o^2 \tau + 2D_B k_o^2 \tau \frac{4\pi}{3} \sum_{m''=-1}^1 Y_{1,m''}^*(\hat{\Omega}') Y_{1,m''}(\hat{\Omega}) \right] \right\} = 0 . \quad (\text{A.46})$$

The integral over $\hat{\Omega}'$ can be calculated for the first two terms between the [...]’s on the third line using the spherical harmonic orthogonality relation (eq. (A.8)). Integrating gives

$$\sum_{l=0}^N \sum_{m=-l}^l \left[\hat{\Omega} \cdot \nabla + \mu_t^{(l)} + g_l k_c \right] \Gamma_{l,m}(\mathbf{r}, \tau) Y_{l,m}(\hat{\Omega}) - q_{l,m} Y_{l,m}(\hat{\Omega}) \\ - k_c \int d\hat{\Omega}' \Gamma_{l,m}(\mathbf{r}, \tau) Y_{l,m}(\hat{\Omega}') \sum_{l'=0}^N \sum_{m'=-l}^l g_{l'} Y_{l',m'}^*(\hat{\Omega}') Y_{l',m'}(\hat{\Omega}) \\ \left[\frac{4\pi}{3} \sum_{m''=-1}^1 Y_{1,m''}^*(\hat{\Omega}') Y_{1,m''}(\hat{\Omega}) \right] = 0 . \quad (\text{A.47})$$

New notation is introduced to simplify eq. (A.47): $\mu_t^{(l)} = \mu_s(1-g_l) + \mu_a$ is the reduced transport coefficient (note $\mu_t^{(0)} = \mu_a$) and $k_c = 2\mu_s D_B k_o^2 \tau$ is a dynamic absorption coefficient.

The $Y_{1,m''}^*(\hat{\Omega}') Y_{l',m'}(\hat{\Omega}')$ and $Y_{1,m''}(\hat{\Omega}') Y_{l',m'}(\hat{\Omega})$ can be rewritten in terms of single spherical harmonics, given (see Arfken section 12.9 [147])

$$Y_{l,m}(\hat{\Omega}) Y_{1,-1}(\hat{\Omega}) = \sqrt{\frac{3}{8\pi}} B_{l+1}^{m-1} Y_{l+1,m-1}(\hat{\Omega}) - \sqrt{\frac{3}{8\pi}} B_l^{-m} Y_{l-1,m-1}(\hat{\Omega}) , \quad (\text{A.48})$$

$$Y_{l,m}(\hat{\Omega}) Y_{1,0}(\hat{\Omega}) = \sqrt{\frac{3}{4\pi}} A_{l+1}^m Y_{l+1,m}(\hat{\Omega}) + \sqrt{\frac{3}{4\pi}} A_l^m Y_{l-1,m}(\hat{\Omega}) , \quad (\text{A.49})$$

$$Y_{l,m}(\hat{\Omega}) Y_{1,1}(\hat{\Omega}) = \sqrt{\frac{3}{8\pi}} B_{l+1}^{-m-1} Y_{l+1,m+1}(\hat{\Omega}) - \sqrt{\frac{3}{8\pi}} B_l^m Y_{l-1,m+1}(\hat{\Omega}) . \quad (\text{A.50})$$

The coefficients A_l^m and B_l^m are given by

$$A_l^m = \left(\frac{(l-m)(l+m)}{(2l-1)(2l+1)} \right)^{1/2} \quad (\text{A.51})$$

$$B_l^m = \left(\frac{(l-m)(l-m-1)}{(2l-1)(2l+1)} \right)^{1/2} \quad (\text{A.52})$$

The product of spherical harmonics in the integral of eq. (A.47) can be rewritten as

$$\begin{aligned} & \frac{4\pi}{3} \sum_{l'm'} g_{l'} Y_{l'}^{m'*}(\hat{\Omega}') Y_{l'}^{m'}(\hat{\Omega}) \sum_{m''=-1}^1 Y_1^{m''*}(\hat{\Omega}') Y_1^{m''}(\hat{\Omega}) \\ &= \frac{4\pi}{3} \sum_{l'm'} g_{l'} \left\{ \right. \\ & + \frac{3}{8\pi} \left[B_{l'+1}^{m'-1} Y_{l'+1}^{m'-1*}(\hat{\Omega}') - B_{l'}^{-m'} Y_{l'-1}^{m'-1*}(\hat{\Omega}') \right] \left[B_{l'+1}^{m'-1} Y_{l'+1}^{m'-1}(\hat{\Omega}) - B_{l'}^{-m'} Y_{l'-1}^{m'-1}(\hat{\Omega}) \right] \\ & + \frac{3}{4\pi} \left[A_{l'+1}^{m'} Y_{l'+1}^{m'*}(\hat{\Omega}') + A_{l'}^{m'} Y_{l'-1}^{m'*}(\hat{\Omega}') \right] \left[A_{l'+1}^{m'} Y_{l'+1}^{m'}(\hat{\Omega}) + A_{l'}^{m'} Y_{l'-1}^{m'}(\hat{\Omega}) \right] \\ & - \frac{3}{8\pi} \left[B_{l'+1}^{-m'-1} Y_{l'+1}^{m'+1*}(\hat{\Omega}') - B_{l'}^{m'} Y_{l'-1}^{m'+1*}(\hat{\Omega}') \right] \left[B_{l'+1}^{-m'-1} Y_{l'+1}^{m'+1}(\hat{\Omega}) - B_{l'}^{m'} Y_{l'-1}^{m'+1}(\hat{\Omega}) \right] \\ & \left. \right\} \end{aligned} \quad (\text{A.53})$$

Doing the final integral over $\hat{\Omega}'$ we obtain

$$\begin{aligned} & \sum_{l=0}^N \sum_{m=-l}^l \left[\hat{\Omega} \cdot \nabla + \mu_t^{(l)} + g_l k_c \right] \Gamma_{l,m}(\mathbf{r}, \tau) Y_{l,m}(\hat{\Omega}) - q_{l,m} Y_{l,m}(\hat{\Omega}) \\ & - k_c \Gamma_{l,m} \frac{4\pi}{3} \left\{ \right. \\ & + \frac{3}{8\pi} g_{l-1} B_l^m \left[B_l^m Y_l^m(\hat{\Omega}) - B_{l-1}^{-m-1} Y_{l-2}^m(\hat{\Omega}) \right] \\ & - \frac{3}{8\pi} g_{l+1} B_{l+1}^{-m-1} \left[B_{l+2}^m Y_{l+2}^m(\hat{\Omega}) - B_{l+1}^{-m-1} Y_l^m(\hat{\Omega}) \right] \\ & + \frac{3}{4\pi} g_{l-1} A_l^m \left[A_l^m Y_l^m(\hat{\Omega}) + A_{l-1}^m Y_{l-2}^m(\hat{\Omega}) \right] \\ & + \frac{3}{4\pi} g_{l+1} A_{l+1}^m \left[A_{l+2}^m Y_{l+2}^m(\hat{\Omega}) + A_{l+1}^m Y_l^m(\hat{\Omega}) \right] \\ & - \frac{3}{8\pi} g_{l-1} B_l^{-m} \left[-B_l^{-m} Y_l^m(\hat{\Omega}) + B_{l-1}^{m-1} Y_{l-2}^m(\hat{\Omega}) \right] \\ & + \frac{3}{8\pi} g_{l+1} B_{l+1}^{m-1} \left[-B_{l+2}^{-m} Y_{l+2}^m(\hat{\Omega}) + B_{l+1}^{m-1} Y_l^m(\hat{\Omega}) \right] \left. \right\} = 0. \quad (\text{A.54}) \end{aligned}$$

Next, we multiply eq. (A.54) by $Y_{\alpha,\beta}^*(\hat{\Omega})$ and integrate over $\hat{\Omega}$. Using the orthogonality relations for the spherical harmonics, eq. (A.8), we arrive at

$$\begin{aligned}
 \mu_t^{(\alpha)} \Gamma_{\alpha,\beta} &+ g_\alpha k_c \Gamma_{\alpha,\beta} \\
 -k_c \left\{ \right. &+ \frac{1}{2} [g_{\alpha-1} B_\alpha^\beta B_\alpha^\beta \Gamma_{\alpha,\beta} - g_{\alpha+1} B_{\alpha+2}^\beta B_{\alpha+1}^{-\beta-1} \Gamma_{\alpha+2,\beta}] \\
 - \frac{1}{2} [g_{\alpha-1} B_{\alpha-1}^{-\beta-1} B_\alpha^\beta \Gamma_{\alpha-2,\beta} - g_{\alpha+1} B_{\alpha+1}^{-\beta-1} B_{\alpha+1}^{-\beta-1} \Gamma_{\alpha,\beta}] \\
 + [g_{\alpha-1} A_\alpha^\beta A_\alpha^\beta \Gamma_{\alpha,\beta} + g_{\alpha+1} A_{\alpha+2}^\beta A_{\alpha+1}^\beta \Gamma_{\alpha+2,\beta}] \\
 + [g_{\alpha-1} A_{\alpha-1}^\beta A_\alpha^\beta \Gamma_{\alpha-2,\beta} + g_{\alpha+1} A_{\alpha+1}^\beta A_{\alpha+1}^\beta \Gamma_{\alpha,\beta}] \\
 - \frac{1}{2} [-g_{\alpha-1} B_\alpha^{-\beta} B_\alpha^{-\beta} \Gamma_{\alpha,\beta} + g_{\alpha+1} B_{\alpha+2}^{-\beta} B_{\alpha+1}^{\beta-1} \Gamma_{\alpha+2,\beta}] \\
 + \frac{1}{2} [-g_{\alpha-1} B_{\alpha-1}^{\beta-1} B_\alpha^{-\beta} \Gamma_{\alpha-2,\beta} + g_{\alpha+1} B_{\alpha+1}^{\beta-1} B_{\alpha+1}^{\beta-1} \Gamma_{\alpha,\beta}] \left. \right\} \\
 + \frac{1}{2} B_{\alpha+1}^{\beta-1} \left(\frac{\partial}{\partial x} - i \frac{\partial}{\partial y} \right) \Gamma_{\alpha+1,\beta-1} - \frac{1}{2} B_\alpha^{-\beta} \left(\frac{\partial}{\partial x} - i \frac{\partial}{\partial y} \right) \Gamma_{\alpha-1,\beta-1} \\
 - \frac{1}{2} B_{\alpha+1}^{-\beta-1} \left(\frac{\partial}{\partial x} + i \frac{\partial}{\partial y} \right) \Gamma_{\alpha+1,\beta+1} + \frac{1}{2} B_\alpha^\beta \left(\frac{\partial}{\partial x} + i \frac{\partial}{\partial y} \right) \Gamma_{\alpha-1,\beta+1} \\
 + A_{\alpha+1}^\beta \frac{\partial}{\partial z} \Gamma_{\alpha+1,\beta} + A_\alpha^\beta \frac{\partial}{\partial z} \Gamma_{\alpha-1,\beta} = q_{\alpha,\beta} . \tag{A.55}
 \end{aligned}$$

This is a coupled set of linear differential equations for $\Gamma_{\alpha,\beta}$.

To obtain the correlation diffusion equation, we neglect all $\Gamma_{\alpha,\beta}$ and g_α for $\alpha > 1$.

The $\alpha = 0$ equation is

$$\begin{aligned}
 \mu_a \Gamma_{0,0} + k_c (1 - g_1) \Gamma_{0,0} + \frac{1}{2} \sqrt{\frac{2}{3}} \left(\frac{\partial}{\partial x} - i \frac{\partial}{\partial y} \right) \Gamma_{1,-1} \\
 - \frac{1}{2} \sqrt{\frac{2}{3}} \left(\frac{\partial}{\partial x} + i \frac{\partial}{\partial y} \right) \Gamma_{1,1} + \sqrt{\frac{1}{3}} \frac{\partial}{\partial z} \Gamma_{1,0} = q_{0,0} , \tag{A.56}
 \end{aligned}$$

and the $\alpha = 1$ equations are

$$\mu_t^{(1)} \Gamma_{1,-1} + \left(g_1 - \frac{1}{3} \right) k_c \Gamma_{1,-1} + \frac{1}{2} \sqrt{\frac{2}{3}} \left(\frac{\partial}{\partial x} + i \frac{\partial}{\partial y} \right) \Gamma_{0,0} = q_{1,-1} , \tag{A.57}$$

$$\mu_t^{(1)} \Gamma_{1,0} + \left(g_1 - \frac{1}{3} \right) k_c \Gamma_{1,0} + \sqrt{\frac{1}{3}} \frac{\partial}{\partial z} \Gamma_{0,0} = q_{1,0} , \tag{A.58}$$

$$\mu_t^{(1)} \Gamma_{1,1} + \left(g_1 - \frac{1}{3} \right) k_c \Gamma_{1,1} - \frac{1}{2} \sqrt{\frac{2}{3}} \left(\frac{\partial}{\partial x} - i \frac{\partial}{\partial y} \right) \Gamma_{0,0} = q_{1,1} . \quad (\text{A.59})$$

Using the definition for the correlation fluence $G_1(\mathbf{r}, \tau)$ (eq. (A.39)) and the correlation flux $\mathbf{J}_g(\mathbf{r}, \tau)$ (eq. (A.40)), the $\alpha = 0$ and $\alpha = 1$ equations can be rewritten as

$$\mu_a G_1(\mathbf{r}, \tau) + \frac{1}{3} \mu'_s k_o^2 \langle \Delta r^2(\tau) \rangle G_1(\mathbf{r}, \tau) + \nabla \cdot \mathbf{J}_g(\mathbf{r}, \tau) = S_0(\mathbf{r}) , \quad (\text{A.60})$$

$$\mu_t^{(1)} \mathbf{J}_g(\mathbf{r}, \tau) + \frac{1}{3} \mu_s \left(g_1 - \frac{1}{3} \right) k_o^2 \langle \Delta r^2(\tau) \rangle \mathbf{J}_g(\mathbf{r}, \tau) + \frac{1}{3} \nabla G_1(\mathbf{r}, \tau) = \mathbf{S}_1(\mathbf{r}) . \quad (\text{A.61})$$

Recall that we have assumed that the correlation $G_1^T(\mathbf{r}, \hat{\Omega}, \tau)$ is nearly isotropic and that the scattering particles have moved a distance that is much smaller than a wavelength of light. The first assumption is satisfied when $\mu_a \ll \mu_s$ and the scattering is not too anisotropic. The second assumption is satisfied when $k_o^2 \langle \Delta r^2(\tau) \rangle \ll 1$. To keep our equations consistent with these approximations it is necessary to drop terms from eq. (A.61); in particular

$$\mu'_s \mathbf{J}_g(\mathbf{r}, \tau) + \frac{1}{3} \nabla G_1(\mathbf{r}, \tau) = \mathbf{S}_1(\mathbf{r}) . \quad (\text{A.62})$$

Decoupling eq. (A.60) and eq. (A.62) for $G_1(\mathbf{r}, \tau)$, we arrive at the correlation diffusion equation

$$\left[-\nabla \cdot \left(\frac{1}{v} D_\gamma \nabla \right) + \mu_a + \frac{1}{3} \mu'_s k_o^2 \langle \Delta r^2(\tau) \rangle \right] G_1(\mathbf{r}, \tau) = S_0(\mathbf{r}) - \nabla \cdot \left(\frac{3}{v} D_\gamma \mathbf{S}_1(\mathbf{r}) \right) , \quad (\text{A.63})$$

where $D_\gamma = v/(3\mu'_s)$ is the *photon diffusion coefficient*.

Appendix B

Henyey-Greenstein Phase Function

The normalized Henyey-Greenstein phase function is [141, 139, 140]

$$f(\hat{\Omega} \cdot \hat{\Omega}') = f(\cos \theta) = \frac{1 - g^2}{2[1 + g^2 - 2g \cos \theta]^{3/2}}, \quad (\text{B.1})$$

where θ is the angle between the input direction $\hat{\Omega}'$ and the output direction $\hat{\Omega}$, and g is the scattering anisotropy. The angle θ is in the interval $[0, \pi]$. This phase function is unique because the average cosine of the scattering angle is g ,

$$\langle \cos \theta \rangle = \int_0^\pi f(\cos \theta) \cos \theta \sin \theta d\theta = g, \quad (\text{B.2})$$

and higher moments of the scattering angle are g^l ,

$$\int_0^\pi f(\cos \theta) P_l(\cos \theta) \sin \theta d\theta = g^l. \quad (\text{B.3})$$

$P_l(\cos \theta)$ is a Legendre polynomial of order l .

Appendix C

Monte Carlo Code

Following is the listing of the Monte Carlo code that I used to simulate the propagation of diffuse photon density waves and temporal correlation through turbid media. The code is written to handle infinite and semi-infinite media which is either homogeneous or contains a spherical inhomogeneity with different optical and dynamical properties. When running simulations with a spherical object the optical properties of the background and object can be anything. The background is assumed static and the object is dynamic.

This code is compiled using

```
gcc -o monte monte.c ran.c ran2.c ran3.c -lm
```

or an equivalent. Parameters for the simulation are entered on the command line using the following format:

```
unix_prompt> monte nphotons musp mua musp2 mua2 radius sz dz DeltaYmax  
DeltaYstep output_file
```

`nphotons` is the number of photons to run in the simulation. `musp` and `mua` are the reduced scattering and absorption coefficient of the background medium. `musp2`, `mua2`, and `radius` are the reduced scattering and absorption coefficient and radius of the spherical object (if it exists). `sz` and `dz` are the z coordinates of the source and detector. `DeltaYmax` and `DeltaYstep` determine the range over which the total momentum transfer from moving particles is histogrammed. `output_file` is the file name for the data generated by the simulation.

The code can be compiled in many different modes, each of which runs a simulation for a different geometry. Which mode the code runs in is determined by the #define statements for HOMOGENEOUS, INFINITE, COLLIMATED, SPHERICAL_DETECTOR, and PARTIAL_DYNAMIC in the beginning of the program. If HOMOGENEOUS is defined then the medium is homogeneous, otherwise a spherical object is centered at the origin. If INFINITE is defined then the medium is infinite otherwise it is semi-infinite. The source is collimated in the +z direction if COLLIMATED is defined, otherwise the source is isotropic. If INFINITE and HOMOGENEOUS are defined and COLLIMATED is not defined then the spherical symmetry of the geometry can be exploited by using spherical detectors. This is done by defining SPHERICAL_DETECTOR, otherwise ring detectors which lie in a plane are used. For ring detectors, the detection plane is in the xy plane at the z-coordinate **dz** and the source is at $x=y=0$ and $z=sz$. For spherical detectors the source is at $x=y=z=0$. Finally, the medium can be homogeneous with a uniformly distributed static and dynamic component. This is a model of capillary blood flow. This geometry is set by defining PARTIAL_DYNAMIC where VOL_FRAC is defined as the volume fraction (actually P_{blood} , see section 4.4.3) of the dynamic component. If PARTIAL_DYNAMIC is not defined then the system is 100% dynamic.

Two different sets of output are generated. The first set contains the time domain data. A file is generated for each detector position. The file names are **output_file_##.##.tdd** where the **##.##** indicates the detector position and **.tdd** indicates time domain data. The second set contains the total momentum transfer data. Once again a file is generated for each detector position. The file names are **output_file_##.##.D_elY** where the **##.##** indicates the detector position and **.D_elY** indicates momentum transfer data. The formats are self explanatory.

C.1 monte.c

```
#include<stdio.h>
#include<stdlib.h>
#include<math.h>
```

```

#define HOMOGENEOUS /* DEFINE IF THE MEDIUM IS HOMOGENEOUS
    OTHERWISE THERE IS A SPHERE AT THE ORIGIN */
#define INFINITE      /* DEFINE IF MEDIUM IS INFINITE OTHERWISE SEMI-INFINITE*/
/*#define COLLIMATED  /* DEFINE IF SOURCE IS COLLIMATED OTHERWISE ISOTROPIC */

#ifndef INFINITE
#ifndef HOMOGENEOUS
#ifndef COLLIMATED
#define SPHERICAL_DETECTOR /* DEFINE IF THE DETECTORS ARE SPHERICAL
    OTHERWISE RING DETECTORS ARE USED */
#endif
#endif
#endif

#ifndef HOMOGENEOUS
/*#define PARTIAL_DYNAMIC /* DEFINE IF SYSTEM IS UNIFORM BUT PART STATIC
    AND PART DYNAMIC. ONLY WORKS IF DEF HOMOGENEOUS*/
#define VOL_FRAC 0.1     /* VOLUME FRACTION OF DYNAMIC COMPONENT
    USED ONLY IF PARTIAL_DYNAMIC IS DEFINED */
#endif

#define pi 3.1415926353
#define TRUE 1
#define FALSE 0
#define MAX_TBIN 1040    /* MAXIMUM NUMBER OF TEMPORAL BINS */
#define MAX_DeltaYBIN 2080 /* MAXIMUM NUMBER OF MOMENTUM TRANSFER BINS */
#define MAX_RHOBIN 40     /* MAXIMUM NUMBER OF RADIAL/RHO BINS */

main( argc, argv )
int argc;
char *argv[];
{
    int i,j,q;
    int idum;           /* FOR RANDOM NUMBER GENERATOR */
    int ncall;          /* NUMBER OF CALLS TO RANDOM NUMBER GENERATOR - USED
    BY THE GENERATOR */
    int ABSORBED;       /* FLAG IF PHOTON HAS BEEN ABSORBED */
    int b;              /* TOTAL NUMBER OF PHOTONS TO RUN */
    int p;              /* NUMBER OF PHOTONS RUN SO FAR */
    int OUTSIDE;        /* FLAG IF OUTSIDE SPHERE */
    int rhoindex,tindex,DeltaYindex; /* INDICES FOR RADIAL/RHO, TIME,
    AND MOMENTUM TRANSFER SCORING */
    int nt,nDeltaY;     /* NUMBER OF TIME AND MOMENTUM BINS NEEDED */
    float rho;           /* rho=sqrt(x*x+y*y) POSITION OF PHOTON */
    float rhostep;       /* WIDTH OF DETECTOR */
    float t,tgate,tbody; /* CURRENT TIME, GATE TIME, WIDTH OF TEMPORAL BINS */
    float DeltaY;         /* CURRENT MOMENTUM TRANSFER */
    float DeltaYmax, DeltaYstep; /* MAXIMUM MOMENTUM TRANSFER, WIDTH OF MOMENTUM BINS */
    float velocity;       /* PHOTON VELOCITY IN THE MEDIUM */
    float g=0.;           /* ANISOTROPY FACTOR */
    float foo;            /* TEMPORARY VARIABLE */
    float mua,musp,mus; /* OPTICAL PROPERTIES OF THE BACKGROUND */
    float muainv,musinv;
    float mua2,musp2,mus2; /* OPTICAL PROPERTIES OF THE SPHERE */
    float muainv2,musinv2;
    float radi2,radisq; /* RADIUS OF THE SPHERE, RADIUS SQUARE */
    float phi,theta,sphi,cphi,sttheta,ctheta;
    /* SCATTERING ANGLES */
    float x,y,z;         /* CURRENT PHOTON POSITION */
    float xold,yold,zold; /* LAST POSITION OF PHOTON */
    float xm,ym,zm,lm; /* x,y, and z OF PHOTON INTERSECTION WITH A PLANE
    DETECTOR. lm IS THE LENGTH FROM LAST SCATTERING
    EVENT TO DETECTOR INTERSECTION */
    float r,rold;         /* CURRENT AND LAST RADIAL POSITION OF PHOTON */
    float c1,c2,c3;       /* DIRECTION COSINES */
    float c1o, c2o, c3o; /* OLD DIRECTION COSINES */
    float la;              /* ABSORPTION DISTANCE - RANDOMLY GENERATED FROM MUA */
    float ls;              /* SCATTERING DISTANCE - RANDOMLY GENERATED FROM MUS */
    float sz, dz;          /* SOURCE AND DETECTOR Z POSITION. THE SOURCE IS
    AT x=Y=0 */
    float hgpart1,hgpart2,hgpart3,hgpart4,hgpart5,hgpart6;
    /* USED IN HENYEY-GREENSTEIN CALCULATION */
    FILE *fp;             /* FILE POINTER FOR SAVING THE DATA */
    double fluxout[MAX_RHOBIN][MAX_TBIN]; /* SCORE THE PHOTON FLUX */
    double fluxin[MAX_RHOBIN][MAX_TBIN];
    double DeltaOut[MAX_RHOBIN][MAX_DeltaYBIN]; /* SCORE THE TOTAL MOMENTUM */
    double DeltaIn[MAX_RHOBIN][MAX_DeltaYBIN]; /* TRANSFER */
    float rnm;             /* RANDOM NUMBER */
    float ran( int *idum, int *ncall ); /* FUNCTION DECLARATION */
    float B,C,L,T,DELL,T1,T2,LSP,LAP,LSP2,LAP2,B2;

```

```

/* USED FOR SPHERE INTERSECTION ROUTINE */
/* B,C to be used in B^2-4AC calculation! */
/* L, T are also for cross passing, entering sphere etc checks */
/* B2=B^2-4AC*/
/* T1,T2,T are for parameterizations */
/* DELL=delta L*/
/* LSP: ls temp */
/* LAP : la temp */
char filenm[32]; /* FILE NAME FOR DATA FILE */

/* GET THE COMMAND LINE ARGUMENTS */
if( argc!=12 ) {
    printf( "usage: monte nphotons musp mua musp2 mua2 radius sz dz DeltaYmax DeltaYstep output_file\n" );
    exit(1);
}

/* GET THE NUMBER OF PHOTONS TO MIGRATE */
sscanf( argv[1], "%f", &foo ); b = (int)foo;

/* GET THE OPTICAL PROPERTIES */
/* mua & musp are for background medium */
/* mua2 & musp2 are for the spherical tumor, all variables with
   '2' as the last character are for the tumor */
sscanf( argv[2], "%f", &musp ); mus = musp/(1.-g); musinv = 1./mus;
sscanf( argv[3], "%f", &mua ); muainv = 1. / mua;
sscanf( argv[4], "%f", &musp2 ); mus2= musp2/(1.-g); musinv2= 1./mus2;
sscanf( argv[5], "%f", &mua2 ); muainv2 = 1. / mua2;

/* GET THE SPHERE RADIUS */
/* radi2 is the radius of the spherical tumor */
/* radisq is for cross pass calculation */
sscanf( argv[6], "%f", &radi2 ); radisq=radi2*radi2;

/* SOURCE AND DETECTOR Z POSITION */
sscanf( argv[7], "%f", &sz );
sscanf( argv[8], "%f", &dz );

/* RANGE OF MOMENTUM TRANSFERS AND BIN STEP */
sscanf( argv[9], "%f", &DeltaYmax );
sscanf( argv[10], "%f", &DeltaYstep );

/* INITIALIZE OTHER PARAMETERS */
velocity = 2.9979e10 / 1.338; /* PHOTON VELOCITY IN WATER */
g = 0.; /* SCATTERING ANISOTROPY */
tbin=20e-12 ; tgate=10.24e-9; /* TEMPORAL BIN WIDTH AND GATE */
rhoStep=0.1; /* DETECTOR WIDTH */

/* CALCULATE THE NUMBER OF TEMPORAL AND MOMENTUM BINS THAT ARE NEEDED */
nt = tgate/tbin;
nDeltaY = DeltaYmax/DeltaYstep+1;

/* MAKE SURE THAT ENOUGH MEMORY HAS BEEN ALLOCATED FOR THE NEEDED BINS */
if( nt>MAX_TBIN ) {
    printf( "Maximum number of time bins exceeded." );
    exit(1);
}
if( nDeltaY>MAX_DeltaYBIN ) {
    printf( "Maximum number of DeltaY bins exceeded." );
    exit(1);
}

/* INITIALIZE THE FLUX TO BE ZERO */
for( i=0; i<MAX_RHOBIN; i++ )
    for( j=0; j<nt; j++ ) {
        fluxin[i][j] = 0.;
        fluxout[i][j] = 0.;
    }
/* INITIALIZE DeltaY TO ZERO */
for( i=0; i<MAX_RHOBIN; i++ )
    for( j=0; j<nDeltaY; j++ ) {
        DeltaYin[i][j] = 0.;
        DeltaYout[i][j] = 0.;

/* NUMBER PHOTONS EXECUTED SO FAR */
p=0;

/* SEED THE RANDOM NUMBER GENERATOR - A LARGE NEGATIVE NUMBER IS REQUIRED */
idum = -149249;
ncall = 0; /* NUMBER OF CALLS MADE TO THE GENERATOR */

```

```

/* START MIGRATING THE PHOTONS */
/* GENERATING PHOTONS UNTIL NUMBER OF PHOTONS EXECUTED (p) IS EQUAL TO THE
   NUMBER TO BE GENERATED (b) */

while (<b>{
    OUTSIDE=FALSE;      /* START OUTSIDE THE OBJECT */
    ABSORBED=FALSE;    /* PHOTON NOT ABSORBED YET */

    t=0.;              /* START PHOTON AT TIME = 0 */
    DeltaY = 0.;        /* NO SCATTERING FROM A MOVING PARTICLE YET.
    ZERO MOMENTUM TRANSFER */
    ++p;               /* INCREMENT THE PHOTONS EXECUTED COUNTER */

    /* INITIAL SOURCE POSITION */
    x=0.; y=0.; z=z;    /* CURRENT POSITION */
    xold=x; yold=y; zold=z; /* PREVIOUS POSITION */

    /* RADIAL POSITION OF PHOTON
       USED FOR CHECKING FOR INTERSECTIONS WITH SPHERICAL DETECTORS
       AND THE SPHERICAL OBJECT */
    r = sqrt(x*x+y*y+z*z); /* RADIAL POSITION OF PHOTON */
    rold = r;             /* OLD RADIAL POSITION */

    /* INITIAL DIRECTION OF PHOTON */
#ifdef COLLIMATED
    /* COLLIMATED ALONG Z-AXIS */
    c1=0.; c1o=c1;
    c2=0.; c2o=c2;
    c3=1.; c3o=c3;
#endif
#ifndef COLLIMATED
    /* ISOTROPIC */
    rnm = ran(&idum,&ncall);
    phi=2*pi*rnm;
    cphi=cos(phi);
    sphi=sin(phi);
    rnm = ran(&idum,&ncall);
    theta=acos(1.-2.*rnm);
    ctheta=cos(theta);
    stheta=sin(theta);
    c1 = stheta*cphi;
    c2 = stheta*sphi;
    c3 = ctheta;
    c1o = c1;
    c2o = c2;
    c3o = c3;
#endif

    /* LOOP UNTIL TIME EXCEEDS GATE, PHOTON IS ABSORBED, OR PHOTON ESCAPES */
#ifndef INFINITE /* SEMI-INFINITE MEDIUM */
    while ( t<tgate && ABSORBED==FALSE && z>=sz ) {
#endif
#ifndef INFINITE /* INFINITE MEDIUM */
    while ( t<tgate && ABSORBED==FALSE ) {
#endif

    /* CALCULATE SCATTERING AND ABSORPTION LENGTHS */

#ifdef HOMOGENEOUS /* HOMOGENEOUS MEDIUM */
    rnm = ran(&idum,&ncall);
    ls = -musinv * log(rnm);
    rnm = ran(&idum,&ncall);
    la = -muainv * log(rnm);
    OUTSIDE=TRUE;
    if(ls<la) {
        L=ls;
    }
    else {
        L=la;
        ABSORBED=TRUE;
    }
#endif

    /* ACCUMULATE THE MOMENTUM TRANSFER FROM A MOVING PARTICLE */
#ifndef PARTIAL_DYNAMIC
    DeltaY += 1.-c1*c1o-c2*c2o-c3*c3o;
#endif
#ifndef PARTIAL_DYNAMIC
    rnm = ran(&idum,&ncall);
    if( rnm<VOL_FRAC ) DeltaY += 1.-c1*c1o-c2*c2o-c3*c3o;
#endif
#endif

```

```

#ifndef HOMOGENEOUS /* HETEROGENEOUS MEDIUM, I.E. A SPHERE IS PRESENT */
/* CHECK IF WE ARE OUTSIDE THE SPHERE, OR INSIDE THE SPHERE */
if(rad1>r){
    if(rad2>r){
        rnm = ran(&idum,&ncall);
        ls=-musinv *log(rnm);
        rnm = ran(&idum,&ncall);
        la=-muainv *log(rnm);
        OUTSIDE=TRUE;
    }
    else {
        /* INCREMENT TOTAL WAVEVECTOR TRANSFER IF INSIDE SPHERE*/
        DeltaY += 1.-c1*c10-c2*c20-c3*c30;

        rnm = ran(&idum,&ncall);
        ls=-musinv2*log(rnm);
        rnm = ran(&idum,&ncall);
        la=-muainv2*log(rnm);
        OUTSIDE=FALSE;
    }

    /* CHECK FOR INTERSECTIONS WITH THE SURFACE OF THE SPHERE */

    /* CALCULATE A,B,C */
    rold = r;
    B=(xold*c1+yold*c2+zold*c3);
    C=rold*rold-radisq;
    B2=B*B-C;

    /* CALCULATE MINIMUM DISTANCE */
    if(ls<la) {
        L=ls;
    }
    else {
        L=la;
        ABSORBED=TRUE;
    }

    /* FINE TUNE */
    if (OUTSIDE){
        if (B2>0){
            T1=(-B+sqrt(B2));
            T2=(-B-sqrt(B2));
        }
        /* FIND IF WE INTERSECTED THE TUMOR */
        /* I.E ENTERED IT */
        if((T1>0 && T1<L) || (T2>0 && T2<L)) {

            /* FIND MINIMUM OF T1, T2*/
            if (T1<T2){
                DELL=T1;
                T=T2;
            }
            else{
                DELL=T2;
                T=T1;
            }
            L=DELL;
            LSP=(ls-DELL)*musinv/muainv2;
            LAP=(la-DELL)*muainv/muainv2;

            /* CHECK IF WE CROSSED OUT THE TUMOR */
            if(LSP>(T-DELL) && LAP>(T-DELL)) {
                L=T;
                LSP2=(LSP-T+DELL)*musinv2/musinv;
                LAP2=(LAP-T+DELL)*muainv2/muainv;
                if(LSP2<LAP2){
                    L+=LSP2;
                    ABSORBED=FALSE;
                }
                else {
                    L+=LAP2;
                    ABSORBED=TRUE;
                }
            }

            /*STILL INSIDE THE TUMOR */
            else {
                if(LSP<LAP){
                    L+=LSP;
                    ABSORBED=FALSE;
                }
            }
        }
    }
}

```

```

        }
    else{
        L+=LAP;
        ABSORBED=TRUE;
    }
}
}

/* END OF INTERSECTION WITH TUMOR */
}

/* INSIDE TUMOR */
else {
    T1=(-B+sqrt(B2));
    T2=(-B-sqrt(B2));

/* FIND IF WE INTERSECTED THE TUMOR */
/* I.E EXITED IT */
if((T1>0 && T1<L) || (T2>0 && T2<L))  {

/* FIND MAXIMUM OF T1, T2*/
if (T1>T2){
    DELL=T1;
}
else{
    DELL=T2;
}
L=DELL;
LSP=(ls-DELL)*musinv/musinv2;
LAP=(la-DELL)*muainv/muainv2;

if(LSP<LAP){
    L+=LSP;
    ABSORBED=FALSE;
}
else {
    L+=LAP;
    ABSORBED=TRUE;
}
}
/*END OF INSIDE TUMOR */
#endif

/* CALCULATE THE NEW POSITION */
xold = x;
yold = y;
zold = z;
rold = r;

x=xold+L*c1;
y=yold+L*c2;
z=zold+L*c3;
r=sqrt(x*x+y*y+z*z);

/* SCORE THE PHOTON */

/* INCREMENT THE TIME */
t+=L/velocity;

/* SCORE THE PHOTON WITH A RING DETECTOR */
#ifndef SPHERICAL_DETECTOR
if( z<dz && zold>dz )  {
    lm=(zold-dz)/(zold-z)*L;
    xm=xold+lm*c1;
    ym=yold+lm*c2;
    rho=sqrt(xm*xm+ym*ym);
    rhoindex=(int)floor(rho/rhostep);
    /* tindex = (t+lm/velocity)/tbins; */
    tindex = t/tbin;
    DeltaYindex=(int)ceil(DeltaY/DeltaYstep);
    if( rhoindex<MAX_RHOBIN && tindex<MAX_TBIN )  {
        fluxout[rhoindex][tindex]+=-1./c3; /* THE EFFECTIVE WIDTH OF THE
DETECTOR VARIES WITH THE
ANGLE OF INCIDENCE.  NORMALIZE
OUT THIS DEPENDENCE ON ANGLE*/
        /* fluxout[rhoindex][tindex]++; */
        if( DeltaYindex<MAX_DeltaYBIN )
            DeltaYout[rhoindex][DeltaYindex]++;
    }
}
#endif
}

```

```

#ifndef INFINITE
    if( z>dz && zold<dz )  {
        lm=(zold-dz)/(zold-z)*L;
        xm=xold+lm*c1;
        ym=yold+lm*c2;
        rho=sqrt(xmxm+ym*ym);
        rhoindex=(int)floor(rho/rhostep);
        /* tindex = (t+lm/velocity)/tbin; */
        tindex = t/tbin;
        DeltaYindex=(int)ceil(DeltaY/DeltaYstep);
        if( rhoindex<MAX_RHOBIN && tindex<MAX_TBIN ) {
            fluxin[rhoindex][tindex]+=1./c3; /* THE EFFECTIVE WIDTH OF THE
DETECTOR VARIES WITH THE
ANGLE OF INCIDENCE. NORMALIZE
OUT THIS DEPENDENCE ON ANGLE*/
            /* fluxin[rhoindex][tindex]++; */
            if( DeltaYindex<MAX_DeltaYBIN )
                DeltaYin[rhoindex][DeltaYindex]++;
        }
    }
#endif
#endif

/* SCORE THE PHOTON WITH SPHERICAL DETECTORS */
#ifndef SPHERICAL_DETECTOR
    tindex = t/tbin;
    DeltaYindex=(int)ceil(DeltaY/DeltaYstep);
    if( r<rold ) {
        rhoindex = (int)ceil(r/rhostep);
        while( (float)rhoindex*rhostep<rold ) {
            if( rhoindex<MAX_RHOBIN ) {
                fluxin[rhoindex][tindex]++;
                if( DeltaYindex<MAX_DeltaYBIN )
                    DeltaYin[rhoindex][DeltaYindex]++;
            }
            rhoindex++;
        }
        if( r>rold ) {
            rhoindex = (int)ceil(rold/rhostep);
            while( (float)rhoindex*rhostep<r ) {
                if( rhoindex<MAX_RHOBIN ) {
                    fluxout[rhoindex][tindex]++;
                    if( DeltaYindex<MAX_DeltaYBIN )
                        DeltaYout[rhoindex][DeltaYindex]++;
                }
                rhoindex++;
            }
        }
    }
#endif

/* CALCULATE THE NEW SCATTERING ANGLE ASSUMING ISOTROPIC SCATTERING */
rnm = ran(&idum,&ncall);
phi=2*pi*rnm;
cphi=cos(phi);
sphi=sin(phi);
rnm = ran(&idum,&ncall);
theta=acos(1.-2.*rnm);
ctheta=cos(theta);
stheta=sin(theta);

/* CALCULATE THE NEW SCATTERING ANGLE USING HENYEY-GREENSTEIN */
/*
phi=2*pi*rnm;
cphi=cos(phi);
sphi=sin(phi);
rnm = ran(&idum,&ncall);
hgpart1=(1.+g*g);
hgpart2=(1.-(g*g));
hgpart3=(1.-g+(2.*g*rnm));
hgpart4=hgpart3*hgpart3;
hgpart5=1/(2.*g);
hgpart6=(hgpart2)*(hgpart2);
foo = (hgpart1-(hgpart6/hgpart4))*(hgpart5);
theta=acos(foo);
stheta=sin(theta);
ctheta=cos(theta);*/

c1o = c1;
c2o = c2;
c3o = c3;

```

```

c1 = stheta*cphi;
c2 = stheta*sphi;
c3 = ctheta;

} /* LOOP UNTIL END OF SINGLE PHOTON */
} /* LOOP UNTIL ALL PHOTONS EXHAUSTED */

/* SAVE TIME DOMAIN DATA USING A FORMAT UNDERSTOOD BY PMI */
for( q=1; q<MAX_RHOBIN; q++ ) {
    rho = rhostep * ((float)q);
    sprintf( filenm, "%s_%05.2f.tdd", argv[11], rho );
    fp=fopen( filenm, "w");
    fprintf( fp, "%d %e 2000\n", nt, tgate );
    fprintf( fp, "O O %f %d 0\n", sz, b );
#ifndef SPHERICAL_DETECTOR
    fprintf( fp, "%f O %f\n", rho+rhostep/2, dz );
#endif
#ifndef SPHERICAL_DETECTOR
    fprintf( fp, "%f O O\n", rho );
#endif
    for( tindex=0; tindex<nt; tindex++ )
#ifndef SPHERICAL_DETECTOR
        fprintf(fp,"%f\n",2.*(float)(fluxin[q][tindex]+fluxout[q][tindex])/(pi*rhostep*rhostep+2*pi*rhostep*rho));
#endif
#ifndef SPHERICAL_DETECTOR
        fprintf(fp,"%f\n",2.*(float)(fluxin[q][tindex]+fluxout[q][tindex])/(4.*pi*rho*rho));
#endif
    fclose(fp);
}

/* SAVE MOMENTUM TRANSFER DATA */
for( q=1; q<MAX_RHOBIN; q++ ) {
    rho = rhostep * ((float)q);
    sprintf( filenm, "%s_%05.2f.DelY", argv[11], rho );
    fp=fopen( filenm, "w");
    fprintf( fp, "%d %e %e\n", nDeltaY, DeltaYmax, DeltaYstep );
    fprintf( fp, "O O %f %d 0\n", sz, b );
#ifndef SPHERICAL_DETECTOR
    fprintf( fp, "%f O %f\n", rho+rhostep/2, dz );
#endif
#ifndef SPHERICAL_DETECTOR
    fprintf( fp, "%f O O\n", rho );
#endif
    for( DeltaYindex=0; DeltaYindex<nDeltaY; DeltaYindex++ )
#ifndef SPHERICAL_DETECTOR
        fprintf(fp,"%f\n",2.*(float)(DeltaYin[q][DeltaYindex]+DeltaYout[q][DeltaYindex])
                /(pi*rhostep*rhostep+2*pi*rhostep*rho));
#endif
#ifndef SPHERICAL_DETECTOR
        fprintf(fp,"%f\n",2.*(float)(DeltaYin[q][DeltaYindex]+DeltaYout[q][DeltaYindex])/(4.*pi*rho*rho));
#endif
    fclose(fp);
}
}

```

C.2 ran.c

I use a combination of two random number generators from Numerical Recipes in C [149]. This particular routine was strongly suggested by Dr. Murray Penney at GE-CRD in Schenectady, NY. Dr. Penney has thoroughly tested the randomness of this routine.

```
#include <stdio.h>
#include <math.h>
```

```

static long idum2;
float ran( int *idum, int *ncall )
{
    float rn;
    float ran3( int *idum );
    float ran2( long *idum2 );

    *ncall = *ncall + 1;
    if( *ncall==1 ) idum2 = *idum*0.79;
    if( fmod(*ncall,1e6)==0 ) *idum=-1111-99999*ran2(&idum2);
    rn = ran3(idum);

    if( rn<1e-4 ) rn=1.e-4*ran3(idum);
    if( rn==0 ) rn=1e-12;

    return rn;
}

```

C.3 ran2.c

This routine is from Numerical Recipes in C [149].

```

#include <math.h>

#define M 714025
#define IA 1366
#define IC 150889

float ran2(idum)
long *idum;
{
    static long iy,ir[98];
    static int iff=0;
    int j;
    void nrerror();

    if (*idum < 0 || iff == 0) {
        iff=1;
        if ((*idum=(IC-(*idum)) % M) < 0) *idum = -(*idum);
        for (j=1;j<=97;j++) {
            *idum=(IA*(*idum)+IC) % M;
            ir[j]=(*idum);
        }
        *idum=(IA*(*idum)+IC) % M;
        iy=(*idum);
    }
    j=1 + 97.0*iy/M;
    if (j > 97 || j < 1) nrerror("RAN2: This cannot happen.");
    iy=ir[j];
    *idum=(IA*(*idum)+IC) % M;
    ir[j]=(*idum);
    return (float) iy/M;
}

#undef M
#undef IA
#undef IC

```

C.4 ran3.c

This routine is from Numerical Recipes in C [149].

```

#define MBIG 1000000000
#define MSEED 161803398
#define MZ 0
#define FAC (1.0/MBIG)

```

```

float ran3(idum)
int *idum;
{
static int inext,inextp;
static long ma[56];
static int iff=0;
long mj,mk;
int i,ii,k;

if (*idum < 0 || iff == 0) {
iff=1;
mj=MSEED-(*idum < 0 ? -*idum : *idum);
mj %= MBIG;
ma[55]=mj;
mk=1;
for (i=1;i<=54;i++) {
ii=(2*i) % 55;
ma[ii]=mk;
mk=mj-mk;
if (mk < MZ) mk += MBIG;
mj=ma[ii];
}
for (k=1;k<=4;k++)
for (i=1;i<=55;i++) {
ma[i] -= ma[1+(i+30) % 55];
if (ma[i] < MZ) ma[i] += MBIG;
}
inext=0;
inextp=31;
*idum=i;
}
if (++inext == 56) inext=1;
if (++inextp == 56) inextp=1;
mj=ma[inext]-ma[inextp];
if (mj < MZ) mj += MBIG;
ma[inext]=mj;
return mj*FAC;
}

#undef MBIG
#undef MSEED
#undef MZ
#undef FAC

```


Bibliography

- [1] B. Chance, ed., *Photon Migration in Tissues* (Plenum Press, 1989).
- [2] A. Yodh and B. Chance, *Spectroscopy and imaging with diffusing light*, Physics Today **48**, 34 (1995).
- [3] B. J. Tromberg, L. O. Svaasand, T. Tsay, and R. C. Haskell, *Properties of photon density waves in multiple-scattering media*, Applied Optics **32**, 607 (1993).
- [4] M. S. Patterson, B. Chance, and B. C. Wilson, *Time resolved reflectance and transmittance for the non-invasive measurement of tissue optical properties*, Applied Optics **28**, 2331 (1989).
- [5] G. A. Millikan, *Experiments on muscle haemoglobin in vivo: The instantaneous measurement of muscle metabolism*, Proc. Roy. Soc. London B **129**, 218 (1937).
- [6] G. A. Millikan, *The oximeter, an instrument for measuring continuously the oxygen saturation of arterial blood in man*, Rev. Sci. Instrum. **13**, 434 (1942).
- [7] F. F. Jobsis, *Noninvasive, infrared monitoring of cerebral and myocardial oxygen sufficiency and circulatory parameters*, Science **198**, 1264 (1977).
- [8] J. M. Schmitt, *Simple photon diffusion analysis of the effects of multiple scattering on pulse oximetry*, IEEE Transaction on Biomedical Engineering **38**, 1194 (1991).
- [9] M. R. Neuman, *Pulse oximetry: physical principles technical realization and present limitations*, Adv. Exp. Med. Biol. **220**, 135 (1987).

- [10] J. W. Severinghaus, *History and recent developments in pulse oximetry*, Scandinavian J. of Clinical and Laboratory Investigations **53**, 105 (1993).
- [11] W. F. Cheong, S. A. Prahl, and A. J. Welch, *A review of the optical properties of biological tissues*, IEEE J. Quantum Electronics **26**, 2166-2185 (1990).
- [12] B. C. Wilson, E. M. Sevick, M. S. Patterson, and B. Chance, *Time-dependent optical spectroscopy and imaging for biomedical applications*, Proceedings of the IEEE **80**, 918 (1992).
- [13] See related works by S. R. Arridge *et al.*, J. P. Kaltenbach *et al.*, and R. L. Barbour *et al.*, in G. Muller *et al.*, eds., *Medical Optical Tomography: Functional Imaging and Monitoring*, SPIE Optical Engineering Press, Bellingham, WA, Vol. IS11, pp. 31-143 (1993).
- [14] S. R. Arridge, P. van der Zee, M. Cope, and D. T. Delpy, *Reconstruction methods for infra-red absorption imaging*, SPIE **1431**, 204 (1991).
- [15] S. P. Gopinath, C. S. Robertson, R. G. Grossman, and B. Chance, *Near-infrared spectroscopic localization of intracranial hematomas*, J. Neurosurg **79**, 43 (1993).
- [16] A. P. Shepherd and P. A. Oberg, eds., *Laser-Doppler Blood Flowmetry* (Kluwer Academic Press, Boston, 1990).
- [17] L. E. Drain, in *The Laser Doppler Technique* (J. Wiley, New York, 1980).
- [18] G. V. Belcaro, U. Hoffmann, A. Bollinger, and A. N. Nicolaides, eds., *Laser Doppler* (Med-Orion Publishing Company, London, 1994).
- [19] A. D. Edwards, C. Richardson, P. van der Zee, M. Cope, and D. T. Delpy, *Measurement of hemoglobin flow and blood flow by near-infrared spectroscopy*, Journal of Applied Physiology **75**, 1884 (1993).

- [20] E. M. Sevick, B. Chance, J. Leigh, S. Nioka, and M. Maris, *Quantitation of time- and frequency-resolved optical spectra for the determination of tissue oxygenation*, Analytical Biochemistry **195**, 330 (1991).
- [21] J. B. Fishkin and E. Gratton, *Propagation of photon density waves in strongly scattering media containing an absorbing “semi-infinite” plane bounded by a straight edge*, J. Opt. Soc. of Am. A **10**, 127 (1993).
- [22] M. A. O’Leary, D. A. Boas, B. Chance, and A. G. Yodh, *Refraction of diffuse photon density waves*, Phys. Rev. Lett. **69**, 2658 (1992).
- [23] B. W. Pogue and M. S. Patterson, *Frequency-domain optical-absorption spectroscopy of finite tissue volumes using diffusion-theory*, Phys. Med. Biol. **39**, 1157 (1994).
- [24] S. J. Matcher, C. E. Elwell, C. E. Cooper, M. Cope, and D. T. Delpy, *Performance comparison of several published tissue near-infrared spectroscopy algorithms*, Analytical Biochemistry **227**, 54 (1995).
- [25] H. Liu, D. A. Boas, Y. Zhang, A. G. Yodh, and B. Chance, *Determination of optical properties and blood oxygenation using continuous NIR light*, Phys. Med. Biol. **40**, 1983 (1995).
- [26] V. G. Peters, D. R. Wyman, M. S. Patterson, and G. L. Frank, *Optical properties of normal and diseased human breast tissues in the visible and near infrared*, Phys. Med. Biol. **35**, 1317 (1990).
- [27] A table of published optical properties compiled by Lihong Wang and Steve Jacques is available at
<ftp://laser.mda.uth.tmc.edu/pub/tissue/Cheong1990.msw> or
<ftp://laser.mda.uth.tmc.edu/pub/tissue/Cheong1990.ps>.

- [28] D. A. Boas, M. A. O'Leary, B. Chance, and A. G. Yodh, *Scattering and wavelength transduction of diffuse photon density waves*, Phys. Rev. E **47**, R2999 (1993).
- [29] D. A. Boas, M. A. O'Leary, B. Chance, and A. G. Yodh, *Scattering of diffuse photon density waves by spherical inhomogeneities within turbid media: analytic solution and applications*, Proc. Natl. Acad. Sci. USA **91**, 4887 (1994).
- [30] P. N. den Outer, T. M. Nieuwenhuizen, and A. Lagendijk, *Location of objects in multiple-scattering media*, J. Opt. Soc. Am. A **10**, 1209 (1993).
- [31] S. Feng, F. Zeng, and B. Chance, *Photon migration in the presence of a single defect: a perturbation analysis*, Appl. Opt. **34**, 3826 (1995).
- [32] J. M. Schmitt, A. Knuttel, and J. R. Knutson, *Interference of diffusive light waves*, J. Opt. Soc. Am. A **9**, 1832 (1992).
- [33] B. Chance, K. Kang, L. He, J. Weng, and E. Sevick, *Highly sensitive object location in tissue models with linear in-phase and anti-phase multi-element optical arrays in one and two dimensions*, Proc. Natl. Acad. Sci. USA **90**, 3423 (1993).
- [34] J. Maier and E. Gratton, *Frequency domain methods in optical tomography: Detection of localized absorbers and a backscattering reconstruction scheme*, in B. Chance and R. R. Alfano, eds., *Proceedings of Photon Migration and Imaging in Random Media and Tissues*, SPIE Optical Engineering Press, Bellingham, WA, Vol. 1888, pp. 440-451 (1993).
- [35] A. Knuttle, J. M. Schmitt, and J. R. Knutson, *Spatial Localization of Absorbing Bodies by Interfering Diffusive Photon Density Waves*, Applied Optics **32**, 381 (1993).
- [36] N. A. Clark, J. H. Lunacek, and G. B. Benedek, *A study of Brownian motion using light scattering*, American Journal of Physics **38**, 575 (1970).

- [37] P. J. Berne and R. Pecora, in *Dynamic Light Scattering* (Wiley, New York, 1976).
- [38] B. J. Berne and R. Pecora, in *Dynamic Light Scattering with Applications to Chemistry, Biology, and Physics* (Robert Krieger Publishing Co., Florida, 1990).
- [39] W. Brown, ed., *Dynamic Light Scattering : The Method and Some Applications* (Clarendon Press, New York, 1993).
- [40] G. G. Fuller, J. M. Rallison, R. L. Schmidt, and L. G. Leal, *The measurement of velocity gradients in laminar flow by homodyne light-scattering spectroscopy*, J. Fluid Mech. **100**, 555 (1980).
- [41] P. Tong, W. I. Goldburg, C. K. Chan, and A. Sirivat, *Turbulent transition by photon-correlation spectroscopy*, Phys. Rev. A **37**, 2125 (1988).
- [42] M. Bertolotti, B. Crosignani, P. Di, Porto, and D. Sette, *Light scattering by particles suspended in a turbulent fluid*, J. Phys. A **2**, 126 (1969).
- [43] P. J. Bourke, J. Butterworth, L. E. Drain, P. A. Egelstaff, E. Jakeman, and E. R. Pike, *A study of the spatial structure of turbulent flow by intensity-fluctuation spectroscopy*, J. Phys. A **3**, 216 (1970).
- [44] T. Tanaka, C. Riva, and I. Ben-Sira, *Blood velocity measurements in human retinal vessels*, Science **186**, 830 (1974).
- [45] M. Stern, *In vivo evaluation of microcirculation by coherent light scattering*, Nature **254**, 56 (1975).
- [46] R. Bonner and R. Nossal, *Model for laser Doppler measurements of blood flow in tissue*, Applied Optics **20**, 2097 (1981).

- [47] H. Z. Cummings and E. R. Pike, eds., *Photon Correlation and Light-Beating Spectroscopy*, Vol. 3 of NATO Advanced Study Institute Series B: Physics (Plenum, New York, 1974).
- [48] D. J. Pine, D. A. Weitz, P. M. Chaikin, and Herbolzheimer, *Diffusing-wave spectroscopy*, Phys. Rev. Lett. **60**, 1134 (1988).
- [49] F. C. MacKintosh and S. John, *Diffusing-wave spectroscopy and multiple scattering of light in correlated random media*, Phys. Rev. B **40**, 2382 (1989).
- [50] G. Maret and P. E. Wolf, *Multiple light scattering from disordered media. The effect of brownian motion of scatterers*, Z. Phys. B **65**, 409 (1987).
- [51] A. Y. Val'kov and V. P. Romanov, Sov. Phys. JETP **63**, 737 (1986), [Zh. Eksp. Teor. Fiz. **90**, 1264-1274 (1986)].
- [52] J. D. Briers, *Laser Doppler and time-varying speckle: A reconciliation*, J. Opt. Soc. of Am. A **13**, 345 (1996).
- [53] M. A. O'Leary, D. A. Boas, B. Chance, and A. G. Yodh, *Experimental images of heterogeneous turbid media by frequency-domain diffusing-photon tomography*, Optics Letters **20**, 426 (1995).
- [54] K. M. Case and P. F. Zweifel, in *Linear Transport Theory* (Addison-Wesley, MA, 1967).
- [55] B. Davison and J. B. Sykes, in *Neutron Transport Theory* (Oxford University Press, London, 1957).
- [56] S. Glasstone and M. C. Edlund, in *the Elements of Nuclear Reactor Theory* (D. van Nostrand Co., Princeton N.J., 1952).
- [57] B. J. Ackerson, R. L. Dougherty, N. M. Reguigui, and U. Nobbman, *Correlation transfer: Application of radiative transfer solution methods to photon correlation problems*, J. Thermophys. and Heat Trans. **6**, 577 (1992).

- [58] R. L. Dougherty, B. J. Ackerson, N. M. Reguigui, F. Dorri-Nowkoorani, and U. Nobmann, *Correlation transfer: Development and application*, J. Quant. Spectrosc. Radiat. Transfer **52**, 713 (1994).
- [59] J. E. Fernandez and V. G. Molinari, *Diffusion of polarized photons in the frame of the transport theory*, Nuclear Instruments and Methods in Physics Research **73**, 341 (1993).
- [60] S. Chandrasekhar, in *Radiative Transfer* (Dover, New York, 1960).
- [61] R. Aronson, *Subcritical problems in spherical geometry*, Nuclear Science and Engineering **86**, 436 (1984).
- [62] M. D. Alexandrov, V. S. Remizovich, and D. B. Rogozkin, *Multiple light scattering in a two-dimensional medium with large scatterers*, J. Opt. Soc. Am. A **10**, 2602 (1993).
- [63] J. D. Jackson, in *Classical Electrodynamics* (Wiley and Sons Inc., New York, 1975).
- [64] K. Furutsu and Y. Yamada, *Diffusion approximation for a dissipative random medium and the applications*, Phys. Rev. E **50**, 3634 (1994).
- [65] A. H. Gandjbakhche, R. F. Bonner, and R. Nossal, *Scaling relationships for anisotropic random walks*, J. Stat. Phys. **69**, 35 (1992).
- [66] A. H. Gandjbakhche, R. Nossal, and R. F. Bonner, *Scaling relationships for theories of anisotropic random walks applied to tissue optics*, Applied Optics **32**, 504 (1993).
- [67] R. Graaff, M. H. Koelink, F. F. M. de Mul, W. G. Zijlstra, A. C. M. Dassel, and J. G. Aarnoudse, *Condensed Monte Carlo simulations for the description of light transport*, Applied Optics **32**, 426 (1993).

- [68] E. Gratton, W. Mantulin, M. J. van de Ven, J. Fishkin, M. Maris, and B. Chance, in *Proceedings of the Third International Conference: Peace through Mind/Brain Science* (Hamamatsu Photonics KK, Hamamatsu, 1990), p. 183.
- [69] For an interesting example of a diffusion wave in the context of heat conduction see A. Sommerfeld, in *Partial Differential Equations in Physics* (Academic Press, NY, 1949) p. 68.
- [70] A. M. Zhabotinsky, M. D. Eager, and I. R. Epstein, *Refraction and reflection of chemical waves*, Phys. Rev. Lett. **71**, 1526 (1993).
- [71] The Intralipid used here can be obtained from Kabi Pharmacia in Clayton, North Carolina.
- [72] H. J. van Staveren, C. J. M. Moes, J. van Marle, S. A. Prahl, and M. J. C. van Gemert, *Light scattering in Intralipid-10% in the wavelength range of 400-1100 nm*, Applied Optics **30**, 4507 (1991).
- [73] S. T. Flock, S. L. Jacques, B. C. Wilson, W. M. Star, and M. J. C. van Gemert, *Optical properties of Intralipid: A phantom medium for light propagation studies*, Lasers in Surgery and Medicine **12**, 510 (1992).
- [74] C. J. M. Moes, M. J. C. van Gemert, W. M. Star, J. P. A. Marijnissen, and S. A. Prahl, *Measurements and calculations of the energy fluence rate in a scattering and absorbing phantom at 633 nm*, Applied Optics **28**, 2292 (1989).
- [75] C. M. Hale and M. R. Querry, Applied Optics **12**, 555 (1973).
- [76] R. C. Haskell, L. O. Svaasand, T. Tsay, T. Feng, M. S. McAdams, and B. J. Tromberg, *Boundary conditions for the diffusion equation in radiative transfer*, J. Opt. Soc. of Am. A **11**, 2727 (1994).
- [77] R. Aronson, *Boundary conditions for diffusion of light*, J. Opt. Soc. of Am. A **12**, 2532 (1995).

- [78] S. Glasstone and M. C. Edlund, in *The Elements of Nuclear Reactor Theory* (D. van Nostrand Co., New York, 1952), Chap. 5 & 14.
- [79] K. M. Case and P. F. Zweifel, in *Linear Transport Theory* (Addison-Wesley, MA, 1967), Chap. 8.
- [80] E. Hecht, in *Optics* (Addison-Wesley, Reading, MA, 1987) Chapters 4, 5, 6.
- [81] J. D. Jackson, in *Classical Electrodynamics* (Wiley and Sons Inc., New York, 1975) ch. 9.
- [82] H. S. Carslaw and J. Jaeger, in *Conduction of heat in solids* (Oxford University Press, New York, 1986).
- [83] A. Ishimaru, in *Wave Propagation and Scattering in Random Media* (Academic Press, New York, 1978).
- [84] J. D. Jackson, in *Classical Electrodynamics* (Wiley and Sons Inc., New York, 1975) Chap. 3 & 16.
- [85] K. A. Kang, D. F. Bruley, J. M. Londono, and B. Chance, *Highly scattering optical system identification via frequency response analysis of NIR-TRS spectra*, Annals of Biomedical Engineering **22**, 240 (1994).
- [86] H. Liu, M. Miwa, B. Beauvoit, N. G. Wang, and B. Chance, *Characterization of absorption and scattering properties of small-volume biological samples using time-resolved spectroscopy*, Analytical Biochemistry **213**, 378 (1993).
- [87] J. M. Kaltenbach and M. Kaschke, *Frequency and time domain modelling of light transport in random media*, Medical Optical Imaging: Functional Imaging and Monitoring **SPIE IS11**, 65 (1993).
- [88] W. M. Star, *Comparing the P3-approximation with diffusion theory and with monte carlo calculations of light propagation in a slab geometry*, SPIE Institute Series **SPIE IS5**, 146 (1989).

- [89] D. Pattanayuk, General Electric Consumer Research and Development Report on *Resolution of optical images formed by diffusive waves in highly scattering media.*
- [90] J. A. Moon and J. Reintjes, *Image resolution by use of multiply scattered light*, Optics Letters **19**, 521 (1994).
- [91] A. H. Gandjbakhche, R. Nossal, and R. F. Bonner, *Resolution limits for optical transillumination of abnormalities deeply embedded in tissues*, Med. Phys. **21**, 185 (1994).
- [92] M. Essenpreis, C. E. Elwell, M. Cope, v. P, S. R. Arridge, and D. T. Delpy, *Spectral dependence of temporal point spread functions in human tissues*, Appl. Opt. **32**, 418 (1993).
- [93] D. G. Papaioannou, G. W. Thoof, J. J. M. Baselmans, and M. J. C. Vangemert, *Image quality in time resolved transillumination of highly scattering media*, Appl. Opt. **34**, 6144 (1995).
- [94] D. A. Boas, L. E. Campbell, and A. G. Yodh, *Scattering and imaging with diffusing temporal field correlations*, Phys. Rev. Lett. **75**, 1855 (1995).
- [95] P. R. Bevington, in *Data Reduction and Error Analysis for the Physical Sciences* (McGraw-Hill Book Company, NY, 1969).
- [96] Y. Yao, Y. Wang, R. L. Barbour, H. L. Graber, and J. Chang, *Scattering characteristics of photon density waves from an object embedded in a spherically two-layer turbid medium*, Proc. SPIE **2389**, 291 (1995).
- [97] P. N. Pusey and J. M. Vaughan, *Light Scattering and Intensity Fluctuation Spectroscopy*, in M. Davies, ed., *Dielectric and Related Molecular Processes - vol. 2 Specialist Periodical Report* (London, The Chemical Society, 1975).

- [98] H. Z. Cummings and H. L. Swinney, *Light beating spectroscopy*, Prog. Opt. **8**, 133 (1970).
- [99] W. B. Davenport and W. L. Root, in *An Introduction to the Theory of Random Signals and Noise* (McGraw-Hill, New York, 1958).
- [100] S. O. Rice in N. Wax, ed., *Noise and Stochastic Processes* (New York, Dover, 1954) p. 133.
- [101] P. N. Pusey, J. M. Vaughan, and D. V. Willets, *Effect of spatial incoherence of the laser in photon-counting spectroscopy*, J. Opt. Soc. Am. **73**, 1012 (1983).
- [102] T. Bellini, M. A. Glaser, N. A. Clark, and V. Degiorgio, *Effects of finite laser coherence in quasielastic multiple scattering*, Phys. Rev. A **44**, 5215 (1991).
- [103] R. Nossal, S. H. Chen, and C. C. Lai, *Use of laser scattering for quantitative determinations of bacterial motility*, Optics Communications **4**, 35 (1971).
- [104] X. L. Wu, D. J. Pine, P. M. Chaikin, J. S. Huang, and D. A. Weitz, *Diffusing-wave spectroscopy in a shear flow*, J. Opt. Soc. Am. B **7**, 15 (1990).
- [105] A. G. Yodh, P. D. Kaplan, and D. J. Pine, *Pulsed diffusing-wave spectroscopy: High resolution through nonlinear optical gating*, Phys. Rev. B **42**, 4744 (1990).
- [106] D. J. Pine, D. A. Weitz, J. X. Zhu, and E. Herbolzheimer, *Diffusing-wave spectroscopy: Dynamic light scattering in the multiple scattering limit*, J. Phys. France **51**, 2101 (1990).
- [107] K. Katayama, G. Nishimura, M. Kinjo, and M. Tamura, *Absorbance measurements in turbid media by the photon correlation method*, Appl. Optics **34**, 7419 (1995).
- [108] G. Nishimura, K. Katayama, M. Kinjo, and M. Tamura, *Diffusing-wave absorption spectroscopy in the homogeneous turbid media*, to be published in Optics Communications (1996).

- [109] M. J. Stephen, *Temporal fluctuations in wave propagation in random media*, Phys. Rev. B **37**, 1 (1988).
- [110] J. Z. Xue, D. J. Pine, S. T. Milner, X. L. Wu, and P. M. Chaikin, *Nonergodicity and light scattering from polymer gels*, Phys. Rev. A **46**, 6550 (1992).
- [111] K. Schatzel, *Accuracy of photon correlation measurements on nonergodic samples*, Applied Optics **32**, 3880 (1993).
- [112] J. G. H. Joosten, E. T. F. Gelade, and P. N. Pusey, *Dynamic light scattering by nonergodic media: Brownian particles trapped in polyacrylamide gels*, Phys. Rev. A **42**, 2161 (1990).
- [113] A. C. Kak and M. Slaney, in *Principles of Computerized Tomographic Imaging* (IEEE Press, New York, 1988).
- [114] D. Bicout and R. Maynard, *Diffusing wave spectroscopy in inhomogeneous flows*, Physica A **199**, 387 (1993).
- [115] D. Bicout and G. Maret, *Multiple light scattering in Taylor-Couette flow*, Physica A **210**, 87 (1994).
- [116] D. J. Bicout and R. Maynard, *Multiple light scattering in turbulent flow*, Physica B **204**, 20 (1995).
- [117] D. Bicout, *Non-newtonian behavior of colloidal suspensions from multiple light scattering*, Physics Letters A **180**, 375 (1993).
- [118] H. C. van de Hulst, in *Light Scattering by Small Particles* (Dover Publications Inc., NY, 1981).
- [119] D. J. Durian, *Accuracy of diffusing-wave spectroscopy theories*, Phys. Rev. E **51**, 3350 (1995).

- [120] A. A. Middleton and D. S. Fisher, *Discrete scatterers and autocorrelations of multiply scattered light*, Phys. Rev. B **43**, 5934 (1991).
- [121] C. E. Elwell, M. Cope, A. D. Edwards, J. S. Wyatt, D. T. Delpy, and E. O. R. Reynolds, *Quantification of adult cerebral hemodynamics by near-infrared spectroscopy*, J. Applied Physiology **77**, 2753 (1994).
- [122] American National Standards Institute, *American National Standard for Safe Use of Lasers*, (The Laser Institute of America, 1993) see table 7 and fig. 8a.
- [123] B. Chance, M. T. Dait, C. Zhang, T. Hamaoka, and F. Hagerman, *Recovery from exercise-induced desaturation in the quadriceps muscles of elite competitive rowers*, Am. J. Physiol. **262**, C766 (1992).
- [124] P. D. Line, K. K. Sorensen, and K. Kvernebo, *Postocclusive hyperemia in skin measured in pigs by laser Doppler - Influence of state of arterial-stenosis in the limb*, European Journal of Surgery **162**, 321 (1996).
- [125] D. Colin and J. L. Saumet, *Influence of external-pressure on transcutaneous oxygen-tension and laser-Doppler flowmetry on sacral skin*, Clinical Physiology **16**, 61 (1996).
- [126] N. C. Abbot and J. S. Beck, *Biological zero in laser Doppler measurements in normal ischemic and inflamed human skin*, International Journal of Microcirculation - Clinical and Experimental **12**, 89 (1993).
- [127] R. Pecora, in *Dynamic Light Scattering: Applications of Photon Correlation Spectroscopy* (Plenum Press, New York, 1985).
- [128] P. N. Pusey and R. J. A. Tough, in *Dynamic Light Scattering* (Plenum, New York, 1985).
- [129] H. A. Green, E. E. Burd, N. S. Nishioka, and C. C. Compton, *Skin-graft take and healing following 193-nm excimer, continuous-wave carbon dioxide (CO₂)*,

pulsed CO₂, or pulsed Holmium-YAG laser-ablation of the graft bed, Archives of Dermatology **129**, 979 (1993).

- [130] M. A. Afromowitz, G. S. Van, Liew, and D. Heimbach, *Clinical evaluation of burn injuries using an optical reflectance technique*, IEEE Trans. Biomed. Eng. **34**, 114 (1987).
- [131] M. A. Afromowitz, J. B. Callis, D. M. Heimbach, L. A. DeSoto, and M. K. Norton, *Multispectral imaging of burn wounds: A new clinical instrument for evaluating burn depth*, IEEE Trans. Biomed. Eng. **35**, 842 (1988).
- [132] J. E. Gatti, D. LaRoosa, D. G. Silverman, and C. E. Hartford, *Evaluation of the burn wound with perfusion fluorometry*, Journal of Trauma **23**, 202 (1983).
- [133] H. A. Green, D. Bua, R. R. Anderson, and N. S. Nishioka, *Burn depth estimation using indocyanine green fluorescence*, Arch. Dermatol. **128**, 43 (1992).
- [134] J. Micheels, B. Alsbjorn, and B. Sorensen, *Clinical use of laser Doppler flowmetry in a burns unit*, Scand. J. Plast. Reconstr. Surg. **18**, 65 (1984).
- [135] K. Waxman, N. Lefcourt, and B. Achauer, *Heated laser Doppler flow measurements to determine depth of burn injury*, Am. J. Surg. **157**, 541 (1989).
- [136] A. Sadhwani, K. T. Schomacker, G. J. Tearney, and N. S. Nishioka, *Determination of Burn Depth using Laser Speckle I. Experiments in Tissue Phantoms*, submitted to Applied Optics (1995).
- [137] M. Firbank and D. T. Delpy, *A design for a stable and reproducible phantom for use in near infra-red imaging and spectroscopy*, Phys. Med. Biol. **38**, 847 (1993).
- [138] M. Firbank, M. Oda, and D. T. Delpy, *An improved design for a stable and reproducible phantom material for use in near-infrared spectroscopy and imaging*, Phys. Med. Biol. **40**, 955 (1995).

- [139] S. L. Jacques and L. Wang, *Monte Carlo modeling of light transport in tissues*, in A. J. Welch and M. J. C. van Gemert, eds., *Optical-Thermal Response of Laser-Irradiated Tissue* (Plenum Press, New York, 1995) pp. 73-100.
- [140] L. Wang, S. L. Jacques, and L. Zheng, *MCML-Monte Carlo modeling of light transport in multi-layered tissues*, Computer Methods and Programs in Biomedicine **47**, 131 (1995).
- [141] L. G. Henyey and J. L. Greenstein, *Diffuse radiation in the galaxy*, Astrophys. J. **93**, 70-83 (1941).
- [142] J. Ricka, *Dynamic light scattering with single-mode and multimode fibers*, Applied Optics **32**, 2860 (1993).
- [143] E. R. Van Keuren, H. Wiese, and D. Horn, *Diffusing-wave spectroscopy in concentrated latex dispersions: An investigation using single-mode fibers*, Colloids and Surfaces A **77**, 29 (1993).
- [144] M. H. Koelink, F. F. M. de Mul, J. Greve, R. Graaff, A. C. M. Dassel, and J. G. Aarnoudse, *Laser Doppler blood flowmetry using two wavelengths: Monte Carlo simulations and measurements*, Appl. Opt. **33**, 3549 (1994).
- [145] C. S. Robertson, S. P. Gopinath, and B. Chance, *A new application for near-infrared spectroscopy: Detection of delayed intracranial hematomas after head injury*, Journal of Neurotrauma **12**, 591 (1995).
- [146] S. P. Gopinath, C. S. Robertson, C. F. Contant, R. K. Narayan, R. G. Grossman, and B. Chance, *Early detection of delayed traumatic intracranial hematomas using near-infrared spectroscopy*, J. Neurosurg. **83**, 438 (1995).
- [147] G. B. Arfken, in *Mathematical Methods for Physicists* (Academic Press, Orlando, 1985).

- [148] M. E. Rose, in *Elementary Theory of Angular Momentum* (Wiley and Sons Inc., New York, 1957).
- [149] W. H. Press, S. A. Teukolsky, W. T. Vetterling, and B. P. Flannery, in *Numerical Recipes in C: The Art of Scientific Computing* (Cambridge University Press, New York, 1992).